

LONGITUDINAL DOUBLE-SPIN ASYMMETRIES FOR DIJET
PRODUCTION AT INTERMEDIATE PSEUDORAPIDITY IN
POLARIZED P+P COLLISIONS AT $\sqrt{s} = 510$ GEV

Joseph H. Kwasizur

Submitted to the faculty of the University Graduate School

in partial fulfillment of the requirements

for the degree

Doctor of Philosophy

in the Department of Physics,

Indiana University

June 2021

Accepted by the Graduate Faculty, Indiana University, in partial fulfillment of the requirements of the degree of Doctor of Philosophy.

Doctoral Committee

Scott W. Wissink, Ph.D. (Chair)

Charles J. Horowitz, Ph.D

William W. Jacobs, Ph.D

Rex Tayloe, Ph.D

May 27, 2021

Copyright ©2021
Joseph H. Kwasizur

Acknowledgements

I would first like to thank my adviser, Scott Wissink, for his constant patience, guidance, and availability to answer questions throughout my thesis work. To Will Jacobs, thank you for many helpful discussions, for imparting your knowledge of the Endcap Electromagnetic Calorimeter, and for extra encouragement when necessary. To Charles Horowitz and Rex Tayloe, thank you for serving on my dissertation committee.

I am also very grateful to current members of the IU STAR/Belle group Dmitry Kalinkin, Huanzhao Liu, and Bill Solyst for many years of friendship and assistance, and former member Mike Skoby for his help early on in my graduate study. I am particularly grateful to former group member Ting Lin, whose thesis analysis paved the way for this one, and who answered many questions and gave many suggestions during his time at IU and after.

In addition, I would like to thank Elke Aschenauer, Carl Gagliardi, Oleg Eysler, Renee Fatemi, Brian Page, and all other members of the STAR Spin/Cold QCD Physics Working Group, for their guidance along the way. I especially want to thank Zilong Chang, who helped with several important components of my analysis of the 2012 RHIC run and was a great resource for anything to do with jet analyses in general, and Amilkar Quintero, whom I consulted with many times for my 2013 analysis.

Finally, to my parents and older brother, thank you for all the support and encouragement over the years.

Joseph H. Kwasizur

LONGITUDINAL DOUBLE-SPIN ASYMMETRIES FOR DIJET PRODUCTION AT
INTERMEDIATE PSEUDORAPIDITY IN POLARIZED P+P COLLISIONS AT $\sqrt{s} =$
510 GEV

The proton is a composite particle made up of smaller constituents called quarks and gluons. The proton's spin, a fundamental physical property of all particles, must therefore arise from the combination of the intrinsic spins and orbital motions of the quarks and gluons. The intrinsic quark contribution is known to be only about one-third of the total proton spin, and how the intrinsic gluon and orbital components make up the remainder is one of the most prominent open questions in nuclear physics. Measurements of spin asymmetries for jet and dijet production in polarized proton-proton collisions at the Relativistic Heavy Ion Collider provide a direct probe of the intrinsic gluon contribution.

We present the first measurement of the longitudinal double-spin asymmetry A_{LL} for dijets in the intermediate pseudorapidity range $0.9 < \eta < 1.8$ produced in polarized pp collisions at a center-of-mass energy of $\sqrt{s} = 510$ GeV. Values of A_{LL} are reported for several different event topologies, which are defined by the jet pseudorapidities and represent increasingly asymmetric partonic collisions. Dijet events where both jets have $0.9 < \eta < 1.8$ provide sensitivity for gluons with Bjorken- x below 0.01, a region where the gluon polarized distribution $\Delta g(x)$ is very poorly constrained. The measured asymmetries are mostly consistent with current theoretical predictions, and feature greatly enhanced statistical precision compared to the previous analysis of intermediate pseudorapidity dijet A_{LL} , which used data from pp collisions at $\sqrt{s} = 200$ GeV.

Table of Contents

List of Tables	x
List of Figures	xii
1 Introduction	1
1.1 Deep Inelastic Scattering and the Parton Model	2
1.2 Polarized DIS and Proton Spin Structure	6
1.3 Accessing Gluon Polarization at RHIC	7
1.3.1 Inclusive Jet Analyses	9
1.3.2 Dijet Analyses	12
1.3.3 Forward Dijets	15
1.3.4 Dijets at 510 GeV	16
1.4 Dissertation Structure	20
2 Experimental Facilities	23
2.1 The Relativistic Heavy Ion Collider	23
2.1.1 Polarized Proton Spin Dynamics During Acceleration	24
2.1.2 Measuring Beam Polarization	26
2.1.3 Zero-Degree Calorimeters	28

2.1.4	Beam-Beam Counters	29
2.1.5	Vertex Position Detectors	30
2.2	The Solenoidal Tracker at RHIC	31
2.2.1	Time Projection Chamber	31
2.2.2	Barrel Electromagnetic Calorimeter	32
2.2.3	Endcap Electromagnetic Calorimeter	33
2.2.4	EEMC Energy Calibration	34
2.2.5	STAR Trigger	41
3	Jet Reconstruction and Dijet Selection	45
3.1	Jet Reconstruction	45
3.1.1	Anti- k_T Algorithm	46
3.1.2	Jet Selection Criteria	47
3.2	Dijet Selection Criteria	49
3.3	Software Trigger Requirements	52
4	Data and Simulation Studies	55
4.1	Data Sample	55
4.1.1	Data Quality Assurance	56
4.2	Simulation Sample	61
4.2.1	Levels of Jet Information	61
4.3	Data-Simulation Comparison	62

5	Underlying Event	68
5.1	Off-Axis Cone Method	68
5.2	Underlying Event Correction	70
6	Experimental Methods in the EEMC	73
6.1	Challenges in the EEMC Region	73
6.2	Artificial Neural Networks	74
6.2.1	Neural Network Parameters and Training	75
6.3	Jet p_T Correction	76
6.4	Jet Invariant Mass Correction	84
7	Double-spin Asymmetries	88
7.1	Beam Polarizations	89
7.2	Spin Patterns	90
7.3	Relative Luminosities	91
7.4	False Asymmetries	92
7.5	Data Corrections	98
7.5.1	Dijet Invariant Mass Shift	98
7.5.2	Trigger and Reconstruction Bias	98
7.6	Systematic Errors	110
7.6.1	Jet Energy Scale	110
7.6.2	Tracking Efficiency Uncertainty	112
7.6.3	Dijet Mass Shift Systematic	114

7.6.4	Underlying Event Systematic Error on the Dijet Mass	114
7.6.5	PYTHIA Tune Uncertainty	114
7.7	Final Results	123
8	Conclusion	136
	APPENDICES	138
A	Lists of Runs and Fills	142
A.1	2012 Analysis	142
A.2	2013 Analysis	144
B	Dijet Invariant Mass Derivation	148
C	Lists of Removed Bunch Crossings	150
	References	152
	Curriculum Vitae	

List of Tables

2.1	Jet patch geometry.	42
2.2	2012 jet patch thresholds.	43
2.3	2013 jet patch thresholds.	43
7.1	The beam helicity combination at STAR associated with each Spin-4 value for the 2012 RHIC run.	90
7.2	The beam helicity combination at STAR associated with each Spin-4 value for the 2013 RHIC run.	91
7.3	Dijet parton level corrections for the Barrel-Endcap and Endcap-Endcap topolo- gies, 2012.	106
7.4	Dijet parton level corrections for the two Barrel-Endcap topologies, 2012. . .	107
7.5	Dijet parton level corrections for the Barrel-Endcap and Endcap-Endcap topolo- gies, 2013.	108
7.6	Dijet parton level corrections for the two Barrel-Endcap topologies, 2013. . .	109
7.7	The default Perugia2012 tune and some variants.	115
7.8	Dijet invariant mass systematics for the Barrel-Endcap and Endcap-Endcap topologies, 2012.	119
7.9	Dijet invariant mass systematics for the two Barrel-Endcap topologies, 2012.	120
7.10	Dijet invariant mass systematics for the Barrel-Endcap and Endcap-Endcap topologies, 2013.	121

7.11	Dijet invariant mass systematics for the two Barrel-Endcap topologies, 2013.	122
7.12	Final dijet A_{LL} for the Barrel-Endcap and Endcap-Endcap topologies, 2012.	130
7.13	Final dijet A_{LL} for the two Barrel-Endcap topologies, 2012.	131
7.14	Final dijet A_{LL} for the Barrel-Endcap and Endcap-Endcap topologies, 2013.	132
7.15	Final dijet A_{LL} for the two Barrel-Endcap topologies, 2013.	133
7.16	Final dijet A_{LL} for the Barrel-Endcap and Endcap-Endcap topologies, 2012+2013.	134
7.17	Final dijet A_{LL} for the two Barrel-Endcap topologies, 2012+2013.	135
C.1	Bunch crossings removed for the 2012 analysis.	150
C.2	Bunch crossings removed for the 2013 analysis.	151

List of Figures

1.1	Schematic diagram of DIS at leading order, showing the exchange of a virtual photon between a lepton and a quark inside a hadron, and the subsequent breakup of the hadron into fragments.	3
1.2	The proton inelastic structure function F_2 as a function of Q^2 for a range of fixed x values [12].	5
1.3	The proton structure function g_1 as a function of Q^2 for a range of fixed x values [23].	8
1.4	The fractions of partonic scattering subprocesses which contribute to jet production at RHIC kinematics, as functions of jet x_T [26], [27].	10
1.5	Gluon polarized distributions at $Q^2 = 10 \text{ GeV}^2$ for DSSV analysis without (DSSV, DSSV*) and with (NEW FIT) the RHIC 2009 polarized pp data [28].	11
1.6	Fit central values and 90% C.L. for integrals of $\Delta g(x, Q^2 = \text{GeV}^2)$ over two ranges in momentum fraction x . Results for DSSV, DSSV*, and the NEW FIT are shown [28].	12
1.7	Distributions of gluon x_1 and x_2 obtained from PYTHIA simulation for same sign in pseudorapidity (upper) and opposite sign in pseudorapidity (lower) dijet events, compared with the gluon x distributions for inclusive jets [32]. .	14
1.8	Measured dijet A_{LL} vs. invariant mass for events with the same sign (upper) and opposite sign (lower) in pseudorapidity, from 2009 STAR data [32]. . . .	16

1.9	Measured dijet cross section vs. invariant mass from 2009 STAR data. The lower panel shows a relative comparison between the experimental results and theoretical predictions [32].	17
1.10	Distributions of parton x_1 and x_2 , weighted by partonic \hat{a}_{LL} , from simulation at $\sqrt{s} = 200$ GeV for different jet pseudorapidity ranges [34].	18
1.11	Measured dijet A_{LL} vs. partonic invariant mass for different jet pseudorapidity ranges, from 2009 STAR data at 200 GeV [34]. The curves represent theoretical predictions of A_{LL} for the DSSV2014 [28] and NNPDFpol1.1 [29] parton distributions.	19
1.12	Distributions of parton x_1 and x_2 from leading order simulation at $\sqrt{s} = 510$ GeV for different jet pseudorapidity ranges [36]. “Topology A” corresponds to dijets with $0.3 < \eta_{3,4} < 0.9$ and $\eta_3 \cdot \eta_4 > 0$; “Topology B” to dijets with $ \eta_{3,4} < 0.3$ and $0.3 < \eta_{4,3} < 0.9$; “Topology C” to dijets with $ \eta_{3,4} < 0.3$; “Topology D” to dijets with $0.3 < \eta_{3,4} < 0.9$ and $\eta_3 \cdot \eta_4 < 0$	21
1.13	Measured dijet A_{LL} vs. partonic invariant mass for different jet pseudorapidity ranges, from 2012 STAR data at 510 GeV [36]. The η ranges associated with each Topology are explained in the caption of Fig. 1.12	22
2.1	Layout of RHIC, with the components that are necessary for polarized pp operation pointed out [37].	24
2.2	A cross-sectional view of the RHIC proton-Carbon polarimeter.	27
2.3	Schematic diagram of the RHIC hydrogen gas jet polarimeter.	28
2.4	Schematic of the Beam-Beam Counters, showing the inner and outer tiles [45].	29
2.5	Schematic of a Vertex Position Detector, showing the 19 individual detectors arrayed around the beam pipe [46].	30
2.6	Cross sectional view of the STAR detector subsystems.	31

2.7	Side view of a BEMC module. The left figure illustrates the projective nature of the towers, while the right figure shows the module’s construction in more detail [50].	33
2.8	Detailed structure of the EEMC. The left figure gives a beam’s-eye view of half of the detector with the towers indicated, while the right figure shows a cutaway view of the lead-scintillator stack [51].	35
2.9	2012 $pp510$ tower gains vs. each tower’s η bin.	37
2.10	2013 $pp510$ tower gains vs. each tower’s η bin.	37
2.11	Histograms and fits of the ratio of calibrated tower gain over ideal gain, for the four quarters of the 2012 $pp510$ running period.	38
2.12	Histograms and fits of the ratio of calibrated tower gain over ideal gain, for the four quarters of the 2013 $pp510$ running period.	39
2.13	2012 $pp510$ tower gain decrease over time.	39
2.14	2013 $pp510$ tower gain decrease over time.	39
2.15	Rate of 2012 $pp510$ tower gain decrease as a function of pseudorapidity. . . .	41
2.16	Rate of 2012 $pp510$ tower gain decrease for each sector of azimuthal angle. . .	41
2.17	Rate of 2013 $pp510$ tower gain decrease as a function of pseudorapidity. . . .	41
2.18	Rate of 2013 $pp510$ tower gain decrease for each sector of azimuthal angle. . .	41
3.1	Correlation between the p_T of the highest p_T track (the “hi track”) and the p_T of the jet containing it, from data.	51
3.2	Correlation between the p_T of the highest p_T track (the “hi track”) and the p_T of the jet containing it, from simulation.	52

4.1	Selected plots from the QA of dijets in the 2012 sample. The points indicate the average value per event of the specified quantity for one run. Plots of jet quantities like p_T and neutral fraction are inspected separately for the high and low p_T jets in the dijet pair.	58
4.2	Selected plots from the event-level QA for the 2013 sample. The points indicate the average value per event of the specified quantity for one run. The variables of interest are examined separately for each trigger category; the figures shown here are for JP2.	59
4.3	Selected plots from the jet-level QA for the 2013 sample. The points indicate the average value per event of the specified quantity for one run. The variables of interest are examined separately for Barrel and Endcap jets, as well as for each trigger category; the figures shown here are for Endcap jets in JP2 events. Several outliers are clearly visible in each of the plots; those runs were examined individually and typically discarded.	60
4.4	Z-vertex distribution for JP2 in 2012.	64
4.5	Z-vertex distribution for JP2 in 2013.	64
4.6	Dijet invariant mass distribution for JP2 in 2012.	64
4.7	Dijet invariant mass distribution for JP2 in 2013.	64
4.8	High p_T jet p_T distribution for JP2 in 2012.	65
4.9	Low p_T jet p_T distribution for JP2 in 2012.	65
4.10	High p_T jet p_T distribution for JP2 in 2013.	65
4.11	Low p_T jet p_T distribution for JP2 in 2013.	65
4.12	High p_T jet η distribution for JP2 in 2012.	66
4.13	Low p_T jet η distribution for JP2 in 2012.	66

4.14	High p_T jet ϕ distribution for JP2 in 2012.	66
4.15	Low p_T jet ϕ distribution for JP2 in 2012.	66
4.16	High p_T jet η distribution for JP2 in 2013.	67
4.17	Low p_T jet η distribution for JP2 in 2013.	67
4.18	High p_T jet ϕ distribution for JP2 in 2013.	67
4.19	Low p_T jet ϕ distribution for JP2 in 2013.	67
5.1	Diagram of the off-axis cone method, showing a jet and its associated cones.	69
5.2	The amount of jet p_T subtracted off by the underlying event correction (dPt) vs. jet p_T , for Barrel (left) and Endcap (right) jets in a subset of Barrel-Endcap events from 2012 data. The units of the vertical and horizontal axes are GeV.	71
5.3	Shifts in jet ϕ due to the underlying event subtraction, $d\text{Phi} = \text{Phi}(\text{uncorrected}) - \text{Phi}(\text{corrected})$	72
5.4	Shifts in jet η due to the underlying event subtraction, $d\text{Eta} = \text{Eta}(\text{uncorrected}) - \text{Eta}(\text{corrected})$	72
6.1	Plot from simulation showing the percentage of tracks which are successfully reconstructed as a function of track pseudorapidity.	74
6.2	Multilayer Perceptron ANN with one hidden layer [63].	75
6.3	Jet particle/detector p_T ratio vs. detector η , before (left) and after (right) the machine learning p_T shift. The top, middle, and bottom rows show results for Barrel jets, Endcap jets in Barrel-Endcap events, and Endcap-Endcap jets, respectively. In each plot, the black symbols and vertical bars indicate the mean and RMS, respectively, of the distribution in each bin. Events are from the 2012 embedding sample.	79

6.4	Jet particle/detector p_T ratio vs. detector η , before (left) and after (right) the machine learning p_T shift. The top, middle, and bottom rows show results for Barrel jets, Endcap jets in Barrel-Endcap events, and Endcap-Endcap jets, respectively. In each plot, the black symbols and vertical bars indicate the mean and RMS, respectively, of the distribution in each bin. Events are from the 2013 embedding sample.	80
6.5	Barrel jet particle/detector p_T ratio vs. detector η , for the Training (left) and Testing (right) samples. The top row shows results from training the trigger samples separately; the bottom row from training all trigger samples together. In each plot, the black symbols and vertical bars indicate the mean and RMS, respectively, of the distribution in each bin.	81
6.6	Endcap jet from Barrel-Endcap events particle/detector p_T ratio vs. detector η , for the Training (left) and Testing (right) samples. The top row shows results from training the trigger samples separately; the bottom row from training all trigger samples together. In each plot, the black symbols and vertical bars indicate the mean and RMS, respectively, of the distribution in each bin.	82
6.7	Endcap jet particle/detector p_T ratio vs. detector η , for the Training (left) and Testing (right) samples. The top row shows results from training the trigger samples separately; the bottom row from training all trigger samples together. In each plot, the black symbols and vertical bars indicate the mean and RMS, respectively, of the distribution in each bin.	83
6.8	Relative difference in p_T for Barrel-Endcap dijets in 2012, for data (points) and simulation (histograms).	84
6.9	Relative difference in p_T for Barrel-Endcap dijets in 2013, for data (points) and simulation (histograms).	84

6.10	Jet particle/detector invariant mass ratio vs. detector η , before (left) and after (right) the machine learning mass shift. The top, middle, and bottom rows show results for Barrel jets, Endcap jets in Barrel-Endcap events, and Endcap-Endcap jets, respectively. In each plot, the black symbols and vertical bars indicate the mean and RMS, respectively, of the distribution in each bin. Events are from the 2012 embedding sample.	86
6.11	Jet particle/detector invariant mass ratio vs. detector η , before (left) and after (right) the machine learning mass shift. The top, middle, and bottom rows show results for Barrel jets, Endcap jets in Barrel-Endcap events, and Endcap-Endcap jets, respectively. In each plot, the black symbols and vertical bars indicate the mean and RMS, respectively, of the distribution in each bin. Events are from the 2013 embedding sample.	87
7.1	False asymmetries for all Barrel-Endcap dijets, 2012.	94
7.2	False asymmetries for East Barrel-Endcap dijets, 2012.	94
7.3	False asymmetries for West Barrel-Endcap dijets, 2012.	95
7.4	False asymmetries for Endcap-Endcap dijets, 2012.	95
7.5	False asymmetries for all Barrel-Endcap dijets, 2013.	96
7.6	False asymmetries for East Barrel-Endcap dijets, 2013.	96
7.7	False asymmetries for West Barrel-Endcap dijets, 2013.	97
7.8	False asymmetries for Endcap-Endcap dijets, 2013.	97
7.9	Mass shifts for all Barrel-Endcap (upper left), East Barrel-Endcap (upper right), West Barrel-Endcap (lower left) and Endcap-Endcap (lower right) dijets, 2012.	99

7.10	Mass shifts for all Barrel-Endcap (upper left), East Barrel-Endcap (upper right), West Barrel-Endcap (lower left) and Endcap-Endcap (lower right) dijets, 2013.	99
7.11	Trigger and reconstruction bias for Barrel-Endcap full topology in 2012: parton level dijet A_{LL} for 100 NNPDF replicas (upper left), detector level dijet A_{LL} for replicas (upper right), parton level polynomial fit (lower left), and final corrections (lower right).	102
7.12	Trigger and reconstruction bias for East Barrel-Endcap topology in 2012: parton level dijet A_{LL} for 100 NNPDF replicas (upper left), detector level dijet A_{LL} for replicas (upper right), parton level polynomial fit (lower left), and final corrections (lower right).	102
7.13	Trigger and reconstruction bias for West Barrel-Endcap topology in 2012: parton level dijet A_{LL} for 100 NNPDF replicas (upper left), detector level dijet A_{LL} for replicas (upper right), parton level polynomial fit (lower left), and final corrections (lower right).	103
7.14	Trigger and reconstruction bias for Endcap-Endcap topology in 2012: parton level dijet A_{LL} for 100 NNPDF replicas (upper left), detector level dijet A_{LL} for replicas (upper right), parton level polynomial fit (lower left), and final corrections (lower right).	103
7.15	Trigger and reconstruction bias for Barrel-Endcap full topology in 2013: parton level dijet A_{LL} for 100 NNPDF replicas (upper left), detector level dijet A_{LL} for replicas (upper right), parton level polynomial fit (lower left), and final corrections (lower right).	104

7.16	Trigger and reconstruction bias for East Barrel-Endcap topology in 2013: parton level dijet A_{LL} for 100 NNPDF replicas (upper left), detector level dijet A_{LL} for replicas (upper right), parton level polynomial fit (lower left), and final corrections (lower right).	104
7.17	Trigger and reconstruction bias for West Barrel-Endcap topology in 2013: parton level dijet A_{LL} for 100 NNPDF replicas (upper left), detector level dijet A_{LL} for replicas (upper right), parton level polynomial fit (lower left), and final corrections (lower right).	105
7.18	Trigger and reconstruction bias for Endcap-Endcap topology in 2013: parton level dijet A_{LL} for 100 NNPDF replicas (upper left), detector level dijet A_{LL} for replicas (upper right), parton level polynomial fit (lower left), and final corrections (lower right).	105
7.19	Average detector to parton level dijet invariant mass shifts, for jets reconstructed with full set of TPC tracks (red points) and a partial set of TPC tracks (blue points). Results for the Barrel-Endcap full topology are shown in the upper left; for East Barrel-Endcap in the upper right; for West Barrel-Endcap in the lower left; for Endcap-Endcap in the lower right.	113
7.20	Change in dijet invariant mass due to underlying event correction for 2012 data (red) and simulation (blue). Results shown for Barrel-Endcap full (upper left), East Barrel-Endcap (upper right), West Barrel-Endcap (lower left), and Endcap-Endcap (lower right) topologies.	115
7.21	Change in dijet invariant mass due to underlying event correction for 2013 data (red) and simulation (blue). Results shown for Barrel-Endcap full (upper left), East Barrel-Endcap (upper right), West Barrel-Endcap (lower left), and Endcap-Endcap (lower right) topologies.	116

7.22	Dijet invariant mass shifts between parton and underlying event corrected particle level, for the various PYTHIA tunes in 2012. Results for the Barrel-Endcap full topology are shown in the upper left; for East Barrel-Endcap in the upper right; for West Barrel-Endcap in the lower left; for Endcap-Endcap in the lower right.	117
7.23	Dijet invariant mass shifts between parton and underlying event corrected particle level, for the various PYTHIA tunes in 2013. Results for the Barrel-Endcap full topology are shown in the upper left; for East Barrel-Endcap in the upper right; for West Barrel-Endcap in the lower left; for Endcap-Endcap in the lower right.	118
7.24	Dijet A_{LL} versus parton-level dijet invariant mass for the Barrel-Endcap full topology in 2012.	124
7.25	Dijet A_{LL} versus parton-level dijet invariant mass for the Endcap-Endcap topology in 2012.	124
7.26	Dijet A_{LL} versus parton-level dijet invariant mass for the East Barrel-Endcap (upper plot) and West Barrel-Endcap (lower plot) topologies in 2012.	125
7.27	Dijet A_{LL} versus parton-level dijet invariant mass for the Barrel-Endcap full topology in 2013.	126
7.28	Dijet A_{LL} versus parton-level dijet invariant mass for the Endcap-Endcap topology in 2013.	126
7.29	Dijet A_{LL} versus parton-level dijet invariant mass for the East Barrel-Endcap (upper plot) and West Barrel-Endcap (lower plot) topologies in 2013.	127
7.30	Dijet A_{LL} versus parton-level dijet invariant mass for the Barrel-Endcap full topology for the combined 2012+2013 sample.	128
7.31	Dijet A_{LL} versus parton-level dijet invariant mass for the Endcap-Endcap topology for the combined 2012+2013 sample.	128

7.32	Dijet A_{LL} versus parton-level dijet invariant mass for the East Barrel-Endcap (upper plot) and West Barrel-Endcap (lower plot) topologies for the combined 2012+2013 sample.	129
8.1	Distributions of parton x_1 and x_2 from leading order simulation at $\sqrt{s} = 510$ GeV for East Barrel-Endcap (upper plot), West Barrel-Endcap (middle plot), and Endcap-Endcap (lower plot) topologies. x_1 is always associated with the parton initially moving toward the Endcap.	139
8.2	Dijet A_{LL} versus parton-level dijet invariant mass divided by \sqrt{s} , for the 2009 [34] and 2012+2013 datasets. Results are shown for the East Barrel-Endcap (top plot), West Barrel-Endcap (middle plot), and Endcap-Endcap (bottom plot) topologies. Note the 2009 analysis used $\eta = 0.8$ as the cutoff between Barrel and Endcap jets.	140
8.3	NNLO parton distribution functions from the MSHT20 global analysis [71], at two different values of Q^2 . The width of each line is the uncertainty in the PDF for that parton.	141

CHAPTER 1

Introduction

Protons are the charged particles present in the nucleus of every atom. Their positive charge binds electrons in orbits about the nucleus, thus allowing atoms to bond together and form the structures we see all around us. The proton was discovered in 1917, when Ernest Rutherford experimented with shooting alpha particles through nitrogen gas and detected hydrogen. This meant that the hydrogen nucleus must be present in the nuclei of other atoms and, realizing it to be a building block of other atomic nuclei, Rutherford renamed it the proton.

Since its discovery, the proton has been studied extensively. Various experiments have determined large-scale properties like its mass and charge radius, as well as the fact that it is actually a composite particle made up of smaller constituents. Theoretical advances resulted in the formulation of Quantum Chromodynamics (QCD) to describe the interactions among these constituents, called quarks and gluons. However, there are still missing pieces in our knowledge of the proton's internal structure. One such gap is the issue of how the spins of the quarks and gluons, collectively called partons, contribute to the total spin of the proton itself. The measurement described in this thesis is meant to provide insight into how the gluon's intrinsic spin contributes to the total proton spin.

1.1 Deep Inelastic Scattering and the Parton Model

Much of what we know about the proton's substructure comes from Deep Inelastic Scattering (DIS). The first DIS experiments were carried out in 1968 at the Stanford Linear Accelerator Center (SLAC) [1], [2]. Overviews of the process can be found in, for example, [3], [4] and [5]. In DIS, a high energy lepton is scattered off of a hadron, in this case a proton. The lepton transfers a large amount of momentum Q to the proton by exchanging a virtual photon with one of the quarks inside the proton. That quark is knocked out of the proton, which subsequently breaks up. A schematic diagram of this process is shown in Fig. 1.1. The DIS cross section is given in Eq. 1.1, where α is the fine structure constant, E' is the energy of the scattered lepton, Q is the momentum transfer, θ is the lepton scattering angle, and W_1 and W_2 are the inelastic structure functions.

$$\frac{d^2\sigma}{d\Omega dE'} = \frac{4\alpha^2(E')^2}{Q^4} \left(2W_1 \sin^2 \frac{\theta}{2} + W_2 \cos^2 \frac{\theta}{2} \right) \quad (1.1)$$

The inelastic structure functions W_1 and W_2 are functions of two variables: $x = \frac{Q^2}{2M\nu}$, where $\nu = E - E'$ is the amount of energy lost by the scattered lepton, and Q^2 . The variable x is known as Bjorken- x after James Bjorken, who in 1968 proposed that the structure functions might depend solely on x in the limit of $Q^2 \rightarrow \infty$ and $\nu \rightarrow \infty$ with x held constant [6]. In the Bjorken limit, the structure functions can be rewritten as:

$$F_1(x, Q^2) = \frac{1}{4\pi} W_1(x, Q^2) \quad (1.2a)$$

$$F_2(x, Q^2) = \frac{Q^2}{8\pi x} W_2(x, Q^2). \quad (1.2b)$$

Early measurements at SLAC found F_1 and F_2 to be almost independent of Q^2 [4], [7], as Bjorken had predicted. The approximate independence of the structure functions on the momentum transfer, known as Bjorken scaling, means that the proton's internal structure

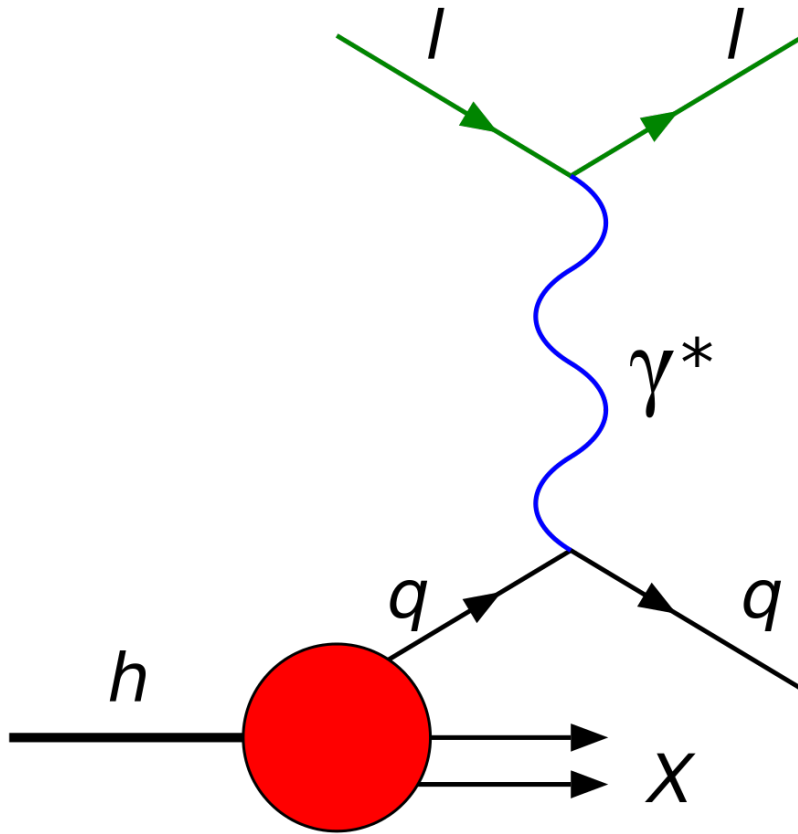


Figure 1.1: Schematic diagram of DIS at leading order, showing the exchange of a virtual photon between a lepton and a quark inside a hadron, and the subsequent breakup of the hadron into fragments.

looks the same regardless of how hard it is struck by the lepton, and strongly implies that the proton contains point-like constituents. Data for the proton inelastic structure function F_2 from several DIS experiments are shown in Fig. 1.2 to illustrate Bjorken scaling. The SLAC DIS experiments also found that, for values of Q^2 greater than a few GeV^2 , F_1 and F_2 satisfy the Callan-Gross relation:

$$F_2(x, Q^2) = 2xF_1(x, Q^2). \quad (1.3)$$

Around the same time as Bjorken's prediction of scaling and the SLAC DIS experiments, Richard Feynman and others developed the parton model [8]. The parton model describes

hadrons like protons and neutrons as composite particles made up of a collection of effectively free, point-like constituents called partons. In this model the cross section for deep inelastic scattering can be thought of as the incoherent sum of the cross sections for elastic scattering of a lepton off of the hadron’s constituent partons. To calculate the lepton-hadron cross section, the parton model introduces parton distribution functions to describe the proton’s substructure. The parton distribution functions $f_j(x)$ give the probability to find a parton of type j inside the proton carrying a fraction x of the proton’s momentum. Note that, in a reference frame where the proton has infinite momentum, Bjorken- x is the fraction of the proton’s momentum carried by the struck parton. This “infinite momentum frame” is a valid approximation at high energies, so the momentum fraction x and Bjorken- x are often used interchangeably. The inelastic structure functions can be written in terms of the parton distribution functions and the parton’s electric charges Q_j as:

$$F_1(x) = \frac{1}{2} \sum_j Q_j^2 f_j(x) \tag{1.4a}$$

$$F_2(x) = x \sum_j Q_j^2 f_j(x). \tag{1.4b}$$

So the parton model satisfies the Callan-Gross relation (Eq. 1.2) and permits the study of the proton’s internal structure through the inelastic structure functions. Since Callan-Gross holds for spin one-half particles, the partons in Feynman’s model were linked to the quarks whose existence was postulated in 1964 by Murray Gell-Mann and George Zweig [9], [10]. The existence of anti-quarks at low values of x was also determined from DIS data; the anti-quarks exist in pairs with quarks in the “sea”. The fact that the quarks and anti-quarks only account for about 50% of the proton’s total momentum suggested that gluons, postulated as the neutral bosons that mediated the strong force, might carry the rest [11]. Following in the footsteps of Quantum Electrodynamics, the relativistic quantum field theory of electromagnetism, QCD developed alongside these experimental studies to explain the Strong Force interactions among quarks and gluons. We should note that QCD predicts

small violations of Bjorken scaling due to the gluons, which can be seen in Fig. 1.2 as a logarithmic dependence of F_2 on Q^2 . Studying these scaling violations can therefore provide information on the gluon parton distribution functions as well.

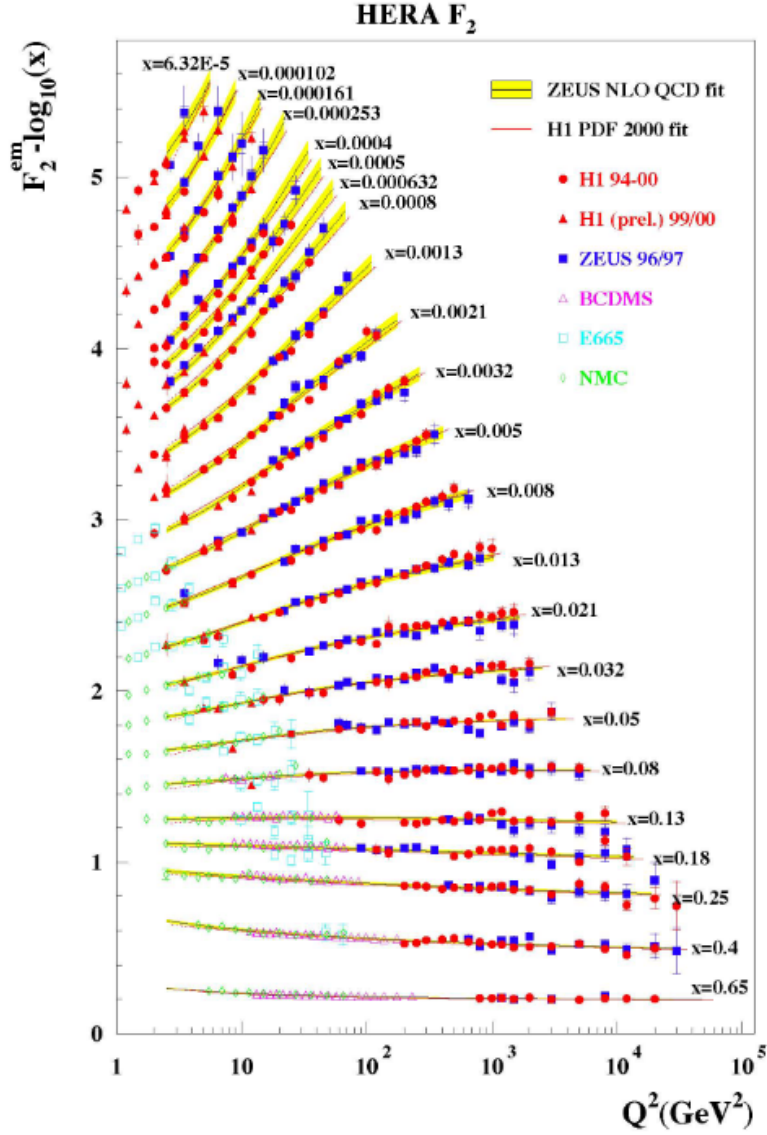


Figure 1.2: The proton inelastic structure function F_2 as a function of Q^2 for a range of fixed x values [12].

1.2 Polarized DIS and Proton Spin Structure

As discussed in the previous section, DIS experiments allowed physicists to probe the proton's fundamental constituents, along with how those constituents account for the proton's total momentum. However, that discussion assumed that the scattered lepton and target proton were unpolarized. In order to study the spin structure of the proton, a new tool was needed: polarized DIS. Overviews of polarized DIS can be found in [13], [14], [15], [16], [17].

The formalism for polarized DIS closely follows that for unpolarized DIS. For a longitudinally polarized lepton scattering off of a longitudinally polarized proton, the difference between the cross sections when the lepton and proton spins are parallel and anti-parallel is

$$\frac{d^2\sigma^A}{d\Omega dE'} - \frac{d^2\sigma^P}{d\Omega dE'} = \frac{4\alpha^2 E'}{Q^2 E} [(E + E' \cos \theta)mG_1 - Q^2 G_2]. \quad (1.5)$$

Here σ^A denotes the cross section when the lepton and proton spins are anti-parallel and σ^P denotes the cross section when the spins are parallel. In the Bjorken limit, the structure functions G_1 and G_2 can be written in terms of two new functions $g_1(x)$ and $g_2(x)$ which depend only on x . Then, in analogy with $F_1(x)$, $g_1(x)$ can be written in terms of polarized parton distribution functions:

$$g_1(x) = \frac{1}{2} \sum_j e_j^2 [\Delta q_j(x) + \Delta \bar{q}_j(x)]. \quad (1.6)$$

It turns out that the function $g_2(x)$ is zero in the Bjorken limit; it does not have a simple interpretation in the parton model, and is not relevant to the discussion here. The polarized parton distribution functions $\Delta q_j(x)$ and $\Delta \bar{q}_j(x)$ give the probability of finding a given parton at a certain momentum x with spin parallel to that of the proton, minus the probability of finding a parton at the same momentum with spin anti-parallel to that of the proton. So, polarized DIS gives insight into how the quark and anti-quark spins contribute to the proton's total spin. In the late 1980s the European Muon Collaboration at CERN measured $g_1(x)$ for

x between 0.01 and 0.7, and determined that quarks and anti-quarks only carried about 20% of the proton’s spin [18], [19]. This value was incompatible with a theoretical prediction by Jaffe and Ellis [20]. The unexpectedly small contribution to the proton spin from the quarks and anti-quarks, along with the mismatch between theory and experiment, was dubbed the “Proton Spin Crisis” and sparked a great deal of interest and research.

A few years later, Jaffe and Manohar showed that the proton’s total spin could be decomposed into individual contributions from the quark and gluon intrinsic spins and orbital angular momenta [21]. This “sum rule” is given in Eq. 1.7 below.

$$\langle S_P \rangle = \frac{1}{2} = \frac{1}{2} \Delta \Sigma + \Delta G + L_q + L_g \quad (1.7)$$

Here $\Delta \Sigma \equiv \int_0^1 (\Delta u(x) + \Delta \bar{u}(x) + \Delta d(x) + \Delta \bar{d}(x) + \Delta s(x) + \Delta \bar{s}(x)) dx$ is the contribution from the light quark intrinsic spins, $\Delta G = \int_0^1 \Delta g(x) dx$ is the contribution from the gluon intrinsic spins, and L_q and L_g are the contributions from the quark and gluon orbital angular momenta, respectively. The value of $\Delta \Sigma$ is known from polarized DIS data to be about 0.37, meaning that the quarks and anti-quark intrinsic spins account for 37% of the total spin of the proton. Scaling violations of g_1 can provide some insight into the intrinsic gluon spin contribution, just as scaling violations of F_2 did for gluon momentum, but data on g_1 (Fig. 1.3) do not cover a large enough kinematic range and are not of sufficient statistical precision to place significant constraints on ΔG [22]. The limited Q^2 reach of polarized DIS experiments was a primary reason for establishing the polarized proton-proton program at the Relativistic Heavy Ion Collider (RHIC), which produced the data analyzed in this dissertation and is the focus of the following section.

1.3 Accessing Gluon Polarization at RHIC

The spin physics program at RHIC consists of several independent programs focusing on different pieces of the proton spin puzzle [24]. These include studies of $W^{+/-}$ boson produc-

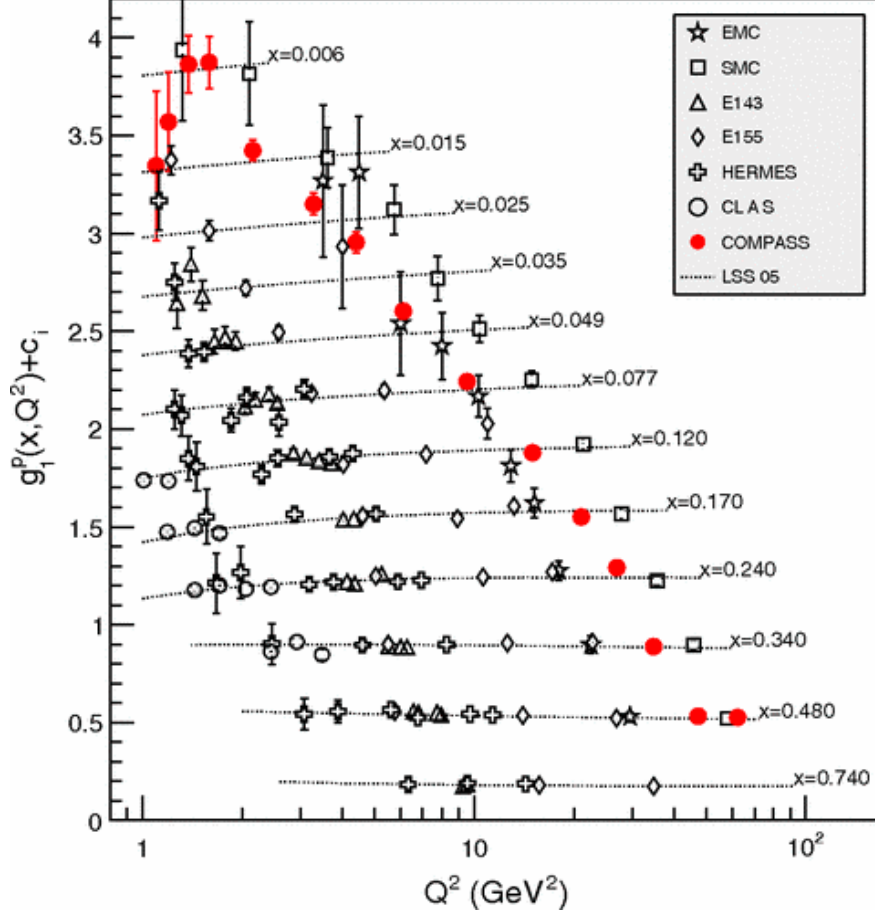


Figure 1.3: The proton structure function g_1 as a function of Q^2 for a range of fixed x values [23].

tion to access sea quark and anti-quark polarized distribution functions, of inclusive hadron and di-hadron production to gain insight into the proton's transverse spin structure, and of the intrinsic gluon spin contribution to the proton's spin. This dissertation will focus on the measurement of an observable that is central to the gluon spin area of study.

In the RHIC spin program, longitudinally polarized proton-proton collisions provide a direct probe of $\Delta g(x, Q^2)$ through quark-gluon and gluon-gluon scattering. The observable most sensitive to $\Delta g(x, Q^2)$ is the longitudinal double-spin asymmetry A_{LL} . A_{LL} is defined in terms of helicity-dependent cross sections as:

$$A_{LL} \equiv \frac{\sigma_{++} - \sigma_{+-}}{\sigma_{++} + \sigma_{+-}}. \quad (1.8)$$

Here σ_{++} and σ_{+-} are the cross sections for scattering of partons from colliding protons with equal and opposite helicities, respectively. Factorizing Eq. 1.8 into perturbative and non-perturbative terms shows why A_{LL} is directly sensitive to the gluon polarized parton distribution:

$$A_{LL} = \frac{\sum_{abc} \Delta f_a \otimes \Delta f_b \otimes d\hat{\sigma}^{f_a f_b \rightarrow f_c x} \hat{a}_{LL}^{f_a f_b \rightarrow f_c x} \otimes D_{f_c}^h}{\sum_{abc} f_a \otimes f_b \otimes d\hat{\sigma}^{f_a f_b \rightarrow f_c x} \otimes D_{f_c}^h}. \quad (1.9)$$

The $\hat{\sigma}$ and \hat{a}_{LL} terms represent the cross section and the double-helicity asymmetry, respectively, for the partonic hard scattering, and are calculable in perturbative QCD [17]. RHIC collides beams of polarized protons at center-of-mass energies of 200 and 510 GeV, both of which are high enough to be in the perturbative regime. The $D_{f_c}^h$ terms are fragmentation functions, which give the probability for a parton c to fragment into a hadron h . The $f_{a,b}$ terms are the unpolarized parton distribution functions for the colliding partons, and are very precisely known [25]. Lastly, the $\Delta f_{a,b}$ terms are the polarized parton distribution functions for the colliding partons. In quark-gluon and gluon-gluon scattering, then, at least one of these terms will be $\Delta g(x, Q^2)$.

1.3.1 Inclusive Jet Analyses

STAR and PHENIX, the two major experiments at RHIC, have both measured A_{LL} for inclusive hadron and jet production to probe $\Delta g(x, Q^2)$. Since this dissertation presents an analysis of a jet measurement at STAR, though, the remainder of this chapter will focus solely on STAR jet analyses. An overview of the STAR detector, as well as of RHIC in general, will be given in Chapter 2. A jet is a collimated beam of particles that forms when a hard-scattered quark or gluon hadronizes. Jets from pp collisions at RHIC kinematics arise predominantly from quark-gluon and gluon-gluon scattering (see Fig. 1.4), and are therefore a convenient way to probe $\Delta g(x, Q^2)$.

The first STAR jet analyses were inclusive studies. Inclusive jet measurements consider all the jets that arise from a given pp collision, and thus the measured A_{LL} integrates over large

ranges of x and Q^2 , in addition to including contributions from several different subprocesses. In order to specifically extract $\Delta g(x, Q^2)$ from such a measurement, theory groups carry out a “QCD global analysis”. These global analyses tune the parameters of an assumed functional form for the gluon polarized distribution, in order to best fit the world’s experimental data from polarized DIS and RHIC measurements for A_{LL} . The DSSV (Daniel de Florian, Rodolfo Sassot, Marco Stratmann and Werner Vogelsang) [28] and NNPDF [29] groups are two of the groups who have carried out global analyses incorporating STAR jet data, and their models will be referenced at various points in this dissertation.

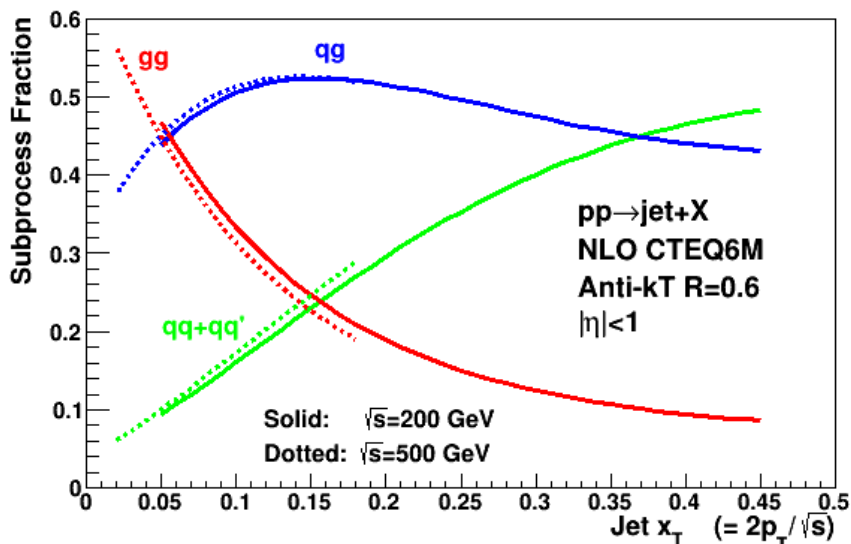


Figure 1.4: The fractions of partonic scattering subprocesses which contribute to jet production at RHIC kinematics, as functions of jet x_T [26], [27].

Inclusive jet A_{LL} from STAR for the 2009 RHIC pp run at $\sqrt{s} = 200$ GeV [30], along with π^0 results from PHENIX [31], had a significant impact when included in the DSSV global analysis [28]. Figure 1.5 shows a comparison of the DSSV model’s $\Delta g(x, Q^2)$ before and after the inclusion of the 2009 STAR inclusive jet and PHENIX π^0 results. The black and blue lines (labelled DSSV and DSSV*, respectively) are two separate global analyses that do not include the 2009 RHIC data, while the red line (NEW FIT) analysis does. The original fits show small gluon polarization in the range of momentum fraction accessible at RHIC,

roughly $x = 0.05-0.2$, but including the 2009 data implies, for the first time, a non-zero gluon polarization at intermediate values of x .

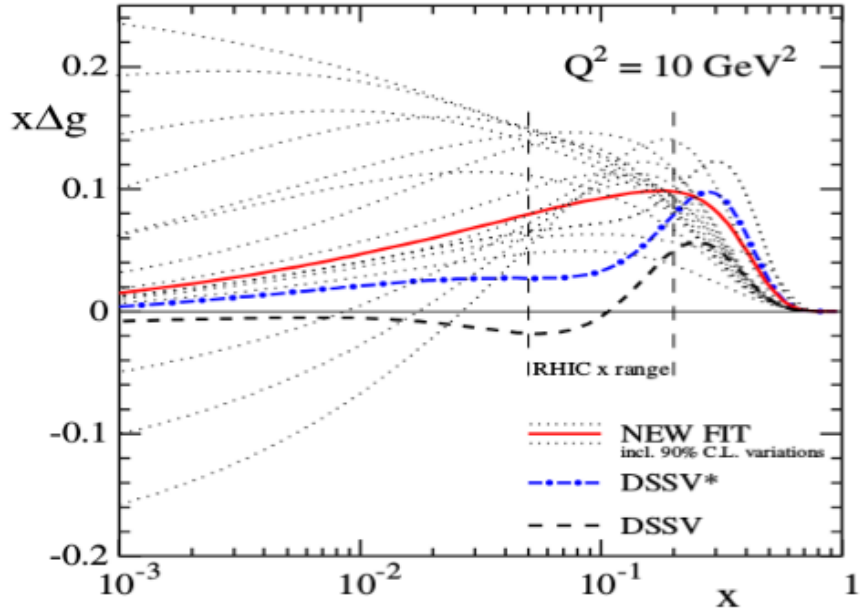


Figure 1.5: Gluon polarized distributions at $Q^2 = 10 \text{ GeV}^2$ for DSSV analysis without (DSSV, DSSV*) and with (NEW FIT) the RHIC 2009 polarized pp data [28].

Figure 1.6 shows the integrals of the different DSSV gluon polarized distribution models in two ranges of x . The horizontal scale shows the contribution to the proton’s spin for gluons carrying larger fractions of the proton’s total momentum, while the vertical axis shows the contribution from low momentum gluons. The inclusion of the 2009 RHIC data leads to a large reduction in the uncertainty band (green region to blue region), particularly for the higher momentum fraction gluons, where the contribution to ΔG is now positive. However, note the difference in scale between the horizontal and vertical axes; the contribution to the proton spin from low x is still very poorly constrained. Studies of jets at more forward pseudorapidities and higher center-of-mass energy can better access these low momentum gluons, as will be discussed later in this Chapter.

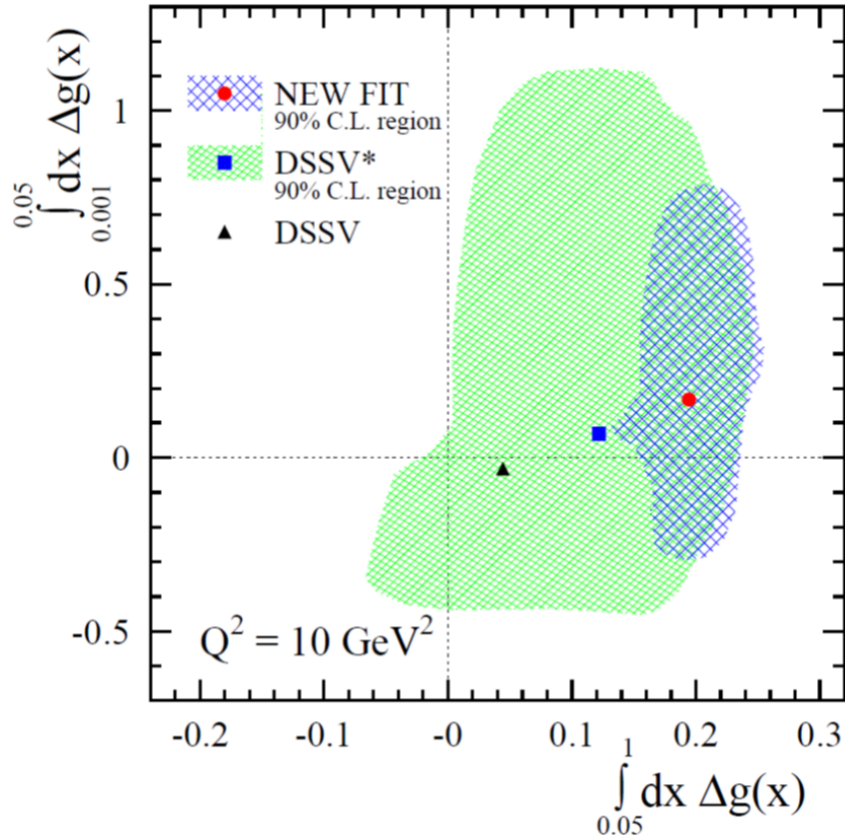


Figure 1.6: Fit central values and 90% C.L. for integrals of $\Delta g(x, Q^2 = \text{GeV}^2)$ over two ranges in momentum fraction x . Results for DSSV, DSSV*, and the NEW FIT are shown [28].

1.3.2 Dijet Analyses

The goal of a jet measurement is to detect as many particles as possible from the fragmentation of the partons involved in the initial hard scattering, and thus reconstruct the kinematics of that collision. Inclusive jet measurements integrate over a large range of x , making the extraction of the initial-state partonic momenta more difficult. However, if two jets corresponding to the two hard-scattered partons can be reconstructed, then the kinematics of the two-jet system can be used to approximate the partonic kinematics. Such a two-jet system is called a dijet, and measurements of A_{LL} for dijet events can provide more direct sensitivity to the x dependence of Δg .

To leading order, the partonic hard collision that produces a dijet is a relativistic $2 \rightarrow 2$

scattering. Assuming that the partons are massless and collide collinearly, with no transverse momentum, the relations between the initial and final state of the system are given in Eqs. 1.10. Here x_1 and x_2 are the momentum fractions of the colliding partons, p_{T_3} and p_{T_4} are the transverse momenta of the outgoing partons, η_3 and η_4 are the pseudorapidities of the outgoing partons, M is the invariant mass of the system, y is the rapidity of the system, θ is the scattering angle in the center-of-mass frame, and \sqrt{s} is the collision center-of-mass energy.

$$x_1 = \frac{p_{T_3}}{\sqrt{s}}(e^{\eta_3} + e^{\eta_4}) \quad (1.10a)$$

$$x_2 = \frac{p_{T_4}}{\sqrt{s}}(e^{-\eta_3} + e^{-\eta_4}) \quad (1.10b)$$

$$M = \sqrt{x_1 x_2 s} \quad (1.10c)$$

$$y = \frac{1}{2} \ln \left(\frac{x_1}{x_2} \right) = \frac{\eta_3 + \eta_4}{2} \quad (1.10d)$$

$$|\cos \theta| = \tanh \left(\frac{\eta_3 - \eta_4}{2} \right) \quad (1.10e)$$

In a dijet measurement, $p_{T_{3,4}}$ and $\eta_{3,4}$ are taken to be the transverse momenta and pseudorapidities, respectively, of the two jets, while the \sqrt{s} is taken to be the center-of-mass energy of the colliding proton beams. RHIC typically operates at $\sqrt{s} = 200$ GeV or 510 GeV when colliding polarized protons. The true dijet invariant mass is the square root of the squared sum of the two constituent jets' 4-momenta, $M = \sqrt{(P_3 + P_4)^2}$, which works out to:

$$M = \sqrt{m_3^2 + m_4^2 + 2\sqrt{m_3^2 + p_{T,3}^2}\sqrt{m_4^2 + p_{T,4}^2} \cosh(y_3 - y_4) - 2p_{T,3}p_{T,4} \cos(\phi_3 - \phi_4)}. \quad (1.11)$$

The derivation of Eq. 1.11 is given in Appendix B.

The first measurement of the longitudinal double-spin asymmetry A_{LL} for dijet pro-

duction at STAR was published using data from the 2009 pp at 200 GeV RHIC run [32]. Figure 1.7, from that publication, illustrates the advantage of dijets over inclusive jets. The figure shows the momentum fraction distributions, weighted by partonic \hat{a}_{LL} , of the gluons for dijets with invariant mass between 19.0 and 23.0 GeV/c^2 , and for inclusive jets with p_T between 8.4 and 11.7 GeV/c^2 . The momentum fraction distributions are from PYTHIA simulation [33]. As evidenced by the narrower distributions, the dijet measurement more tightly constrains the kinematics of the colliding partons than does the inclusive measurement. Also note that the asymmetric nature of the events in which both jets in the dijet pair have the same sign in η (upper panel) provides access to lower x gluons than in the opposite sign case.

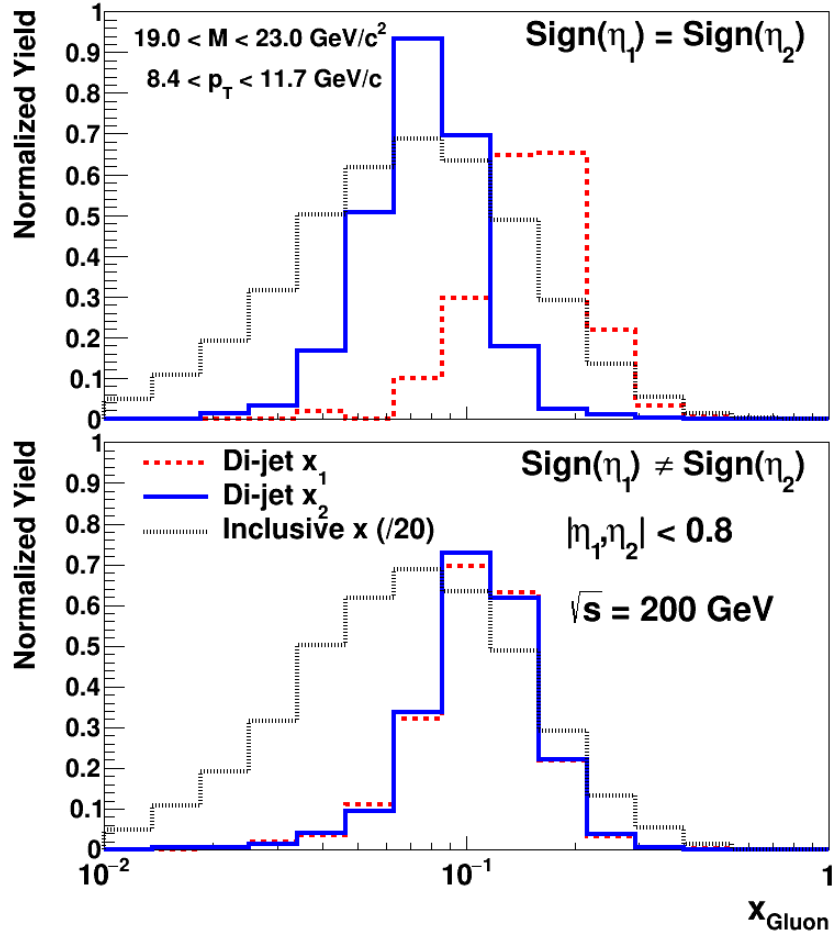


Figure 1.7: Distributions of gluon x_1 and x_2 obtained from PYTHIA simulation for same sign in pseudorapidity (upper) and opposite sign in pseudorapidity (lower) dijet events, compared with the gluon x distributions for inclusive jets [32].

Figure 1.8 shows the measured dijet A_{LL} as a function of dijet invariant mass for the same-sign in pseudorapidity and opposite-sign in pseudorapidity cases, along with theory predictions from the DSSV and NNPDF global analyses. The dijet cross section was also presented, and is shown in Fig. 1.9 as a function of dijet invariant mass, along with uncertainties and theory predictions. The points and green bands are the data and their associated systematic uncertainties, while the blue bands are a theoretical prediction based on next-to-leading-order (NLO) perturbative QCD calculations. The theory prediction was corrected for underlying event and hadronization (UEH) effects, and the red bands show the systematic uncertainty associated with that correction. The good agreement of the measured cross section with the theoretical predictions indicates that dijet production at STAR is well understood, and that NLO pQCD predictions can be used to interpret measurements of dijet A_{LL} .

1.3.3 Forward Dijets

From Eq. 1.10, we can see that one way to probe lower values of x is to consider jets with larger pseudorapidities. More forward dijets arise from asymmetric collisions, with $x_1 \gg x_2$, which often involve a very low momentum gluon scattering off of a high momentum quark. The detection of such jets requires the use of the STAR Endcap Electromagnetic Calorimeter; the unique challenges associated with jet reconstruction in the Endcap will be discussed in detail later. The first measurement of A_{LL} for forward dijets at STAR was also carried out using data from the 2009 pp at 200 GeV run [34]. The distributions of x_1 and x_2 , obtained from PYTHIA simulation and weighted by partonic \hat{a}_{LL} [35] for three dijet event topologies are shown in Fig. 1.10. They correspond to dijet events with invariant masses in the lowest range analyzed, $16.0 < M < 19.0$ GeV/ c^2 . Note that the collisions become increasingly asymmetric for jets at higher pseudorapidity, with Endcap-Endcap dijet events showing almost total separation between the x_1 and x_2 distributions. Comparison with Fig. 1.7, from the earlier mid-rapidity dijet analysis, demonstrates that higher rapidity dijets are able to

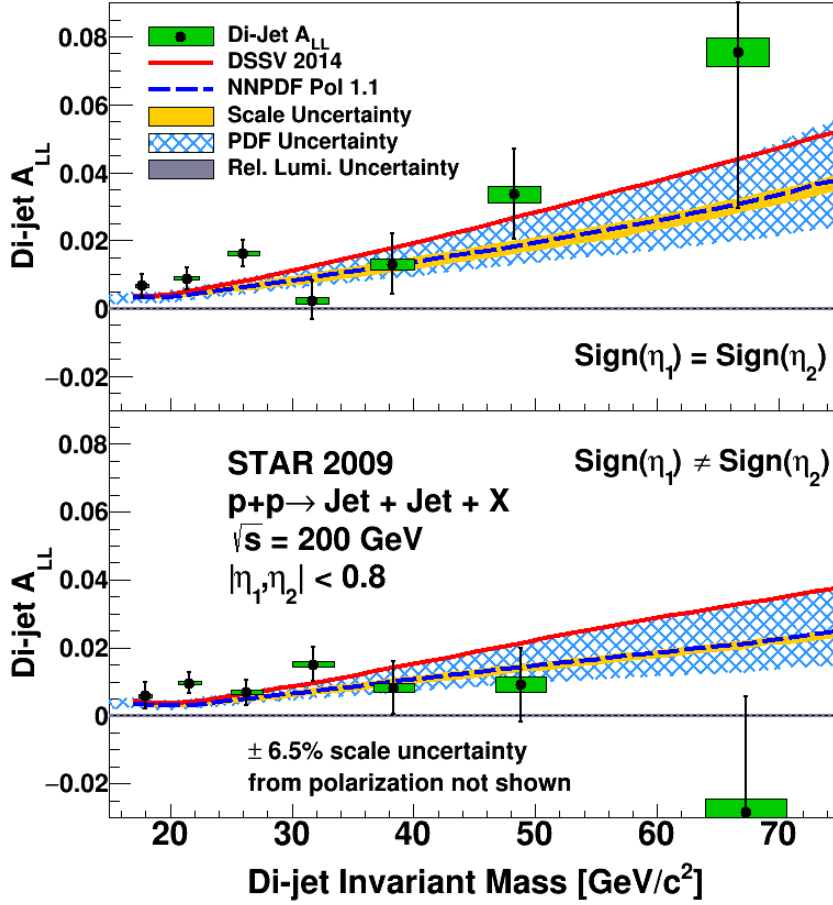


Figure 1.8: Measured dijet A_{LL} vs. invariant mass for events with the same sign (upper) and opposite sign (lower) in pseudorapidity, from 2009 STAR data [32].

probe lower momentum gluons. Figure 1.11 shows the longitudinal double-spin asymmetry A_{LL} as a function of partonic dijet invariant mass for the three different topologies. Although the measured A_{LL} for dijet events where both jets are in the Endcap (bottom panel) has the largest statistical uncertainties, the asymmetry is expected to be largest for this topology, as evidenced by the theory curves.

1.3.4 Dijets at 510 GeV

A second way to access lower momentum-fraction gluons is to analyze dijet events from collisions with higher center-of-mass energies. For polarized pp running, RHIC operates

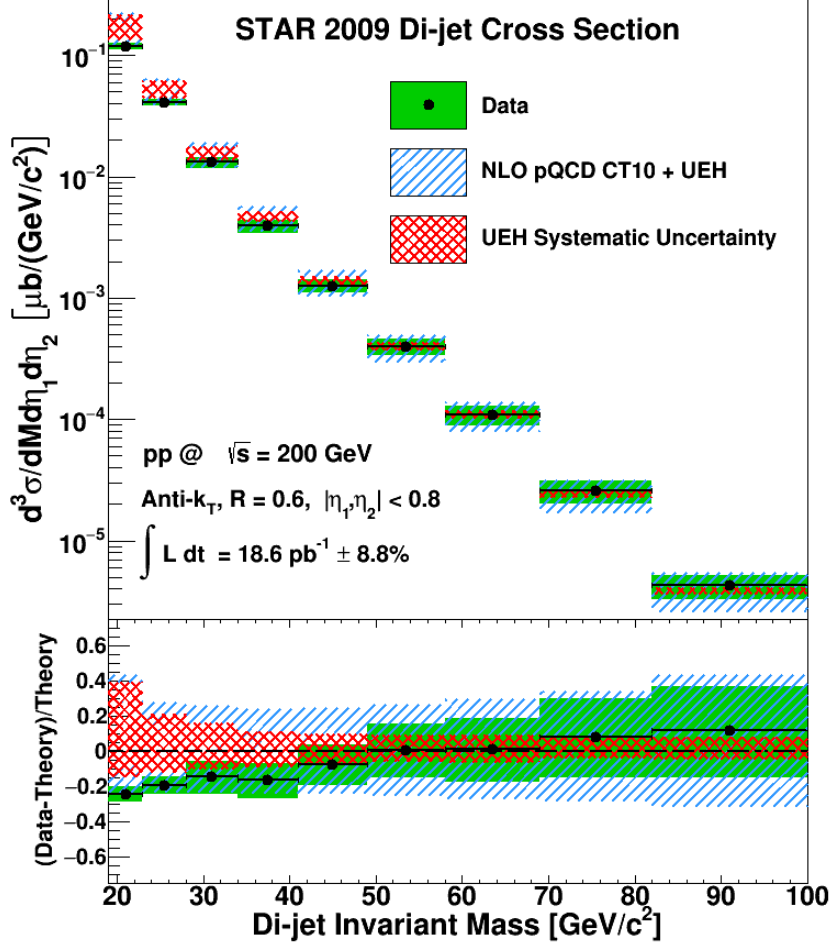


Figure 1.9: Measured dijet cross section vs. invariant mass from 2009 STAR data. The lower panel shows a relative comparison between the experimental results and theoretical predictions [32].

at $\sqrt{s} = 200$ GeV or 510 GeV. The previously discussed analyses were all carried out on data taken at 200 GeV; the first and only STAR publication for jets at 510 GeV presented both inclusive and dijet results at midrapidity from the 2012 RHIC run [36]. The partonic momentum fractions accessible in the dijet portion of that analysis, from simulation for dijets with invariant masses between 17.0 and 20.0 GeV/c^2 , can be seen in Fig. 1.12. The topmost panel, labelled “Topology A”, corresponds to dijets with $0.3 < |\eta_{3,4}| < 0.9$ and $\eta_3 \cdot \eta_4 > 0$, and so includes events similar to those in the top panel of Fig. 1.7. Comparing these two plots illustrates that dijets arising from collisions with a higher center-of-mass energy probe lower values of x . The results for the measurement of the dijet A_{LL} are shown in Fig. 1.13, for the

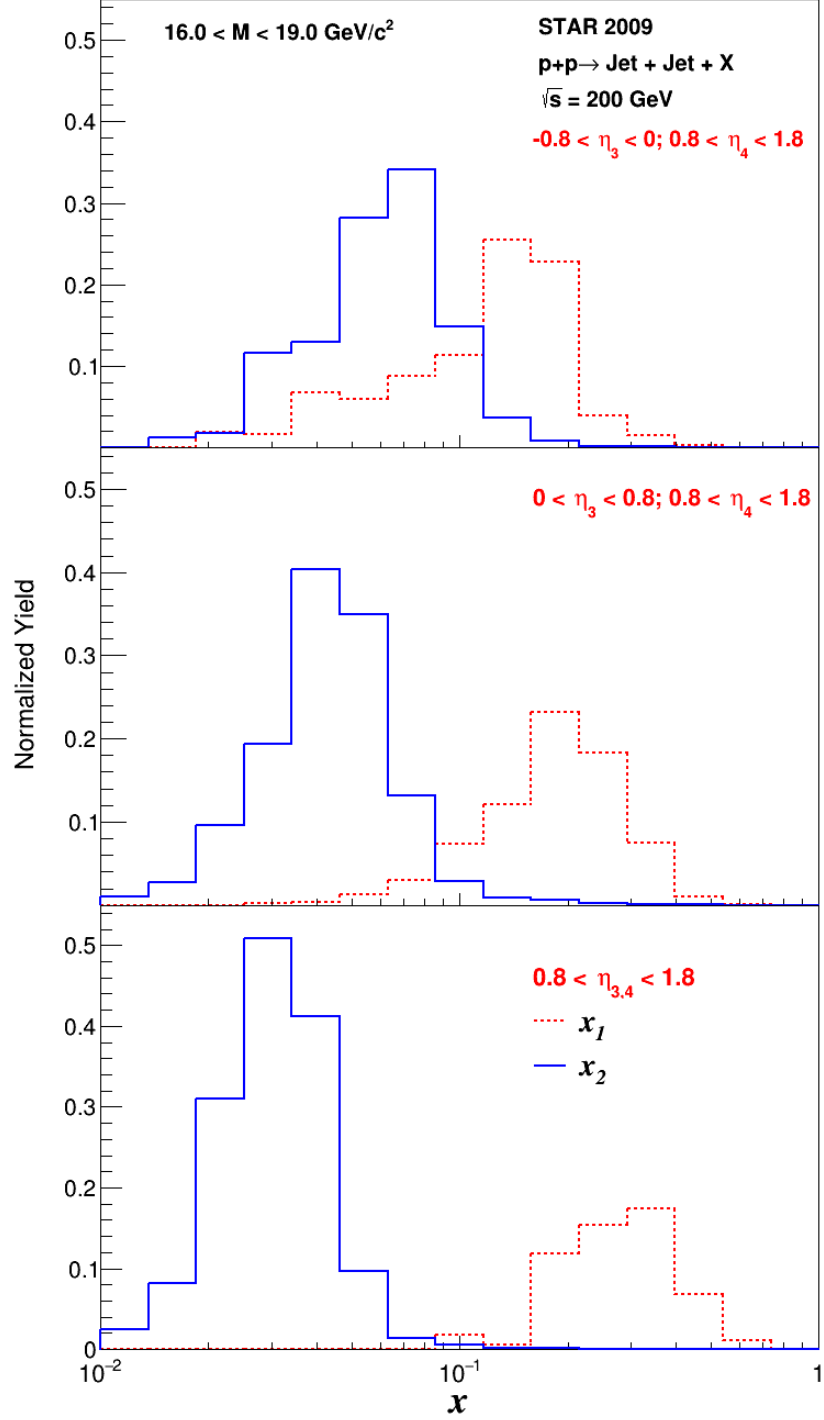


Figure 1.10: Distributions of parton x_1 and x_2 , weighted by partonic \hat{a}_{LL} , from simulation at $\sqrt{s} = 200 \text{ GeV}$ for different jet pseudorapidity ranges [34].

same four topologies. Note that in Figs. 1.12 and 1.13, the term “Forward” corresponds to jets with $0.3 < \eta < 0.9$, while everywhere else in this document it will refer to jets with $\eta >$

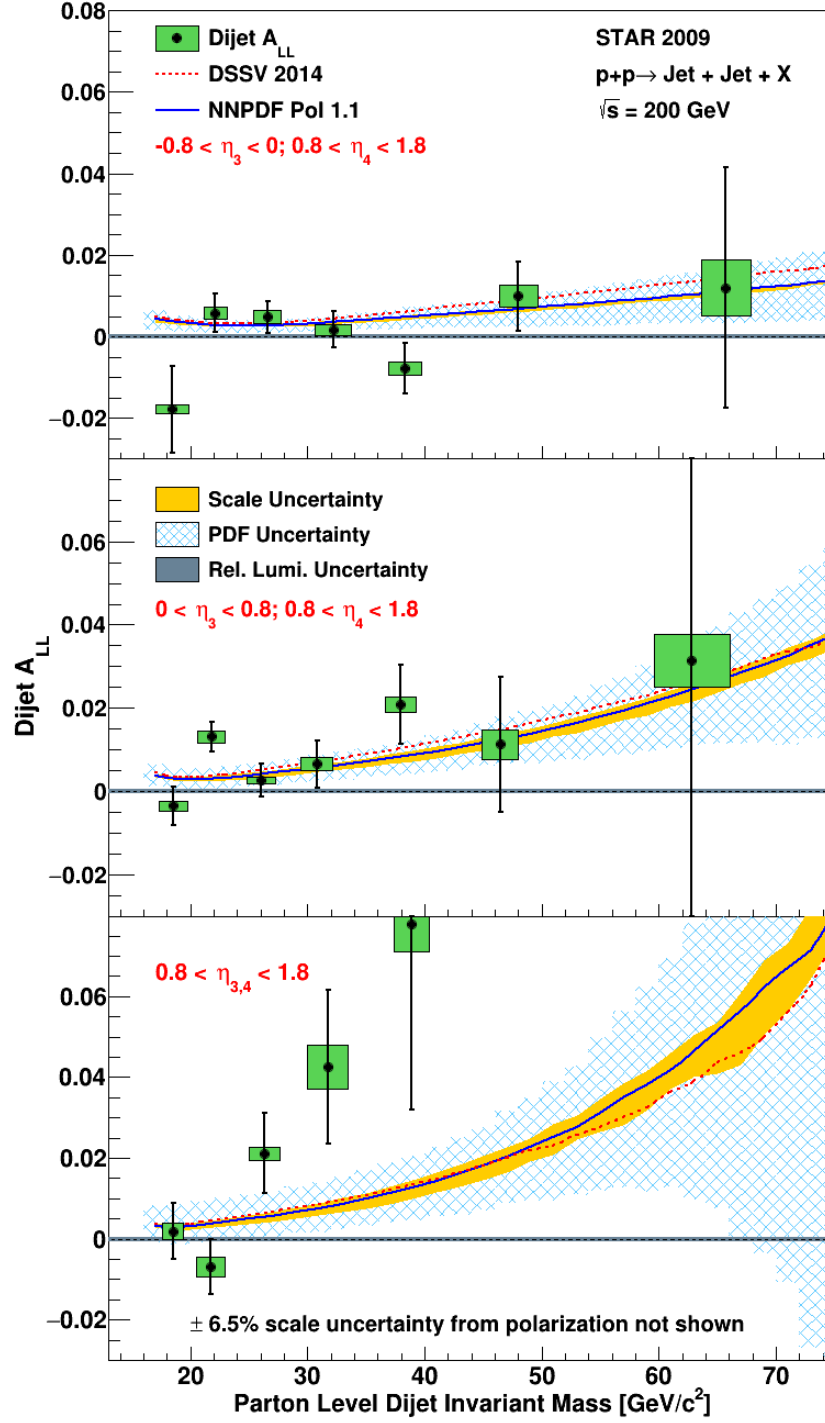


Figure 1.11: Measured dijet A_{LL} vs. partonic invariant mass for different jet pseudorapidity ranges, from 2009 STAR data at 200 GeV [34]. The curves represent theoretical predictions of A_{LL} for the DSSV2014 [28] and NNPDFpol1.1 [29] parton distributions.

0.8 or $\eta > 0.9$.

1.4 Dissertation Structure

This chapter has provided an overview of the proton spin puzzle and the efforts of the STAR collaboration to constrain the gluon polarized distribution function $\Delta g(x, Q^2)$. The last two sections outlined how recent measurements of the dijet longitudinal double-spin asymmetry A_{LL} at either forward pseudorapidity or a higher collision center-of-mass energy can better constrain the magnitude and shape of Δg in the low x region, where the uncertainties are the largest. This dissertation presents the results of the first measurement of A_{LL} for dijet production at both forward pseudorapidity and high center-of-mass energy, to access the lowest x gluons possible at STAR. The rest of this dissertation is structured as follows. Chapter 2 includes a description of the RHIC facility and the STAR detector, while Chapter 3 describes how jets are reconstructed, along with the dijet event selection criteria. Chapter 4 details the data and simulation samples that were used, and Chapter 5 describes the underlying event subtraction. The challenges associated with analyzing jets in the Endcap and the methods used to overcome them are outlined in Chapter 6. The final two chapters present the results of the measurement and conclusions.

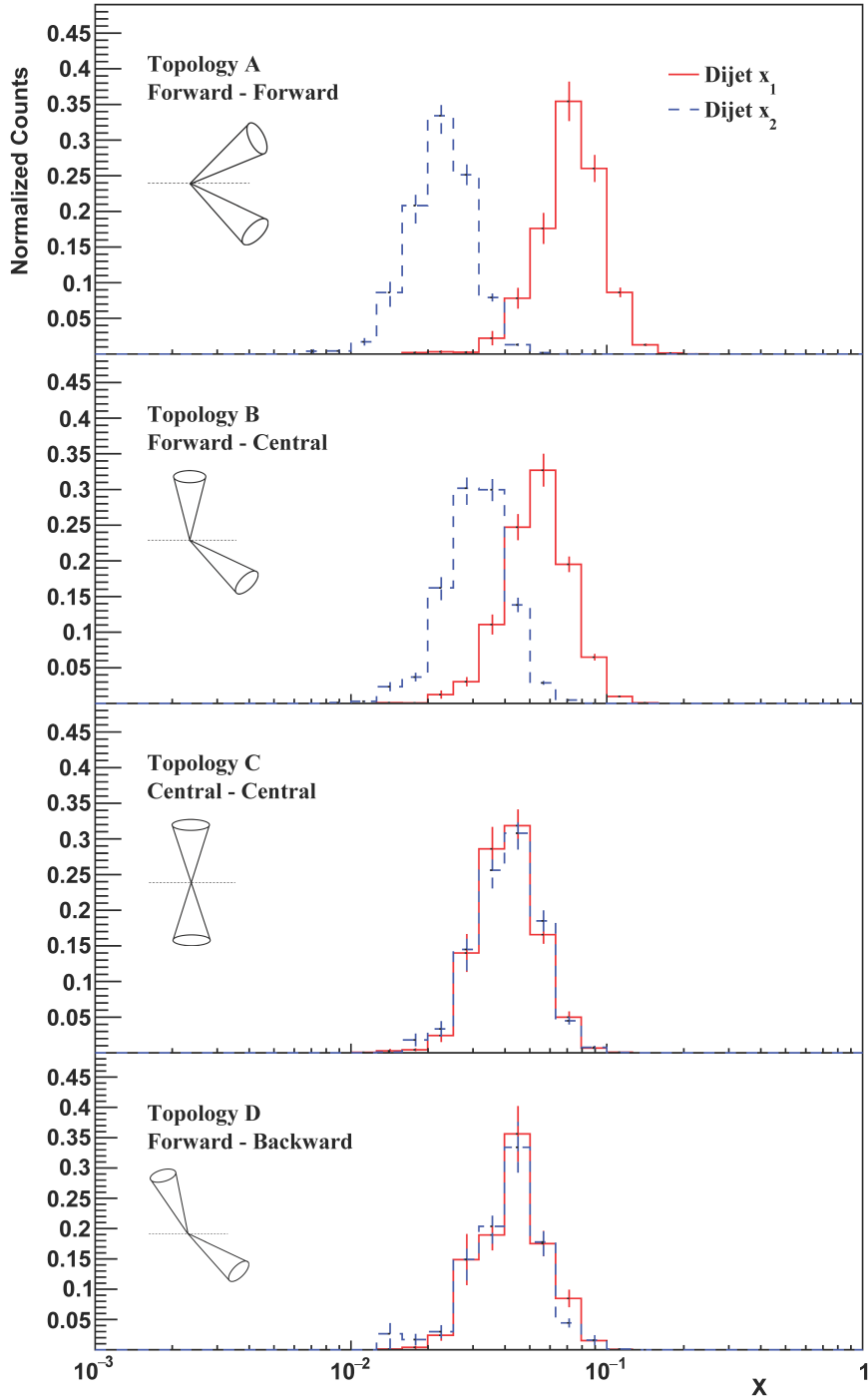


Figure 1.12: Distributions of parton x_1 and x_2 from leading order simulation at $\sqrt{s} = 510$ GeV for different jet pseudorapidity ranges [36]. “Topology A” corresponds to dijets with $0.3 < |\eta_{3,4}| < 0.9$ and $\eta_3 \cdot \eta_4 > 0$; “Topology B” to dijets with $|\eta_{3,4}| < 0.3$ and $0.3 < |\eta_{4,3}| < 0.9$; “Topology C” to dijets with $|\eta_{3,4}| < 0.3$; “Topology D” to dijets with $0.3 < |\eta_{3,4}| < 0.9$ and $\eta_3 \cdot \eta_4 < 0$.

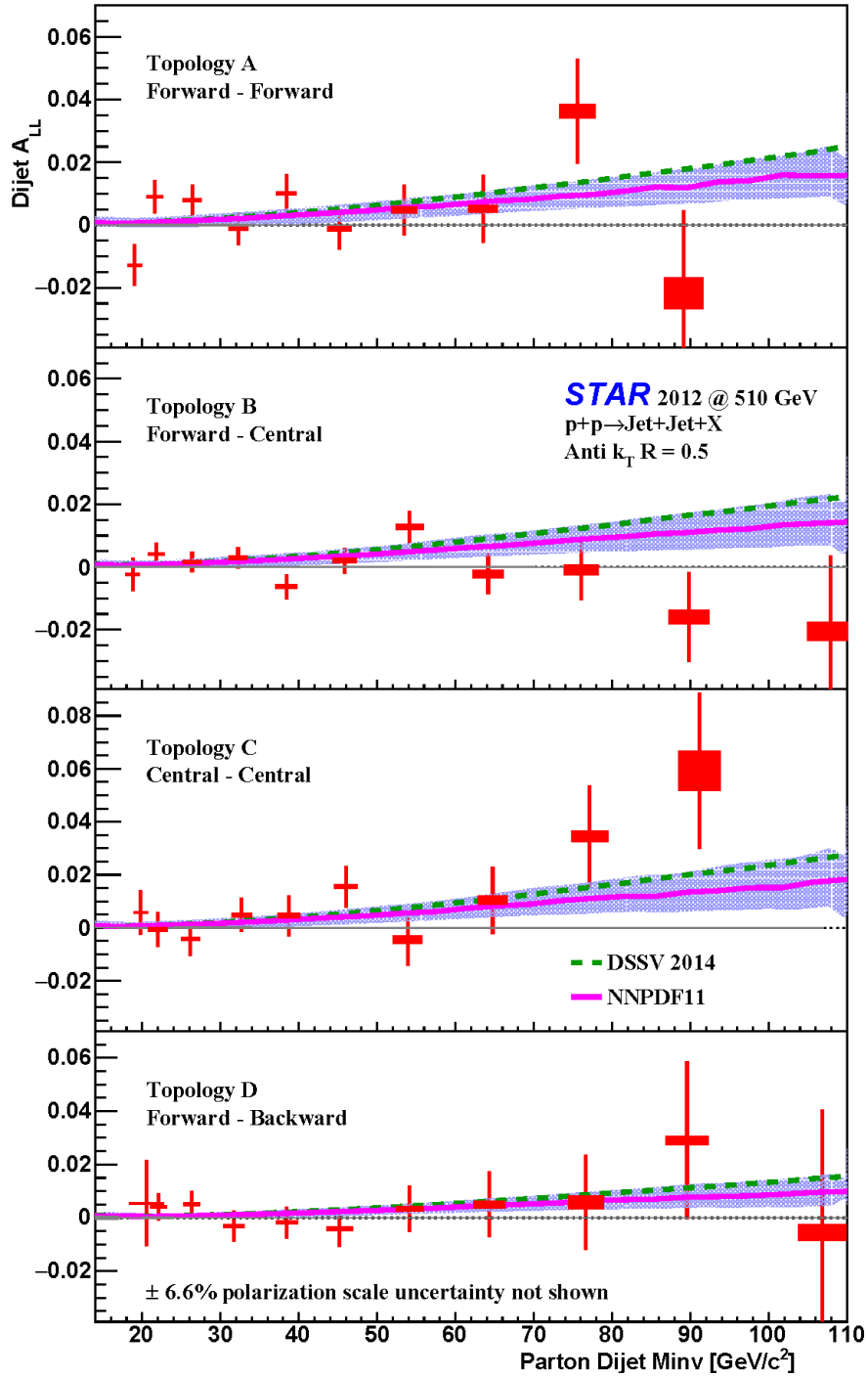


Figure 1.13: Measured dijet A_{LL} vs. partonic invariant mass for different jet pseudorapidity ranges, from 2012 STAR data at 510 GeV [36]. The η ranges associated with each Topology are explained in the caption of Fig. 1.12

CHAPTER 2

Experimental Facilities

2.1 The Relativistic Heavy Ion Collider

The Relativistic Heavy Ion Collider (RHIC) at Brookhaven National Lab (BNL) on New York's Long Island is the world's first polarized proton collider. Construction was completed in 1999 and RHIC saw its first collisions in 2000. Overviews of the RHIC facility can be found in [37] and [38]. RHIC is capable of colliding many different types of ions, including Au, Al, Zr, and Ru, to study the QCD phase diagram, but we will only discuss it in the context of polarized proton collisions. Figure 2.1 shows a schematic of the various components of RHIC that are relevant for polarized pp running. An overview of RHIC specifically as a polarized proton collider can be found in [39].

The protons for polarized pp collisions at RHIC start out from an optically pumped H^- ion source called OPPIS [40]. OPPIS produces a 500 μA current of H^- ions with 80% polarization in 300 μs pulses, at an intensity of about 9×10^{11} ions per pulse. The ions are then accelerated to 200 MeV with a radio-frequency quadrupole and LINAC before being strip-injected into the booster and captured as a single bunch. The acceleration to 200 MeV is about 50% efficient, resulting in bunches in the booster consisting of 4×10^{11} polarized protons. Bunches are accelerated to 1.5 GeV in the booster, and then transferred to the Alternating Gradient Synchrotron (AGS) for further acceleration up to 25 GeV. Finally, the bunches are injected into RHIC for acceleration up to the final center-of-mass energy.

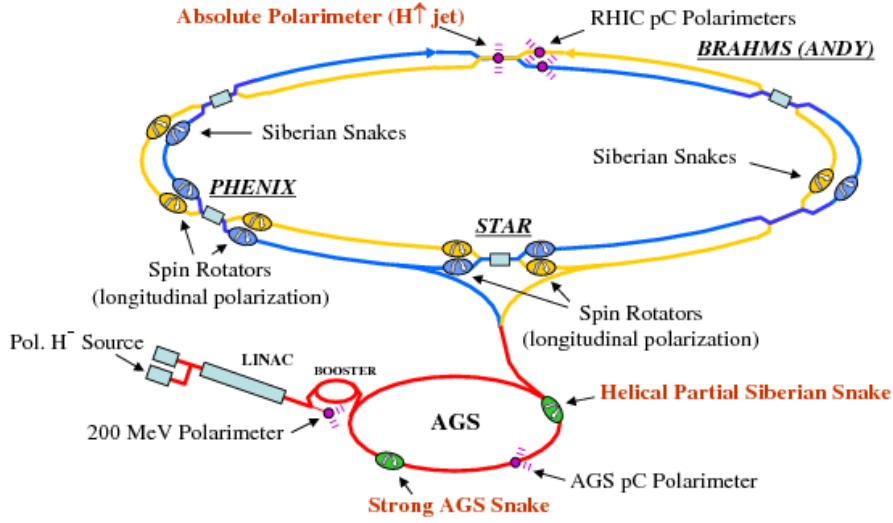


Figure 2.1: Layout of RHIC, with the components that are necessary for polarized pp operation pointed out [37].

Additional losses during the AGS to RHIC transfer result in bunch intensities of 2×10^{11} protons per bunch in RHIC.

RHIC consists of two nearly circular, coplanar rings, for acceleration and storage of clockwise (“Blue Ring”) and counter-clockwise (“Yellow Ring”) beams. Each ring can hold 120 proton bunches, where the bunches are injected one at a time with independent, carefully chosen spin orientations. It takes approximately 10 minutes to fill both rings and accelerate the bunches to the desired energy. The time from the first bunch injection until the beam is dumped is called a “fill”; good fills without any unexpected beam aborts typically last for about 8 hours for pp running at 510 GeV.

2.1.1 Polarized Proton Spin Dynamics During Acceleration

While OPPIS produces ions with a high degree of polarization, preserving as much of that initial polarization as possible during the acceleration process is a challenge. The evolution of the spin direction of a polarized proton in an external magnetic field is given by the

Thomas-BMT equation,

$$\frac{d\vec{P}}{dt} = -\left(\frac{e}{\gamma m}\right)[G\gamma\vec{B}_\perp + (1 + G)\vec{B}_\parallel] \times \vec{P}, \quad (2.1)$$

where \vec{P} is the proton's spin vector as seen in a reference frame that moves with the proton, $G = 1.7928$ is the proton's anomalous magnetic moment, $\gamma = E/m$ is the Lorentz factor, and \vec{B}_\perp and \vec{B}_\parallel are the transverse and longitudinal components of the magnetic field. The Thomas-BMT equation is similar to the Lorentz force equation for the orbital motion of a charged particle in an external magnetic field,

$$\frac{d\vec{v}}{dt} = -\left(\frac{e}{\gamma m}\right)[\vec{B}_\perp] \times \vec{v}, \quad (2.2)$$

where \vec{v} is the proton's velocity vector. Comparing Eqs. 2.1 and 2.2 in the approximation of an ideal circular accelerator, where the magnetic field is purely transverse, we can see that the proton's spin vector precesses $G\gamma$ times per revolution. This number is called the spin tune ν_{sp} , and at the top RHIC proton kinetic energy of 250 GeV can reach 478.

Accelerated beams of polarized protons encounter various depolarizing resonances as they are boosted. These resonances arise predominantly from magnet imperfections and misalignments (imperfection resonances) and from the non-vertical components of the focusing fields (intrinsic resonances). The conditions for both types of depolarizing resonances are given in terms of the spin tune. Imperfection resonances occur when the proton's spin vector is in the same orientation each time the particle reaches the imperfection, expressed mathematically as $\nu_{sp} = G\gamma = n$ for integer n . Solving for the energy shows that successive imperfection resonances are separated by 523 MeV. The condition for intrinsic resonances is $\nu_{sp} = G\gamma = kP \pm \nu_y$, where k is an integer, P is the superperiodicity, and ν_y is the betatron tune.

At low beam energies, like in the booster, various accelerator parameters can be adjusted to mitigate the effects of the depolarizing resonances. These techniques are not feasible at the

higher energies achieved in the AGS and RHIC rings, however, so the proton polarizations are maintained using arrays of constant field helical dipole magnets called “Siberian Snakes” [41]. Each Siberian Snake generates a 180° rotation of the spin vector about a horizontal axis transverse to the beam direction, without disturbing the proton’s orbit. Since this spin rotation is much larger than the spin perturbations from the imperfection and intrinsic resonances, the conditions for the loss of beam polarization are never met. Each RHIC ring contains two Snakes, which flip the proton spin about perpendicular axes. The Partial Siberian Snake in the AGS rotates the spin by less than 180° , which is sufficient to prevent depolarization from the weaker resonances in that accelerator.

When the beams of protons are injected into RHIC they are vertically polarized, which is the stable spin orientation. However, many measurements require longitudinally polarized beams. So the interaction points for the STAR and PHENIX experiments have spin rotators on either side that can switch the polarization direction from vertical to longitudinal and then back again. Like the Siberian Snakes, the spin rotators are arrays of four superconducting helical dipole magnets.

2.1.2 Measuring Beam Polarization

Accurate measurements of the beam polarization are critical to the spin physics measurements carried out at RHIC. To this end, RHIC employs two separate polarimeter systems, both based on a spin asymmetry for elastic scattering in the Coulomb-Nuclear Interference region, which provide complementary information. The proton-Carbon (pC) polarimeters record many relative measurements over time, while the hydrogen gas jet (H-jet) polarimeter is used to determine the absolute scale. The pC polarimeters consist of a thin carbon ribbon target and six silicon strip detectors in a vacuum chamber, as shown in Fig. 2.2. The carbon target is thin compared to the width of the beam, and can be moved around to measure the beam’s polarization at different points in the transverse plane. The proton beam polarization in the vertical direction is measured by determining the left-right asymmetry in the yields

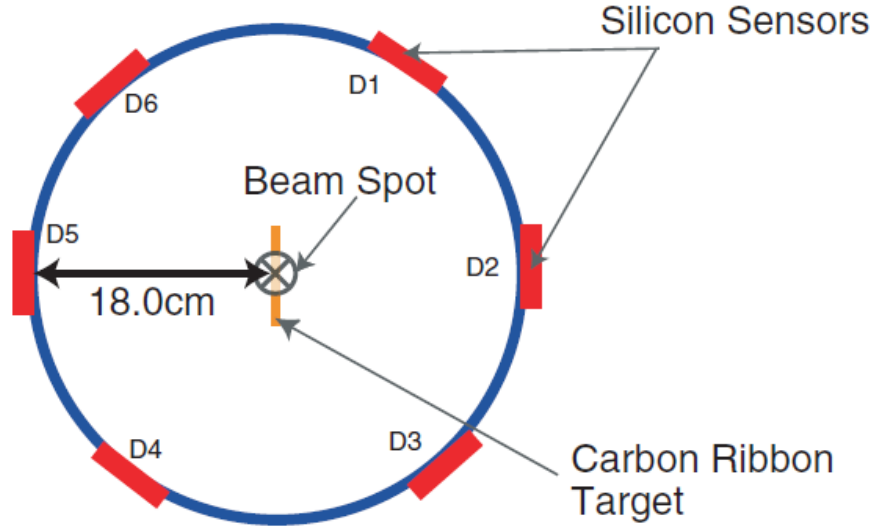


Figure 2.2: A cross-sectional view of the RHIC proton-Carbon polarimeter.

for scattered carbon nuclei:

$$P_{beam} = \frac{1}{A_N^{pC}} \frac{N_L - N_R}{N_L + N_R} = \frac{\epsilon_{beam}}{A_N}, \quad (2.3)$$

where P_{beam} is the beam polarization, N_L and N_R are the number of nuclei scattered left and right (normalized by luminosity), and ϵ_{beam} is the raw asymmetry. A_N^{pC} is the analyzing power, which in general can be determined from theory or experiment but is not well known at RHIC energies. Thus, the pC polarimeter cannot measure absolute polarizations by itself. However, the large cross section for proton-carbon elastic scattering allows this polarimeter to accumulate statistics quickly, and it can provide information on polarization loss during fills in addition to relative polarizations between fills.

Absolute beam polarization measurements are provided by the H-jet polarimeter at RHIC, shown schematically in Fig. 2.3, which employs a transversely polarized atomic hydrogen beam target [42] and silicon strip detectors to count the recoil protons. In this case, the incident and target particles are identical, so the analyzing powers are the same:

$$A_N^{pp} = \frac{\epsilon_{beam}}{P_{beam}} = \frac{\epsilon_{target}}{P_{target}}. \quad (2.4)$$

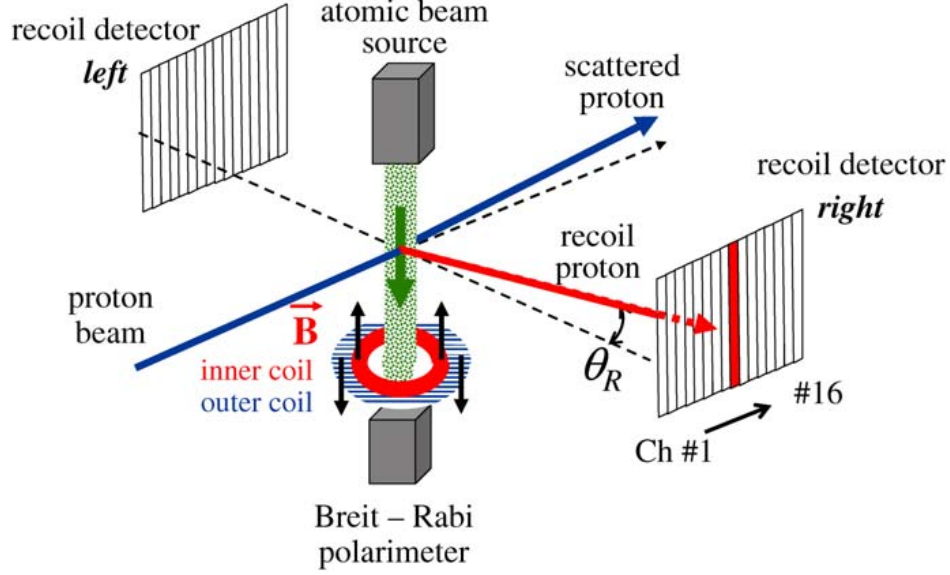


Figure 2.3: Schematic diagram of the RHIC hydrogen gas jet polarimeter.

Rearranging, we see that the beam polarization can be written in terms of the raw beam and target asymmetries and the target polarization:

$$P_{beam} = \frac{\epsilon_{beam}}{\epsilon_{target}} P_{target}. \quad (2.5)$$

See Refs. [43] and [42] for more details. The raw beam and target asymmetries are determined by averaging over the spin states of the target and beam, respectively. The absolute polarization of the atomic hydrogen target, P_{target} , is measured to within about 2% by a Breit-Rabi polarimeter. The measurements from the H-jet polarimeter set the absolute scale for the fill-to-fill relative polarizations from the pC polarimeter.

2.1.3 Zero-Degree Calorimeters

The Zero-Degree Calorimeters (ZDC) [44], located on either side of each interaction point, are designed to provide event characterization and luminosity monitoring for the various RHIC experiments. The ZDCs are hadronic calorimeters consisting of alternating layers of scintillator and tungsten plates, and detect neutral beam fragments emitted at divergence

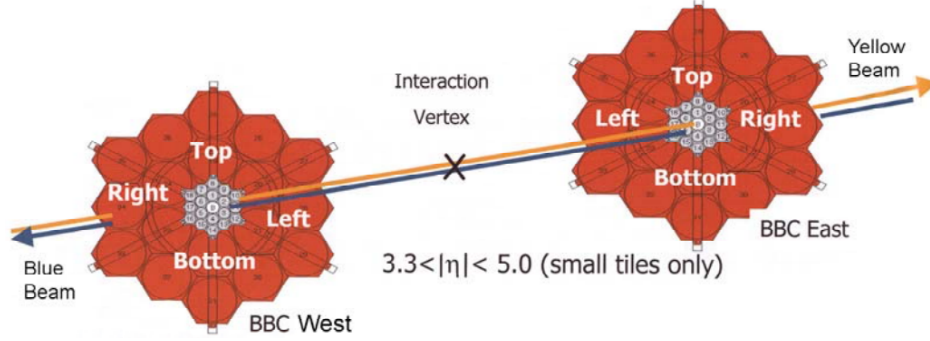


Figure 2.4: Schematic of the Beam-Beam Counters, showing the inner and outer tiles [45].

angles less than 4 mrad from the beamline. The coincidence of signals from the ZDCs on either side of the interaction point, within some interval after a bunch crossing, can be used to trigger on minimum bias events. Information from the ZDC coincidences is used to help determine the relative luminosities of the various proton helicity combinations; the importance of relative luminosities in the measurement of the longitudinal double-spin asymmetry A_{LL} is discussed in a later section.

2.1.4 Beam-Beam Counters

The Beam-Beam Counters (BBC) [44] are another set of detectors located on either side of the STAR interaction point. The BBCs are fast detectors that provide information for event triggering, provide local polarimetry, and monitor total and spin-state sorted luminosities. Each detector consists of two sets of scintillator annuli mounted around the beam pipe just outside the STAR magnet, 374 cm from the interaction point. Figure 2.4 shows a schematic of the East and West BBC. A BBC module consists of two scintillator annuli each containing 18 hexagonal tiles: 6 tiles in the inner ring and 12 in the outer ring. The tiles in the outer annulus are called large tiles, and are not used in this analysis. The small tiles of the inner annulus cover a pseudorapidity range of $3.4 < |\eta| < 5.0$ and $0 < \phi < 2\pi$ in azimuth, and send signals to the STAR trigger system indicating at least a minimum level of event activity.

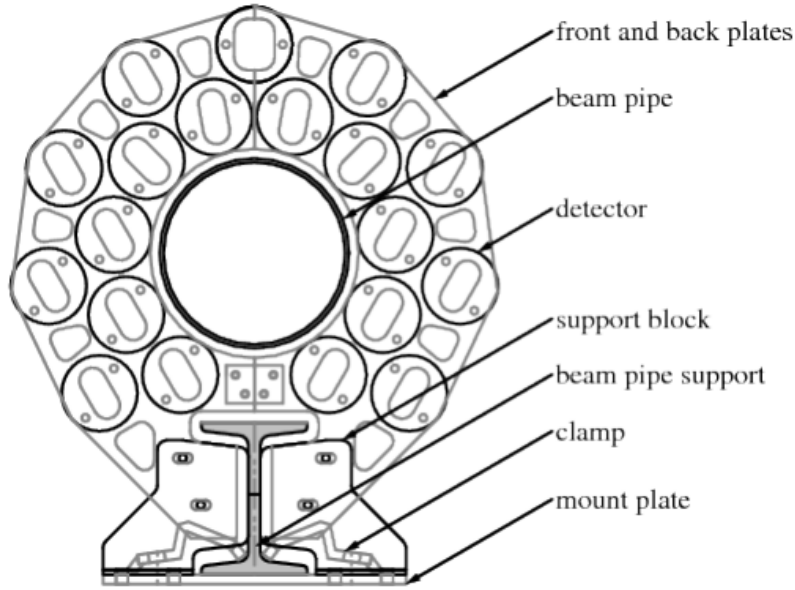


Figure 2.5: Schematic of a Vertex Position Detector, showing the 19 individual detectors arrayed around the beam pipe [46].

2.1.5 Vertex Position Detectors

The Vertex Position Detectors (VPD) [46], similar to the ZDCs and BBCs, provide triggering for minimum bias events and measurements of the relative luminosities. There are two of these as well, with one VPD on either side of the interaction point at a distance of 5.7 m from the center of STAR. As shown in Fig. 2.5, each VPD is made up of 19 individual detectors, which together cover $4.24 < |\eta| < 5.1$ in pseudorapidity and $0 < \phi < 2\pi$ in azimuth. Each individual detector consists of an aluminum cylinder with front and back caps enclosing a 6.4 mm thick lead absorber, a 10 mm thick scintillator, and a photomultiplier tube (PMT). The VPD sends signals to both the STAR trigger system and the STAR data acquisition system.

2.2 The Solenoidal Tracker at RHIC

The Solenoidal Tracker at RHIC (STAR) [47] is a large acceptance detector suited for measuring the hadronic and electromagnetic particles produced in heavy ion and proton-proton collisions. STAR consists of many detector subsystems specialized for various purposes; a schematic is shown in Fig. 2.6. Along with the monitoring systems discussed in the previous section, the main detectors used for the measurement described in this thesis are the Time Projection Chamber (TPC), which provides tracking and identification for charged particles, and the Barrel (BEMC) and Endcap (EEMC) Electromagnetic Calorimeters, which are used to measure the energy of electromagnetic particles, primarily photons and electrons.

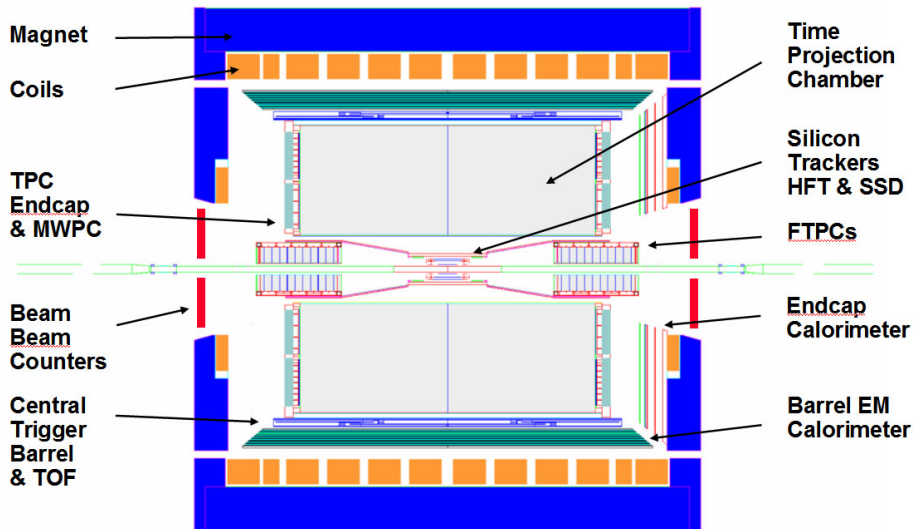


Figure 2.6: Cross sectional view of the STAR detector subsystems.

2.2.1 Time Projection Chamber

The Time Projection Chamber (TPC) [48] is the central component of STAR, providing charged particle tracking over the range of roughly $-1.3 < \eta < 1.3$ in pseudorapidity and 2π in azimuthal angle ϕ . The TPC measures 4.2 meters long and 4 meters in diameter, and consists of an inner and outer field cage, a central membrane, and two end-cap planes. The

empty volume between the central membrane and each end-cap is filled with a mixture of 10% methane and 90% argon gas. The whole volume sits in a 0.5 Tesla solenoidal magnetic field generated by the STAR magnet [49]. There is also a uniform electric field of approximately 135 V/cm parallel to the beamline which is produced by the central membrane held at 28 kV and the end-caps at ground. The inner and outer field cages define the boundary of this electric field.

Charged particles produced in proton-proton or heavy ion collisions travel through the TPC, ionizing the gas as they curve in the applied magnetic field. The released electrons then drift in the electric field towards the end-caps, where they produce a signal in Multi-Wire Proportional Chambers that is recorded by readout pads. The readout pads track the position of an ionization event in the x-y plane (perpendicular to the beamline), while the event's z position is determined by combining measurements of the electron drift time and drift velocity. In this way, the full trajectory of charged particles can be reconstructed. The TPC determines the transverse momenta of charged particles by measuring the curvature of their trajectories, and provides particle identification through measurements of ionization energy loss dE/dx , deduced from changes in the track curvature.

2.2.2 Barrel Electromagnetic Calorimeter

The Barrel Electromagnetic Calorimeter (BEMC) [50] is the main STAR calorimeter subsystem, located just outside the TPC. It is a segmented lead-scintillator sampling calorimeter consisting of 4800 optically isolated projective towers, providing full azimuthal coverage for $-1 < \eta < 1$ in pseudorapidity. The BEMC is divided into 120 modules of 40 towers, with each module covering 1.0 unit of pseudorapidity and 6° of azimuth. Each tower covers 0.05 units of η and 0.052 radians in ϕ , and projects back to the nominal interaction point (see left side of Fig. 2.7).

The towers are stacks of alternating layers of lead radiator and plastic scintillator: 20

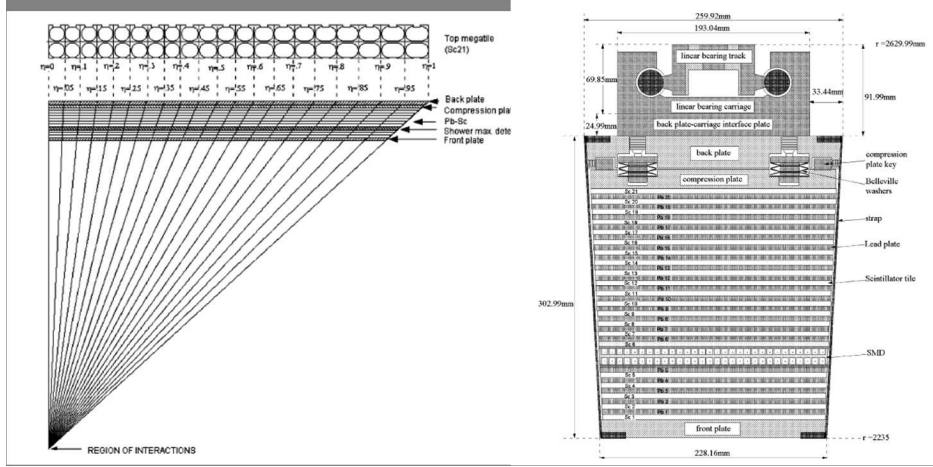


Figure 2.7: Side view of a BEMC module. The left figure illustrates the projective nature of the towers, while the right figure shows the module’s construction in more detail [50].

layers of 5 mm thick lead and 19 layers of 5 mm thick scintillator. Additionally, there are 2 layers of 6 mm thick scintillator at the front of each tower which together comprise the preshower detector (see right side of Fig. 2.7). There is also a shower maximum detector (SMD) located about 5 radiation lengths in, which provides precise information on the transverse shape of electromagnetic showers for use in π^0 reconstruction and direct photon detection. The light from all scintillator layers in a given tower is combined and read out by a single PMT, then converted to a digital signal which is roughly proportional to the energy deposited by particles incident on that tower. Note that signals from the towers are separate from signals from the preshower layers and SMD; only the calorimeter towers are used in this analysis.

2.2.3 Endcap Electromagnetic Calorimeter

The Endcap Electromagnetic Calorimeter (EEMC) [51] is located at the west end of the TPC. Like the BEMC, the EEMC is a segmented lead-scintillator sampling calorimeter. It consists of 720 optically isolated projective towers, and covers $1.086 < \eta < 2$ for 2π in ϕ (see Fig. 2.8). Thus, there is a small service gap in pseudorapidity between the two calorimeters. The EEMC is physically divided into two halves, with the towers grouped into

12 30° modules. The towers cover 6° in ϕ but have varying coverage in η , from 0.057 near $\eta = 1$ up to 0.099 at $\eta = 2$. The front face of the EEMC is 270 cm from the interaction point.

The EEMC towers, like those in the BEMC, are stacks of alternating layers of lead radiator and plastic scintillator. Each tower consists of 23 layers of 5 mm thick lead and 24 layers of 4 mm thick scintillator. There are also two preshower layers of 4.75 mm thick scintillator and a 5 mm thick postshower layer, which are read out separately from the tower stack. Finally, a pair of SMD planes is located about 5 radiation lengths in from the front of the EEMC, to provide fine spatial resolution for π^0 reconstruction and photon detection. Each SMD plane is made of polystyrene scintillator strips, with the strips in one plane oriented orthogonal to the strips in the other. The scintillator strips have triangular cross-sections, which promotes energy sharing and thus improves the position resolution of the shower profile. Figure 2.8 also shows the layered structure of the towers in more detail. As with the BEMC, only the EEMC towers are used in this analysis.

2.2.4 EEMC Energy Calibration

Both the Barrel and Endcap Electromagnetic Calorimeters must be calibrated in order to accurately relate recorded ADC signals to the transverse energy deposited in the calorimeters. The BEMC calibration procedure relies on the ratio E/p for identified electrons, matching the energy deposited in the calorimeter with the momentum measured by the TPC. However, the rapidly falling TPC tracking efficiency at EEMC pseudorapidities necessitates a calibration approach that does not rely on the TPC. Reconstruction of the π^0 invariant mass could provide an absolute calibration, but was not feasible before 2009 because of inadequate simulations of the EEMC. So, a calibration method that relies on the identification of minimum ionizing particles (MIPs) was chosen for the EEMC.

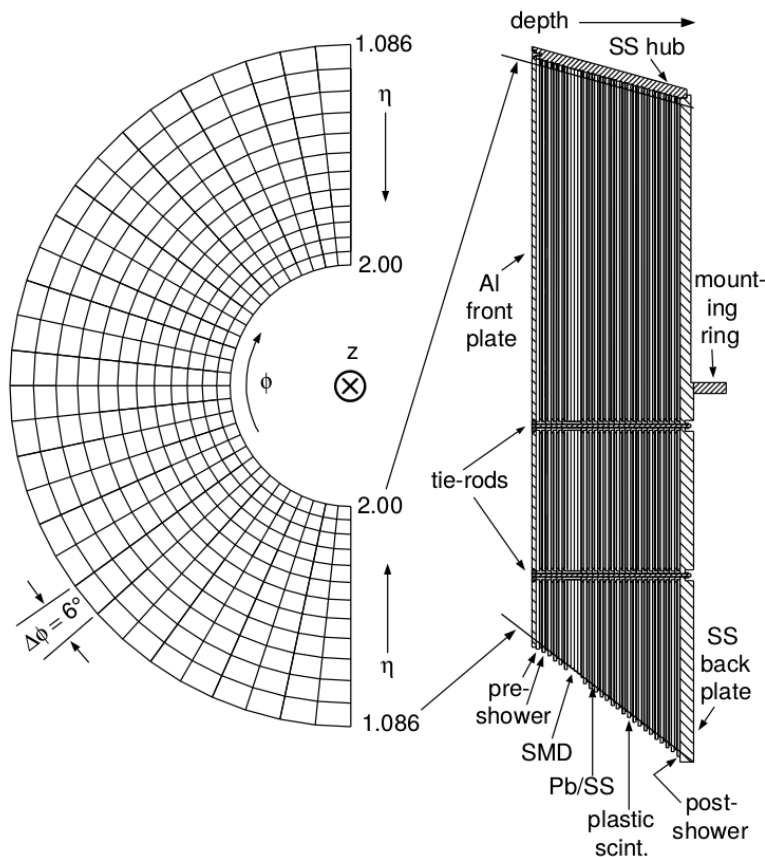


Figure 2.8: Detailed structure of the EEMC. The left figure gives a beam's-eye view of half of the detector with the towers indicated, while the right figure shows a cutaway view of the lead-scintillator stack [51].

MIP Method Overview

The MIP calibration method determines the calorimeter gains using the mean expected energy loss of minimum ionizing particle passing through the scintillator layers. MIPs, which at STAR are mostly charged pions, are produced in large quantities and with high purity. However, the MIP method has a few limitations which must be kept in mind:

1. the actual energy loss of a MIP passing through a scintillator layer depends slightly on the type of particle, its energy, and its angle of incidence;
2. the distribution of deposited energy in thin scintillator layers is not Gaussian;

3. because MIPs do not generate electromagnetic showers, calculating absolute gain factors requires knowing the calorimeter sampling fraction.

The calorimeter sampling fraction is the percentage of ionization that occurs in the scintillator layers, as opposed to the proportion that occurs in the lead radiator layers. The EEMC sampling fraction is about 5%. The mean energy loss of a normally incident MIP in plastic scintillator is approximately 2 MeV/cm, and the EEMC lead-scintillator stacks contain a little less than 10 cm of plastic. Thus, the EEMC response to a normally incident MIP should be similar to that of a 0.4 GeV photon.

Procedure

The MIP identification procedure relies on finding isolated energy deposits in all layers of the calorimeter for a given tower. A transverse isolation cut requiring a coincidence of “hits” in two neighboring SMD strips in both planes, with multiple empty strips on either side, is imposed to ensure that only a single MIP is present. The intersection of the orthogonal sets of fired strips in the two SMD planes is used as a fiducial cut to ensure that the MIP stayed within a single tower. The calibration is then carried out with the resulting MIP sample using an “all layers but one” approach. A given layer is calibrated by requiring that an energy consistent with a MIP be deposited in all of the other layers. For example, the tower gains are obtained by requiring that MIP energy be deposited in the two preshower layers, the postshower layer, and the two SMD planes. While this procedure may seem circular, in practice the simple requirement of a “hit” well above pedestal in all other layers is by itself sufficient to yield a well-defined MIP signal in the layer of interest.

Relative Gain Change and Results

As a preliminary step to the measurement of A_{LL} for dijet production at forward pseudo-rapidity, the gains for all EEMC layers were obtained using the MIP calibration method.

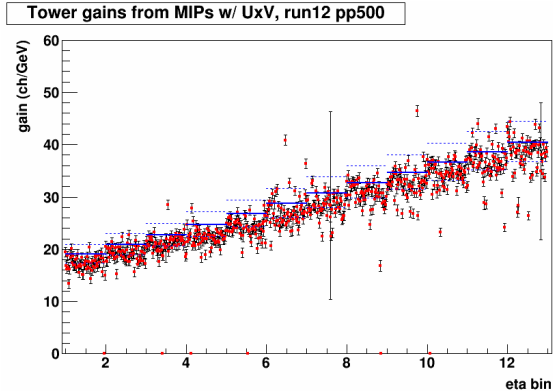


Figure 2.9: 2012 $pp510$ tower gains vs. each tower's η bin.

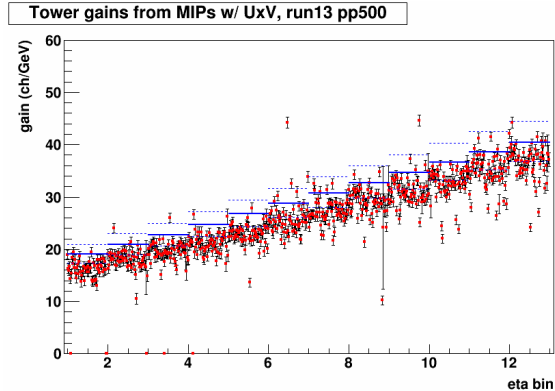


Figure 2.10: 2013 $pp510$ tower gains vs. each tower's η bin.

The data for the analysis described in this dissertation were collected during the $\sqrt{s} = 510$ GeV portions of the 2012 and 2013 RHIC runs, so the EEMC was calibrated (separately) for these two periods. An additional consideration for these calibration efforts was that the EEMC gains can decrease over the months of RHIC running. The cause of this gain decrease is unknown, though it may be related to radiation damage to the scintillators. Since the 2013 pp at 510 GeV run lasted for a relatively long time and featured high luminosities, the changing gains were expected to have a noticeable effect on jet analyses. Thus, a slight modification of the EEMC tower calibration was developed and implemented for both the 2012 and 2013 datasets to provide more accurate gains.

The modified calibration procedure was carried out for both datasets in the exact same manner. First, the gains for each layer were obtained for the entirety of the calibration dataset using the method described above. The results for the towers, the only layer of interest for the dijet analysis described in this thesis, can be seen in Figs. 2.9 and 2.10. The gains (red points) are plotted as a function of pseudorapidity bin, along with the ideal gains (blue lines) for each η bin. A tower's ideal gain is defined as the gain for which an electromagnetic particle with 60 GeV of transverse energy would show up in channel 4095. The high voltages for the EEMC tower PMTs are adjusted occasionally to maintain tower gains close to the ideal values.

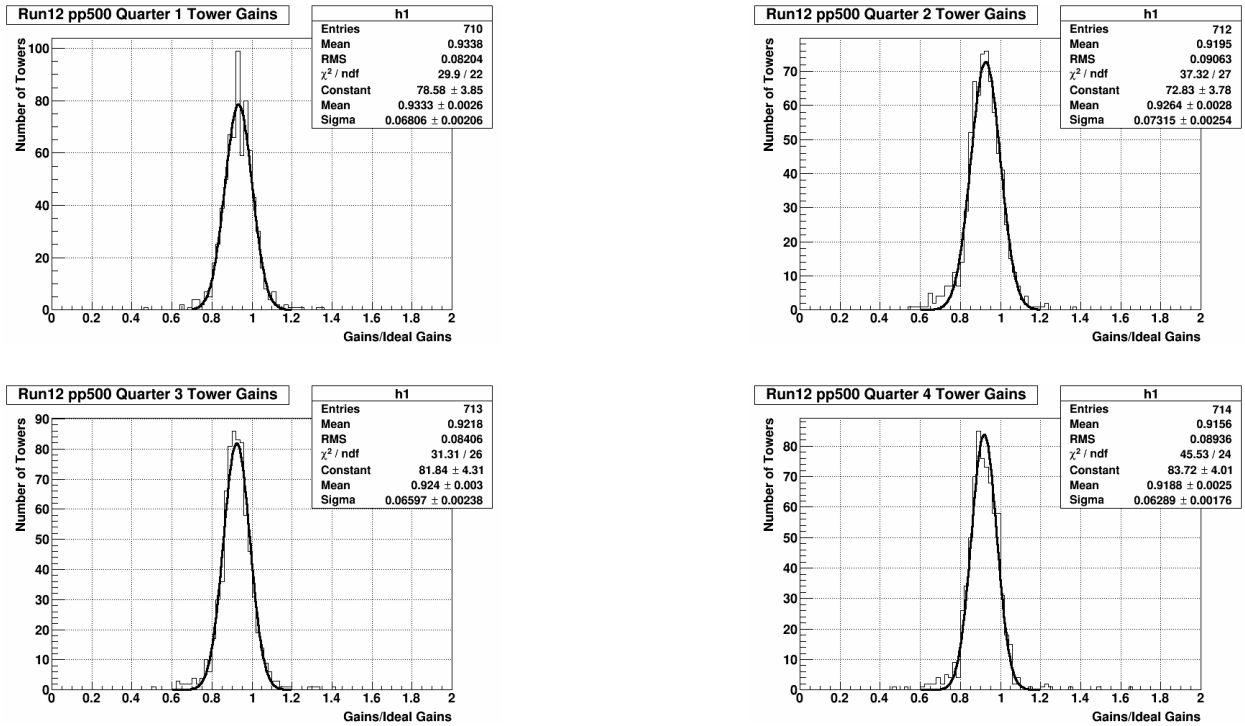


Figure 2.11: Histograms and fits of the ratio of calibrated tower gain over ideal gain, for the four quarters of the 2012 $pp510$ running period.

Next, the calibration dataset was divided into four quarters covering roughly equal time periods. Each quarter was calibrated independently according to the MIP calibration procedure, and tower gains obtained. Then, histograms were filled with ratios of calculated gain over ideal gain for each tower, and fit with Gaussians. The histograms and fits for the 2012 run are shown in Fig. 2.11, and for the 2013 run in Fig. 2.12. The mean of the Gaussian fit was taken to be the average gain ratio for that particular quarter.

With the four average gain ratios calculated, they were plotted as a function of date and fit with a straight line. The results for both years are shown in Figs. 2.13 and 2.14. As evidenced by the plots, the decreasing tower gains over the course of a running period are modeled quite well by the linear fit. It is likely that the decreasing gains are related to the integrated luminosity seen by the detector, for which the amount of elapsed time since the running period began is a good approximation. Note the substantial change in vertical scale, and hence in the fractional gain change, in 2013 compared to 2012.

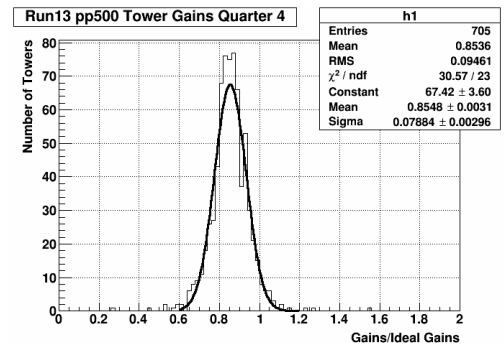
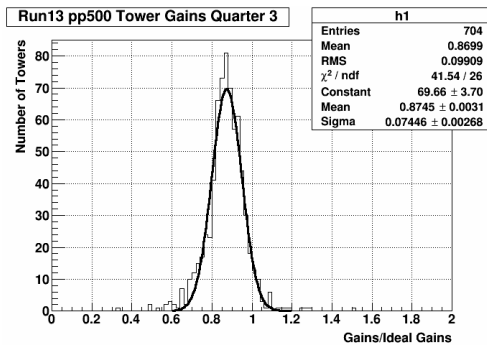
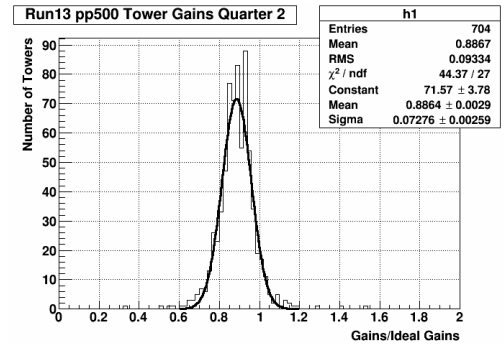
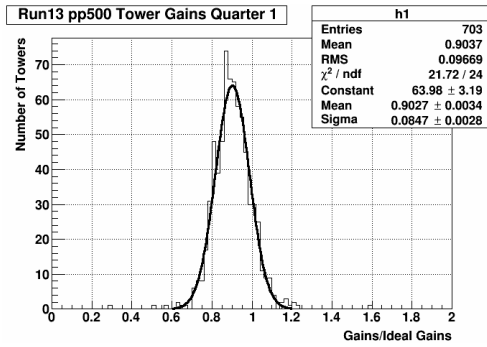


Figure 2.12: Histograms and fits of the ratio of calibrated tower gain over ideal gain, for the four quarters of the 2013 *pp510* running period.

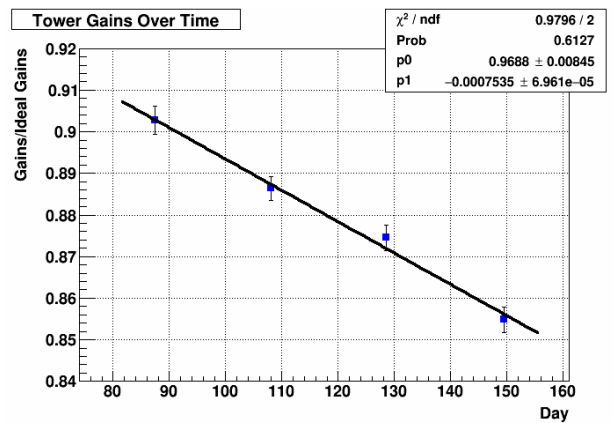
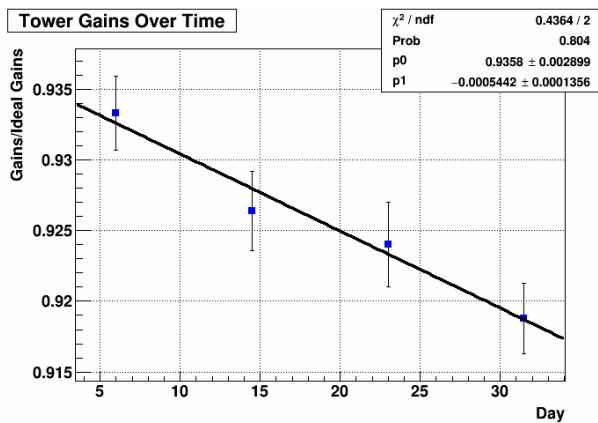


Figure 2.13: 2012 *pp510* tower gain decrease over time.

Figure 2.14: 2013 *pp510* tower gain decrease over time.

An additional consideration in the study of the changing tower gains was to see if the gain decrease was uniform over the entire EEMC. For example, one could imagine that towers closer to the beam pipe (higher η) or in a certain azimuthal position are more susceptible to degradation. To check this, the EEMC towers were split into groups based on η bin and ϕ sector. Then, for each η and ϕ group, the average ratio of tower gains to ideal gains for each quarter of the running period was calculated and fit with a line, as described above for all of the towers. This yielded 12 slopes for the different η bins, and 12 slopes for the different ϕ bins. These two sets of slopes are shown in Figs. 2.15 and 2.16 for 2012, and in Figs. 2.17 and 2.18 for 2013. The 2012 run showed no significant η dependence, and the 2013 run showed no smooth η dependence, so it was concluded that the rate of tower gain decrease did not vary with pseudorapidity in a way that needed to be accounted for. Neither running period showed significant ϕ dependence. Since the tower gain decrease was observed to be mostly uniform across the whole EEMC, the slopes shown in Figs. 2.13 and 2.14 were taken to be the rate of change of all towers' gains for the 2012 and 2013 runs, respectively.

The last step in the modified tower gain calibration procedure was to use the global gain change slopes along with each tower's gain from the calibration of the entire dataset (Figs. 2.9 and 2.10) to extrapolate a set of four gains for every tower. Each running period was split into four equal quarters, with the tower gains calculated at the middle of each quarter. This extrapolation was done, instead of just using the tower gains from the four separate calibrations, in order to yield gains for as many towers as possible, since the reduced statistics in each quarter render more towers unusable. The end result of the calibration effort was four sets of tower gains and one set of gains for the other layers (preshower, postshower, SMD) for each of 2012 and 2013, which were then uploaded to the STAR database and made available for use in any analysis that incorporates the EEMC.

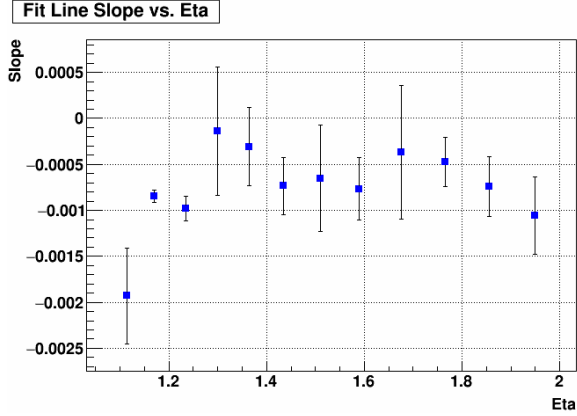


Figure 2.15: Rate of 2012 $pp510$ tower gain decrease as a function of pseudorapidity.

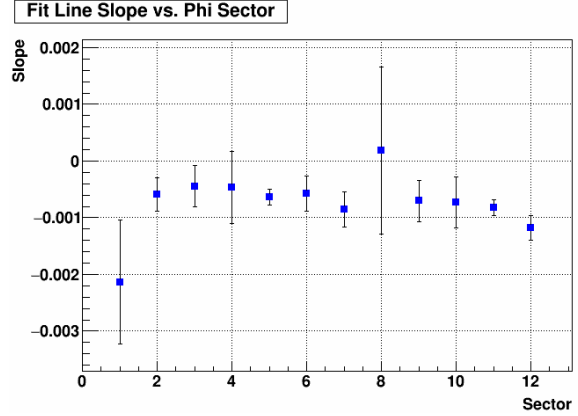


Figure 2.16: Rate of 2012 $pp510$ tower gain decrease for each sector of azimuthal angle.

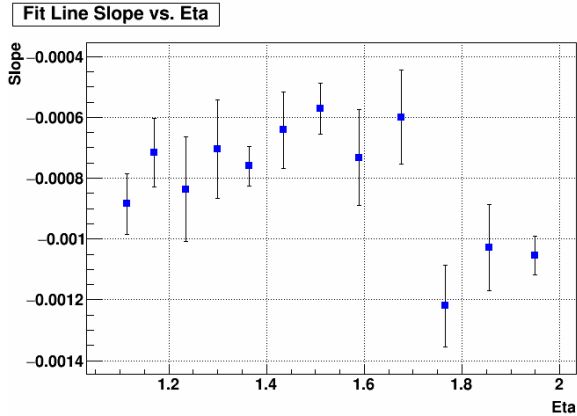


Figure 2.17: Rate of 2013 $pp510$ tower gain decrease as a function of pseudorapidity.

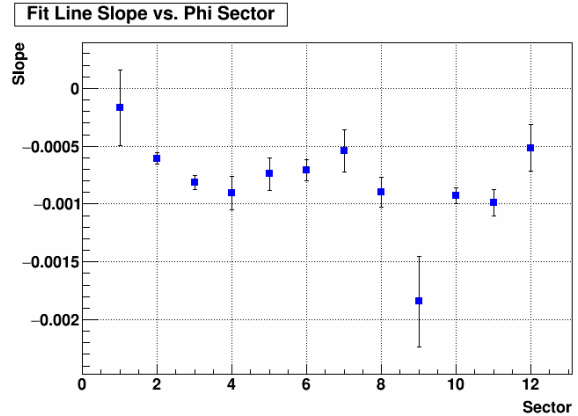


Figure 2.18: Rate of 2013 $pp510$ tower gain decrease for each sector of azimuthal angle.

2.2.5 STAR Trigger

STAR utilizes a multi-level trigger system [52], consisting of hardware and software components, to select useful events from the millions of bunch crossings which occur every second. The trigger system analyses readout from fast-triggering detector subsystems at the RHIC bunch crossing rate in order to determine whether to read out information from slower components. There are many different ways to trigger on the various signals from the fast detectors, depending on the types of events one hopes to record; the part of the trigger system relevant to this analysis is Level-0.

The first layer of the STAR trigger system is called Level-0 (L0), and consists of electronics

which make trigger decisions based on energy deposition in fixed regions of the BEMC and EEMC known as jet patches. There are 30 total jet patches spanning the entire azimuthal and pseudorapidity acceptance of the two calorimeters, with 18 jet patches in the BEMC, 6 in the EEMC, and the remaining 6 overlapping the BEMC-EEMC boundary. Each jet patch covers a 1.0×1.0 region in $\eta - \phi$ space; Table 2.1 shows how they are configured across the calorimeters.

ϕ Position	BEMC East $-1 < \eta < 0$	BEMC Middle $-0.6 < \eta < 0.4$	BEMC West $0 < \eta < 1$	EMC Overlap $0.4 < \eta < 1.4$	EEMC $1 < \eta < 2$
10 o'clock	BEMC-JP6	BEMC-JP12	BEMC-JP0	Overlap-JP0	EEMC-JP0
12 o'clock	BEMC-JP7	BEMC-JP13	BEMC-JP1	Overlap-JP1	EEMC-JP1
2 o'clock	BEMC-JP8	BEMC-JP14	BEMC-JP2	Overlap-JP2	EEMC-JP2
4 o'clock	BEMC-JP9	BEMC-JP15	BEMC-JP3	Overlap-JP3	EEMC-JP3
6 o'clock	BEMC-JP10	BEMC-JP16	BEMC-JP4	Overlap-JP4	EEMC-JP4
8 o'clock	BEMC-JP11	BEMC-JP17	BEMC-JP5	Overlap-JP5	EEMC-JP5

Table 2.1: Jet patch geometry.

In order to decide whether to record a given event, the trigger logic sums the ADC outputs from all towers within each jet patch and then compares the patch sums to a set of thresholds. There were three jet patch thresholds during the 2012 RHIC running period, which are listed in Table 2.2 along with the corresponding approximate transverse energy values. If any of the 30 jet patches fired above the highest threshold, the JP2 bit is set. If any patches fire above the middle threshold the JP1 bit is set, and similarly for the lowest threshold and JP0 bit.

The 2013 RHIC running period implemented the same logic for JP2, JP1, and JP0 but with different thresholds, which are given in Table 2.3. Note from the Table that the 2013 trigger system also kept track of an additional fourth threshold, the “dijet” threshold. The new trigger logic utilizing this dijet threshold bit was introduced in order to enhance the number of recorded dijet events. There are three “dijet” triggers in the 2013 data which are relevant to this analysis: JP1dijet, JP0dijet, and EEMCdijet. The JP1dijet bit is set if there is a jet patch in the BEMC with the JP1 bit set, and another jet patch in either

the BEMC or EEMC with the dijet bit set. In addition, the two jet patches must not be adjacent in azimuthal angle ϕ . Similarly, the JP0dijet bit is set if there is a BEMC jet patch with the JP0 bit set, and a non-adjacent jet patch in either calorimeter with the dijet bit set. Finally, the EEMCdijet bit will be set if an EEMC jet patch has the JP0 bit set and a patch in the other half of the calorimeter (the “halves” are top and bottom) has the dijet bit set. Unlike with the JP2, JP1, and JP0 thresholds, no trigger decisions were made based solely on comparisons between jet patch sums and the dijet threshold.

Trigger	Threshold	Nominal E_T (GeV)
JP0	28	5.4
JP1	36	7.3
JP2	66	14.4

Table 2.2: 2012 jet patch thresholds.

Trigger	Threshold	Nominal E_T (GeV)
dijet	17	2.8
JP0	34	6.8
JP1	43	9.0
JP2	66	14.4

Table 2.3: 2013 jet patch thresholds.

Prescaling

Another important function carried out by the Level-0 logic is trigger prescaling. Triggers which are satisfied at lower threshold requirements, such as JP0 and JP1, fire at a much faster rate than those with higher requirements, like JP2. In order to prevent the low threshold triggers from filling up all of the available DAQ bandwidth, a certain fraction of their events are “prescaled”, and the remaining events are discarded. For example, 100 is a typical JP0 prescale factor, meaning that the DAQ system will only record 1 out of every 100 events where JP0 fired at Level-0. The prescales are different for each trigger and can change on a run-by-run basis, depending on factors such as the instantaneous luminosity seen by STAR. The three dijet triggers present in 2013 have much lower prescales than the JP0 and

JP1 triggers, allowing for many events which likely contain dijets to be recorded when they otherwise would have been discarded. The JP2 trigger is not prescaled, so events where it fired are always recorded.

CHAPTER 3

Jet Reconstruction and Dijet Selection

When two high-energy protons collide, their constituent partons mostly pass by each other. However, sometimes a parton in one proton undergoes a hard scattering with a parton in the other proton, ejecting both partons from their parent hadrons at high energy. Color-charged particles cannot exist in isolation, so the hard-scattered partons each radiate gluons that can split into quark-antiquark pairs as they move away from the interaction point. The resulting collections of collimated color-neutral particles, oriented mostly in the directions of the initial scattered partons, are known as jets. Collecting the final state particles in these jets therefore gives information about the kinematics of the scattered partons, and hence about the initial state of those partons prior to scattering, making jets an important observable for many QCD studies [53].

3.1 Jet Reconstruction

Hadrons from the fragmentation of hard scattered partons are not the only particles produced in polarized pp collisions, so a method for deciding which particles are part of a jet and which are not is necessary in order for jet analyses to provide useful results. Such a method is known as a jet algorithm, which provides well-defined rules for grouping detected particles together into jets. Jet algorithms must be flexible enough to account for jets with different particle content, momentum, and shape, while also being insensitive to infrared radiation and collinear emission (IRC). Infrared radiation refers to emission of soft particles from a

higher energy particle, while collinear emission occurs when a high energy particle splits into two lower energy particles which then continue on in nearly the same direction. An IRC-safe jet algorithm will find the same set of hard jets regardless of how much infrared radiation or collinear emission is present in a given event, allowing for accurate comparisons among data, simulation, and theory [54]. Once a set of particles has been grouped into a jet by an IRC-safe algorithm, their momenta must be combined to yield the momentum of the entire jet. The recombination scheme employed in this analysis is simple addition of the individual 4-momenta of a jet's constituents, though there are other possible methods. A jet algorithm and its associated parameters, together with a recombination scheme, is called a jet definition.

3.1.1 Anti- k_T Algorithm

The jet algorithm used in this thesis, as well as in all STAR inclusive jet or dijet analyses since 2009, is the anti- k_T algorithm [55]. The anti- k_T algorithm is a sequential recombination algorithm which repeatedly combines pairs of particles to build up the jets. Such algorithms combine particles which are the closest together according to a certain measure of distance. The two relevant distances in the anti- k_T algorithm are:

$$d_{ij} = \min(1/p_{ti}^2, 1/p_{tj}^2) \frac{\Delta R_{ij}^2}{R^2} \quad (3.1a)$$

$$d_{iB} = 1/p_{ti}^2, \quad (3.1b)$$

where i, j denote particles and pseudojets (collections of particles) and B represents the beamline. The transverse momentum of object i is given by p_{ti} , while the variable $\Delta R_{ij}^2 = (\eta_i - \eta_j)^2 + (\phi_i - \phi_j)^2$ with η_i and ϕ_i being the pseudorapidity and azimuthal angle of object i . R is known as the radius parameter, and it determines the approximate size of the reconstructed jets in $\eta - \phi$ space, along with how close together they can be. For the analysis described in this thesis, R has been set to 0.5. The algorithm calculates the distances d_{ij}

and d_{iB} for all objects and pairs, and then identifies the minimum. If d_{ij} is the minimum distance measure, then the algorithm recombines objects i and j and recalculates all of the d_{ij} and d_{iB} . If d_{iB} is the minimum, then object i is a final state jet, and the algorithm removes it from the list of particles and pseudojets before recalculating all of the d_{ij} and d_{iB} . The algorithm iterates this process until all of the initial particles have been grouped into final state jets.

3.1.2 Jet Selection Criteria

The jet reconstruction procedure used in this analysis follows that used in the first measurement of A_{LL} for forward dijets at STAR [34], with the exception of an anti- k_T radius parameter of $R = 0.5$ rather than 0.6. The smaller radius parameter was chosen in line with previous inclusive and dijet analyses [36] at $\sqrt{s} = 510$ GeV, which found that a smaller R was less sensitive to pile-up effects. Jets were found using an implementation of the anti- k_T algorithm developed by the FastJet group [56]. The remainder of this subsection details the cuts placed on the TPC tracks and calorimeter tower hits which are the inputs to the jet finding algorithm.

Track Conditions

TPC tracks must satisfy several conditions to be included in the jet finding process, in order to ensure track quality and minimize unwanted beam effects. The tracks are required to have $p_T \geq 0.2$ GeV/ c and pseudorapidity η between -2.5 and 2.5, to remove soft tracks and tracks far outside the TPC acceptance. They are also subject to a p_T -dependent distance of closest approach (DCA) cut, where the DCA is the smallest distance between the event vertex and the track's trajectory. This cut requires tracks with $p_T < 0.5$ GeV/ c to have a DCA < 2 cm and tracks with $p_T > 1.0$ GeV/ c to have a DCA < 1 cm, and is linearly interpolated for tracks with p_T between 0.5 GeV/ c and 1.0 GeV/ c . The DCA cut is meant to reduce pile-up effects close to the beamline.

The readout pads that detect the electrons produced by ionization of the TPC gas are arranged in rows, and hits in these “padrows” provide the fit points used to reconstruct charged particle trajectories. As in the previous analysis of dijets in the EEMC region, the tracks for jet finding must be reconstructed from at least five TPC padrow hits. STAR jet analyses at mid-rapidity require tracks to have at least 12 hits, but this condition is relaxed for measurements at more forward rapidities, given that tracks which point to the EEMC do not traverse the full radial extent of the TPC and therefore deposit charge over fewer padrows. This 5-point tracking is only implemented for tracks with $\eta > 0.5$, as other tracks are subject to the 12-point tracking condition. Finally, the tracks must include at least 51% of the maximum possible number of padrow hits, given the TPC geometry and active electronics channels.

Tower Conditions

The calorimeter towers must also satisfy a few conditions before being input to the jet finding algorithm. The towers must have $E_T \geq 0.2$ GeV, and ADC values larger than both pedestal + 4 and pedestal + $3*\sigma_{ped}$. Soft towers are removed just as soft tracks are, and the ADC conditions are meant to ensure that the signal is from energy actually deposited in the tower and not from the pedestal. Additionally, towers with tracks pointing to them have the p_{Tc} of the track subtracted from the E_T of the tower. If the track p_{Tc} is greater than the tower E_T , then the tower’s transverse energy is set to zero. This is done to avoid double-counting contributions to the jet p_T from charged hadrons that both leave tracks in the TPC and deposit energy in the calorimeters.

Tracks and towers that pass these cuts have their momenta converted to Lorentz 4-vectors and passed to the anti- k_T jet algorithm described above. Reconstructed jets were required to have $p_T > 5$ GeV/ c in order to be eligible for further analysis.

3.2 Dijet Selection Criteria

A dijet is a system of two jets which arises from a single partonic hard-scattering event. The requirements used to determine which jets found by the jet reconstruction algorithm constitute the dijet pair for a given event are similar to those used in previous STAR dijet analyses:

1. Select the vertex with the highest positive rank in the event,
2. Require the vertex to have $|z| < 90$ cm ($z = 0$ at the middle of the TPC),
3. Select all jets satisfying $-1.2 \leq \eta \leq 2.2$ and $-1.0 \leq \eta_{detector} \leq 2.0$,
4. Select the two highest p_T jets,
5. Require one of the triggers to be satisfied (see below).

These conditions are the same as those used in the first measurement of forward dijet A_{LL} except for the pseudorapidity cuts, which were $-0.8 \leq \eta \leq 1.8$ and $-0.7 \leq \eta_{detector} \leq 1.7$ at this step. The detector pseudorapidity $\eta_{detector}$ is defined to be the pseudorapidity of the point where the jet thrust axis intersects the BEMC or EEMC, relative to the nominal STAR interaction point. The requirement that the dijet candidate satisfy one of the triggers will be explained in more detail in Section 3.3. The two jets selected according to the above criteria constitute the one and only dijet candidate for a given event. The dijet candidate must then satisfy further requirements in order to be included in the analysis:

1. Opening angle cut: $\Delta\phi = \pi \pm \pi/3$,
2. At least one jet must have neutral fraction < 1.0 ,
3. Both jets must satisfy $-0.8 \leq \eta \leq 1.8$ and $-0.7 \leq \eta_{detector} \leq 1.7$,
4. p_T balance and high track cut,

5. Asymmetric p_T cut: High jet $p_T \geq 7.0$ GeV/ c and low jet $p_T \geq 5.0$ GeV/ c .

All of these cuts are imposed after the Underlying Event subtraction (described in Chapter 5), with the asymmetric p_T cut being placed after the jet p_T shift (described in Chapter 6) as well.

Partons involved in a hard scattering event should come out of the collision back-to-back in azimuthal angle ϕ , assuming they have no initial transverse momentum. The opening angle cut is imposed to remove dijet events where the two jets are less than 120° apart in azimuth, as the jets in these events likely do not represent the outgoing hard-scattered partons. The cut on the fraction of jet energy from neutral particles is applied to remove events where both jets are composed primarily of background energy, as these jets typically will not contain any valid TPC tracks. In inclusive jet and BEMC dijet analyses this cut is usually set to remove jets with greater than 95% neutral energy, but the falling TPC efficiency at forward pseudorapidities means that jets in the EEMC region often have very high percentages of their energy coming from the calorimeter towers. Therefore, this cut is relaxed in EEMC dijet analyses to only require at least one jet to have some energy from charged particles, as it is very unlikely that an event will have a pair of coincident background jets which happen to also satisfy the opening angle condition. The requirements on the η and $\eta_{detector}$ are imposed to ensure that the jet thrust axes are not too close to the edges of the detector acceptance.

The p_T balance cut is applied to remove events where one of the jets in the dijet pair has much greater p_T than the other, usually due to a track with anomalously high transverse momentum. Dijet events which contain a track with 15 GeV/ $c \leq p_T < 40$ GeV/ c are kept if the ratio of the two jets' transverse momenta is between $\frac{2}{3}$ and $\frac{3}{2}$, and discarded otherwise. Dijet events which contain a track with $p_T \geq 40$ GeV/ c are discarded regardless of the jet p_T ratio, as tracks with this much apparent transverse momentum are likely to be inaccurately reconstructed due to the finite resolution of the track curvature method which

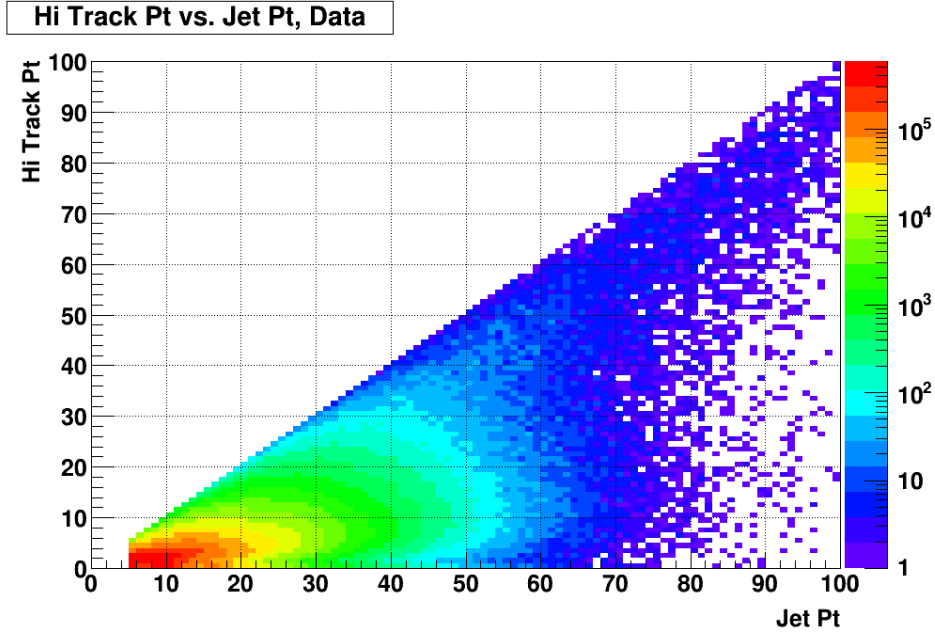


Figure 3.1: Correlation between the p_T of the highest p_T track (the “hi track”) and the p_T of the jet containing it, from data.

is used to calculate track p_T . The correlation between the highest p_T track in a jet and the p_T of the jet itself is shown in Fig. 3.1 for data and Fig. 3.2 for simulation. The figures show that above a highest track p_T of about 40 GeV/ c , a significant fraction of the jets receive most of their total p_T from that single track, an effect which becomes even more dramatic with increasing highest track transverse momentum. This effect is seen in both data and simulation, indicating that the source of these very high p_T tracks is understood and accurately modeled by the simulation. The observation that the total p_T of jets with such high p_T tracks tends to be dominated by the contributions from those tracks motivated the decision to simply discard all such events as suspect; note also from the figures that jets containing tracks with p_T that large constitute a very small fraction of the total sample of jets.

Finally, an asymmetric cut on the transverse momenta of the two jets was imposed to facilitate comparison with theoretical predictions [57]. Comparison with theory also motivates sorting jets into two categories based on their pseudorapidities: jets with $-0.8 < \eta < 0.9$ are called “Barrel jets”, while jets with $0.9 < \eta < 1.8$ are called “Endcap jets”. This condition

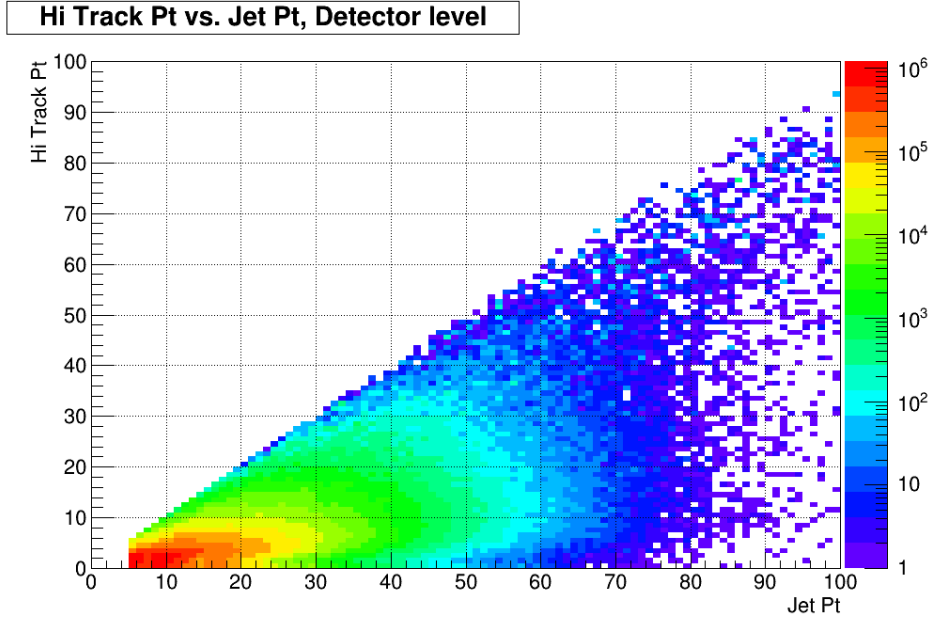


Figure 3.2: Correlation between the p_T of the highest p_T track (the “hi track”) and the p_T of the jet containing it, from simulation.

is related to the physics of the hard scattering, not to the actual detector geometry, so a Barrel jet might have a detector pseudorapidity greater than 1.0 or an Endcap jet a detector pseudorapidity less than 1.0. Dijet events where one jet is a “Barrel” jet and the other is an “Endcap” jet will be referred to as “Barrel-Endcap” dijets, while dijet events containing two “Endcap” jets will be referred to as “Endcap-Endcap” dijets.

3.3 Software Trigger Requirements

Dijet candidates must satisfy the conditions of one of the trigger categories in order to be included in the analysis. The conditions for an individual jet to satisfy the categories for the triggers used in the 2012 RHIC run are:

1. JP2: The jet must have $p_T \geq 15.0$ GeV and be geometrically matched to a jet patch which fired the JP2 hardware trigger;
2. JP1: The jet must have $p_T \geq 9.5$ GeV and be geometrically matched to a jet patch

which fired the JP1 hardware trigger;

3. JP0: The jet must have $p_T \geq 7.3$ GeV and be geometrically matched to a jet patch which fired the JP0 hardware trigger.

The geometric matching condition requires that the reconstructed jet thrust axis must point within 0.6 in $\eta - \phi$ space of the center of the triggered jet patch. The dijet pair itself is then assigned a trigger designation based on the trigger categories its constituent jets fall into: if at least one of the jets satisfied JP2 then the event is considered a JP2 event; if the event is not JP2 and at least one of the jets satisfied JP1 then the event is a JP1 event; if the event is neither JP2 nor JP1 and at least one of the jets satisfied JP0 then the event is a JP0 event. In this way, each dijet event is sorted into exactly one trigger category.

The 2013 RHIC run included “dijet” triggers in addition to the jet patch triggers JP2, JP1, and JP0: JP1DiJet, EEMCdijet, and JP0DiJet. Satisfying the requirements of one of these triggers requires consideration of both jets in the dijet pair. The conditions for the categories of triggers used in the 2013 RHIC run are:

1. JP2: The jet must have $p_T \geq 15.0$ GeV and be geometrically matched to a jet patch which fired the JP2 hardware trigger;
2. JP1DiJet: The higher p_T jet must have $p_T \geq 9.5$ and be geometrically matched to a jet patch which has an ADC value above the JP1 threshold, while the lower p_T jet must have $p_T \geq 5.0$ GeV and be geometrically matched to a jet patch which has an ADC value above the dijet threshold;
3. JP1: The jet must have $p_T \geq 9.5$ GeV and be geometrically matched to a jet patch which fired the JP1 hardware trigger;
4. EEMCdijet: The higher p_T jet must have $p_T \geq 7.3$ and be geometrically matched to an EEMC jet patch which has an ADC value above the JP0 threshold, while the lower

p_T jet must have $p_T \geq 5.0$ GeV and be geometrically matched to an EEMC jet patch which has an ADC value above the dijet threshold;

5. JP0DiJet: The higher p_T jet must have $p_T \geq 7.3$ and be geometrically matched to a jet patch which has an ADC value above the JP0 threshold, while the lower p_T jet must have $p_T \geq 5.0$ GeV and be geometrically matched to a jet patch which has an ADC value above the dijet threshold;
6. JP0: The jet must have $p_T \geq 7.3$ GeV and be geometrically matched to a jet patch which fired the JP0 hardware trigger.

The geometric matching condition is the same for 2013 as for 2012. The three “dijet” triggers (JP1DiJet, EEMCdijet, JP0DiJet) have further requirements on the locations of the matched jet patches, which were described in Section 2.2.5. A dijet event is then given one and only one trigger classification following a similar procedure to that in 2012: if at least one of the jets satisfied JP2 then the event is considered a JP2 event; if the event is not JP2 and the jets together satisfied JP1DiJet then the event is a JP1DiJet event; if the event is neither JP2 nor JP1DiJet and at least one of the jets satisfied JP1 then the event is a JP1 event, and so on.

CHAPTER 4

Data and Simulation Studies

4.1 Data Sample

The data for this analysis were taken by STAR during the 2012 and 2013 pp at $\sqrt{s} = 510$ GeV RHIC running periods. The integrated luminosity was 82 pb^{-1} in 2012 and approximately 250 pb^{-1} in 2013. The data samples are made up of hundreds of “runs,” which typically last about 30 minutes but can be shorter depending on operational conditions at STAR and RHIC. The 2012 sample consists of 464 runs, and the 2013 sample consists of 663 runs; all of the runs used are listed in [Appendix A](#), along with the fills they are from.

We note here that a new detector subsystem, the Heavy Flavor Tracker (HFT), was partially installed a little more than half way through the 2013 running period. This changed the STAR geometry, so the TPC calibration and raw data file production were carried out separately for the periods before and after the HFT installation. The part of the run before the HFT was installed is referred to as “Period 1”, while the part after is referred to as “Period 2.” Period 2 also featured higher luminosities, in an attempt to increase the yield of events of interest. The 2013 portion of this analysis was restricted to runs from Period 1 only, because of the changes noted above as well as even lower than usual tracking efficiencies in the Endcap region for Period 2 due to the increased luminosities.

4.1.1 Data Quality Assurance

During each RHIC running period, STAR will take data during thousands of runs. The runs can vary in length from a few minutes up to almost an hour and include different combinations of detector subsystems and triggering schemes, in order to accommodate the needs of diagnostic testing and myriad physics analyses. This section will describe the procedure used to select those runs which were appropriate for the measurement of dijet A_{LL} , as well as the methods for performing quality assurance (QA) on the selected runs.

The general QA procedure takes place over several steps, and involves both automated and manual methods. First, a script is used to create an initial list of runs that are longer than three minutes and include the detector subsystems (TPC, BEMC, EEMC) and triggers (jet patch triggers like JP2, JP1, JP0) necessary for a jet analysis. This script also discards diagnostic runs and runs which are marked “bad” by the STAR personnel on shift while the data were being taken. The next step in the QA process is to examine various relevant quantities on a run-by-run basis using the files which serve as inputs to the jet finding algorithm, such as the p_T of reconstructed tracks and the energy deposited in the calorimeter towers, and look for outliers. This step is called “event-level QA.” Runs with outlier values are investigated further, for example by examining the Electronic ShiftLog for information about the state of the STAR detector and RHIC beam at the time. In addition, runs will be removed if they do not have beam polarization information, relative luminosity values, or valid spin bit information, as these pieces are required for the calculation of the double-spin asymmetries. Finally, in the “jet-level QA” step, properties of all reconstructed jets are examined on a run-by-run basis, with unexplained outliers being excluded from the final list of runs.

QA for 2012 Data Sample

The run selection and QA procedure described above was carried out for the 2012 sample as part of the earlier mid-rapidity inclusive and dijet measurements. However, those measurements did not include jets in the EEMC, so it was necessary to do further, Endcap-specific, QA for this analysis. This QA was done using the reconstructed dijet pairs, as the files containing the information necessary for event-level and jet-level QA were no longer readily available. Figure 4.1 shows some examples of the types of plots which were manually examined for the QA. The figures show the average value of various quantities in a run, as a function of the chronological order in which the runs were taken. The discontinuities seen in the plots indicate the end of each fill and the beginning of the next one. For example, note that the average jet p_T decreases over the course of a fill. This is because the prescale factors for triggers with lower p_T thresholds, like JP1 and JP0, are chosen in proportion to the instantaneous luminosity at the beginning of each run. Since the delivered luminosity decreases over the course of a fill, JP1 and JP0 events are recorded at a higher rate at the end of fills, which drives the average reconstructed jet p_T down.

QA for 2013 Data Sample

Whereas the 2012 sample had already been studied carefully in previous jet analyses, the 2013 sample needed to be run through the full multi-step QA procedure. Figure 4.2 shows some examples of the types of plots used for the event-level QA, and Fig. 4.3 gives examples of plots used for the jet-level QA. It was unnecessary to do the dijet QA, described in the previous subsection for 2012, for the 2013 data because the event-level and jet-level QA were carried out.

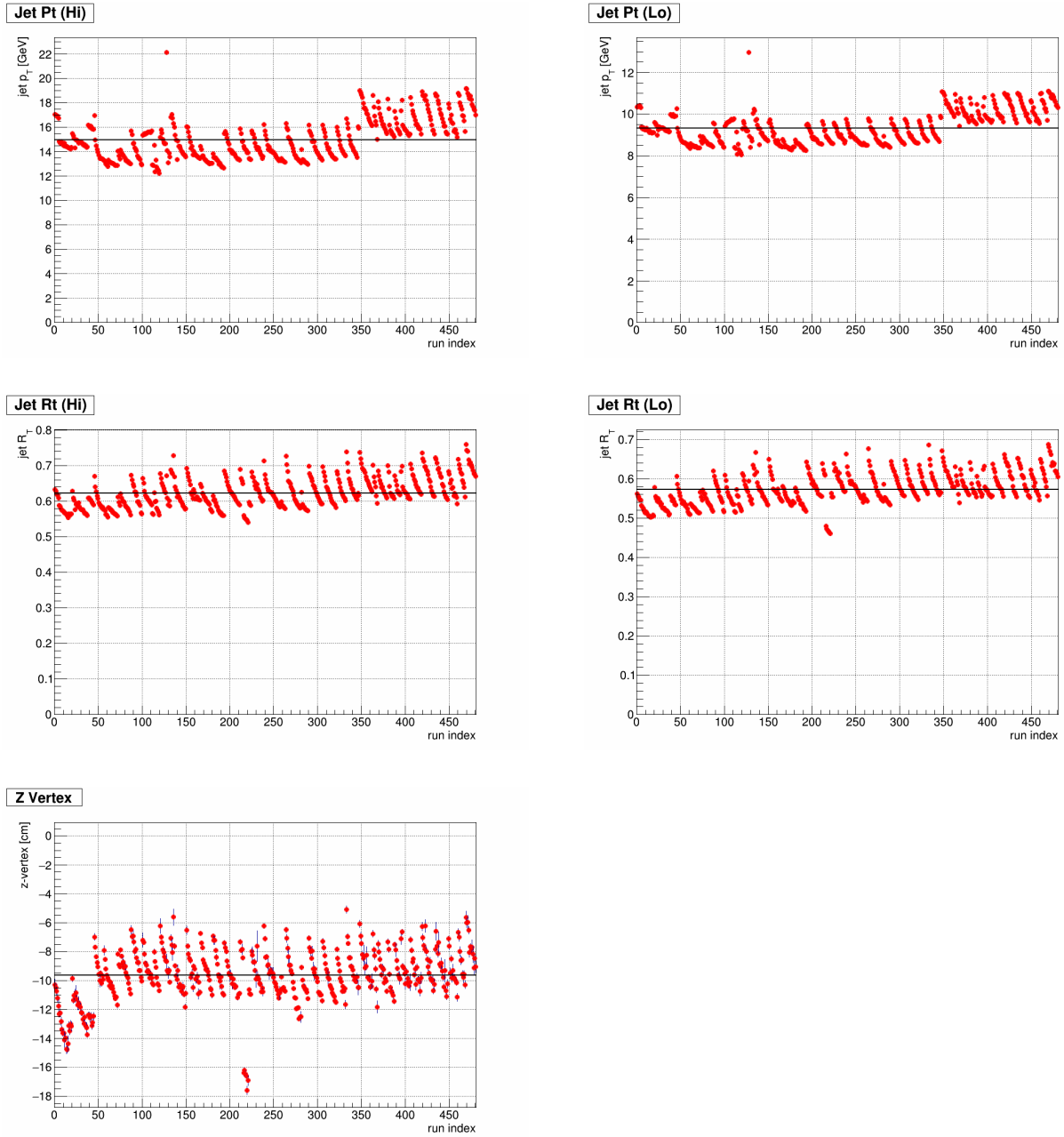


Figure 4.1: Selected plots from the QA of dijets in the 2012 sample. The points indicate the average value per event of the specified quantity for one run. Plots of jet quantities like p_T and neutral fraction are inspected separately for the high and low p_T jets in the dijet pair.

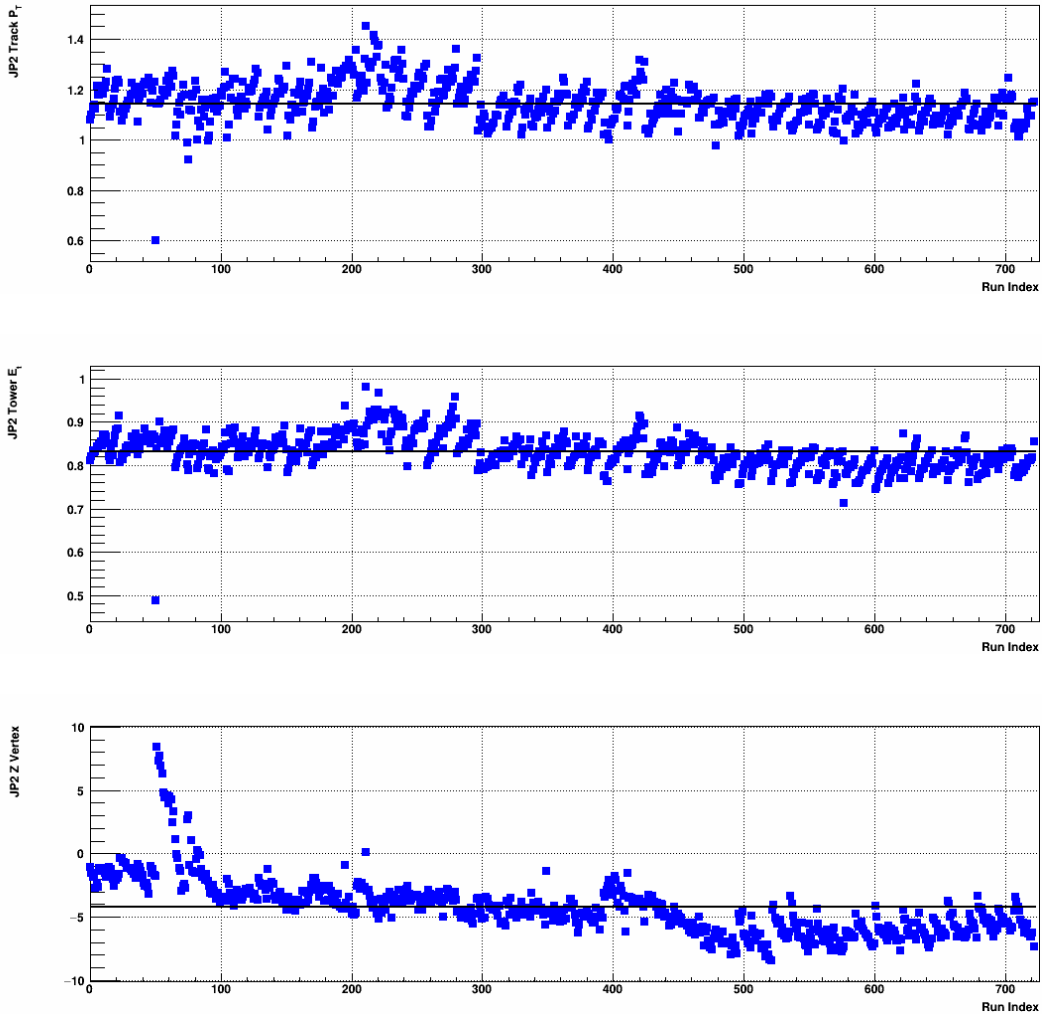


Figure 4.2: Selected plots from the event-level QA for the 2013 sample. The points indicate the average value per event of the specified quantity for one run. The variables of interest are examined separately for each trigger category; the figures shown here are for JP2.

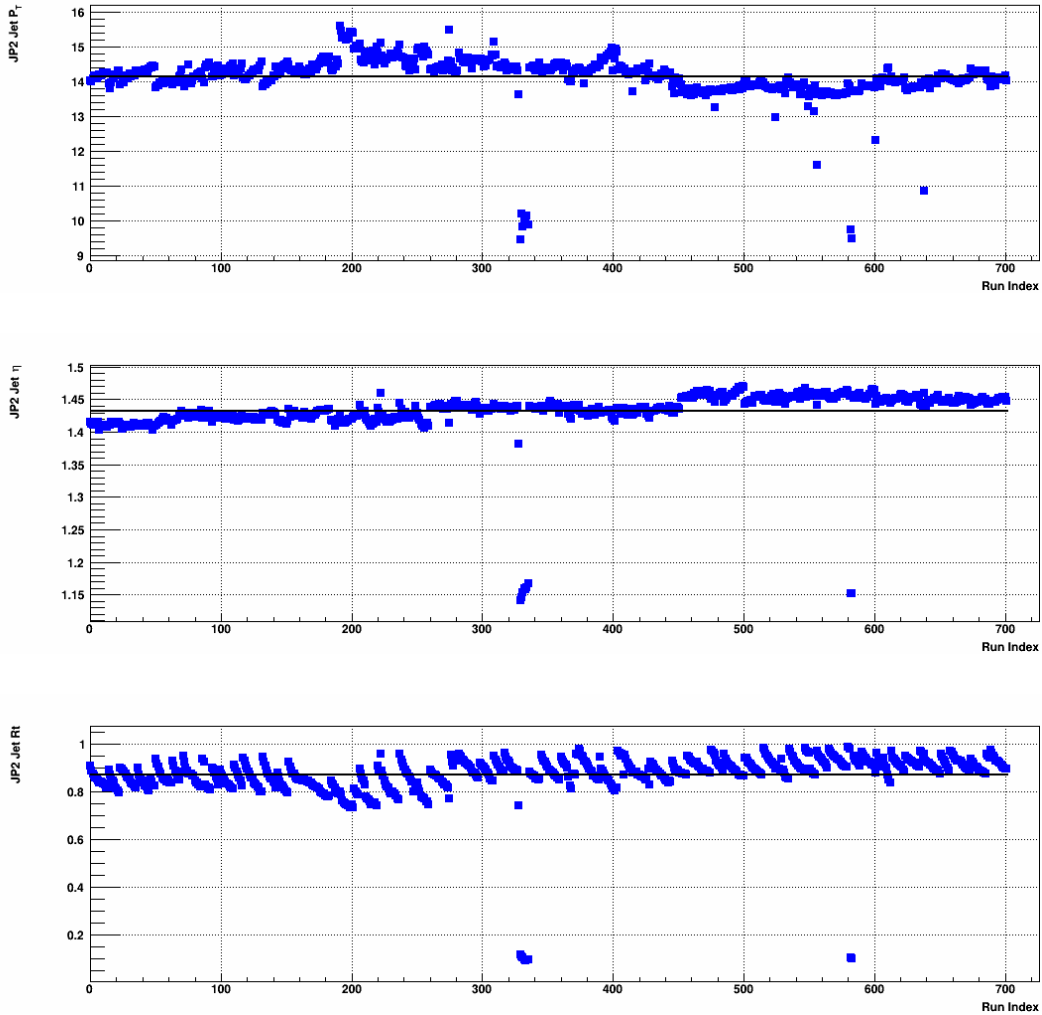


Figure 4.3: Selected plots from the jet-level QA for the 2013 sample. The points indicate the average value per event of the specified quantity for one run. The variables of interest are examined separately for Barrel and Endcap jets, as well as for each trigger category; the figures shown here are for Endcap jets in JP2 events. Several outliers are clearly visible in each of the plots; those runs were examined individually and typically discarded.

4.2 Simulation Sample

This section will describe the simulation samples used for this dijet A_{LL} analysis, as accurately simulated events are integral to the correction of measured jet quantities for detector effects, the estimation of systematic errors due to hadronization and detector response, and the eventual comparison of data results to theory. The simulation samples consist of millions of pp collision events generated across 13 partonic p_T bins using PYTHIA 6.4.28 [58] with the Perugia 2012 tune 370 [59]. The 2012 simulation sample contains 3.6 million events, while the 2013 sample has 10.3 million. The final state particles generated by PYTHIA are fed through the GSTAR package in GEANT3 [60] to simulate the response of the STAR detector. The simulated detector responses are then broken into individual runs and “embedded” into zero-bias events collected on random bunch crossings throughout the RHIC running period. This embedding procedure ensures that the simulated events more accurately model the beam background, pile-up, and detector status conditions which are present in the real data sample.

4.2.1 Levels of Jet Information

The information about a simulated event is split into three distinct stages: the partonic hard scattering, the fragmentation and hadronization of the scattered partons into final state particles, and the response of the detector to those final state particles. These stages are referred to as the parton level, particle level, and detector level, respectively. Jets can be reconstructed at all three levels, using the same reconstruction algorithm (except at the parton level) but different inputs for each stage.

Parton Level

The parton level contains information about the partons involved in the $2 \rightarrow 2$ hard scattering generated by PYTHIA. Kinematic properties of the hard scattering, such as the center-of-

mass energy, scattering angle, and initial partonic momentum fractions are stored at this level of the simulation. Reconstructed parton level jets consist only of the partons involved in the hard scattering and partons arising from initial or final state radiation.

Particle Level

The particle level consists of the stable, color-neutral particles formed from the hadronization of the hard scattered partons. This level records kinematic information, particle identification, and the parent parton for each stable particle. The jet finding algorithm at this level uses all stable particles, including those from the underlying event and beam remnants.

Detector Level

The final level of the simulation records the detector response to the particles from the previous level. GEANT models how the particles would interact with the different components of STAR, such as ionizing the gas in the TPC and depositing energy in the scintillator layers of the calorimeters, as well as simulating the operation of the readout electronics. Jet reconstruction at the detector level takes the simulated response of the TPC, calorimeters, and associated electronics as inputs. The GEANT model is designed to respond to particles in the same way as the real detector, so the detector level is the stage of simulation which is used when making comparisons with data.

4.3 Data-Simulation Comparison

Dijets at the detector level in simulation are reconstructed using the same jet-finding algorithm and selection criteria as those in the data, and then are subject to two additional matching conditions. First, each reconstructed detector level jet is associated with a particle level jet by requiring a geometric match of $\Delta R = \sqrt{(\eta_{Det} - \eta_{Par})^2 + (\phi_{Det} - \phi_{Par})^2} < 0.5$.

This condition must be satisfied by both jets in the dijet pair. Second, the z-vertex of the detector level dijet and the z-vertex of the matching particle and parton level dijets are required to be within two centimeters of each other. The particle and parton level dijets have the same vertex, which is the “true” vertex from PYTHIA, while the detector level vertex is found by emulating the vertex finder used for the data. The found detector level vertex might differ from the vertex generated by PYTHIA because the simulated events are embedded into real zero-bias data.

Good agreement between various dijet quantities in data and simulation indicates that the STAR detector response is well understood. The following plots show comparisons between data and the detector level in simulation for the JP2 trigger. Figures 4.4 and 4.5 show the z-vertex distributions for 2012 and 2013, respectively, while Figs. 4.6 and 4.7 show the dijet invariant mass distributions. Figures 4.8 and 4.9 show the jet p_T spectra for the high and low p_T jets separately for 2012, and Figs. 4.10 and 4.11 show the same for 2013. The geometric matching is shown in Figs. 4.12-4.15 for 2012 and Figs. 4.16-4.19 for 2013. The smaller number of reconstructed jets in the West Barrel ($\eta > 0$) compared to the East Barrel, which is clearest for the high- p_T jet in the 2013 sample, has been observed in previous jet analyses but is not fully understood. The azimuthal geometry of the STAR jet patches is evident in the periodic behavior of the jet ϕ spectra. These azimuthal distributions are particularly sensitive to TPC hardware failures.

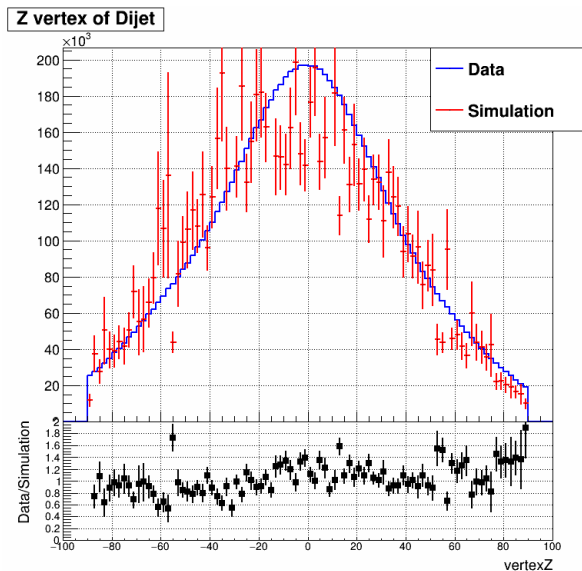


Figure 4.4: Z-vertex distribution for JP2 in 2012.

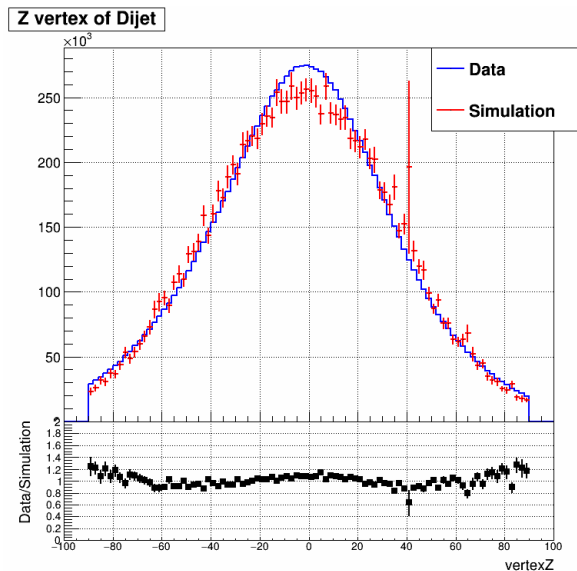


Figure 4.5: Z-vertex distribution for JP2 in 2013.

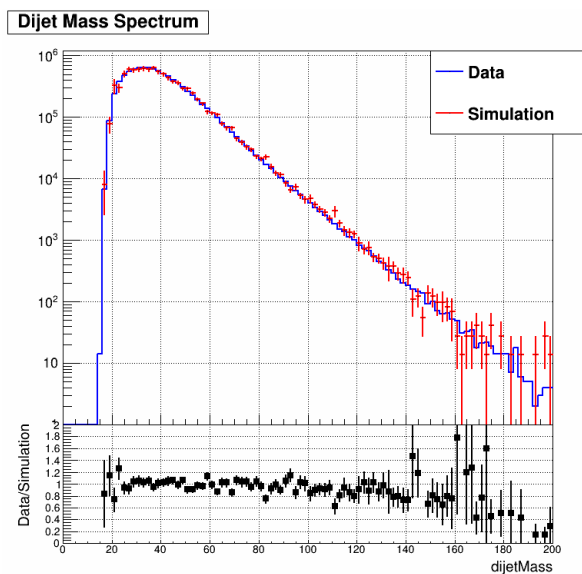


Figure 4.6: Dijet invariant mass distribution for JP2 in 2012.

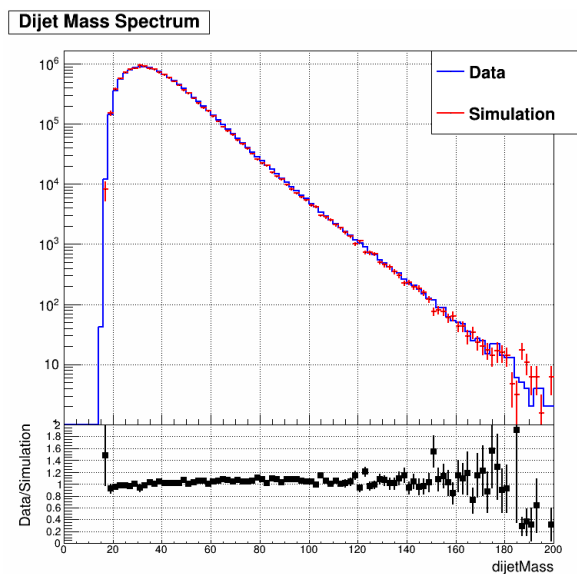


Figure 4.7: Dijet invariant mass distribution for JP2 in 2013.

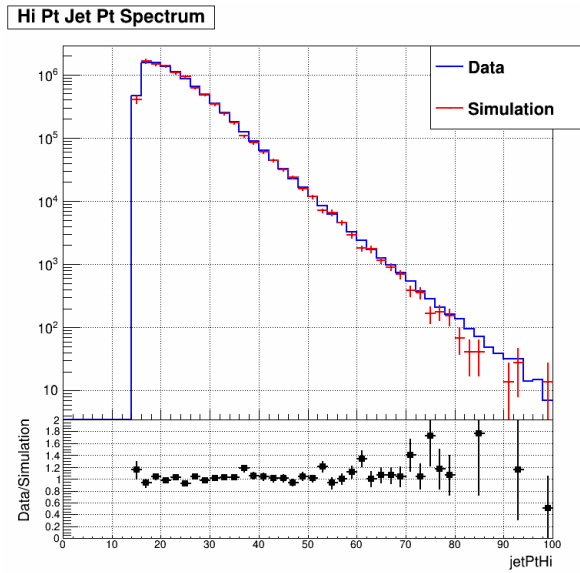


Figure 4.8: High p_T jet p_T distribution for JP2 in 2012.

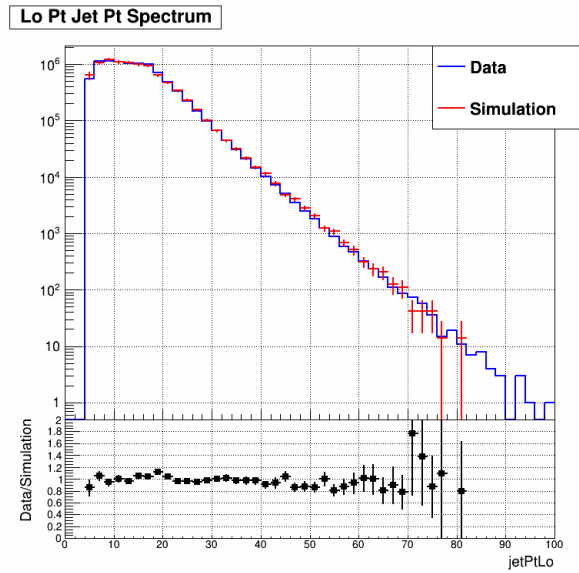


Figure 4.9: Low p_T jet p_T distribution for JP2 in 2012.

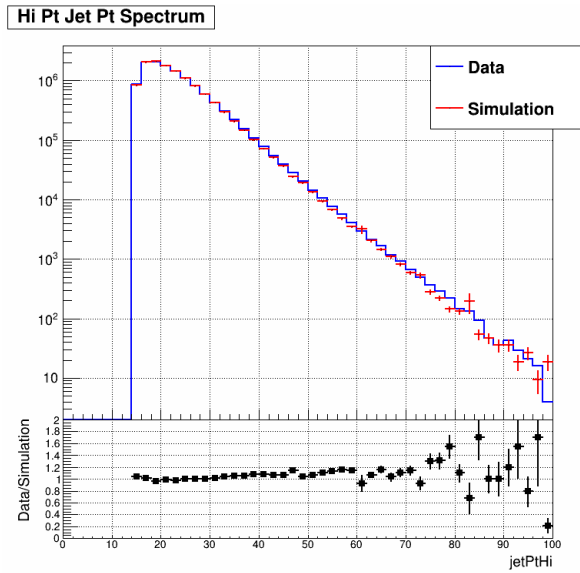


Figure 4.10: High p_T jet p_T distribution for JP2 in 2013.

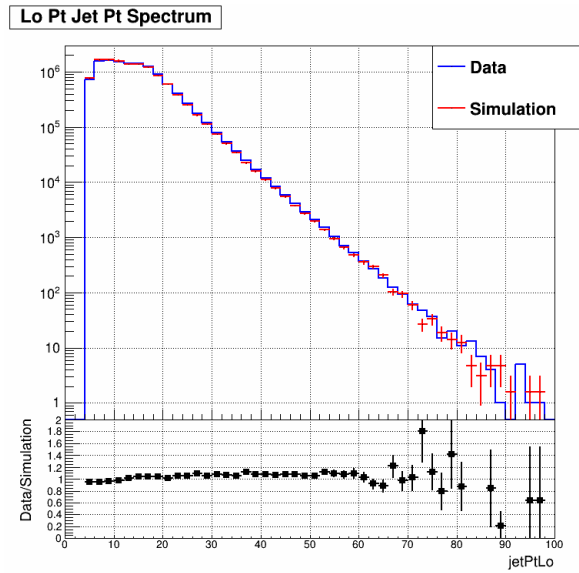


Figure 4.11: Low p_T jet p_T distribution for JP2 in 2013.

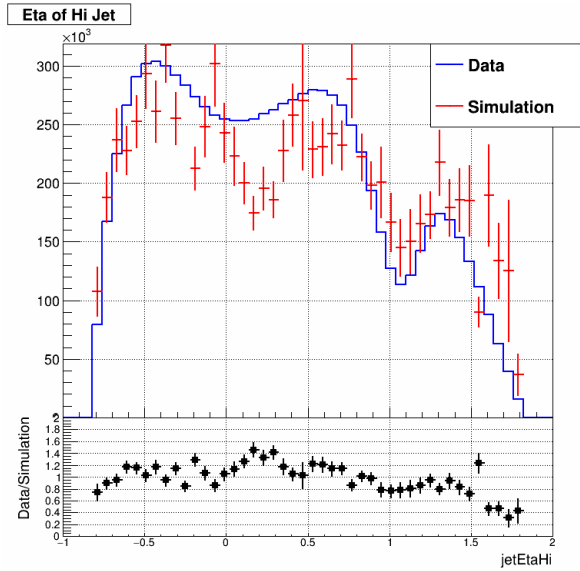


Figure 4.12: High p_T jet η distribution for JP2 in 2012.

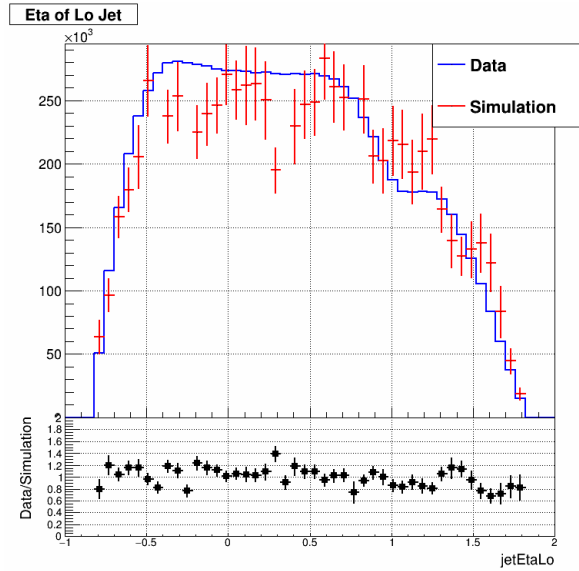


Figure 4.13: Low p_T jet η distribution for JP2 in 2012.

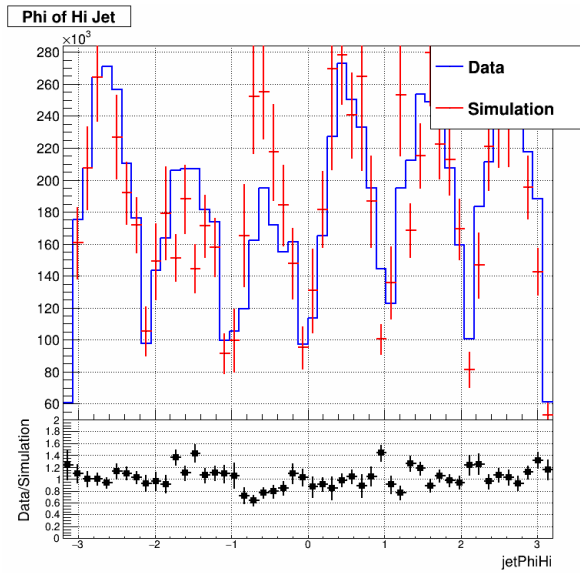


Figure 4.14: High p_T jet ϕ distribution for JP2 in 2012.

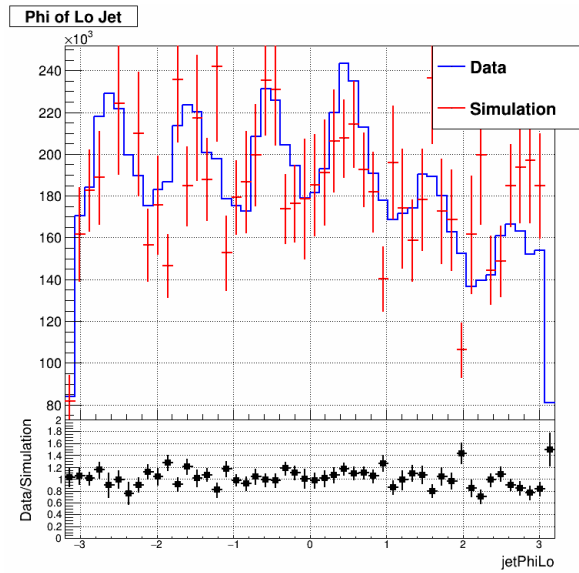


Figure 4.15: Low p_T jet ϕ distribution for JP2 in 2012.

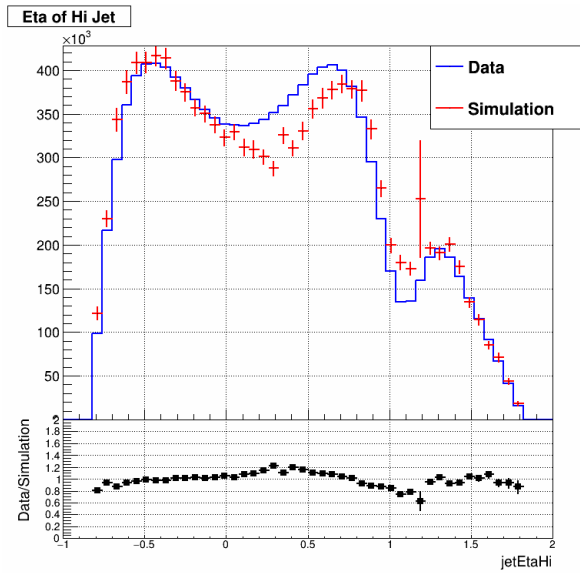


Figure 4.16: High p_T jet η distribution for JP2 in 2013.

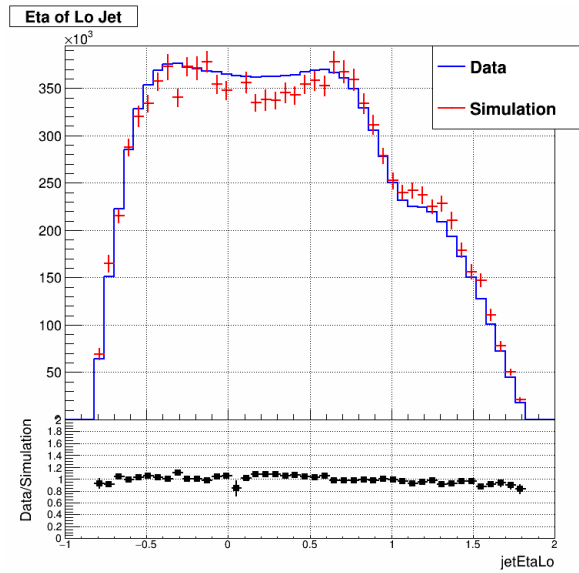


Figure 4.17: Low p_T jet η distribution for JP2 in 2013.

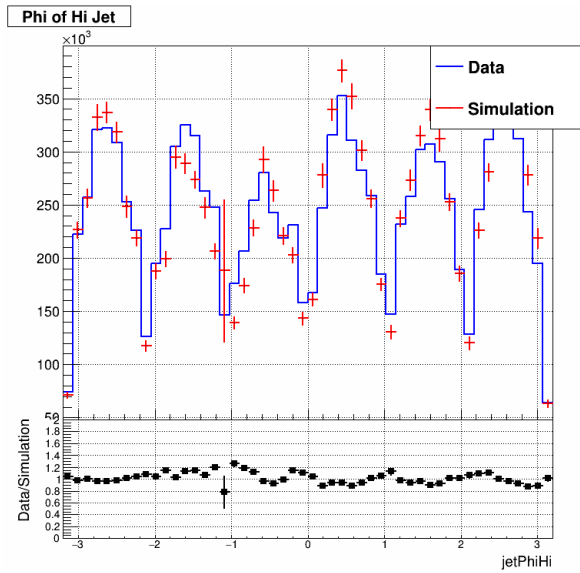


Figure 4.18: High p_T jet ϕ distribution for JP2 in 2013.

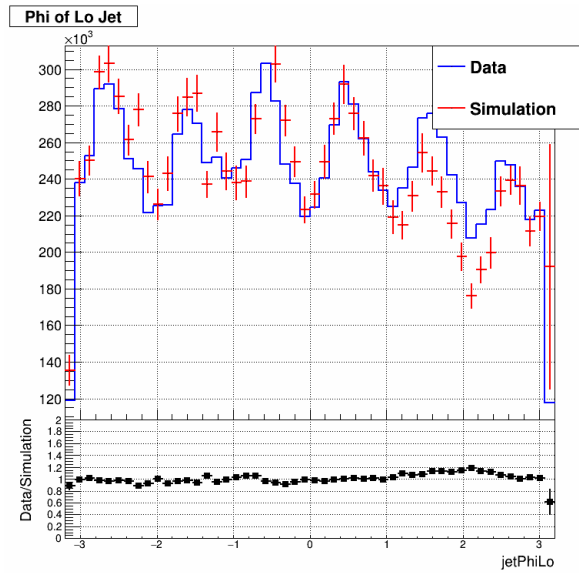


Figure 4.19: Low p_T jet ϕ distribution for JP2 in 2013.

CHAPTER 5

Underlying Event

At high energies, proton-proton collisions can be thought of as two clusters of partons colliding with each other. Most of the partons will not experience any hard interactions, but occasionally two of them will collide directly and be ejected with significant transverse momentum. These hard partonic scatterings result in the dijet events which are of interest in this analysis. However, the other softer scatterings produce particles that are picked up by the detectors along with the hard scattering signal. The diffuse background generated by the soft scatterings and remnants of the fragmented protons is called the underlying event (UE) contribution. The UE contribution is distinct from detector pile-up effects due to nearby pp collisions within the same bunch crossing, as the UE particles have the same vertex as the jets from the hard scattering.

5.1 Off-Axis Cone Method

The underlying event background contribution is estimated on a jet-by-jet basis, using a procedure which builds on the “off-axis cone” method developed by STAR collaborator Zilong Chang for the 2012 inclusive jets at 510 GeV analysis. The off-axis cone method itself was adapted from the perpendicular cones method used by the ALICE experiment [61]. The first step is to consider two off-axis cones for each jet in the dijet event, each of which is centered at the same η as the jet but offset by 90° in ϕ from the jet ϕ , as shown in Fig. 5.1. The radius of the cone is chosen to be equal to the anti- k_T radius parameter,

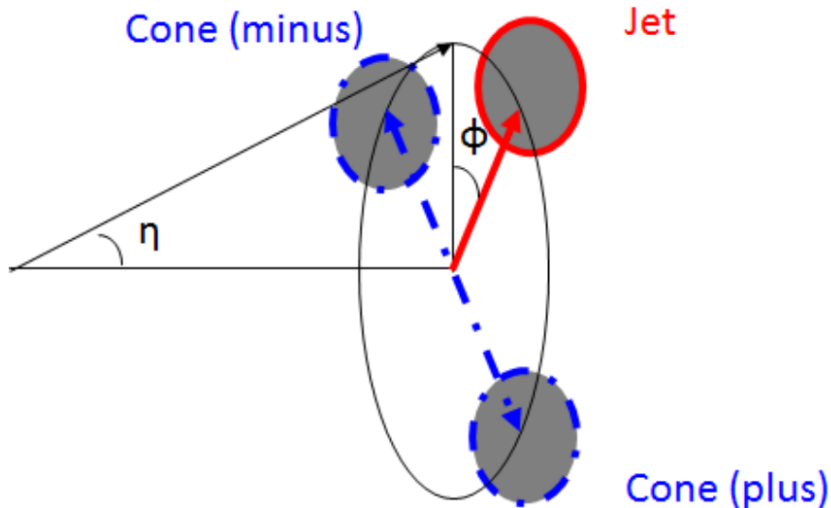


Figure 5.1: Diagram of the off-axis cone method, showing a jet and its associated cones.

$R = 0.5$. Next, we collect particles which fall inside the two cones, using the same list of particles that served as input to the jet finding algorithm. Then the energy density $\rho_{ue,cone}$ of each cone is calculated as the scalar sum of the p_T of all the particles inside the cone, divided by the cone area (πR^2). Similarly, the mass density $\rho_{m,ue,cone}$ is calculated as the invariant mass of the four-vector sum of all the particles inside the cone divided by the cone area. Finally, the underlying event density for a given jet is taken to be the average density of its two off-axis cones, $\rho_{ue} = \frac{1}{2}(\rho_{ue,+} + \rho_{ue,-})$.

Note that STAR's acceptance and efficiencies are not uniform in η , given the service gap between the two calorimeters and the rapidly falling TPC tracking efficiency in the EEMC region, so it is important that the off-axis cones are centered at the jet η . STAR does have uniform azimuthal acceptance and efficiency, though, and the UE physics is expected to be symmetric in ϕ , so the method provides a reasonable approximation of the soft background underlying each jet.

5.2 Underlying Event Correction

This analysis uses the same underlying event correction procedure as the previous measurement of forward dijet A_{LL} , which incorporates the average UE densities described in the previous section. Since dijet measurements are sensitive to the jets' directions, the UE subtraction scheme should correct their full four-momenta. This is accomplished by combining the p_T and mass densities with the jet's four-vector area. For each jet in a dijet event, the correction is calculated as:

$$P_{\mu}^{UE} = [\rho A_x, \rho A_y, (\rho + \rho_m) A_z, (\rho + \rho_m) A_E], \quad (5.1)$$

where ρ and ρ_m are the underlying event transverse momentum and mass densities determined using the off-axis cone method, and A_{μ} is the jet's four-vector area. A_{μ} is calculated in the FastJet package [56] using the ghost particle technique [62], which involves throwing a grid of extremely soft particles over the $\eta - \phi$ space and then rerunning the jet finding algorithm with the “ghosts” added to the input pool. The four-vector area is determined based on which ghosts were grouped in with the reconstructed jet. P_{μ}^{UE} is then subtracted from the initial jet four-vector to obtain the corrected jet four-vector.

Each off-axis cone only contains about two particles on average, so there are two additional requirements imposed on the corrected jet four-vectors in order to avoid over-corrections due to local fluctuations in the UE density:

1. If the corrected jet has negative p_T , then its four-vector is set to have zero transverse momentum, zero mass, and the pseudorapidity and azimuthal angle of the original jet.
2. If the corrected jet has an imaginary mass (a negative squared jet mass), then its four-vector is set to have zero mass and the pseudorapidity of the original jet, while the corrected p_T and ϕ are left at their corrected values.

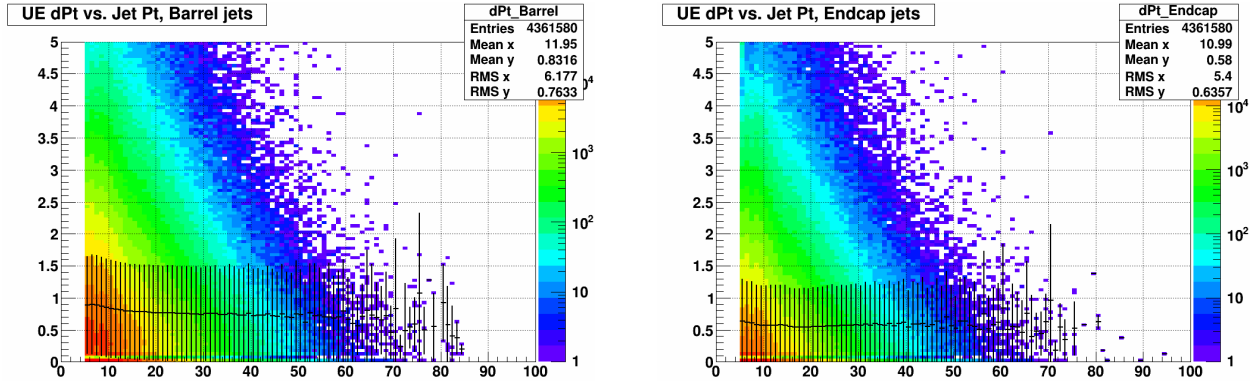


Figure 5.2: The amount of jet p_T subtracted off by the underlying event correction (dPt) vs. jet p_T , for Barrel (left) and Endcap (right) jets in a subset of Barrel-Endcap events from 2012 data. The units of the vertical and horizontal axes are GeV.

The underlying event correction decreases the jet p_T by less than a GeV in most cases. Figure 5.2 shows the p_T subtracted off by the UE correction versus the jet p_T , for some Barrel-Endcap dijet events in 2012 data. The markers indicate the average UE δp_T and RMS for each bin. The average underlying event correction is seen to be quite constant and largely independent of the p_T of the associated jet.

Since the underlying event subtraction corrects a jet's four-momentum vector, it is possible that the direction of the corrected jet will be slightly different. Figure 5.3 shows the change in jet ϕ from the UE subtraction vs. jet detector level p_T , while Fig. 5.4 shows the change in jet η vs. detector level p_T , for 2012 simulation. In both plots the vertical axis is calculated by subtracting the corrected jet's η or ϕ from that of the uncorrected jet. As expected, the underlying event subtraction does not change jets' azimuthal angles in any systematic way, and only a very small percentage of corrections deviate significantly from zero. On the other hand, the correction does show a slight asymmetry in pseudorapidity, with a small nonzero average change in η at low jet p_T . This means that jets have lower pseudorapidities after the correction, implying that the UE background is slightly more dense closer to the beamline. Similarly to the ϕ shifts, the large majority of the shifts to jet η are much smaller than the tower sizes.

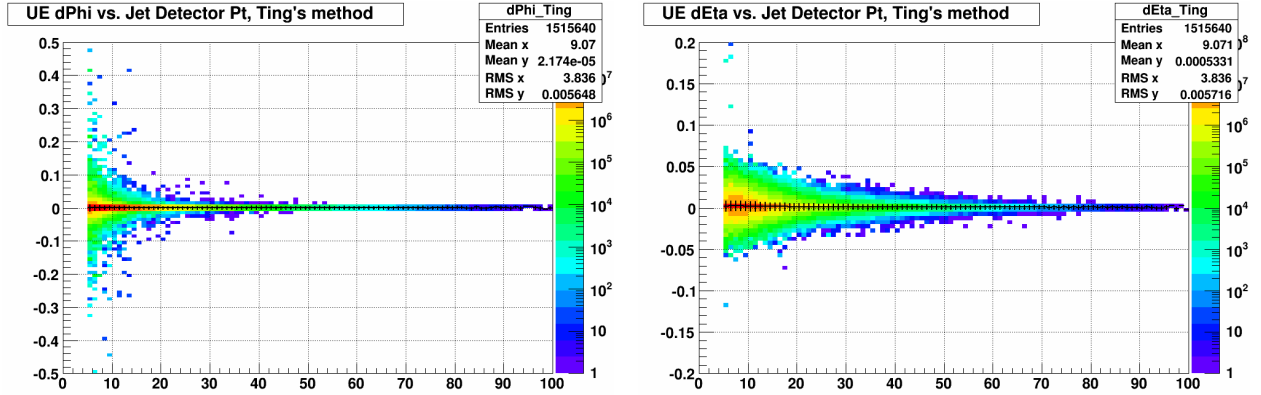


Figure 5.3: Shifts in jet ϕ due to the underlying event subtraction, $d\text{Phi} = \text{Phi}(\text{uncorrected}) - \text{Phi}(\text{corrected})$.

Figure 5.4: Shifts in jet η due to the underlying event subtraction, $d\text{Eta} = \text{Eta}(\text{uncorrected}) - \text{Eta}(\text{corrected})$.

In the analysis described in the following chapters, the data and simulation (detector level and particle level) jets used are those after the underlying event 4-vector correction has been applied.

CHAPTER 6

Experimental Methods in the EEMC

6.1 Challenges in the EEMC Region

The STAR TPC only provides charged particle tracking for roughly $|\eta| \leq 1.3$, as can be seen in Fig. 6.1, with rapidly decreasing efficiency outside that range. As a result, jets which are reconstructed in the EEMC region will miss many tracks, resulting in values of jet p_T which are systematically lower than the true values. The inaccurate jet p_T measurements distort the extraction of the momenta of the colliding partons. The invariant mass of each jet is also reconstructed inaccurately, which further skews the calculation of the dijet invariant mass. Finally, jets with a higher percentage of neutral energy will be preferentially selected in both triggering and reconstruction, resulting in a biased sample.

A machine-learning regression method was developed for the measurement of the 2009 EEMC dijet A_{LL} to correct jet p_T and invariant mass for the effects of the reduced tracking efficiency at forward pseudorapidities [34]. The algorithm used to carry out the supervised regression is the Multilayer Perceptron, a type of Artificial Neural Network, from ROOT's Toolkit for Multivariate Data Analysis (TMVA) [63]. Supervised regression algorithms use training events, for which the desired output is known, to approximate the functional behavior linking the input variables to the target.

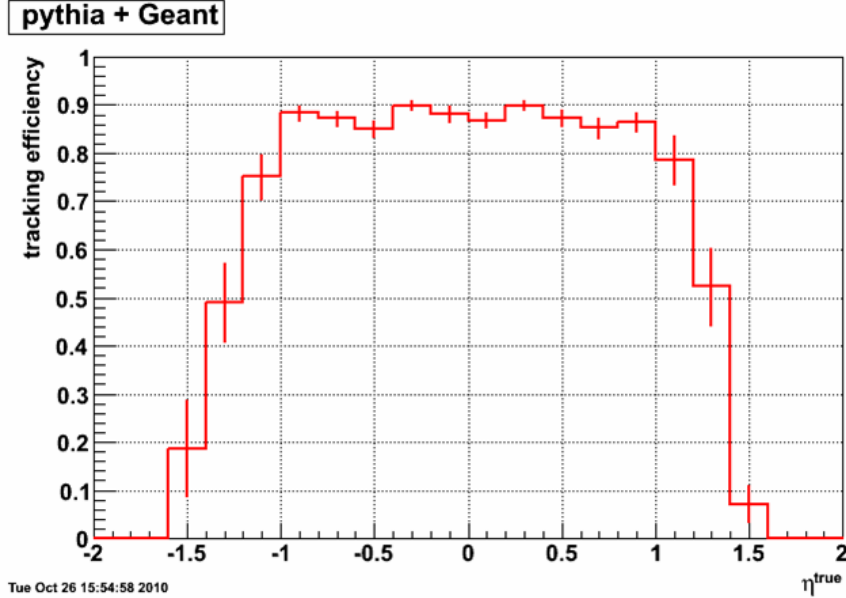


Figure 6.1: Plot from simulation showing the percentage of tracks which are successfully reconstructed as a function of track pseudorapidity.

6.2 Artificial Neural Networks

An Artificial Neural Network (ANN) is a simulated collection of interconnected neurons, with each neuron producing a certain response from a given set of inputs. The network consists of an input layer, some configuration of hidden neurons, and an output layer. The neural network functions as a mapping from a space of input variables x_1, \dots, x_m onto a space of output variables y_1, \dots, y_n . The output of the network, given a certain set of inputs, is determined by the layout of the neurons, the weights of the inter-neuron connections, and the response of the neurons to their input signals. The mapping between the input and output variable spaces will be nonlinear if at least one of the neurons has a nonlinear response to its input.

The Multilayer Perceptron (MLP) is a simplified ANN where the neurons are organized into layers, and the neurons in a given layer are only directly connected to those in the following layer. The first layer of a MLP network is the input layer, which holds the input variable(s), while the last layer is the output layer, which contains the output variable(s).

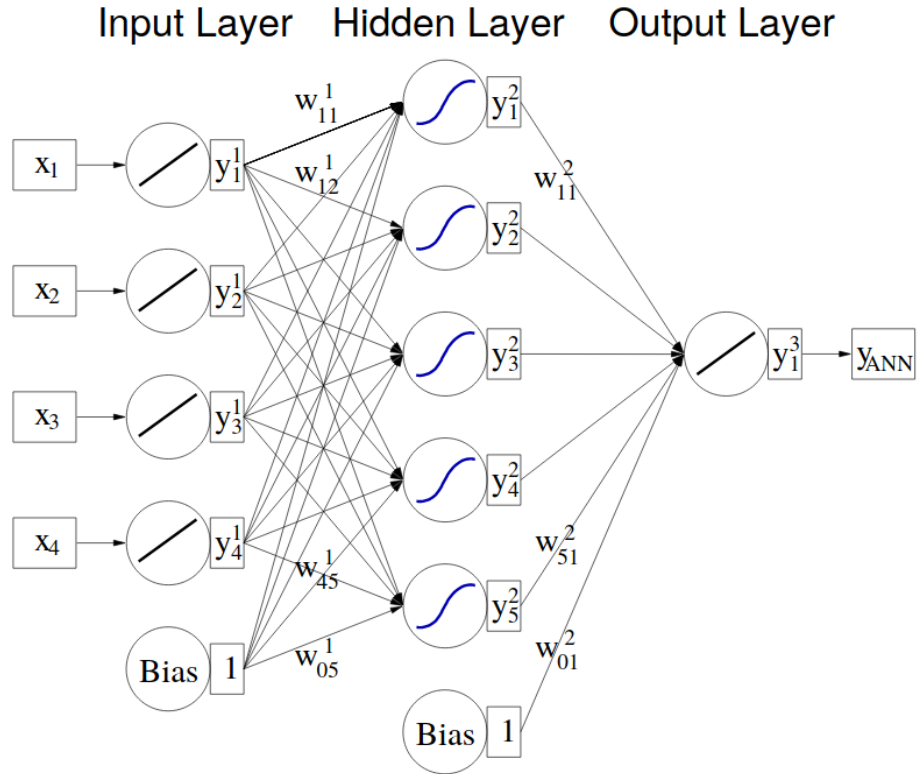


Figure 6.2: Multilayer Perceptron ANN with one hidden layer [63].

All of the layers in between are called hidden layers. Each inter-neuron connection has an associated weight value, and the output value of a given neuron is multiplied by that weight factor before being sent as input to the next neuron. Figure 6.2 illustrates the architecture of a MLP network with four input variables, one output variable, and a single hidden layer.

6.2.1 Neural Network Parameters and Training

The parameter settings for a MLP network require some trial and error in order to work efficiently for a given application. The settings used in this analysis are the same as those selected for the initial forward dijet A_{LL} measurement. The settings are specified when the network is declared:

- `factory->BookMethod(TMVA::Types::kMLP, "MLP", "!H: !V: VarTransform=Norm: NeuronType=tanh: NCycles=10000: HiddenLayers=N+100: EstimatorType=MSE:`

```
TestRate=10: LearningRate=0.02: NeuronInputType=sum: DecayRate=0.6: TrainingMethod=BFGS: Sampling=0.1: SamplingEpoch=0.8: ConvergenceImprove=1e-6: ConvergenceTests=15: !UseRegulator”);
```

The “NeuronType=tanh” option indicates that the neuron response function is the hyperbolic tangent, so the network’s mapping of input variables to output variable will be nonlinear. “HiddenLayers=N+100” specifies that this network has a single hidden layer containing $N+100$ neurons, where N is the number of input variables. For a multilayer perceptron, a single hidden layer is enough to approximate a given continuous correlation function to arbitrary precision as long as that hidden layer contains a sufficiently large number of neurons. Another important option is “TrainingMethod=BFGS”, which indicates that the Broyden-Fletcher-Goldfarb-Shannon method will be used to update the network’s synapse weights during training. The BFGS method differs from the typical back propagation method by using second derivatives of the error function to reach the optimal set of weights. Finally, “NCycles=10000” means that the algorithm will run for 10000 training epochs. Further details on the MLP options, and more general information on ANNs in TMVA, can be found in chapter 8 of Ref. [63].

6.3 Jet p_T Correction

The artificial neural networks for the corrections to the jet quantities are trained using the embedding samples discussed in Chapter 4. There is a separate network for each of three categories of jets: Barrel jets, Endcap jets from dijet events where the other jet is in the Barrel, and Endcap jets from dijet events where both jets are in the Endcap. The embedding sample for a given category is randomly split in half at the beginning of the regression process: the events in the “Training” set are used to determine the network weights, while the “Testing” events are used as an independent check on the training results.

For the jet p_T correction, the target value is the particle-level jet p_T , which is the physics

quantity of interest. The variables used to train the networks were optimized in the 2009 analysis. For Barrel jets, the variables are:

- Inputs: jet detector-level p_T , detector pseudorapidity $\eta_{detector}$, jet neutral energy fraction R_t ;
- Target: particle-level jet p_T .

For Endcap jets in Barrel-Endcap dijet events, the variables are:

- Inputs: Endcap jet detector-level p_T , detector pseudorapidity $\eta_{detector}$, jet neutral energy fraction R_t , Barrel jet detector-level p_T ;
- Target: particle-level jet p_T .

The transverse momenta of the two jets in a dijet pair are expected to be approximately equal, and adding in the p_T of the corresponding Barrel jet (which was measured more precisely due to a much higher tracking efficiency) was found to improve the correction for these Endcap jets.

Finally, the variables for Endcap jets in Endcap-Endcap events are:

- Inputs: Endcap jet detector-level p_T , detector pseudorapidity $\eta_{detector}$, jet neutral energy fraction R_t ;
- Target: particle-level jet p_T .

The network for jets in Endcap-Endcap events is trained using all Endcap jets, including those from Barrel-Endcap events, in order to increase the statistics.

The results of the regression training for the jet p_T correction can be seen in Fig. 6.3 for 2012 and Fig. 6.4 for 2013. The figures plot the ratio of particle-level jet p_T over detector-level jet p_T as a function of detector pseudorapidity, with the average ratio in each detector

η bin indicated. The left-hand plots show this ratio for the uncorrected detector-level jet p_T , while the right-hand plots show the ratio after the networks have been trained. The uncorrected plots show average ratios greater than one, indicating that the detector-level p_T is lower than the particle-level p_T , as expected. The average ratios increase rapidly in the Endcap region, illustrating the effect of the decreasing tracking efficiency at more forward detector pseudorapidities, but are also greater than one in the Barrel, since tracking there is not perfect either. The corrected plots show ratios very near to one in all detector η bins, as well as reduced spreads in the distribution of p_T ratios, indicating that the machine learning techniques account for correlations among the input variables.

In the 2009 analysis, the networks were trained and tested separately for each trigger, based on the reasoning that the spectra of the input quantities might differ among the trigger samples. While the various distributions do differ depending on which trigger category the dijet event was sorted into, the performance of the machine learning process was found to be unaffected by these differences. Figures 6.5, 6.6, and 6.7 compare the results of the regression training when done separately for the different trigger samples to when they are done for all events together, using the 2012 embedding. They illustrate that there is very little difference between the two methods, with the combined training giving a slightly smaller spread in the resulting p_T ratio distribution in most cases. So, in this analysis all of the events in the embedding sample were trained and tested together, regardless of trigger. This is the only aspect of the machine learning correction where this analysis differs from the 2009 measurement.

Another way to see the net effect of the machine learning p_T correction is to look at the dijet p_T imbalance for Barrel-Endcap events. The dijet p_T imbalance is the difference in magnitude of the two jet p_T 's, and is shown in Fig. 6.8 for 2012 and 6.9 for 2013. The figures show the p_T imbalance distributions for data (points) and simulation (histograms), both before (red) and after (blue) the correction, for JP2 events. Before the correction, the Barrel jet p_T is systematically larger than that of the Endcap jet, so the distributions are

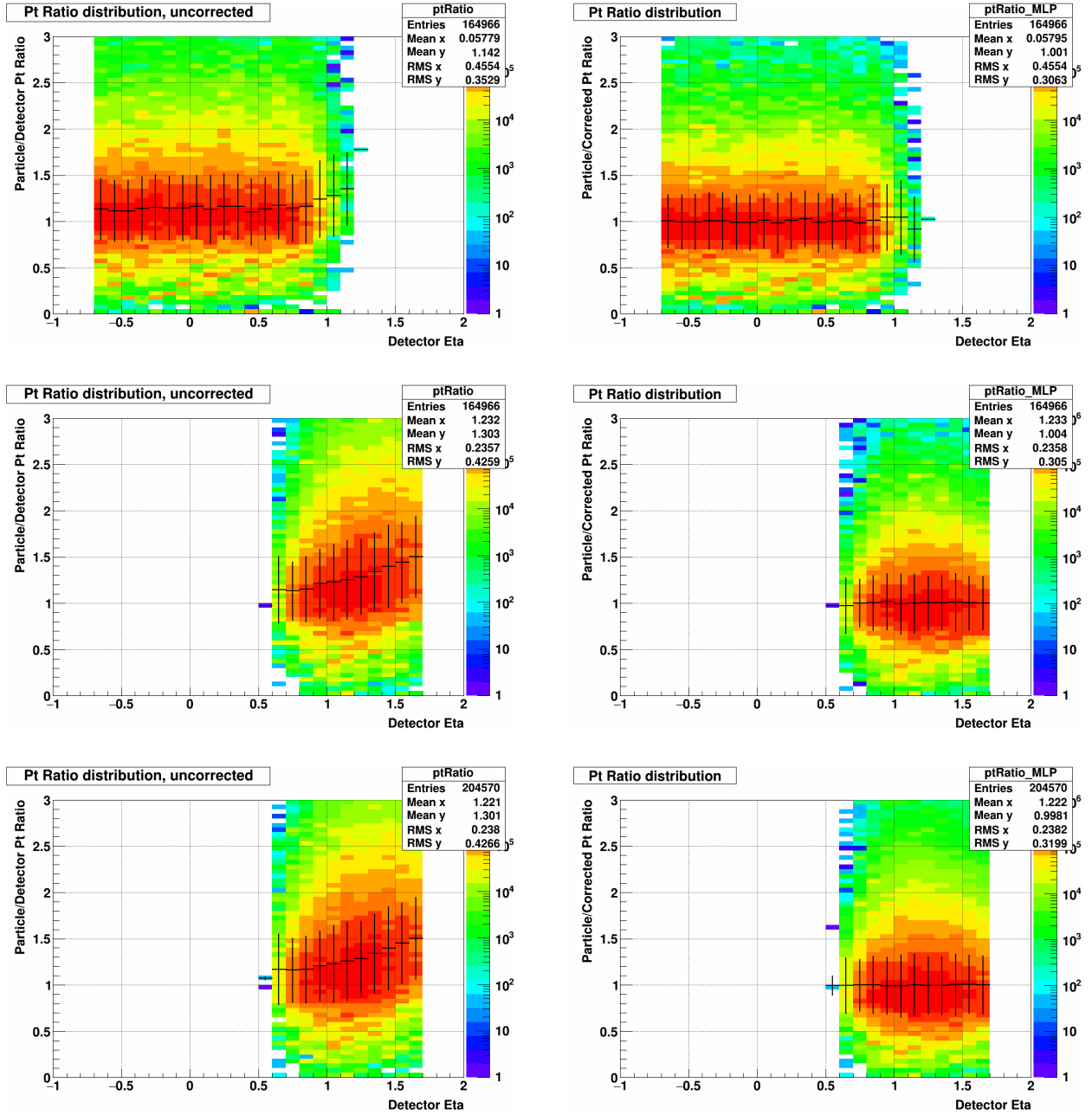


Figure 6.3: Jet particle/detector p_T ratio vs. detector η , before (left) and after (right) the machine learning p_T shift. The top, middle, and bottom rows show results for Barrel jets, Endcap jets in Barrel-Endcap events, and Endcap-Endcap jets, respectively. In each plot, the black symbols and vertical bars indicate the mean and RMS, respectively, of the distribution in each bin. Events are from the 2012 embedding sample.

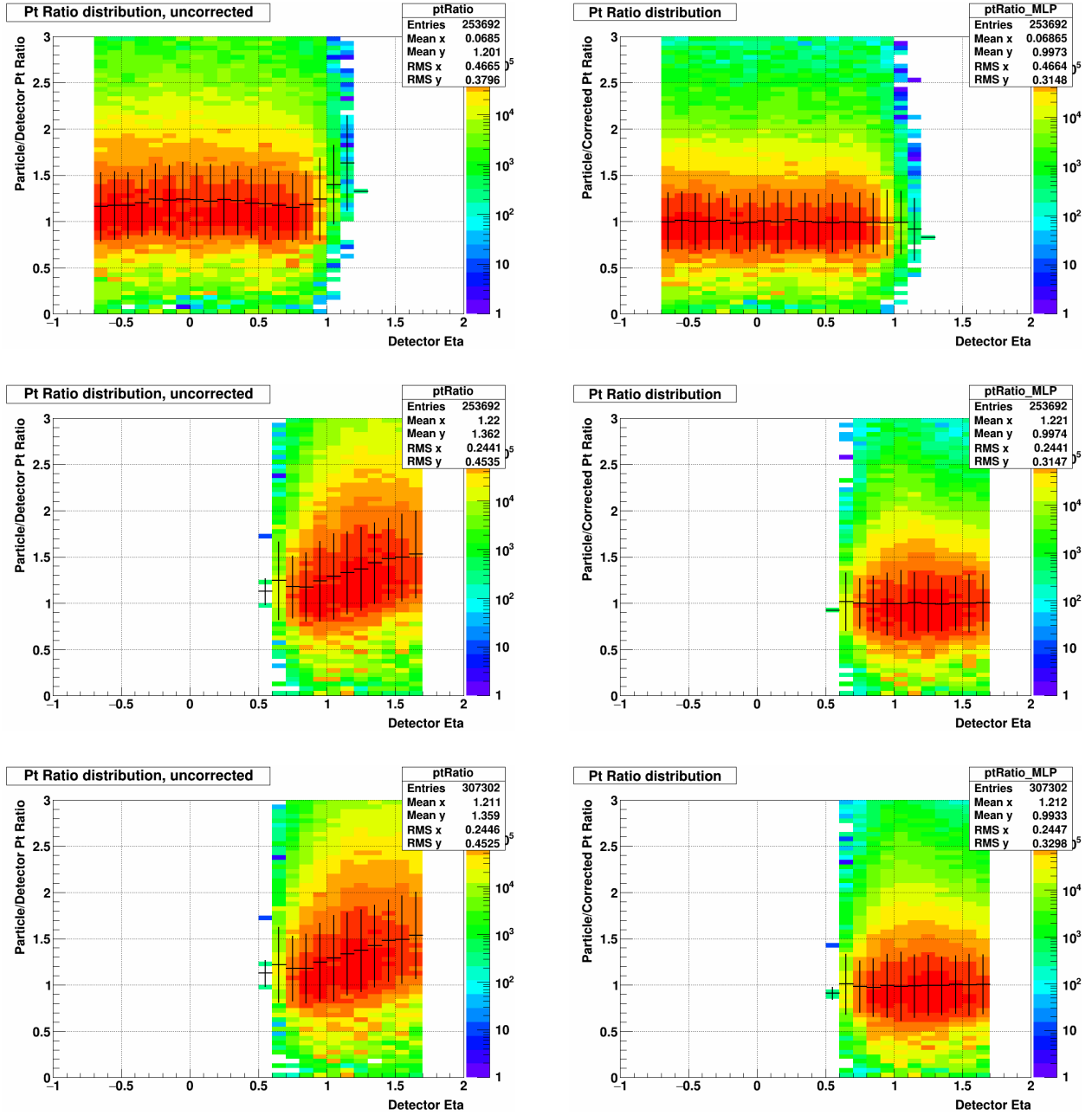


Figure 6.4: Jet particle/detector p_T ratio vs. detector η , before (left) and after (right) the machine learning p_T shift. The top, middle, and bottom rows show results for Barrel jets, Endcap jets in Barrel-Endcap events, and Endcap-Endcap jets, respectively. In each plot, the black symbols and vertical bars indicate the mean and RMS, respectively, of the distribution in each bin. Events are from the 2013 embedding sample.

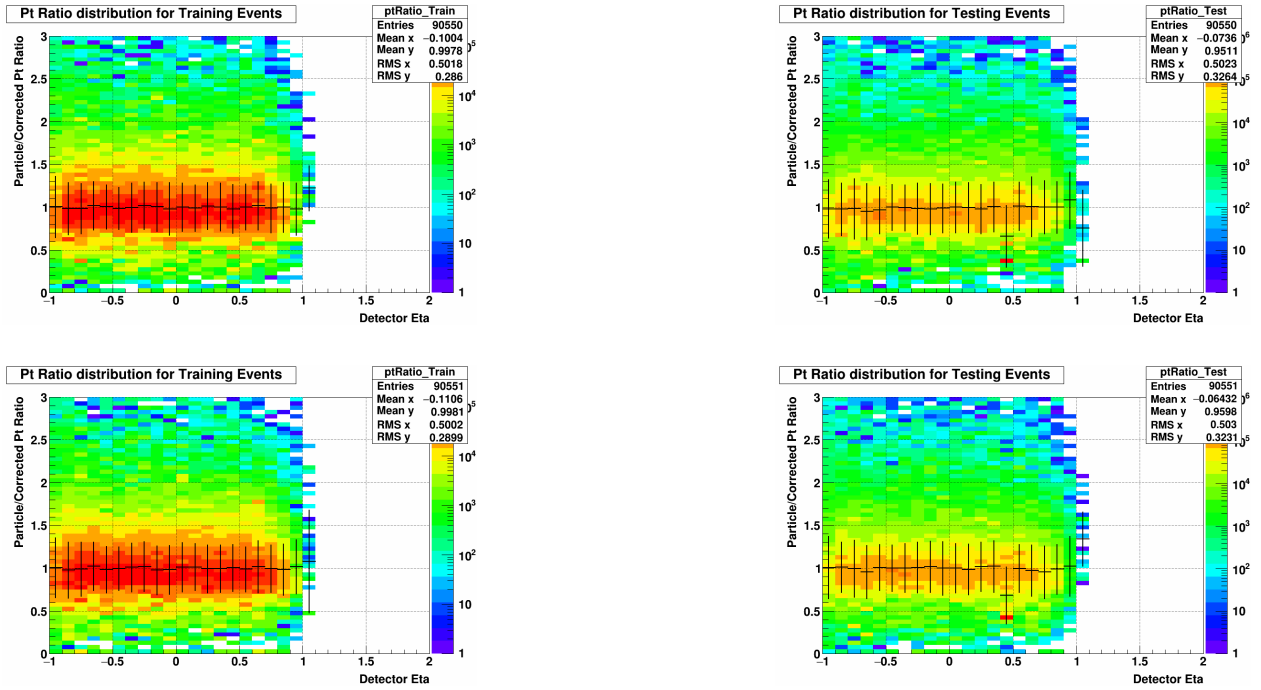


Figure 6.5: Barrel jet particle/detector p_T ratio vs. detector η , for the Training (left) and Testing (right) samples. The top row shows results from training the trigger samples separately; the bottom row from training all trigger samples together. In each plot, the black symbols and vertical bars indicate the mean and RMS, respectively, of the distribution in each bin.

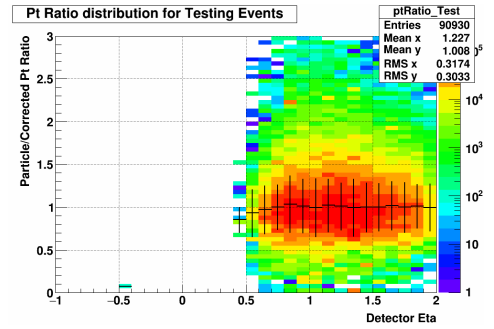
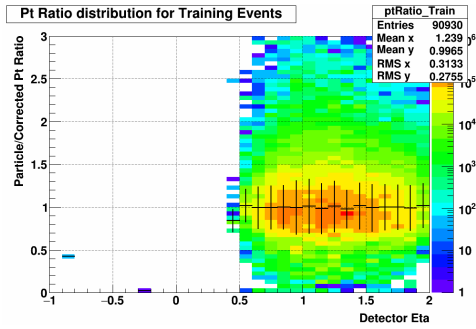
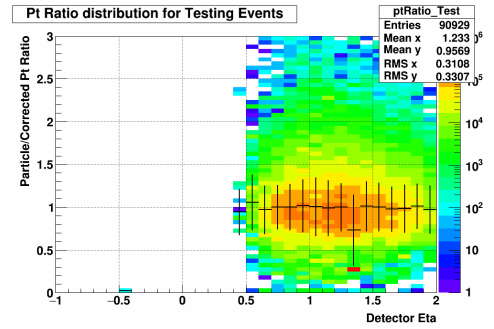
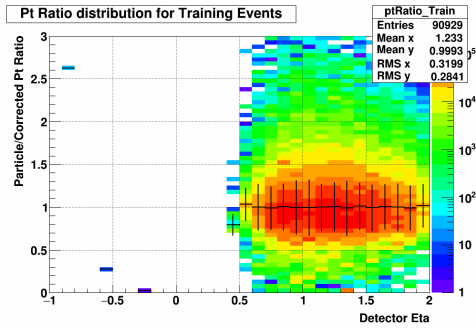


Figure 6.6: Endcap jet from Barrel-Endcap events particle/detector p_T ratio vs. detector η , for the Training (left) and Testing (right) samples. The top row shows results from training the trigger samples separately; the bottom row from training all trigger samples together. In each plot, the black symbols and vertical bars indicate the mean and RMS, respectively, of the distribution in each bin.

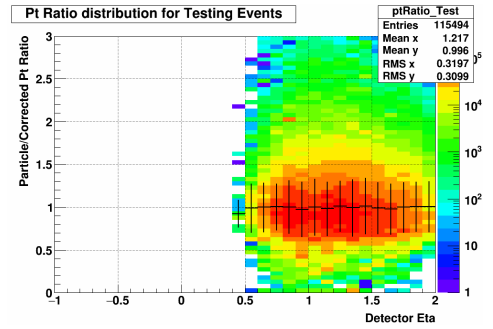
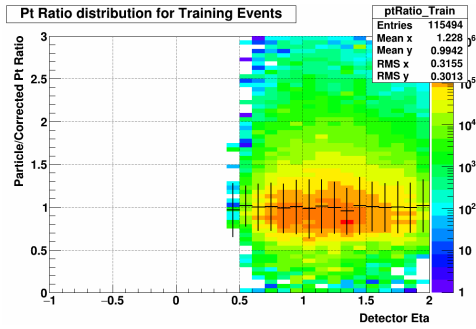
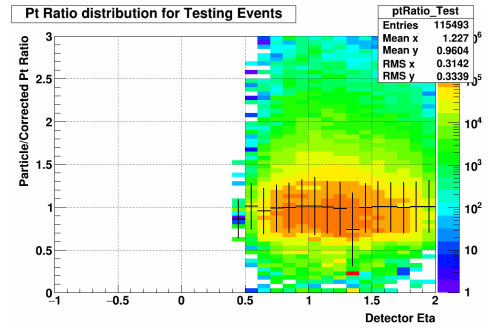
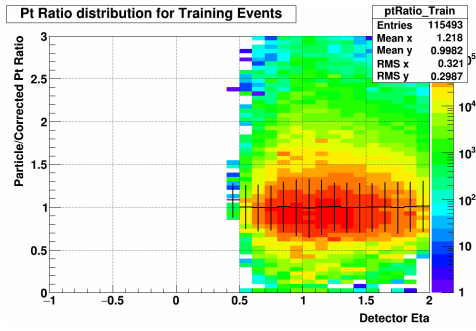


Figure 6.7: Endcap jet particle/detector p_T ratio vs. detector η , for the Training (left) and Testing (right) samples. The top row shows results from training the trigger samples separately; the bottom row from training all trigger samples together. In each plot, the black symbols and vertical bars indicate the mean and RMS, respectively, of the distribution in each bin.

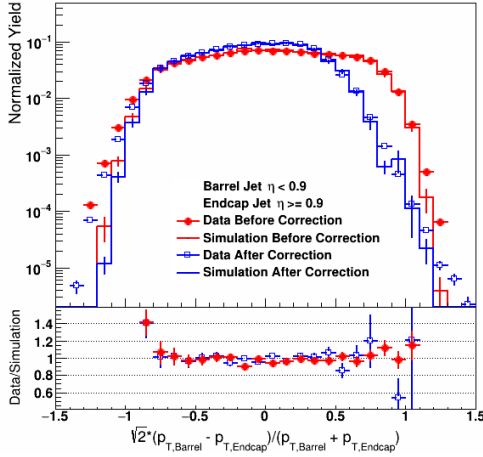


Figure 6.8: Relative difference in p_T for Barrel-Endcap dijets in 2012, for data (points) and simulation (histograms).

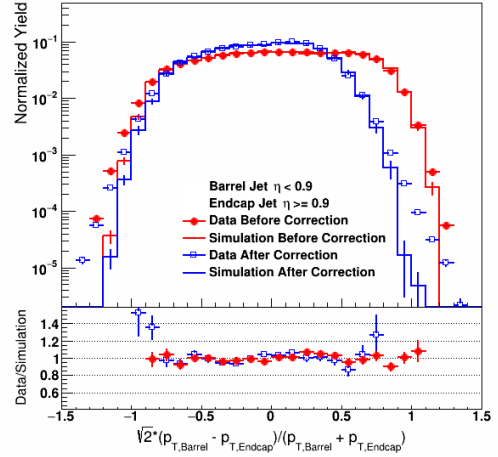


Figure 6.9: Relative difference in p_T for Barrel-Endcap dijets in 2013, for data (points) and simulation (histograms).

shifted toward positive values. After the correction, the distributions are shifted back toward zero and have smaller spreads. Note that these effects are seen in both the simulation used to train the regression algorithm and the data it is applied to.

6.4 Jet Invariant Mass Correction

The jet invariant mass is a small component of the dijet invariant mass compared to the jet transverse momentum, but it is still an important piece of that calculation and thus is also corrected for detector effects. The jet mass corrections use MLP networks with the same parameter settings as the jet p_T corrections, but with a few more inputs. The other difference is that the correction of the jet mass for an Endcap jet in a Barrel-Endcap event does not take any information from the corresponding Barrel jet as input. So, the jet invariant mass correction uses the same set of variables for all Barrel and Endcap jets:

- Inputs: detector-level jet mass, detector-level p_T , detector pseudorapidity $\eta_{detector}$, neutral fraction R_t , track multiplicity N_{tracks} , tower multiplicity N_{towers} ;
- Target: particle-level jet invariant mass.

As with the jet p_T correction, this analysis uses the same variables which were selected for the 2009 forward dijet result, but differs slightly in that events from all trigger categories are trained and tested together. Before being used in the training, the events in the embedding sample are required to have a detector-level jet mass greater than 0.2 GeV. This is because many jets have masses very close to zero after the Underlying Event subtraction is carried out, which might bias the training process. The results of the jet mass regression training can be seen in Fig. 6.10 for 2012 and Fig. 6.11 for 2013. As can be seen in the plots, and unlike the jet p_T correction, the jet mass correction is unable to get the detector-level quantity right on average, though there is a large improvement. This relative underperformance is primarily because all tower hits are assumed to be photons and all tracks are assumed to be charged pions, due to a lack of good particle identification. Thus, even if all the constituents of a given jet are successfully detected, its reconstructed invariant mass would not necessarily be correct. The jet mass ratios also start off farther from the correct value on average and have a wider spread than the jet p_T ratios.

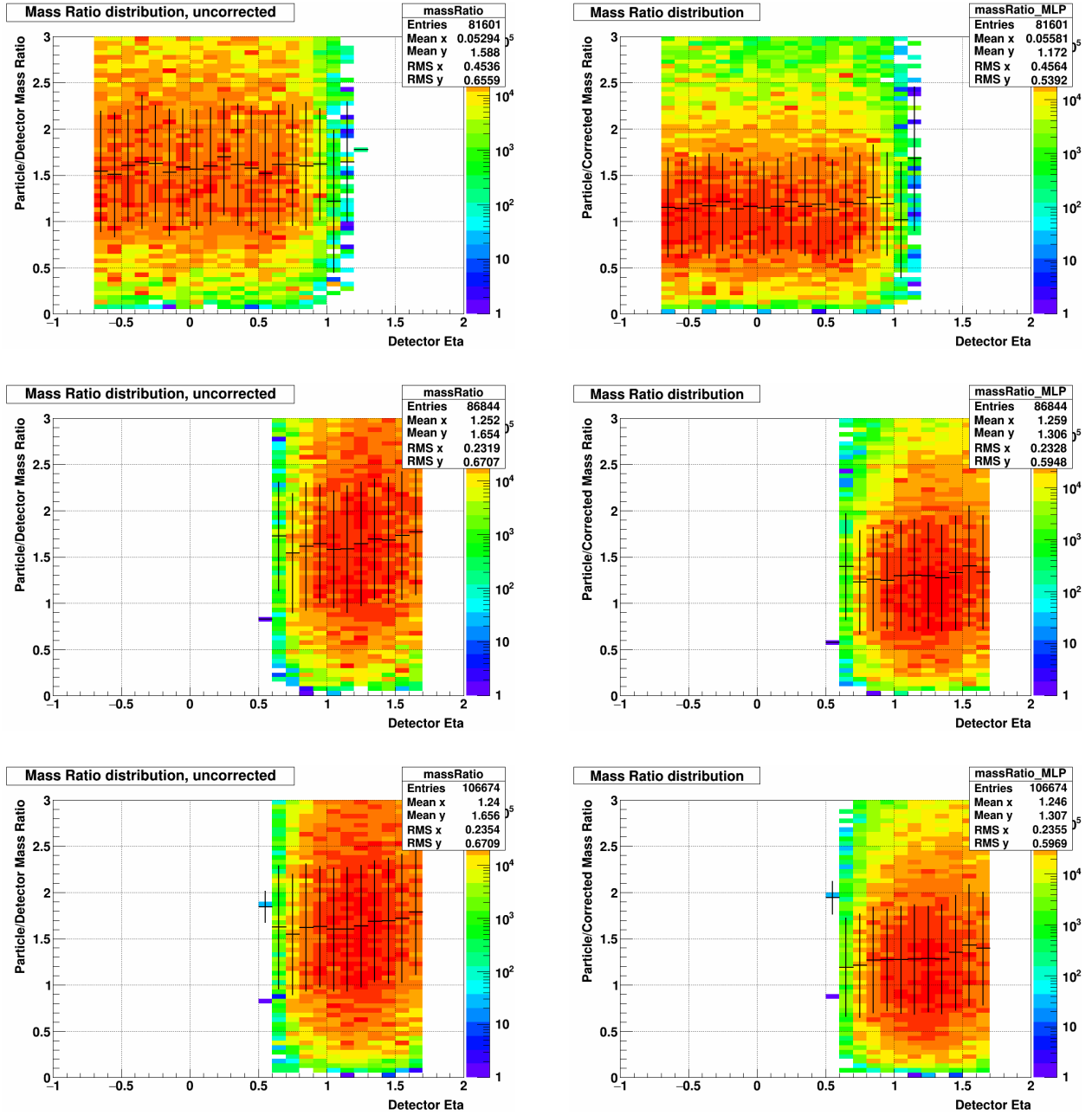


Figure 6.10: Jet particle/detector invariant mass ratio vs. detector η , before (left) and after (right) the machine learning mass shift. The top, middle, and bottom rows show results for Barrel jets, Endcap jets in Barrel-Endcap events, and Endcap-Endcap jets, respectively. In each plot, the black symbols and vertical bars indicate the mean and RMS, respectively, of the distribution in each bin. Events are from the 2012 embedding sample.

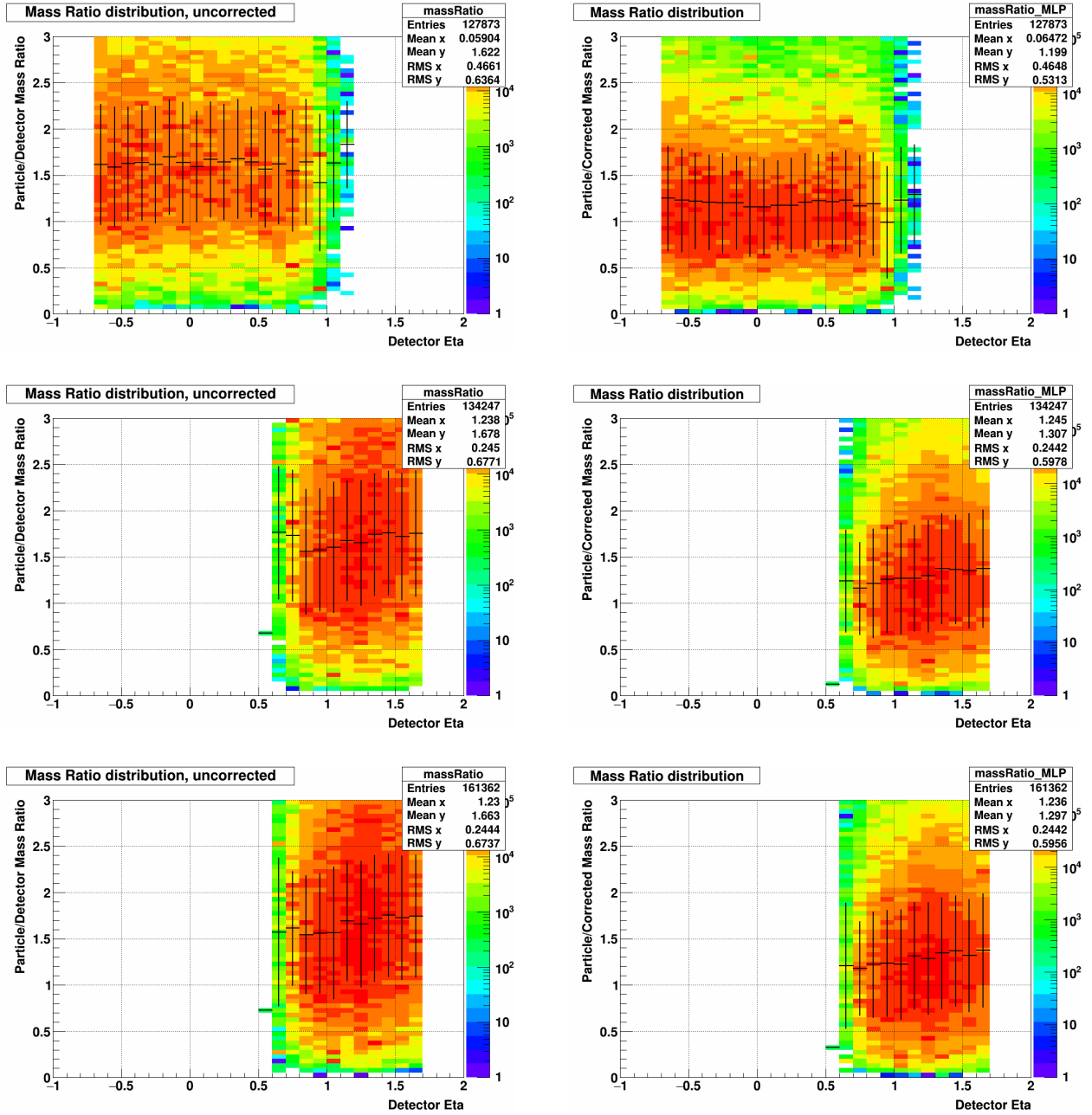


Figure 6.11: Jet particle/detector invariant mass ratio vs. detector η , before (left) and after (right) the machine learning mass shift. The top, middle, and bottom rows show results for Barrel jets, Endcap jets in Barrel-Endcap events, and Endcap-Endcap jets, respectively. In each plot, the black symbols and vertical bars indicate the mean and RMS, respectively, of the distribution in each bin. Events are from the 2013 embedding sample.

CHAPTER 7

Double-spin Asymmetries

The longitudinal double-spin asymmetry A_{LL} is the primary observable used to study the gluon polarization ΔG at RHIC. As described in Chapter 1, STAR has published measurements of A_{LL} for inclusive jets [30], [36], dijets at middle [32], [36] and intermediate pseudorapidity [34], and π^0 production at intermediate pseudorapidity [64]. These results have placed strong constraints on the behavior of the gluon polarized parton distribution function $\Delta g(x)$ for higher values of x , while the measurements presented in this dissertation will serve to better constrain the contribution to the spin of the proton from very low momentum gluons.

The longitudinal double-spin asymmetry is defined as:

$$A_{LL} \equiv \frac{\sigma_{++} - \sigma_{+-}}{\sigma_{++} + \sigma_{+-}}, \quad (7.1)$$

where σ_{++} and σ_{+-} are the scattering cross-sections for dijet production when the proton beams have equal and opposite helicities, respectively. Experimentally, the longitudinal double-spin asymmetry is measured as:

$$A_{LL} = \frac{\sum_i P_{Y_i} P_{B_i} [(N_i^{++} + N_i^{--}) - R_{3_i} (N_i^{+-} + N_i^{-+})]}{\sum_i P_{Y_i}^2 P_{B_i}^2 [(N_i^{++} + N_i^{--}) + R_{3_i} (N_i^{+-} + N_i^{-+})]}. \quad (7.2)$$

The summations are over all of the runs i in the data set. P_Y and P_B are the polarizations

of the yellow and blue beams. N^{++} , N^{--} , N^{+-} , and N^{-+} are the dijet yields for the four different beam helicity combinations, where the first index denotes the helicity of the yellow beam, and the second index indicates the helicity of the blue beam. Finally, R_3 is the ratio of the integrated luminosities for the equal and opposite beam helicity configurations. The polarizations, spin state combinations, and luminosity ratios will be explained more in the following sections. The statistical error on A_{LL} is closely approximated by:

$$\delta A_{LL} = \frac{\sqrt{\sum_i P_{Y_i}^2 P_{B_i}^2 [(N_i^{++} + N_i^{--}) + R_{3_i}^2 (N_i^{+-} + N_i^{-+})]}}{\sum_i P_{Y_i}^2 P_{B_i}^2 [(N_i^{++} + N_i^{--}) + R_{3_i} (N_i^{+-} + N_i^{-+})]}. \quad (7.3)$$

7.1 Beam Polarizations

The raw double-spin asymmetry depends on the polarizations of the colliding proton beams; the asymmetry should be zero for unpolarized beams. So, as can be seen in Eq. 7.2, the raw asymmetry is scaled by the two beam polarizations. The polarizations are determined by combining information from the proton-Carbon and hydrogen gas jet polarimeters, as described in Section 2.1.2. For each beam, the RHIC polarimetry group reports an initial polarization (P_0) and the polarization change over time ($\frac{dP}{dt}$) for each fill. From this information, along with the assumption of a linear polarization decay, the average polarization for a given run is calculated as:

$$P = P_0 + \frac{dP}{dt} t_{run}, \quad (7.4)$$

where t_{run} is the time from the beginning of the fill (when P_0 is measured) to the exact middle of the run. The length of each run is short compared to the nominal time for changes in beam conditions, so calculating the beam polarizations on a run-by-run basis provides sufficiently accurate values. In 2012, the luminosity-weighted average polarizations were 54% for the blue beam and 55% for the yellow beam. In 2013, the average polarizations were 56% and 54% for the blue and yellow beams, respectively.

7.2 Spin Patterns

The spin orientation of each of the up to 120 bunches in a RHIC ring is part of a predetermined spin pattern, and is fixed when the bunches are filled. There are four such spin patterns, each consisting of eight bunches, and whichever pattern was selected for a given fill repeats over the course of that fill. During the 2012 RHIC run, the patterns were: P1, +---+---; P2, ----+---; P3, +---+---; P4, ---+---+. In 2013, the patterns were: P1, +---+---; P2, ---+---+; P3, +---+---; P4, ---+----. The pattern P1 or P2 in one beam is collided with pattern P3 or P4 in the other, for a total of eight combinations of colliding spin patterns.

At STAR, the helicity combination of a pair of colliding bunches is encoded in the “Spin-4” value. The helicities of each beam at the STAR interaction point and their corresponding Spin-4 values are given in Table 7.1 for 2012 and Table 7.2 for 2013. Values of Spin-4 other than 5, 6, 9, 10 correspond to the “abort gaps”, which are bunch crossings where either one or both bunches are empty, and are therefore excluded from the analysis. The yellow beam abort gap consists of bunch crossings 31-39, and the blue beam abort gap is bunch crossings 111-119. The Spin-4 values are stored in an offline database, and must be checked for every event so that the dijet yields for each helicity combination are accumulated properly.

Spin-4	Yellow Beam Helicity	Blue Beam Helicity
5	-	-
6	-	+
9	+	-
10	+	+

Table 7.1: The beam helicity combination at STAR associated with each Spin-4 value for the 2012 RHIC run.

Spin-4	Yellow Beam Helicity	Blue Beam Helicity
5	+	+
6	+	-
9	-	+
10	-	-

Table 7.2: The beam helicity combination at STAR associated with each Spin-4 value for the 2013 RHIC run.

7.3 Relative Luminosities

Although the spin patterns are carefully chosen such that the different helicity combinations of the colliding beams are sampled equally, the bunches themselves vary in intensity from one to the next. So the various spin state combinations will end up having slightly different luminosities, which means that the asymmetry cannot be correctly measured by just using the raw dijet yields. Rather, the dijet yield for each spin state must be normalized by its associated relative luminosity factor, which is a ratio of the luminosities of different helicity combinations. The relative luminosities are calculated on a run-by-run basis using scaler information from the VPDs and ZDCs, and the differences between the measurements from those two subsystems are used to estimate the systematic error on the final values. The VPDs and ZDCs are ideal for collecting luminosity information because they sit near the beamline, which is where most of the particles produced in high energy pp collisions are concentrated. The VPD and ZDC detectors were described in Sections 2.1.5 and 2.1.3, respectively. More information on how the relative luminosities are calculated can be found in [65].

The six relative luminosity ratios relevant for the dijet A_{LL} analysis are defined as follows:

$$R_1 = \frac{\mathcal{L}^{++} + \mathcal{L}^{-+}}{\mathcal{L}^{+-} + \mathcal{L}^{--}} \quad (7.5a)$$

$$R_2 = \frac{\mathcal{L}^{++} + \mathcal{L}^{+-}}{\mathcal{L}^{-+} + \mathcal{L}^{--}} \quad (7.5b)$$

$$R_3 = \frac{\mathcal{L}^{++} + \mathcal{L}^{--}}{\mathcal{L}^{+-} + \mathcal{L}^{-+}} \quad (7.5c)$$

$$R_4 = \frac{\mathcal{L}^{++}}{\mathcal{L}^{--}} \quad (7.5d)$$

$$R_5 = \frac{\mathcal{L}^{-+}}{\mathcal{L}^{--}} \quad (7.5e)$$

$$R_6 = \frac{\mathcal{L}^{+-}}{\mathcal{L}^{--}}. \quad (7.5f)$$

R_3 is the ratio needed to normalize the spin-sorted dijet yields in the A_{LL} calculation, while the other ratios are used to calculate the false asymmetries described in the next section. Unphysical asymmetries arising from incorrect relative luminosities can be much larger than the expected physical asymmetries, so it is very important to get them right. Detailed investigations often uncover bunch crossings with anomalous behavior which need to be discarded from the analysis, and several such bad bunches were found on a fill-by-fill basis during the calculation of the 2012 and 2013 relative luminosities. Tables C.1 and C.2 in Appendix C list the bad bunch crossings by fill for 2012 and 2013, respectively. The bad bunches were removed from both the relative luminosity calculation and the dijet asymmetry analysis, along with the yellow and blue beam abort gaps.

7.4 False Asymmetries

The four “false asymmetries” are useful tools to check the relative luminosity values, as well as the analysis more generally. The false asymmetries, defined in Eq. 7.6, are expressed in terms of the spin-sorted yields, just like A_{LL} . A_L^Y and A_L^B are the longitudinal single-spin asymmetries for the yellow and blue beams, and A_{LL}^{ls} and A_{LL}^{us} are the like- and unlike-sign

longitudinal double-spin asymmetries.

$$A_L^Y = \frac{\sum_i P_{Y_i} [(N_i^{++} + N_i^{-+}) - R_{1_i} (N_i^{+-} + N_i^{--})]}{\sum_i P_{Y_i}^2 [(N_i^{++} + N_i^{-+}) + R_{1_i} (N_i^{+-} + N_i^{--})]} \quad (7.6a)$$

$$A_L^B = \frac{\sum_i P_{B_i} [(N_i^{++} + N_i^{+-}) - R_{2_i} (N_i^{-+} + N_i^{--})]}{\sum_i P_{B_i}^2 [(N_i^{++} + N_i^{+-}) + R_{2_i} (N_i^{-+} + N_i^{--})]} \quad (7.6b)$$

$$A_{LL}^{ls} = \frac{\sum_i P_{Y_i} P_{B_i} (N_i^{++} - R_{4_i} N_i^{--})}{\sum_i P_{Y_i}^2 P_{B_i}^2 (N_i^{++} + R_{4_i} N_i^{--})} \quad (7.6c)$$

$$A_{LL}^{us} = \frac{\sum_i P_{Y_i} P_{B_i} (R_{5_i} N_i^{+-} - R_{6_i} N_i^{-+})}{\sum_i P_{Y_i}^2 P_{B_i}^2 (R_{5_i} N_i^{+-} + R_{6_i} N_i^{-+})} \quad (7.6d)$$

A_L^Y , A_L^B , and A_{LL}^{ls} could be slightly nonzero due to parity-violating interactions, but these effects are very small so all three are expected to be consistent with zero within the current statistical precision. A_{LL}^{us} must be zero by geometric symmetry, as collisions where the yellow beam has positive helicity and the blue negative should be identical to the reverse. If any of these false asymmetries were found to deviate significantly from zero, it would suggest a problem with the relative luminosities or with the calculation of A_{LL} . Figures 7.1, 7.2, 7.3, and 7.4 show these false asymmetries in the 2012 data for all Barrel-Endcap dijets ($-0.8 < \eta_1 < 0.9$, $0.9 < \eta_2 < 1.8$), East Barrel-Endcap dijets ($-0.8 < \eta_1 < 0$, $0.9 < \eta_2 < 1.8$), West Barrel-Endcap dijets ($0 < \eta_1 < 0.9$, $0.9 < \eta_2 < 1.8$), and Endcap-Endcap dijets ($0.9 < \eta_{1,2} < 1.8$), respectively. Figures 7.5, 7.6, 7.7, and 7.8 show the same for the 2013 data. Constant fits to the false asymmetries are mostly consistent with zero, as expected, and have reasonable χ^2 values. The blue dotted lines in the plots are drawn at zero, while the solid black lines are the constant fits, i.e., the average value of the data points.

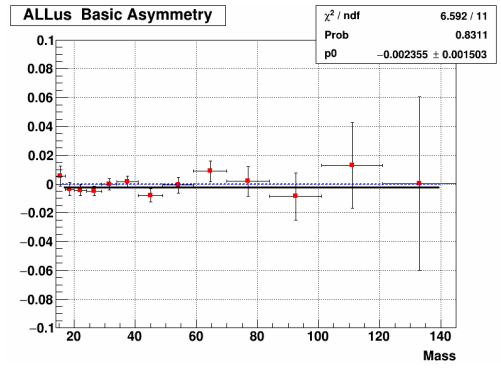
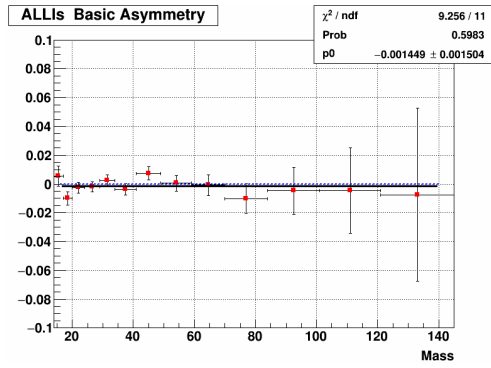
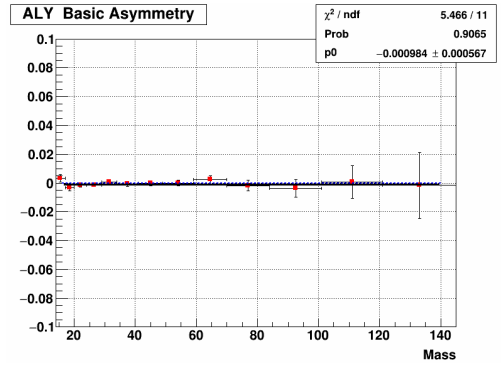
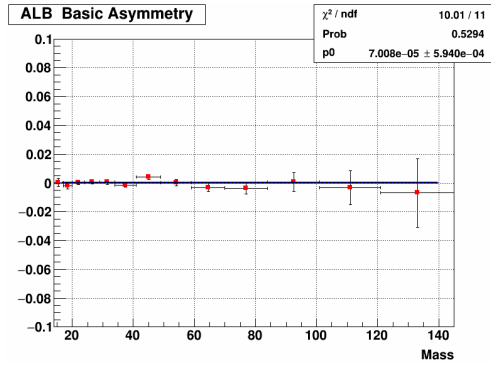


Figure 7.1: False asymmetries for all Barrel-Endcap dijets, 2012.

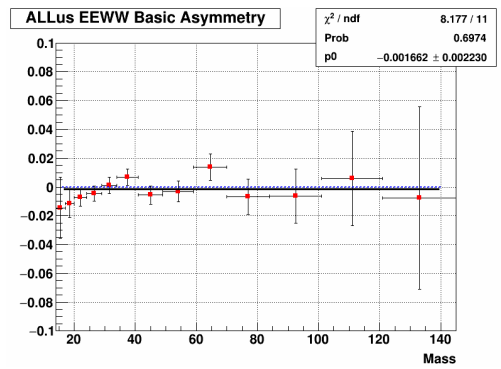
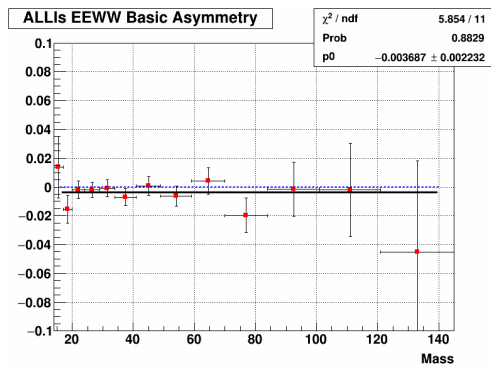
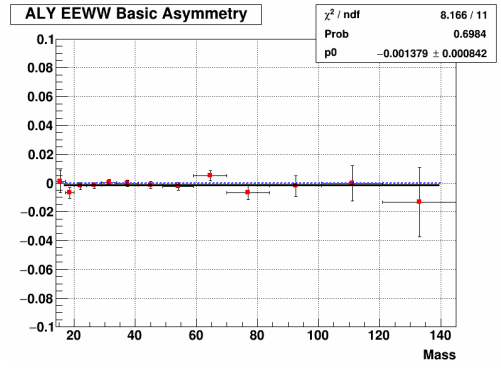
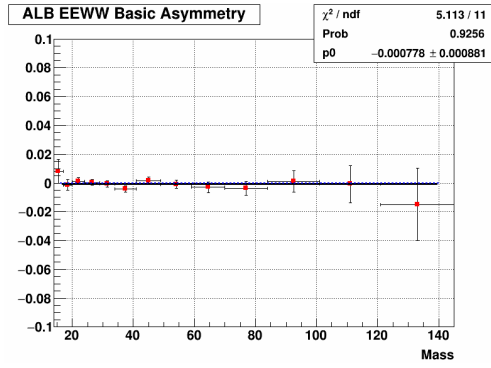


Figure 7.2: False asymmetries for East Barrel-Endcap dijets, 2012.

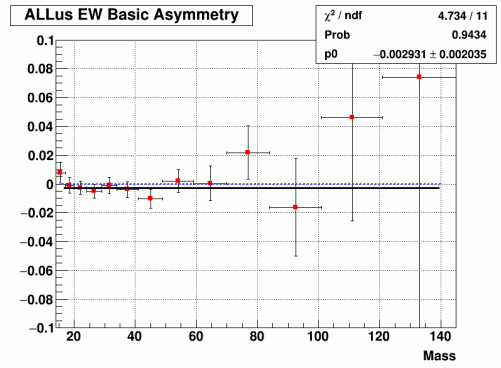
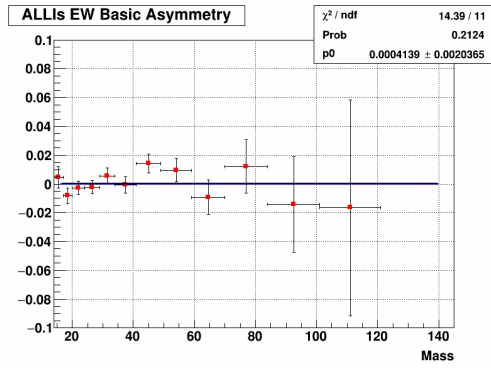
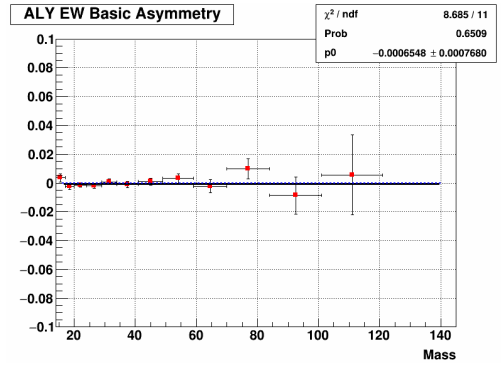
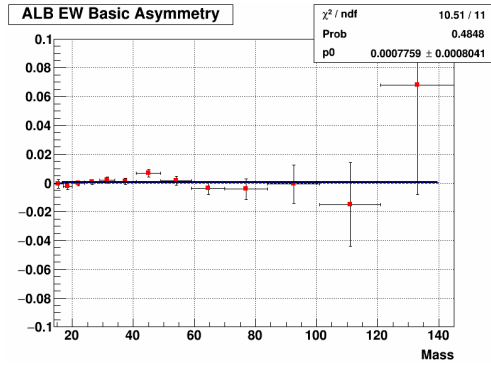


Figure 7.3: False asymmetries for West Barrel-Endcap dijets, 2012.

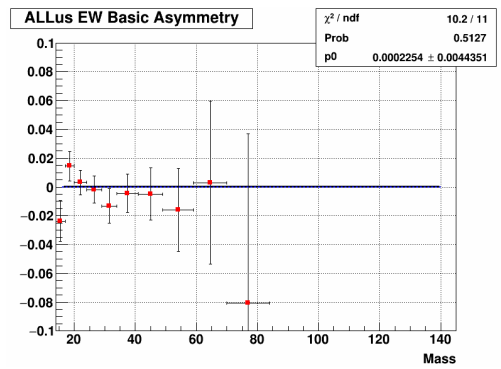
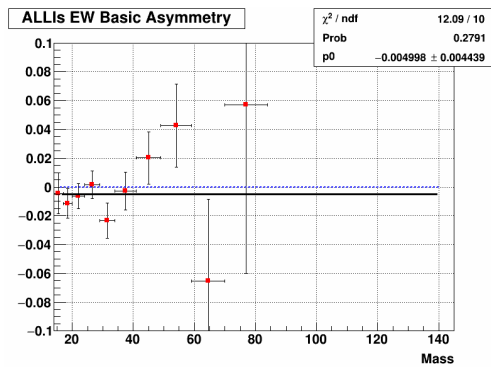
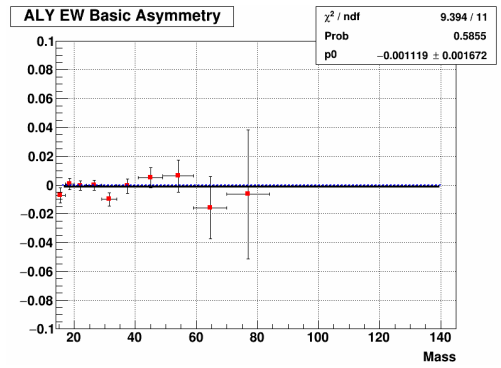
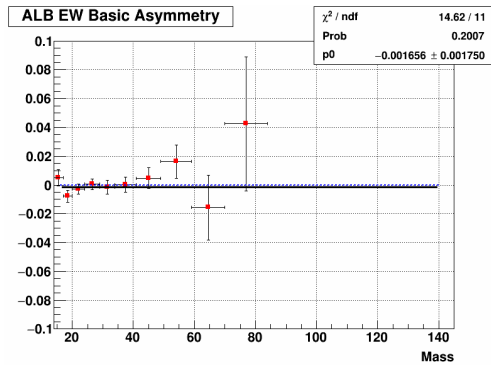


Figure 7.4: False asymmetries for Endcap-Endcap dijets, 2012.

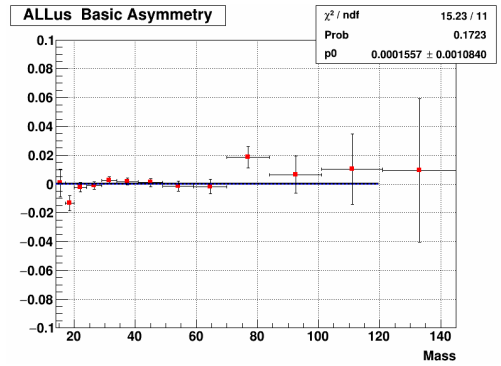
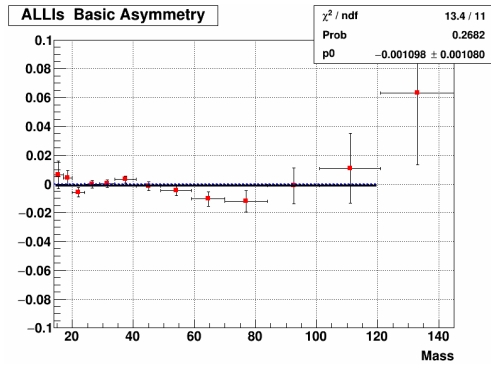
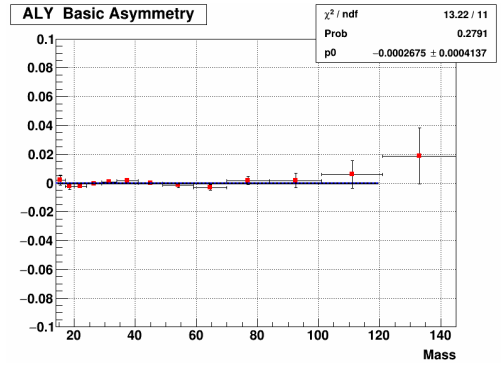
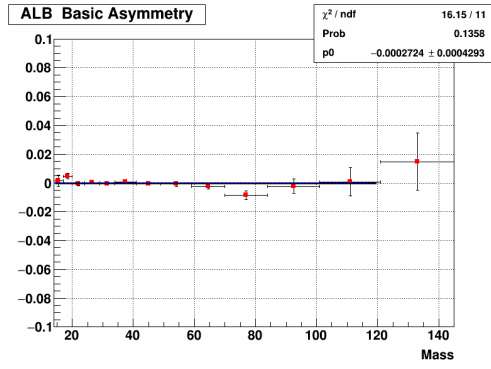


Figure 7.5: False asymmetries for all Barrel-Endcap dijets, 2013.

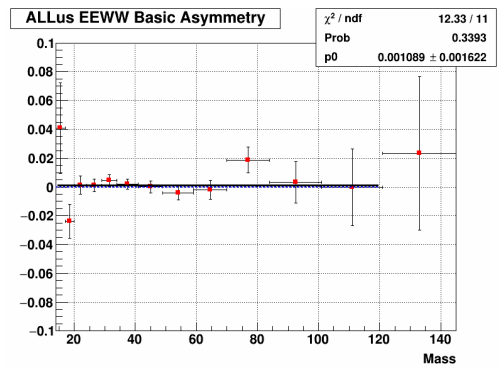
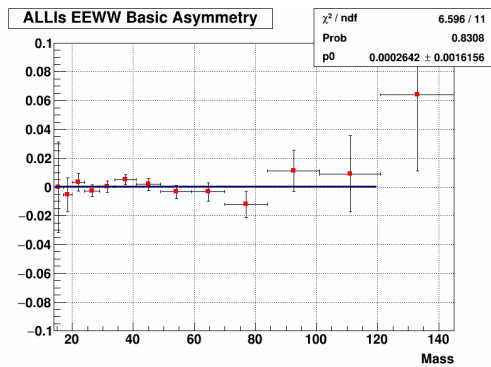
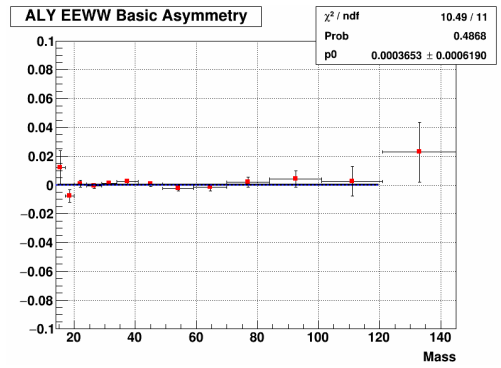
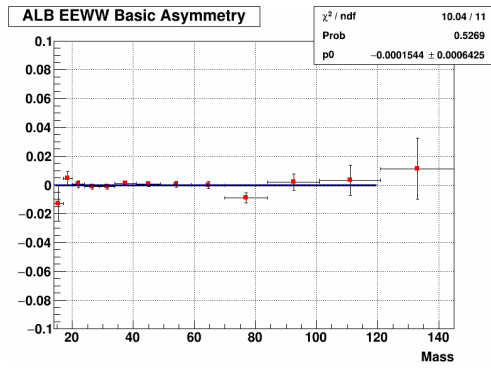


Figure 7.6: False asymmetries for East Barrel-Endcap dijets, 2013.

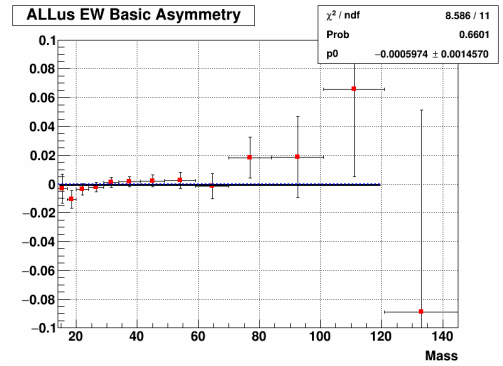
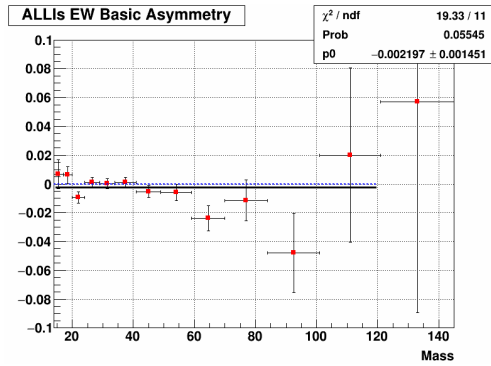
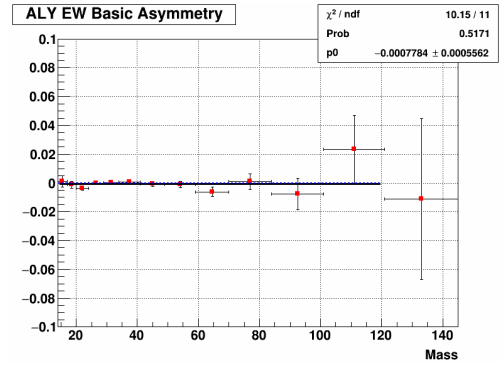
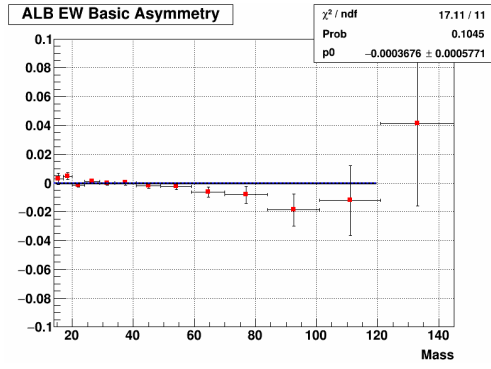


Figure 7.7: False asymmetries for West Barrel-Endcap dijets, 2013.

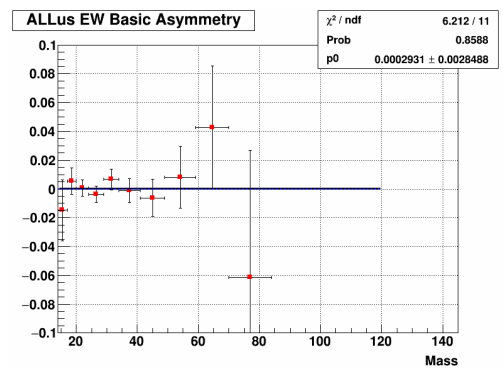
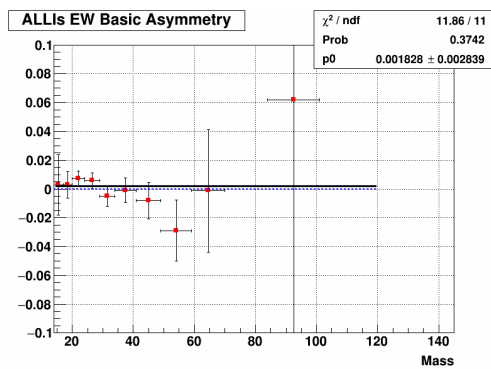
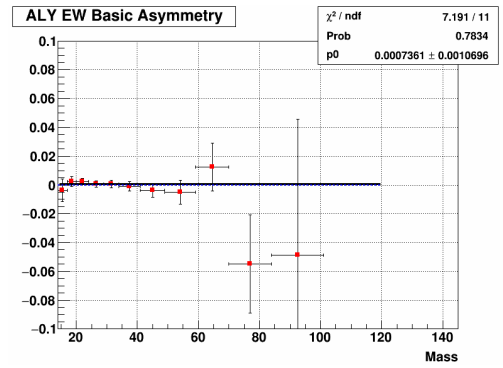
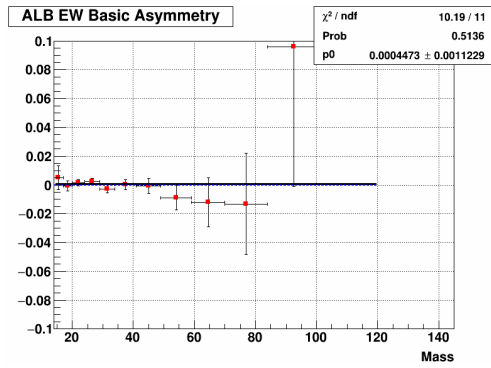


Figure 7.8: False asymmetries for Endcap-Endcap dijets, 2013.

7.5 Data Corrections

Corrections are applied to the dijet invariant mass and the “raw” A_{LL} defined in Eq. 7.2, in order to facilitate better comparisons with theory and account for biases arising from the measurement process and analysis. These corrections are detailed in the following two subsections.

7.5.1 Dijet Invariant Mass Shift

The machine learning jet p_T and mass corrections described in the previous chapter essentially shift the dijet invariant masses measured in the data back to particle level. However, theoretical predictions for dijet A_{LL} are calculated at the parton level, so one more shift is applied to account for the difference in parton and particle level dijet invariant masses. For a given mass bin in the simulation, the mass difference $\Delta M = M_{parton} - M_{particle}$ between the dijet invariant masses for the matching parton and particle level dijets is calculated for each event in that mass bin. The mass shift for that bin is simply the average ΔM . The final data points, then, are plotted at the average corrected mass (particle level) plus this mass shift. Figure 7.9 shows the bin-by-bin average mass shifts for the four different dijet topologies in 2012, and Fig. 7.10 shows them in 2013. The initial average masses and their corresponding mass shifts are listed in columns 2 and 3, respectively, in Tables 7.3 and 7.4 for 2012, and Tables 7.5 and 7.6 for 2013.

7.5.2 Trigger and Reconstruction Bias

The dijet events of interest in this analysis are predominantly produced by three different subprocesses: quark-quark, quark-gluon, and gluon-gluon scattering. Each of these subprocesses has a different parton level asymmetry, and the final measured A_{LL} will be a mixture of contributions from the various interactions. However, jet events are triggered based on

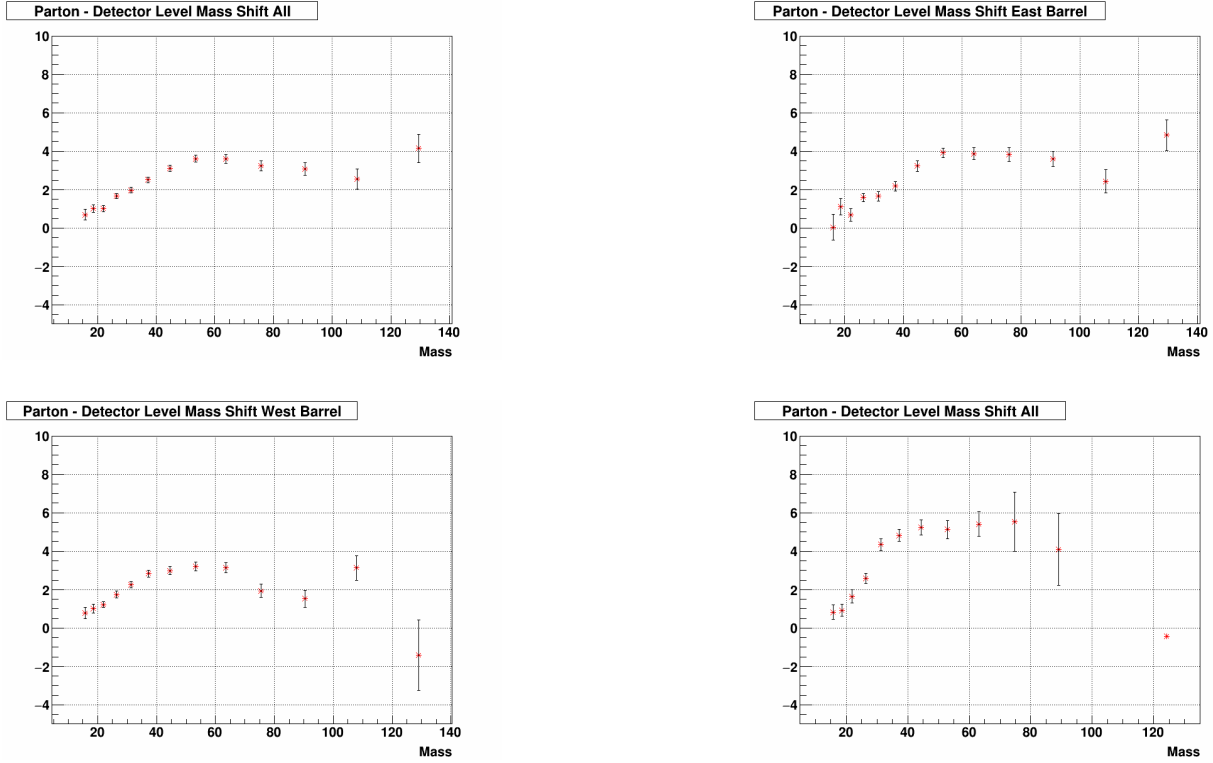


Figure 7.9: Mass shifts for all Barrel-Endcap (upper left), East Barrel-Endcap (upper right), West Barrel-Endcap (lower left) and Endcap-Endcap (lower right) dijets, 2012.

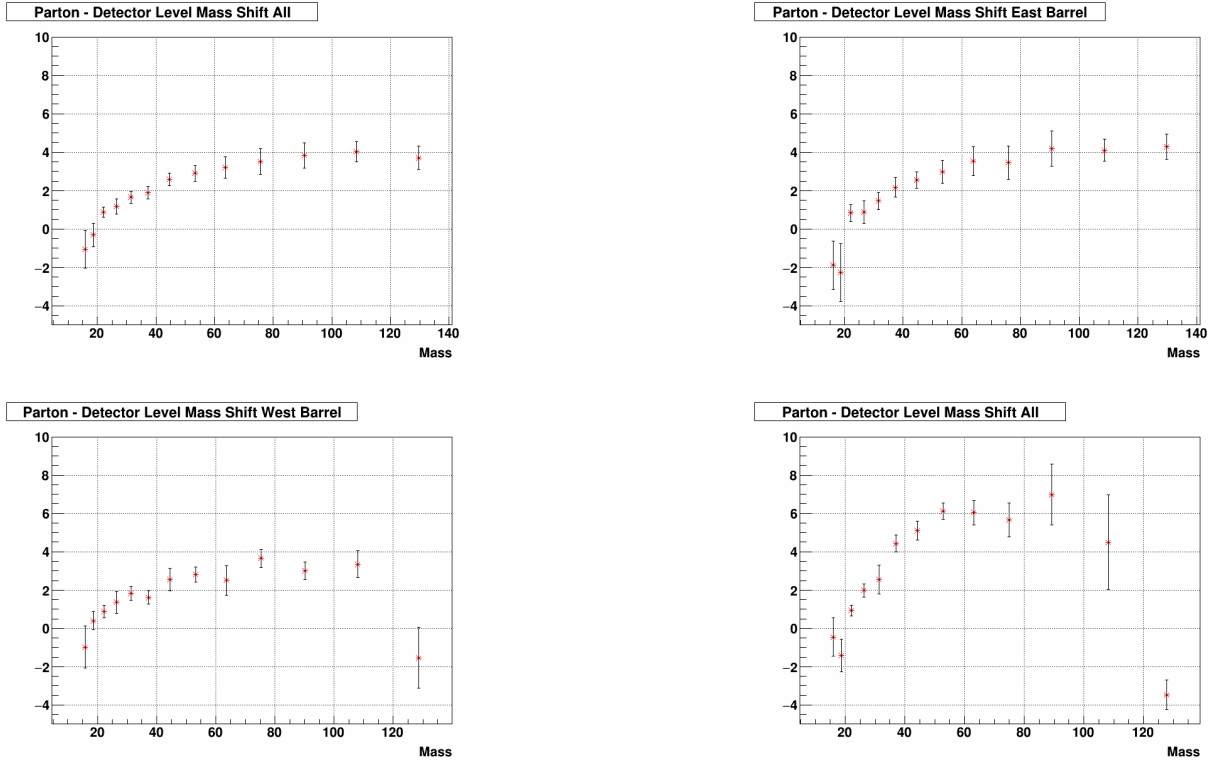


Figure 7.10: Mass shifts for all Barrel-Endcap (upper left), East Barrel-Endcap (upper right), West Barrel-Endcap (lower left) and Endcap-Endcap (lower right) dijets, 2013.

energy deposited in the BEMC and EEMC towers, and those triggering requirements might preferentially select jets which fragment in certain ways. Furthermore, jet reconstruction in the Endcap region is biased towards jets with more neutral energy due to the reduced tracking efficiency, and the neutral fraction is correlated with subprocess. These biases result in the subprocess fractions sampled by the final set of dijet events differing from the fractions at parton level, which shifts the measured A_{LL} from its true physical value and necessitates that the raw A_{LL} be corrected.

The biases introduced by the triggering and reconstruction processes are estimated by examining A_{LL} as a function of dijet invariant mass in the simulation, at both parton and detector levels. The predictions for A_{LL} in the simulation depend on the polarized parton distribution functions (PDFs), though, which must be taken from theory and have their own uncertainties. To generate theoretical predictions for A_{LL} and account for the associated uncertainty, we use the NNPDFpol1.1 [29] set of parton distributions, which has 100 replicas corresponding to different parameterizations of the polarized parton distribution functions. The procedure used is the same as for the 2009 pp 200 GeV Endcap dijet analysis:

1. For each event, find the parton level dijet from the unbiased PYTHIA sample. Apply the $\Delta\phi$, jet η , and asymmetric p_T cuts. Plot A_{LL} from the 100 polarized PDF replicas versus the parton level dijet invariant mass. These plots are in the upper left of Figs. 7.11-7.14 for 2012 and Figs. 7.15-7.18 for 2013.
2. Fit the parton level theory curve with a 3rd order polynomial, and extract A_{LL} from the fitted function. This is shown in the lower left plots of Figs. 7.11-7.14 for 2012 and Figs. 7.15-7.18 for 2013.
3. For each event, find the detector level dijet which passed the trigger filter and apply all detector level cuts, but do not require the detector to particle level matching. Plot A_{LL} of the polarized PDFs versus the detector level dijet invariant mass (shown in upper right plots of Figs. 7.11-7.14 for 2012 and Figs. 7.15-7.18 for 2013). The final

A_{LL} is the trigger-fraction weighted sum of the A_{LL} from each trigger (three in 2012, six in 2013). Points are placed at the mass-weighted mean of each bin.

4. Calculate $\Delta A_{LL} = A_{LL}^{detector}(M_{detector}) - A_{LL}^{parton}(M_{detector} + \Delta M_{shift})$ for each mass bin, where ΔM_{shift} is the mass shift described in the previous subsection.

The trigger and reconstruction bias correction is the average of the ΔA_{LL} for the 100 NNPDF replicas, which is plotted in the lower right of Figs. 7.11-7.14 for 2012 and Figs. 7.15-7.18 for 2013. The final data point is then $A_{LL}^{final} = A_{LL}^{raw} - \Delta A_{LL}$. The statistical uncertainties on the average shifts from theoretical detector level to unbiased parton level A_{LL} are taken as systematic errors on the final values of the dijet A_{LL} . The raw A_{LL} values, trigger and reconstruction bias corrections, and errors on the trigger and reconstruction bias corrections are given in columns 4, 5, and 6, respectively, of Tables 7.3, 7.4, 7.5, and 7.6.

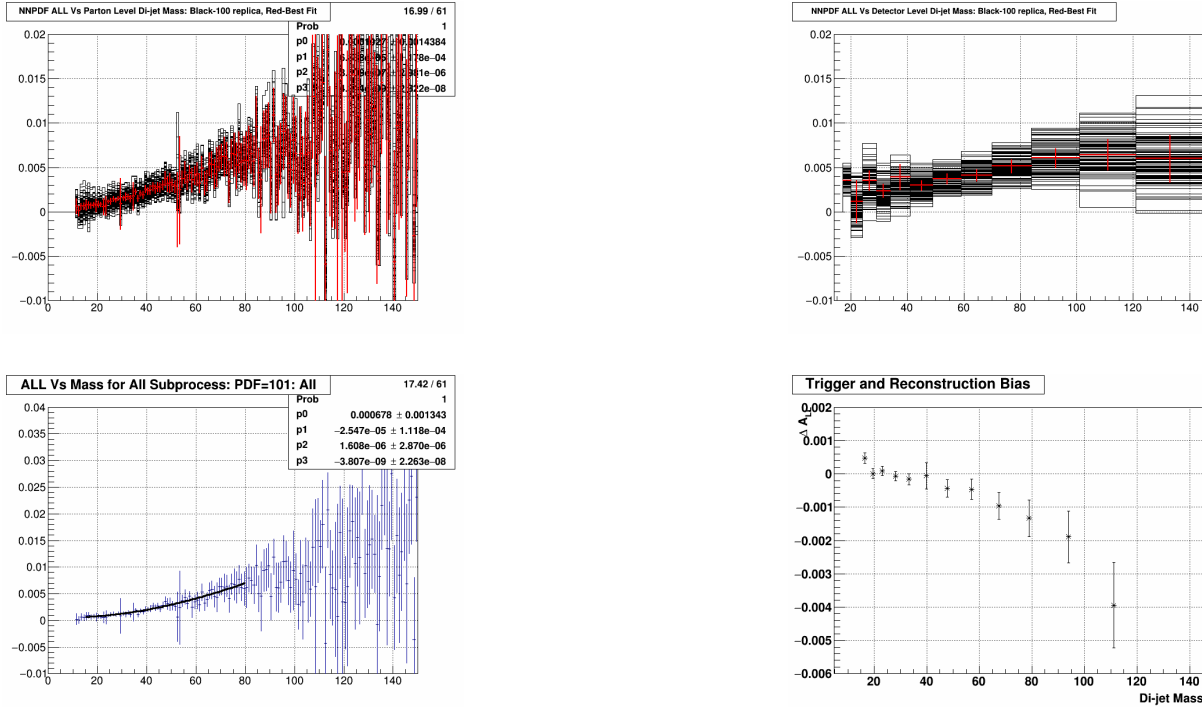


Figure 7.11: Trigger and reconstruction bias for Barrel-Endcap full topology in 2012: parton level dijet A_{LL} for 100 NNPDF replicas (upper left), detector level dijet A_{LL} for replicas (upper right), parton level polynomial fit (lower left), and final corrections (lower right).

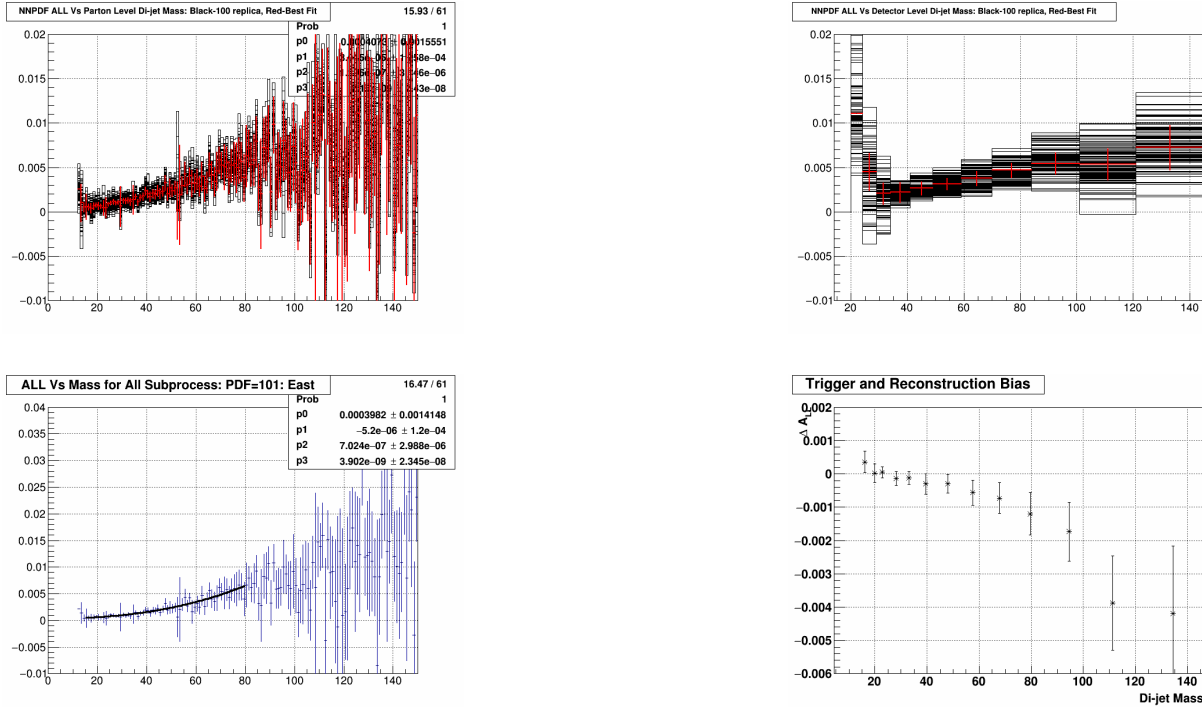


Figure 7.12: Trigger and reconstruction bias for East Barrel-Endcap topology in 2012: parton level dijet A_{LL} for 100 NNPDF replicas (upper left), detector level dijet A_{LL} for replicas (upper right), parton level polynomial fit (lower left), and final corrections (lower right).

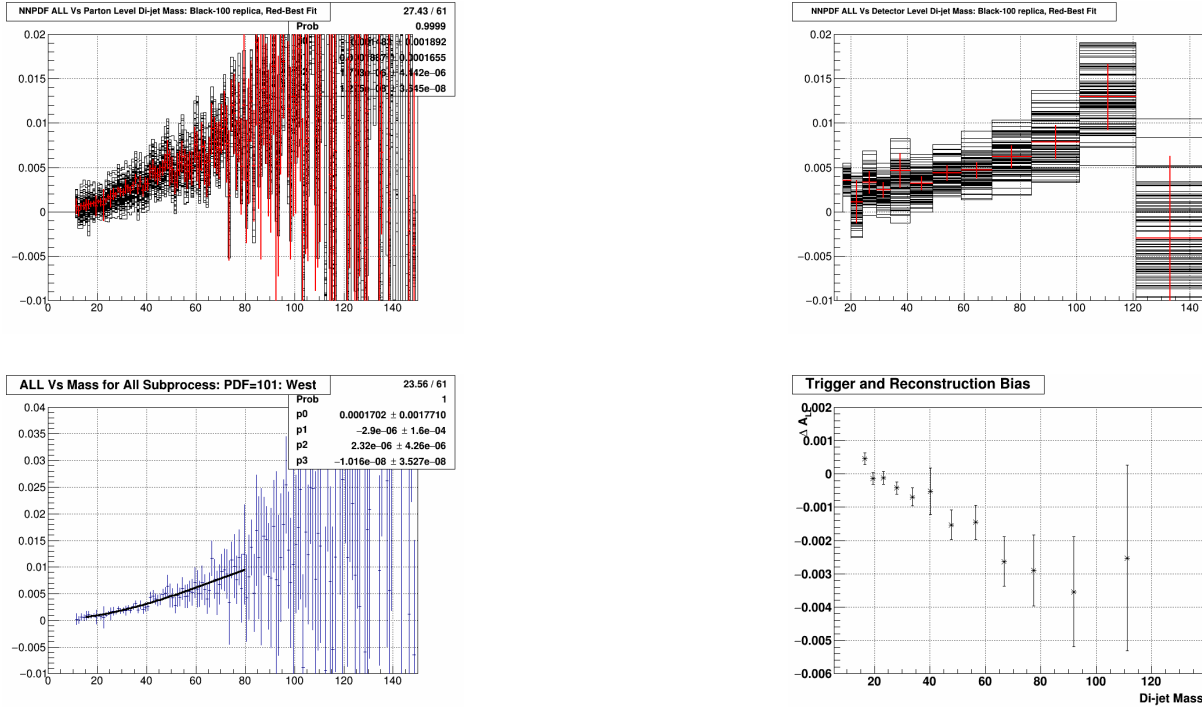


Figure 7.13: Trigger and reconstruction bias for West Barrel-Endcap topology in 2012: parton level dijet A_{LL} for 100 NNPDF replicas (upper left), detector level dijet A_{LL} for replicas (upper right), parton level polynomial fit (lower left), and final corrections (lower right).

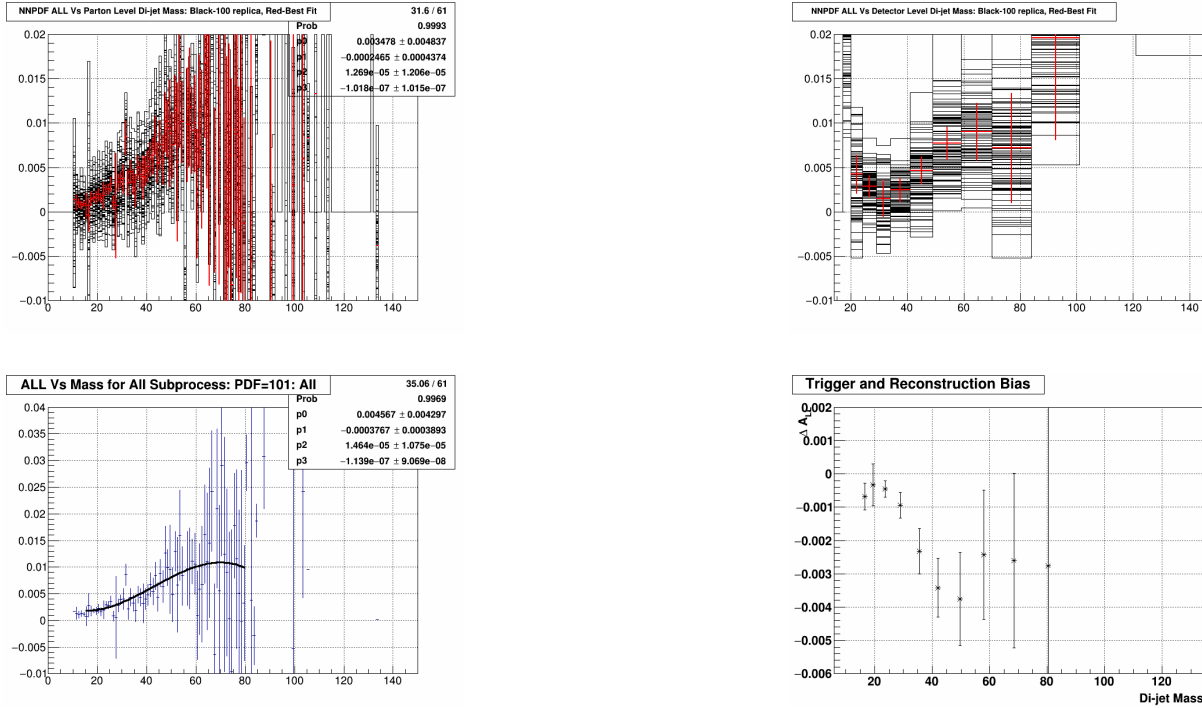


Figure 7.14: Trigger and reconstruction bias for Endcap-Endcap topology in 2012: parton level dijet A_{LL} for 100 NNPDF replicas (upper left), detector level dijet A_{LL} for replicas (upper right), parton level polynomial fit (lower left), and final corrections (lower right).

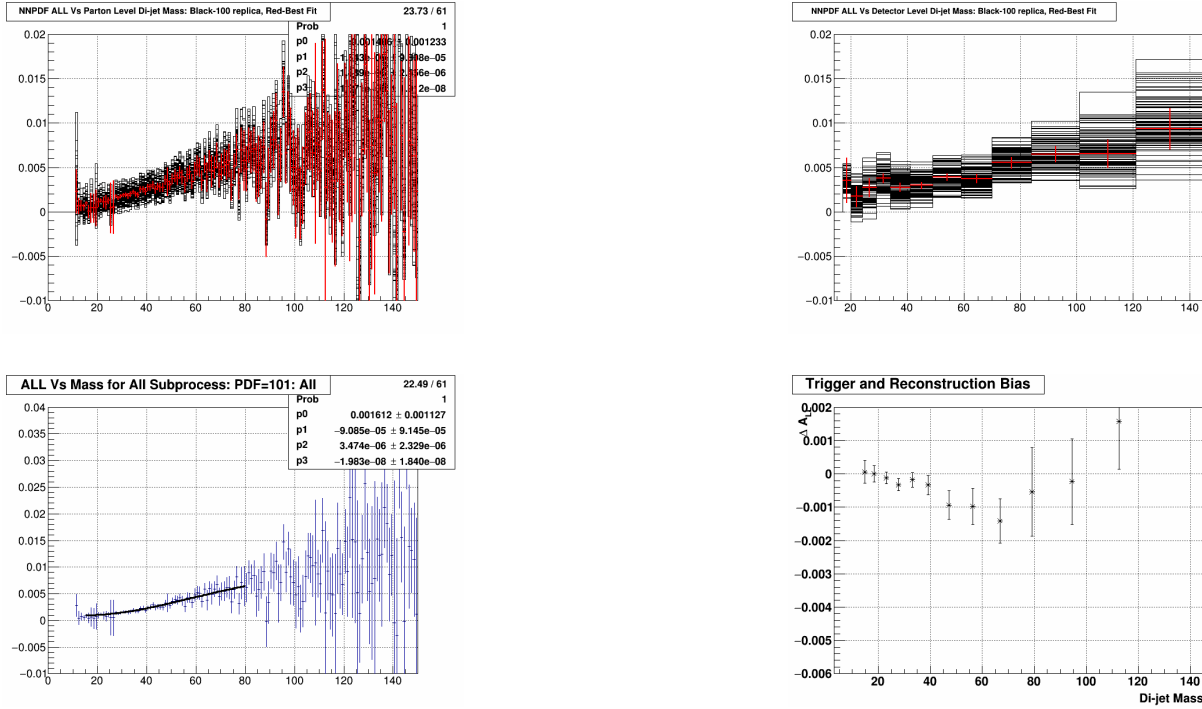


Figure 7.15: Trigger and reconstruction bias for Barrel-Endcap full topology in 2013: parton level dijet A_{LL} for 100 NNPDF replicas (upper left), detector level dijet A_{LL} for replicas (upper right), parton level polynomial fit (lower left), and final corrections (lower right).

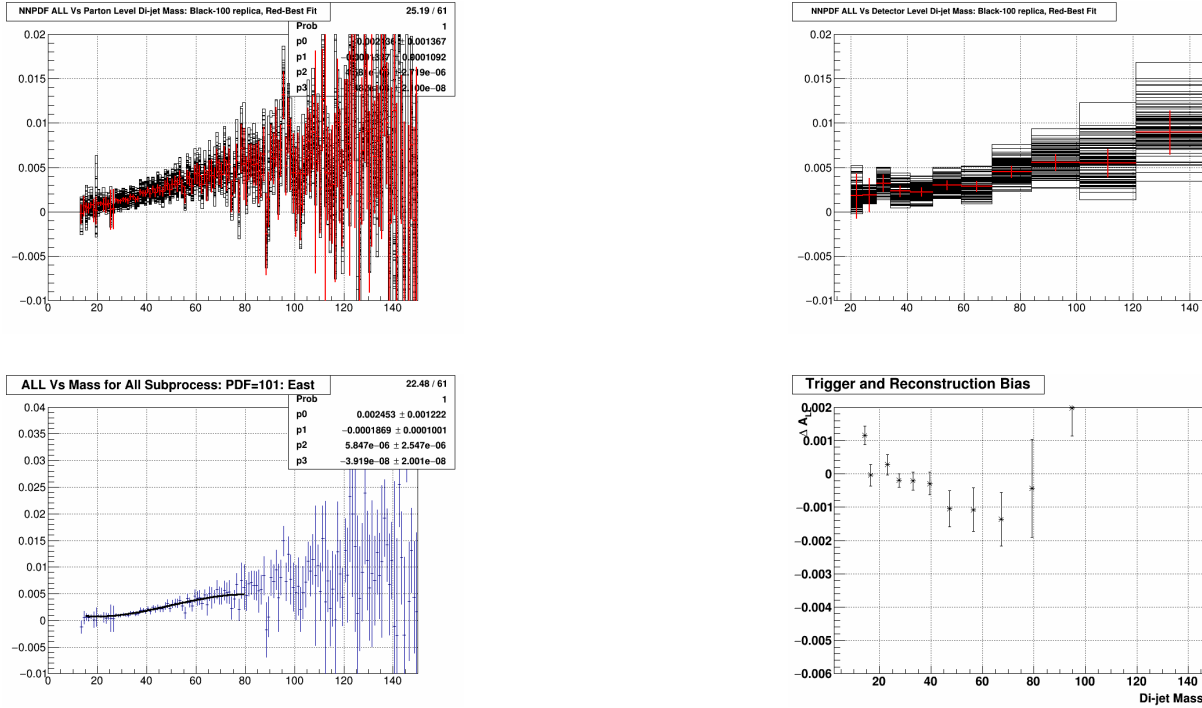


Figure 7.16: Trigger and reconstruction bias for East Barrel-Endcap topology in 2013: parton level dijet A_{LL} for 100 NNPDF replicas (upper left), detector level dijet A_{LL} for replicas (upper right), parton level polynomial fit (lower left), and final corrections (lower right).

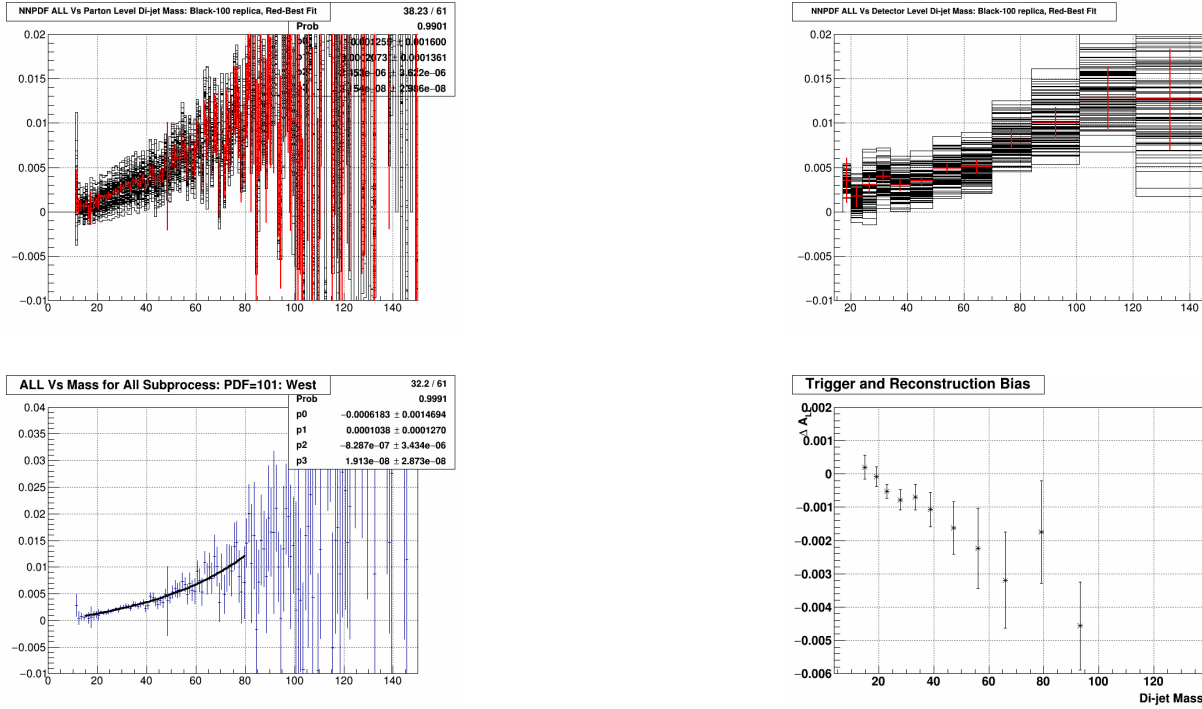


Figure 7.17: Trigger and reconstruction bias for West Barrel-Endcap topology in 2013: parton level dijet A_{LL} for 100 NNPDF replicas (upper left), detector level dijet A_{LL} for replicas (upper right), parton level polynomial fit (lower left), and final corrections (lower right).

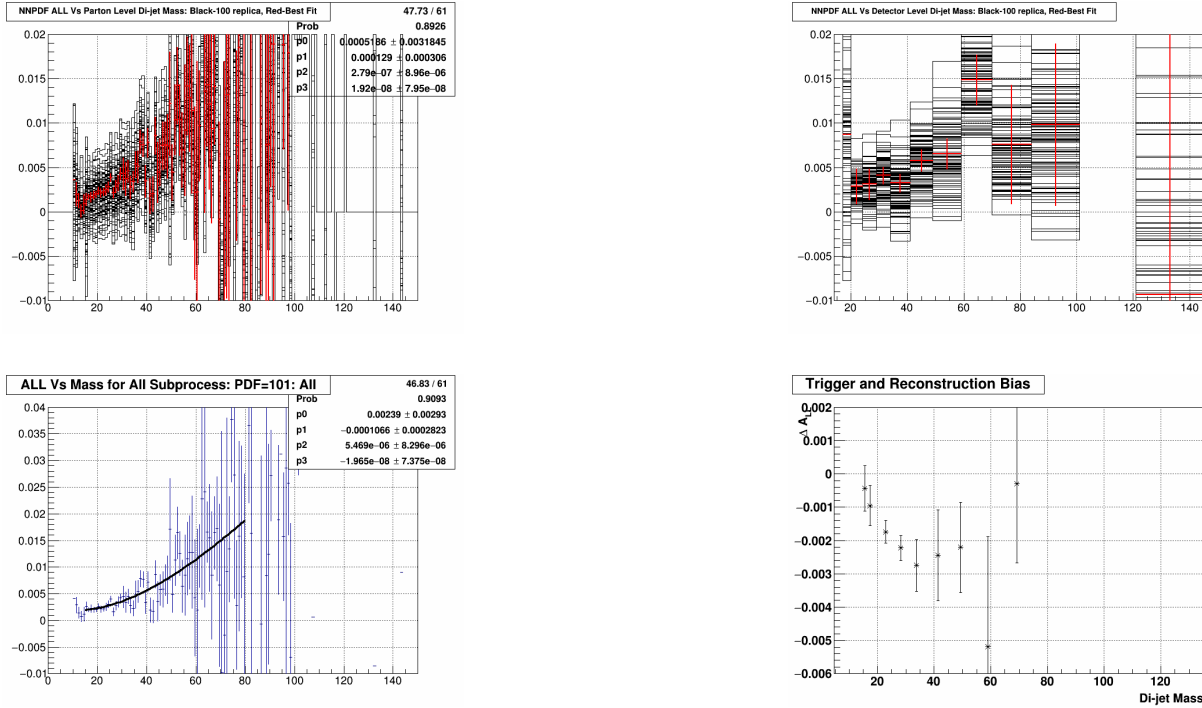


Figure 7.18: Trigger and reconstruction bias for Endcap-Endcap topology in 2013: parton level dijet A_{LL} for 100 NNPDF replicas (upper left), detector level dijet A_{LL} for replicas (upper right), parton level polynomial fit (lower left), and final corrections (lower right).

Barrel-Endcap Full Topology					
Bin	Avg. Mass (GeV)	Mass Shift (GeV)	A_{LL}	Trig. and Reco. Shift	Errors
1	15.825	0.69	0.005254	0.00047	0.00016
2	18.602	1.014	-0.00137	0.00001	0.00015
3	22.014	1.01	0.00209	0.00009	0.00014
4	26.402	1.671	0.001579	-0.00007	0.00014
5	31.37	1.97	0.00583	-0.00016	0.00017
6	37.263	2.511	0.001879	-0.00006	0.0004
7	44.704	3.098	0.000819	-0.00043	0.00026
8	53.479	3.607	0.008329	-0.00046	0.00031
9	63.777	3.597	0.004173	-0.00096	0.0004
10	75.782	3.232	-0.003337	-0.00133	0.00055
11	90.785	3.074	0.034169	-0.00189	0.00078
12	108.638	2.543	0.006312	-0.00395	0.00128
13	129.493	4.147	-0.00005	-0.00733	0.00221

Endcap-Endcap					
Bin	Avg. Mass (GeV)	Mass Shift (GeV)	A_{LL}	Trig. and Reco. Shift	Errors
1	15.787	0.827	0.001079	-0.00068	0.0004
2	18.573	0.921	0.017057	-0.00033	0.00064
3	21.919	1.645	-0.006133	-0.00045	0.00024
4	26.28	2.588	0.010818	-0.00095	0.00038
5	31.309	4.351	-0.016845	-0.00232	0.00068
6	37.143	4.817	0.017601	-0.00342	0.00088
7	44.375	5.237	-0.016741	-0.00376	0.0014
8	52.895	5.128	0.014264	-0.00242	0.00194
9	63.14	5.41	-0.003661	-0.0026	0.00262
10	74.881	5.538	0.029429	-0.00275	0.00653
11	89.122	4.091	0.240822	0.01519	0.00927
12	106.467	11.118	0.186634	0.06938	0.00211
13	124.213	-0.443	-3.03341	0.0938	0

Table 7.3: Dijet parton level corrections for the Barrel-Endcap and Endcap-Endcap topologies, 2012.

East Barrel-Endcap					
Bin	Avg. Mass (GeV)	Mass Shift (GeV)	A_{LL}	Trig. and Reco. Shift	Errors
1	16.137	0.026	-0.009994	0.00036	0.00033
2	18.731	1.097	0.002094	0.00003	0.00028
3	22.109	0.667	-0.00009	0.00005	0.00016
4	26.466	1.587	0.001656	-0.00014	0.0002
5	31.389	1.654	0.001055	-0.00011	0.00019
6	37.265	2.18	0.007552	-0.0003	0.00031
7	44.756	3.224	-0.001826	-0.00029	0.00029
8	53.587	3.91	0.009993	-0.00056	0.00038
9	63.867	3.867	0.007131	-0.00072	0.00047
10	75.876	3.821	-0.001039	-0.0012	0.00063
11	90.896	3.598	0.028464	-0.00173	0.00088
12	108.781	2.428	0.037056	-0.00388	0.00141
13	129.546	4.842	-0.004305	-0.0042	0.00204
West Barrel-Endcap					
Bin	Avg. Mass (GeV)	Mass Shift (GeV)	A_{LL}	Trig. and Reco. Shift	Errors
1	15.788	0.78	0.007093	0.00046	0.00017
2	18.561	1.005	-0.002478	-0.00014	0.00017
3	21.962	1.219	0.003298	-0.00012	0.00019
4	26.352	1.744	0.001518	-0.00043	0.00018
5	31.352	2.27	0.010259	-0.00069	0.00027
6	37.26	2.837	-0.003594	-0.00053	0.0007
7	44.649	2.986	0.003545	-0.00153	0.00044
8	53.337	3.201	0.006174	-0.00146	0.00052
9	63.619	3.141	-0.001001	-0.00263	0.00074
10	75.563	1.931	-0.008674	-0.00291	0.00107
11	90.435	1.522	0.052218	-0.00354	0.00165
12	107.922	3.132	-0.14904	-0.00253	0.00279
13	129.013	-1.409	0.039732	-0.0219	0.01034

Table 7.4: Dijet parton level corrections for the two Barrel-Endcap topologies, 2012.

Barrel-Endcap Full Topology					
Bin	Avg. Mass (GeV)	Mass Shift (GeV)	A_{LL}	Trig. and Reco. Shift	Errors
1	15.916	-1.057	-0.007336	0.00006	0.00034
2	18.704	-0.314	0.004363	0.00001	0.00025
3	22.152	0.865	0.000564	-0.00013	0.00018
4	26.542	1.176	0.004339	-0.00032	0.00018
5	31.445	1.654	0.001096	-0.00018	0.00022
6	37.282	1.896	0.001264	-0.00033	0.00029
7	44.638	2.571	0.004877	-0.00094	0.00043
8	53.358	2.9	0.00687	-0.00098	0.00054
9	63.687	3.209	0.011672	-0.00141	0.00067
10	75.684	3.514	0.0129	-0.00054	0.00132
11	90.61	3.826	0.025616	-0.00023	0.00129
12	108.459	4.02	0.01214	0.00157	0.00143
13	129.599	3.708	0.005319	0.00796	0.00159
Endcap-Endcap					
Bin	Avg. Mass (GeV)	Mass Shift (GeV)	A_{LL}	Trig. and Reco. Shift	Errors
1	16.019	-0.453	-0.014903	-0.00043	0.00069
2	18.819	-1.413	0.001281	-0.00095	0.0006
3	22.046	0.927	0.006109	-0.00174	0.00034
4	26.295	1.982	0.000315	-0.00223	0.00037
5	31.258	2.563	0.004414	-0.00275	0.00078
6	36.983	4.428	-0.001492	-0.00244	0.00137
7	44.272	5.104	0.012583	-0.00221	0.00136
8	52.845	6.118	0.018543	-0.00519	0.0033
9	63.154	6.043	0.010672	-0.00029	0.00239
10	74.838	5.666	-0.023048	-0.01293	0.00534
11	89.32	6.99	-0.02058	-0.02057	0.00927
12	108.149	4.495	0.423723	0.09212	0.10707
13	127.738	-3.469	-1.67225	-0.06336	0.03318

Table 7.5: Dijet parton level corrections for the Barrel-Endcap and Endcap-Endcap topologies, 2013.

East Barrel-Endcap					
Bin	Avg. Mass (GeV)	Mass Shift (GeV)	A_{LL}	Trig. and Reco. Shift	Errors
1	16.197	-1.886	-0.008839	0.00116	0.00028
2	18.813	-2.28	0.004485	-0.00004	0.00032
3	22.242	0.83	0.001094	0.00028	0.0003
4	26.64	0.889	0.005027	-0.0002	0.0002
5	31.499	1.453	0.001	-0.00021	0.00027
6	37.34	2.172	0.000301	-0.00029	0.00034
7	44.701	2.548	0.003947	-0.00104	0.00054
8	53.444	2.967	0.00816	-0.00108	0.00066
9	63.774	3.54	0.014158	-0.00136	0.0008
10	75.795	3.464	0.015	-0.00044	0.00147
11	90.714	4.192	0.020742	0.00197	0.00084
12	108.53	4.105	0.014383	0.00569	0.00131
13	129.74	4.288	0.02145	0.01786	0.00167

West Barrel-Endcap					
Bin	Avg. Mass (GeV)	Mass Shift (GeV)	A_{LL}	Trig. and Reco. Shift	Errors
1	15.887	-0.976	-0.007182	0.0002	0.00036
2	18.677	0.386	0.004332	-9e-05	0.0003
3	22.116	0.882	0.000355	-0.00052	0.0002
4	26.486	1.354	0.003947	-0.00078	0.0003
5	31.403	1.831	0.001169	-0.00069	0.00039
6	37.228	1.612	0.002156	-0.00107	0.00052
7	44.565	2.551	0.005926	-0.00163	0.00078
8	53.234	2.819	0.005033	-0.00223	0.00121
9	63.524	2.504	0.007008	-0.00319	0.00144
10	75.395	3.659	0.007455	-0.00174	0.00154
11	90.22	2.998	0.043988	-0.00457	0.00132
12	108.092	3.347	0.000449	-0.00673	0.0026
13	128.569	-1.539	-0.112059	-0.01259	0.00532

Table 7.6: Dijet parton level corrections for the two Barrel-Endcap topologies, 2013.

7.6 Systematic Errors

The systematic uncertainties are similar to those encountered in the 2009 forward dijet measurement [34]. They are separated into two categories: systematic errors on the dijet mass points, and systematic errors on the A_{LL} values. The dijet mass systematics include the dijet invariant mass shift uncertainty, jet energy scale uncertainty, tracking efficiency uncertainty, underlying event systematic error, and PYTHIA tune uncertainty. The A_{LL} systematics include the relative luminosity uncertainty, polarization uncertainty, and trigger and reconstruction bias uncertainties. Tables 7.8 and 7.9 summarize the systematic errors on the dijet invariant mass for 2012, while Tables 7.10 and 7.11 do the same for 2013.

The polarization uncertainty is an overall scale uncertainty and represents the systematic uncertainty on the product of the two beam polarizations $P_B P_Y$. It is determined by the RHIC polarimetry group, based on the measurement uncertainties from the hydrogen gas jet and proton-Carbon polarimeters. The polarization uncertainty is 6.6% for 2012, and 6.4% for 2013 [66]. The relative luminosity is calculated based on differences between relative luminosity measurements made by the VPD and ZDC. The values were calculated during the corresponding inclusive jet analyses: 2.2×10^{-4} for 2012 and 4.7×10^{-4} for 2013. The polarization and relative luminosity uncertainties are both common to all data points.

7.6.1 Jet Energy Scale

The largest systematic error on the dijet mass is the jet energy scale uncertainty, which comes from the uncertainty in measuring the energy deposited in the BEMC and EEMC towers. Since neutral and charged particles both deposit energy in the towers, this error is composed of two pieces: uncertainties in the scale and status of the calorimeter towers, and uncertainties in the TPC track momentum and tower track response.

For the BEMC, the jet energy scale uncertainty on the dijet invariant mass is

$$\Delta M = \sqrt{(\Delta M_{neutral})^2 + (\Delta M_{track})^2} = \langle M \rangle \sqrt{(\Delta f_{neutral})^2 + (\Delta f_{track})^2}. \quad (7.7)$$

The BEMC neutral energy fractional uncertainty $\Delta f_{neutral}$ is due to the gain calibration uncertainty and the efficiency uncertainty:

$$\Delta f_{neutral} = R_t \times \sqrt{\Delta gain^2 + \Delta eff^2}, \quad (7.8)$$

where R_t is the average neutral energy fraction in a given invariant mass bin. The gain calibration uncertainty was estimated during the BEMC calibration process, and was 3.8% for 2012 and 5% for 2013. The efficiency uncertainty is 1% [67].

The fractional tracking uncertainty is an estimate of how well charged hadrons are measured in the TPC and BEMC:

$$\Delta f_{track} = (1 - R_t) \times \sqrt{\Delta f_{trk,p}^2 + \Delta f_{BEMC,nonph}^2}. \quad (7.9)$$

The TPC track momentum fractional uncertainty $\Delta f_{trk,p}$ is estimated at 1% [36] from the TPC calibration. The fractional uncertainty due to non-photonic hadrons is defined as:

$$\Delta f_{BEMC,nonph} = \left(\frac{S_{hadron}}{\epsilon_{track}} - f_{proj} \right) \times f_{nonph} \times \Delta f_{nonph}. \quad (7.10)$$

Here S_{hadron} is the scale-up factor for neutral hadrons, taken to be 1.1628 [68]; ϵ_{track} is the TPC tracking efficiency, estimated to be 81% [69]; and f_{proj} is the fraction of energy deposited in the projected tower by a track, estimated as 72% [70]. The BEMC response to non-photonic hadron energy f_{nonph} is 32%, with an uncertainty Δf_{nonph} of 6% [70]. Plugging in all the numbers, we have $\Delta f_{neutral} = 0.0393 \times R_t$ and $0.051 \times R_t$ for 2012 and 2013, respectively, and $\Delta f_{track} = 0.017 \times (1 - R_t)$.

The calculation of the jet energy scale uncertainty is different in the EEMC, because of the poor tracking efficiency. The uncertainty due to non-photon hadrons is estimated using the particle and detector level jet R_t at a pseudorapidity of about 1.3. The average R_t is 0.5 at particle level and 0.7 at detector level, and the tracking efficiency is about 10%, so we have a $0.5 \times 0.3 \times 0.1$ piece. The scale factor for hadrons is conservatively estimated as $1/(0.5 + 0.3 \times 0.5) = 1/0.65$, so the non-photon hadron uncertainty is taken to be $1/0.65 \times 0.5 \times 0.3 \times 0.1 = 0.023$. There are also terms for the tower status and scale uncertainties, which are estimated at 1% and 4.5%, respectively. The final value for the EEMC jet energy scale uncertainty is thus $\sqrt{0.023^2 + 0.01^2 + 0.045^2} = 0.0515$, and is not scaled by the neutral fraction. Final values for this uncertainty are listed in column 2 of Tables 7.8, 7.9, 7.10, and 7.11.

7.6.2 Tracking Efficiency Uncertainty

The uncertainty on the dijet invariant mass due to the TPC tracking efficiency is estimated by taking the difference of the average dijet mass shift from detector level to parton level for two samples of jets: jets reconstructed using the full set of TPC tracks, and jets reconstructed using a partial set of TPC tracks. The partial set of TPC tracks was chosen by randomly rejecting 7% of the reconstructed TPC tracks fed to the jet finding algorithm. Figure 7.19 shows the average dijet mass shifts from detector to parton level for the two sets of jets. The systematic is the bin-by-bin difference between the red and blue points. This systematic was only calculated for 2013, because the files with the 7% track loss jets were not readily available for 2012, and the effect would not be expected to differ significantly from one running period to the next. Thus, results from the 2013 analysis were used for both years. Final values are listed in column 3 of Tables 7.8, 7.9, 7.10, and 7.11.

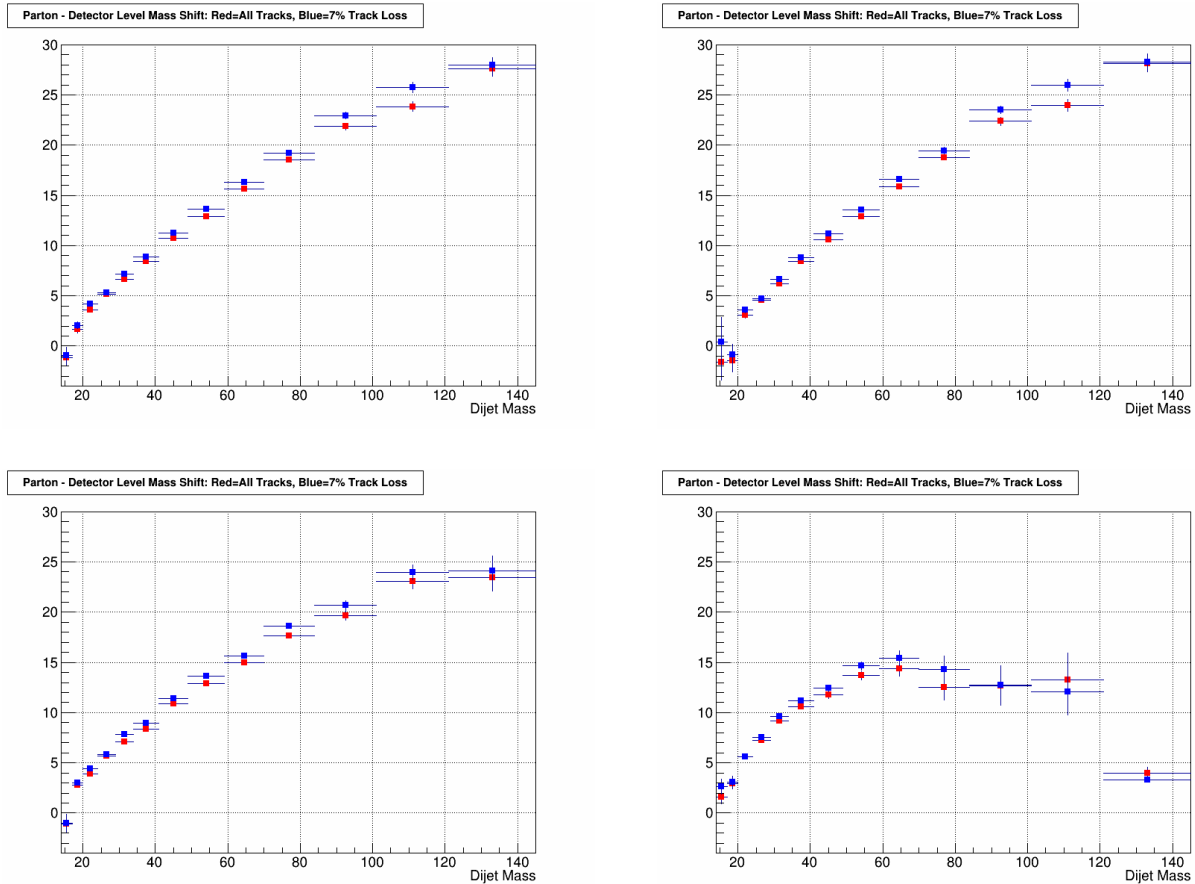


Figure 7.19: Average detector to parton level dijet invariant mass shifts, for jets reconstructed with full set of TPC tracks (red points) and a partial set of TPC tracks (blue points). Results for the Barrel-Endcap full topology are shown in the upper left; for East Barrel-Endcap in the upper right; for West Barrel-Endcap in the lower left; for Endcap-Endcap in the lower right.

7.6.3 Dijet Mass Shift Systematic

The errors on the dijet mass shift described in Section 7.5.1 are taken as one of the systematics on the dijet invariant mass. This error was calculated by adding in quadrature the trigger-fraction weighted errors for each trigger sample, and is represented by the error bars on the points in Figs. 7.9 and 7.10. Final values are given in column 4 of Tables 7.8, 7.9, 7.10, and 7.11.

7.6.4 Underlying Event Systematic Error on the Dijet Mass

The systematic error on the dijet mass due to the underlying event correction is taken to be the difference in underlying event contribution to the dijet invariant mass between data and simulation. Figures 7.20 and 7.21 show the change in dijet mass due to the underlying event correction for data and simulation. The systematic is the bin-by-bin difference between the red and blue points; values are listed in column 5 of Tables 7.8, 7.9, 7.10, and 7.11.

7.6.5 PYTHIA Tune Uncertainty

PYTHIA has a multitude of parameters which can be varied to fit the simulation to different data sets. There are many different “tune” sets available in PYTHIA, and the choice of tune is one of the systematic uncertainties on the dijet invariant mass calculation. To estimate this systematic, we utilize variants of Perugia2012 in PYTHIA6.4.28 and calculate dijet mass shift differences among them. The different tunes considered for the systematic are listed in Table 7.7; the PYTHIA tunes manual [59] contains more details.

Parton and particle level jets are reconstructed from the tunes using the same algorithm as the rest of the analysis, and the particle jets are matched to the parton jets. Then the mass shift $\Delta M = M_{parton} - M_{particle,UE}$, where $M_{particle,UE}$ is the dijet invariant mass at particle level after the underlying event subtraction, is calculated for each of the eight tunes.

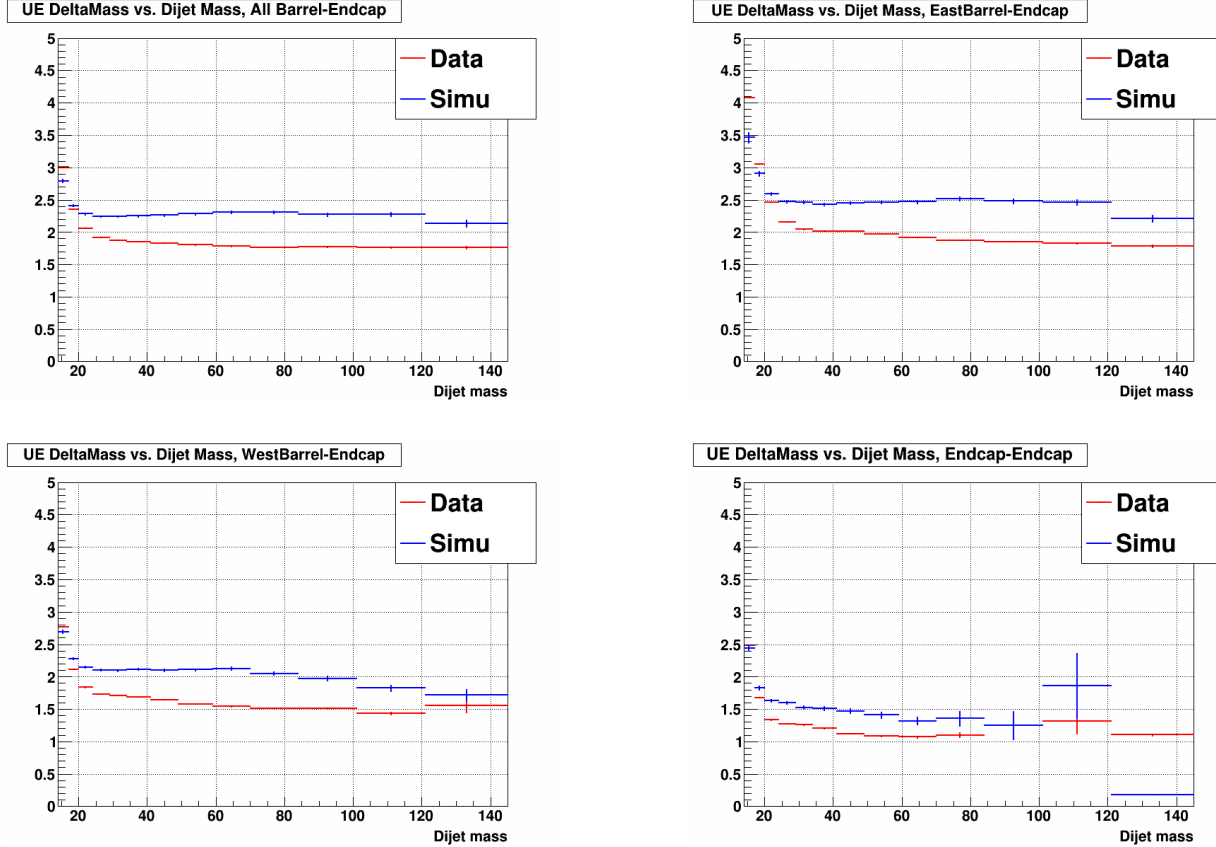


Figure 7.20: Change in dijet invariant mass due to underlying event correction for 2012 data (red) and simulation (blue). Results shown for Barrel-Endcap full (upper left), East Barrel-Endcap (upper right), West Barrel-Endcap (lower left), and Endcap-Endcap (lower right) topologies.

Tune number	Description
370	default
371	radHi, $\alpha_s(\frac{1}{2}p_{\perp})$ for ISR and FSR
372	radLo, $\alpha_s(p_{\perp})$ for ISR and FSR
374	loCR, less color reconnections
376	FL, more longitudinal fragmentation
377	FT, more transverse fragmentation
378	MSLO, MSTW 2008 LO PDFs
383	IBK, Innsbruck hadronization parameters

Table 7.7: The default Perugia2012 tune and some variants.

These mass shifts are shown in Fig. 7.22 for 2012 and Fig. 7.23 for 2013. The mass shifts used to calculate this systematic are between parton and particle level, rather than parton and detector level, because the generation of full embedding samples is too computationally

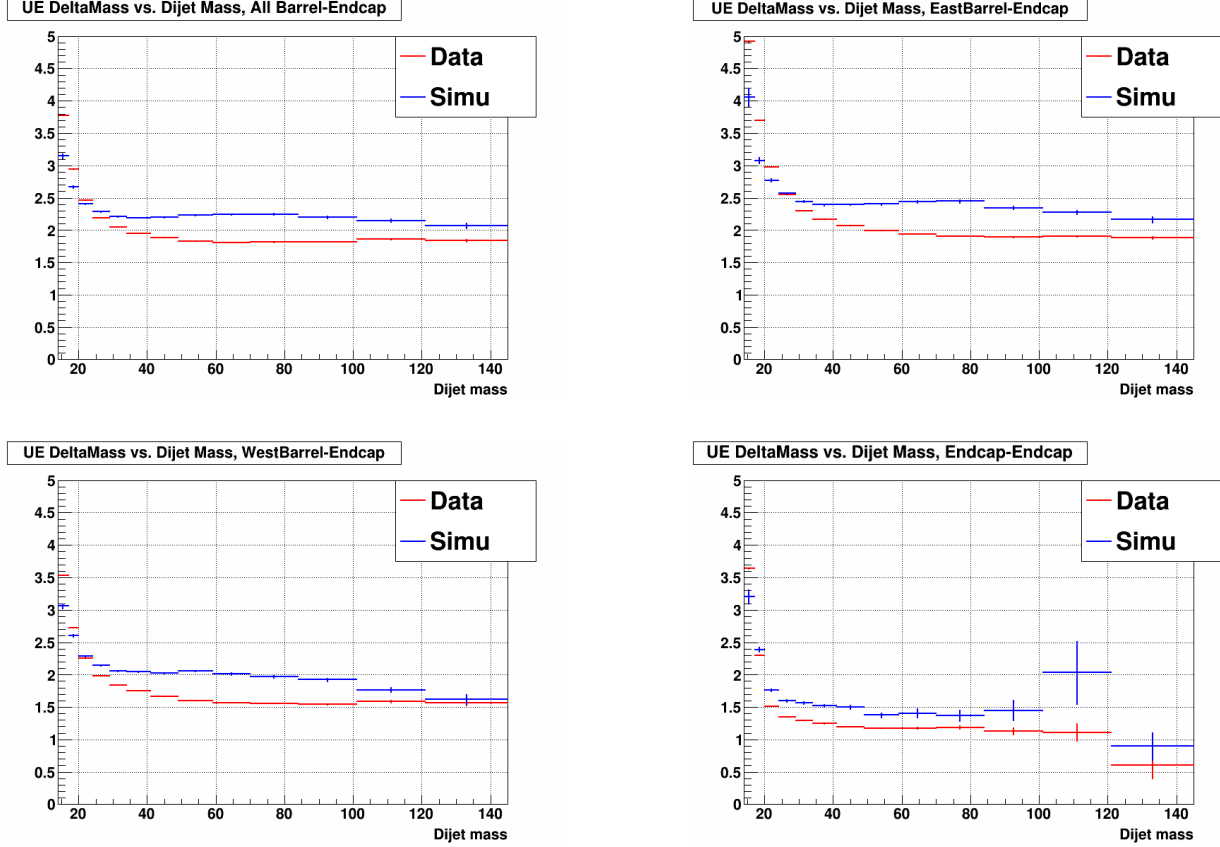


Figure 7.21: Change in dijet invariant mass due to underlying event correction for 2013 data (red) and simulation (blue). Results shown for Barrel-Endcap full (upper left), East Barrel-Endcap (upper right), West Barrel-Endcap (lower left), and Endcap-Endcap (lower right) topologies.

intensive to do for each variant, and the differences between particle and detector level are not expected to differ among the variants. The PYTHIA tune systematic uncertainty is calculated as:

$$\text{Uncertainty} = [(\Delta M_{370} - \Delta M_{374})^2 + (\Delta M_{370} - \Delta M_{378})^2 + (\Delta M_{370} - \Delta M_{383})^2 + ((\Delta M_{371} - \Delta M_{372})/2)^2 + ((\Delta M_{376} - \Delta M_{377})/2)^2]^{1/2}, \quad (7.11)$$

where ΔM_i is the mass shift for tune i . The pairs of tunes (371,372) and (376,377) are variations in the same set of parameters, so we take half the difference of their mass shifts for the term being added in quadrature, as opposed to comparing them to the default tune. Final values for the tune systematic are listed in column 6 of Tables 7.8, 7.9, 7.10, and 7.11.

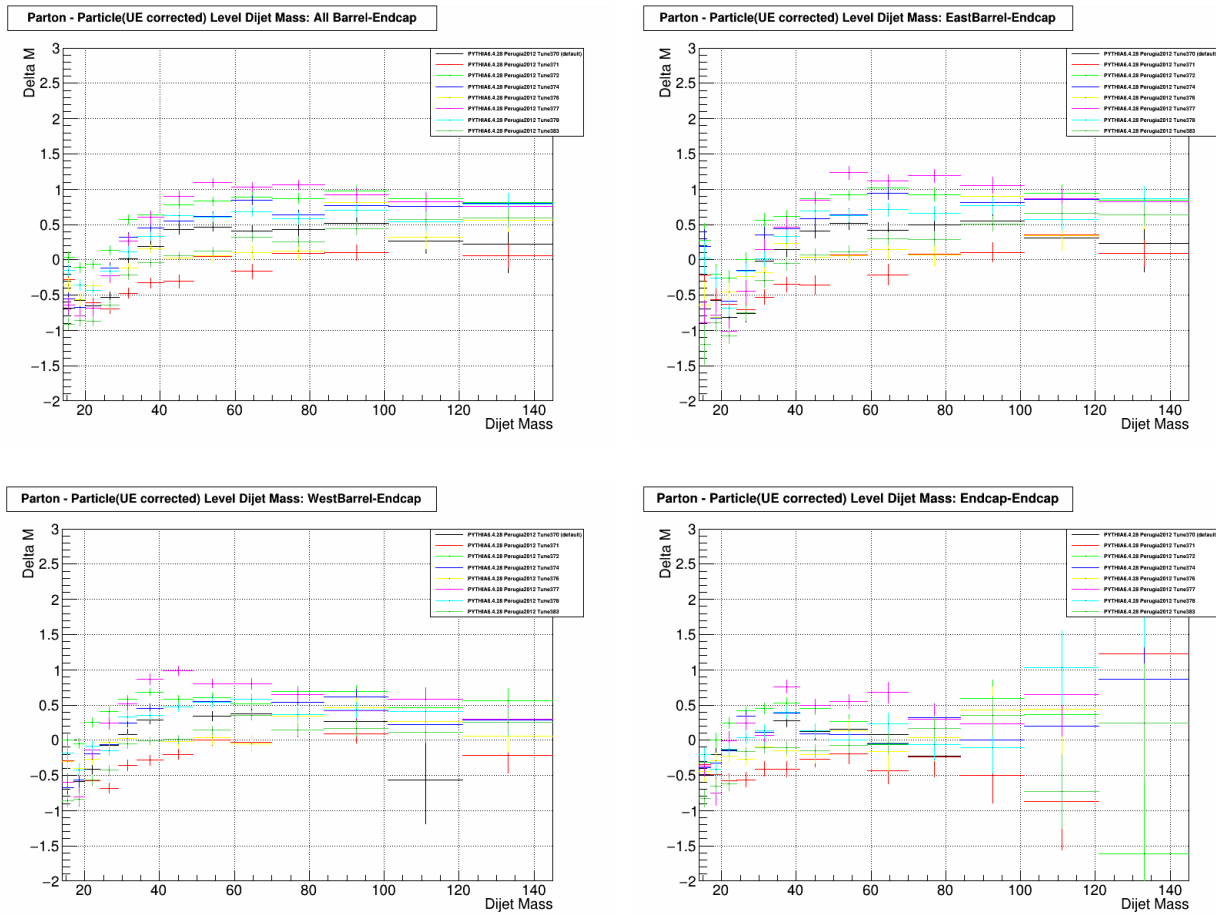


Figure 7.22: Dijet invariant mass shifts between parton and underlying event corrected particle level, for the various PYTHIA tunes in 2012. Results for the Barrel-Endcap full topology are shown in the upper left; for East Barrel-Endcap in the upper right; for West Barrel-Endcap in the lower left; for Endcap-Endcap in the lower right.

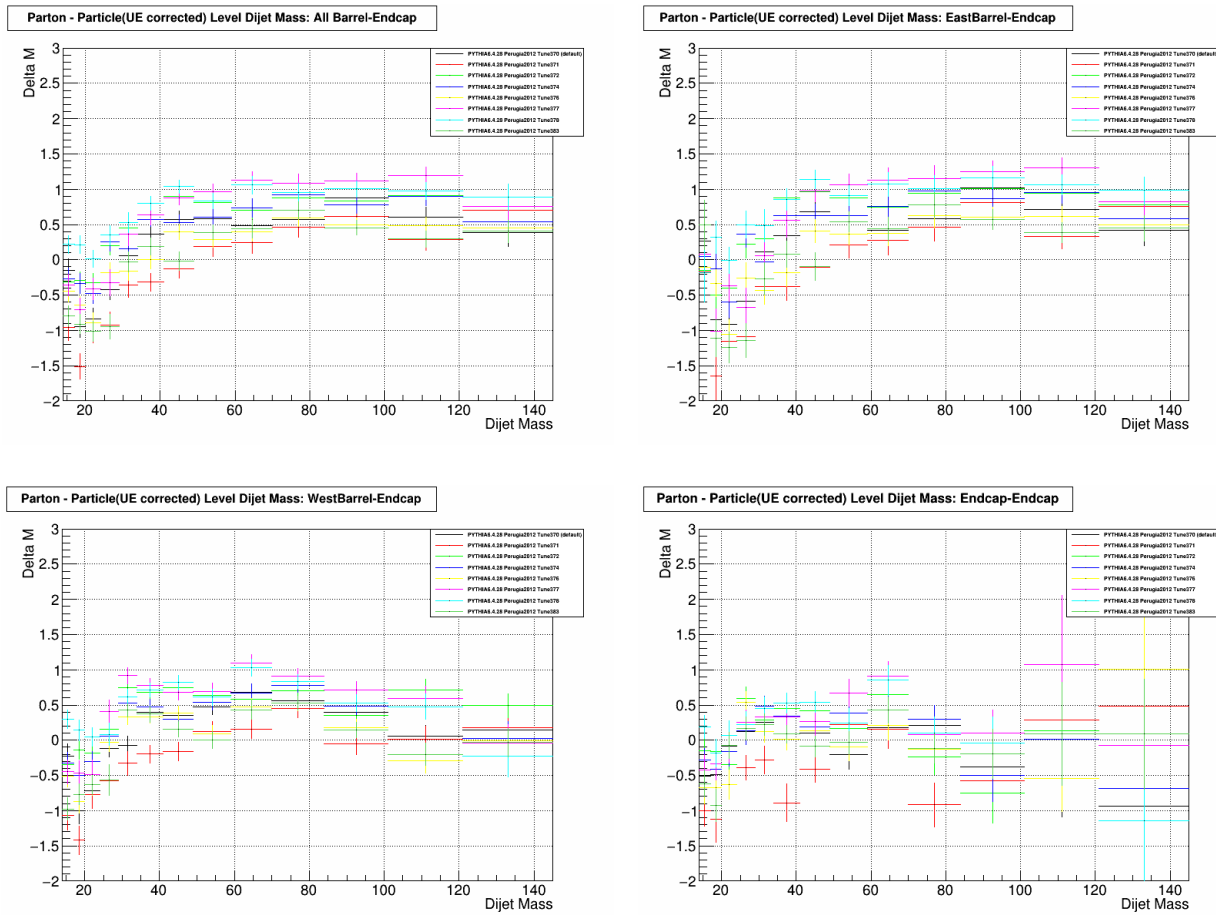


Figure 7.23: Dijet invariant mass shifts between parton and underlying event corrected particle level, for the various PYTHIA tunes in 2013. Results for the Barrel-Endcap full topology are shown in the upper left; for East Barrel-Endcap in the upper right; for West Barrel-Endcap in the lower left; for Endcap-Endcap in the lower right.

Barrel-Endcap Full Topology						
Bin	Jet Energy	Tracking	Mass Shift	UE Sys.	Tune	Total
1	0.457	0.192285	0.282	0.216043	0.630366	0.877144
2	0.544	0.416636	0.202	0.0586012	0.44898	0.845779
3	0.639	0.539662	0.156	0.223472	0.492328	1.00808
4	0.78	0.145739	0.138	0.322173	0.709262	1.12051
5	0.927	0.549701	0.146	0.377968	0.683038	1.33874
6	1.108	0.452041	0.151	0.39704	0.650436	1.42671
7	1.338	0.555368	0.17	0.429517	0.825528	1.73019
8	1.599	0.748186	0.173	0.483969	0.761654	1.99019
9	1.882	0.688238	0.215	0.527577	0.875786	2.2599
10	2.2	0.734282	0.265	0.541837	0.684248	2.49222
11	2.606	1.08493	0.319	0.503292	0.549761	2.93694
12	3.088	1.87679	0.518	0.516036	0.746225	3.76159
13	3.73	0.320956	0.738	0.36926	0.978471	3.95655

Endcap-Endcap						
Bin	Jet Energy	Tracking	Mass Shift	UE Sys.	Tune	Total
1	0.605	1.00573	0.365	0.0411312	0.45343	1.31074
2	0.71	0.144946	0.31	0.153851	0.604307	1.00502
3	0.858	0.0293716	0.357	0.297971	0.64207	1.16855
4	1.052	0.246515	0.254	0.331785	0.662777	1.33467
5	1.299	0.425719	0.312	0.265884	0.48837	1.50837
6	1.529	0.560516	0.317	0.308651	0.772382	1.8559
7	1.807	0.667791	0.394	0.350361	0.575458	2.07854
8	2.114	0.965138	0.47	0.322388	0.419833	2.42932
9	2.497	1.02695	0.643	0.247778	0.516646	2.83397
10	2.93	1.80486	1.536	0.25174	0.761054	3.85283
11	3.396	0.0277368	1.861	0.0032732	6.4683	7.53895
12	4.284	-1.16601	6.034	0.542225	1.42098	7.64425
13	4.509	-0.676858	0	0.92778	2.71882	5.38906

Table 7.8: Dijet invariant mass systematics for the Barrel-Endcap and Endcap-Endcap topologies, 2012.

East Barrel-Endcap						
Bin	Jet Energy	Tracking	Mass Shift	UE Sys.	Tune	Total
1	0.448	2.00734	0.673	0.618896	1.27984	2.58922
2	0.551	0.566649	0.431	0.145284	0.546148	1.06294
3	0.634	0.525728	0.328	0.127924	0.500606	1.02611
4	0.781	0.123451	0.224	0.31611	0.933242	1.28306
5	0.92	0.403956	0.241	0.418857	0.73551	1.33569
6	1.1	0.389842	0.242	0.408921	0.640381	1.41345
7	1.344	0.551435	0.267	0.433093	0.874416	1.77028
8	1.616	0.735813	0.244	0.492263	0.845399	2.04192
9	1.898	0.694646	0.307	0.551951	0.996072	2.34008
10	2.224	0.674612	0.355	0.640191	0.767026	2.5545
11	2.628	1.12049	0.402	0.627102	0.585601	3.00993
12	3.091	2.0114	0.605	0.631781	0.806522	3.875
13	3.751	0.173905	0.802	0.425094	1.05512	4.00468

West Barrel-Endcap						
Bin	Jet Energy	Tracking	Mass Shift	UE Sys.	Tune	Total
1	0.458	0.0767508	0.302	0.0742246	0.570015	0.798301
2	0.542	0.275246	0.227	0.171479	0.44391	0.804683
3	0.643	0.535845	0.155	0.313317	0.592786	1.08359
4	0.779	0.140677	0.176	0.378582	0.668925	1.11731
5	0.933	0.726649	0.164	0.392826	0.629736	1.4058
6	1.117	0.540134	0.181	0.421869	0.736658	1.51421
7	1.331	0.56656	0.216	0.461942	0.787958	1.72438
8	1.577	0.774373	0.241	0.527787	0.602867	1.94594
9	1.855	0.673045	0.258	0.58759	0.592497	2.15798
10	2.147	0.947268	0.346	0.533449	0.553349	2.49347
11	2.542	0.995407	0.443	0.467267	0.50149	2.84933
12	3.073	0.886418	0.645	0.390617	1.44713	3.59052
13	3.561	0.725867	1.835	0.157412	5.55762	6.89106

Table 7.9: Dijet invariant mass systematics for the two Barrel-Endcap topologies, 2012.

Barrel-Endcap Full Topology						
Bin	Jet Energy	Tracking	Mass Shift	UE Sys.	Tune	Total
1	0.443	0.192285	0.999	0.629181	0.818023	1.51534
2	0.555	0.416636	0.6	0.270822	1.44554	1.73336
3	0.698	0.539662	0.259	0.0574445	1.02544	1.37853
4	0.842	0.145739	0.391	0.092324	1.28089	1.59132
5	1.001	0.549701	0.303	0.167421	0.691291	1.37909
6	1.176	0.452041	0.34	0.242991	0.828722	1.56485
7	1.406	0.555368	0.327	0.314632	0.942313	1.83825
8	1.664	0.748186	0.417	0.397428	0.55725	1.99275
9	1.968	0.688238	0.554	0.432108	0.757784	2.32692
10	2.32	0.734282	0.683	0.435705	0.620634	2.63877
11	2.763	1.08493	0.665	0.377128	0.559942	3.11596
12	3.297	1.87679	0.521	0.290707	0.735311	3.91014
13	3.906	0.320956	0.601	0.230693	0.546669	4.00913

Endcap-Endcap						
Bin	Jet Energy	Tracking	Mass Shift	UE Sys.	Tune	Total
1	0.567	1.00573	1.002	0.429023	0.868858	1.80996
2	0.634	0.144946	0.842	0.0888235	0.737377	1.29751
3	0.837	0.0293716	0.27	0.248644	0.329389	0.971932
4	1.03	0.246515	0.339	0.253385	0.526799	1.25631
5	1.232	0.425719	0.753	0.26629	0.422577	1.58605
6	1.509	0.560516	0.447	0.280649	0.75598	1.85508
7	1.799	0.667791	0.487	0.30321	0.64628	2.10455
8	2.148	0.965138	0.437	0.204435	0.856077	2.55167
9	2.521	1.02695	0.643	0.229567	0.881488	2.94164
10	2.933	1.80486	0.874	0.180659	0.500528	3.59264
11	3.509	0.0277368	1.588	0.316913	0.413659	3.88679
12	4.104	-1.16601	2.468	0.924976	2.41913	5.56787
13	4.527	-0.676858	0.782	0.291269	3.19635	5.6449

Table 7.10: Dijet invariant mass systematics for the Barrel-Endcap and Endcap-Endcap topologies, 2013.

East Barrel-Endcap						
Bin	Jet Energy	Tracking	Mass Shift	UE Sys.	Tune	Total
1	0.426	2.00734	1.256	0.862923	0.548698	2.61422
2	0.498	0.566649	1.506	0.617986	1.54897	2.37031
3	0.702	0.525728	0.434	0.20215	1.13256	1.51033
4	0.842	0.123451	0.594	0.017265	1.6855	1.97946
5	1.005	0.403956	0.449	0.142866	0.689098	1.36751
6	1.197	0.389842	0.498	0.228189	0.966977	1.67926
7	1.418	0.551435	0.422	0.324772	1.08997	1.94587
8	1.679	0.735813	0.586	0.414544	0.570415	2.04965
9	1.987	0.694646	0.748	0.503627	0.85434	2.44412
10	2.326	0.674612	0.869	0.536326	0.711798	2.72302
11	2.78	1.12049	0.924	0.45274	0.600906	3.22548
12	3.304	2.0114	0.589	0.372724	0.70433	3.993
13	3.93	0.173905	0.649	0.284456	0.616103	4.04436

West Barrel-Endcap						
Bin	Jet Energy	Tracking	Mass Shift	UE Sys.	Tune	Total
1	0.445	0.0767508	1.093	0.476829	0.987825	1.61299
2	0.575	0.275246	0.475	0.122325	1.44291	1.65196
3	0.697	0.535845	0.325	0.0341714	0.930316	1.32107
4	0.841	0.140677	0.56	0.160032	0.668954	1.23036
5	0.997	0.726649	0.37	0.218732	1.21244	1.78235
6	1.154	0.540134	0.336	0.298314	0.59439	1.47602
7	1.389	0.56656	0.603	0.362265	0.699345	1.7984
8	1.644	0.774373	0.398	0.454998	0.63181	2.01668
9	1.93	0.673045	0.758	0.447791	0.570656	2.29752
10	2.306	0.947268	0.476	0.414412	0.42985	2.6073
11	2.716	0.995407	0.453	0.37635	0.4485	2.98588
12	3.256	0.886418	0.714	0.175746	0.922566	3.57478
13	3.705	0.725867	1.587	0.051442	0.455734	4.12102

Table 7.11: Dijet invariant mass systematics for the two Barrel-Endcap topologies, 2013.

7.7 Final Results

The final results for the dijet A_{LL} as a function of parton level dijet invariant mass are shown in Figs. 7.24, 7.25, and 7.26 for 2012 and Figs. 7.27, 7.28, and 7.29 for 2013. The final measured values for the points and their systematics are listed in Tables 7.12 and 7.13 for 2012, and Tables 7.14 and 7.15 for 2013. In the plots, the heights of the green uncertainty boxes represent the trigger and reconstruction bias systematic errors, while the widths represent the total systematic error on the dijet invariant mass. The total systematic error on the dijet mass was calculated by taking the square root of the quadrature sum of the jet energy scale, tracking efficiency, invariant mass shift, underlying event, and PYTHIA tune uncertainties. The relative luminosity uncertainty is a scaling uncertainty common to all points, and is represented by a gray band on the horizontal axis which is not easily visible due to its small size. The error bars on the points are the statistical uncertainties. The figures also include theoretical predictions for dijet A_{LL} obtained using the DSSV2014 [28] and NNPDFpol1.1 [29] polarized PDF sets from global fits to existing data.

The results from 2012 and 2013 are independent measurements of the same observable, made under similar running conditions, so we can combine them into a single result for the EEMC dijet A_{LL} at $\sqrt{s} = 510$ GeV. The A_{LL} , statistical uncertainties on A_{LL} , and systematic uncertainties on A_{LL} were combined as follows:

$$A_{LL,combined} = \frac{\sum_i w_i \times A_{LL,i}}{\sum_i w_i} \quad (7.12a)$$

$$\Delta A_{LL}^{stat} = \sqrt{\frac{1}{\sum_i w_i}} \quad (7.12b)$$

$$\Delta A_{LL}^{sys} = \frac{\sum_i w_i \times A_{LL,i}^{sys}}{\sum_i w_i}, \quad (7.12c)$$

where $w_i \equiv 1/(\Delta A_{LL,i}^{stat})^2$ and the sums i run over the two data sets. The dijet invariant mass points and their systematic errors were combined in the same way as the A_{LL} points

and their systematic errors. Figures 7.30, 7.31, and 7.32 show the combined results, with the final values for the points and their systematics given in Tables 7.16 and 7.17. The combined results generally show good agreement with current theoretical predictions, while suggesting a larger A_{LL} for dijets with the East Barrel-Endcap topology. The physics implications of the combined results will be discussed in the next Chapter.

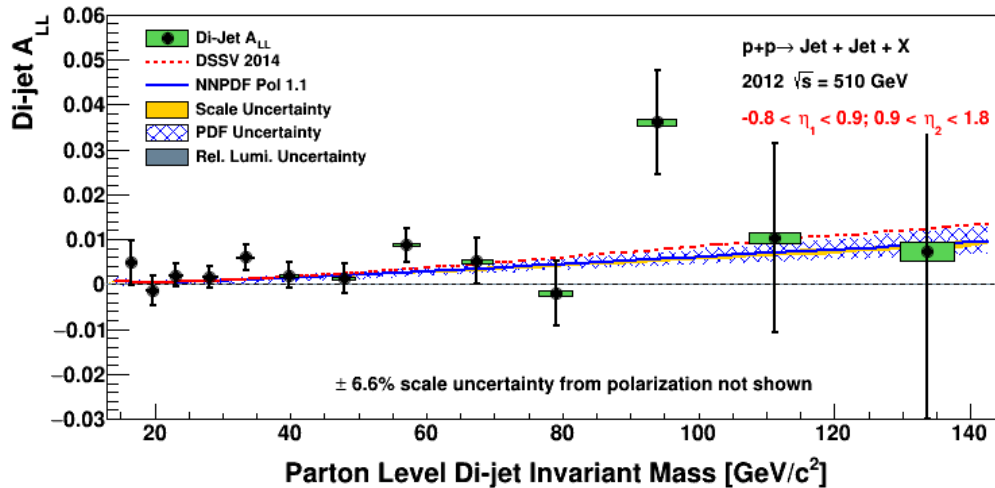


Figure 7.24: Dijet A_{LL} versus parton-level dijet invariant mass for the Barrel-Endcap full topology in 2012.

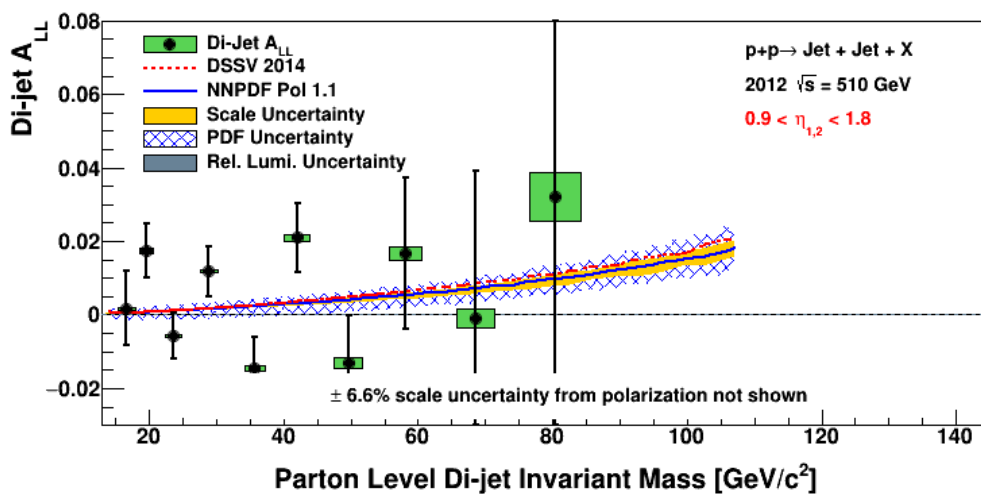


Figure 7.25: Dijet A_{LL} versus parton-level dijet invariant mass for the Endcap-Endcap topology in 2012.

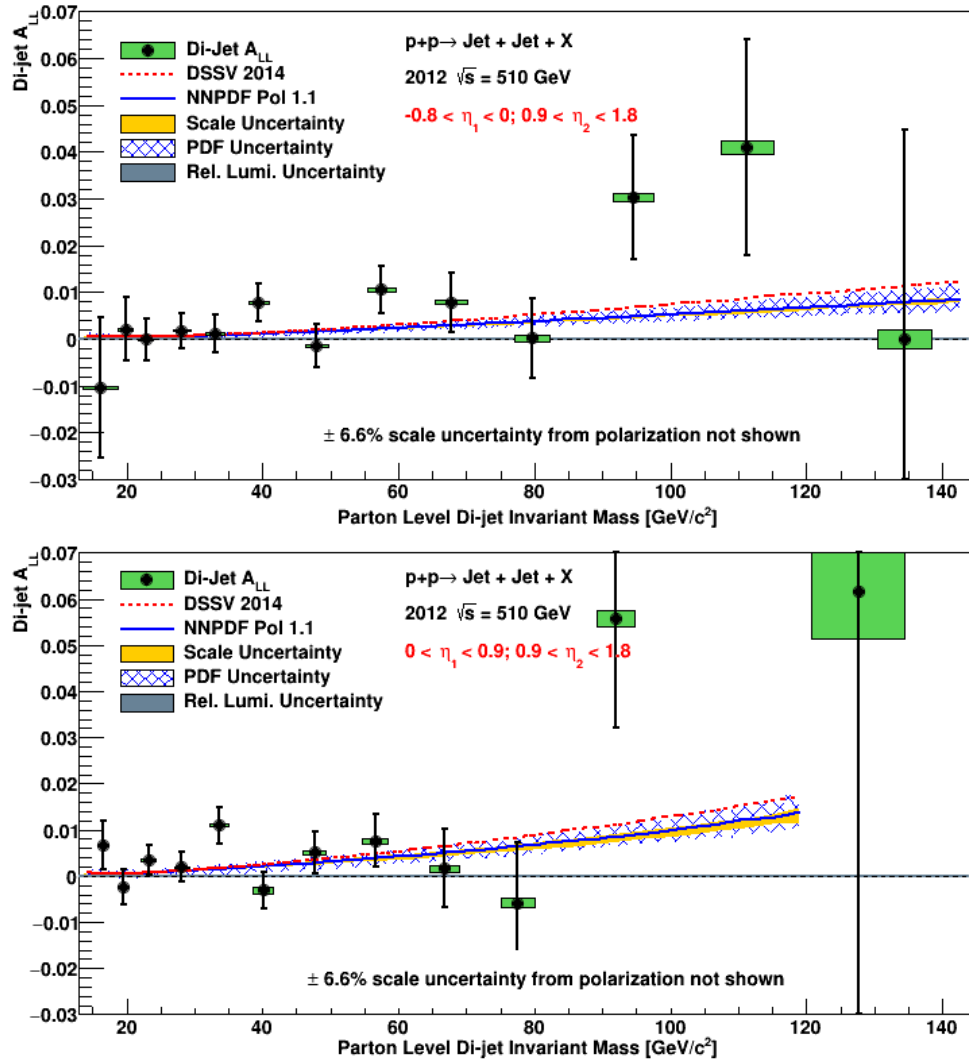


Figure 7.26: Dijet A_{LL} versus parton-level dijet invariant mass for the East Barrel-Endcap (upper plot) and West Barrel-Endcap (lower plot) topologies in 2012.

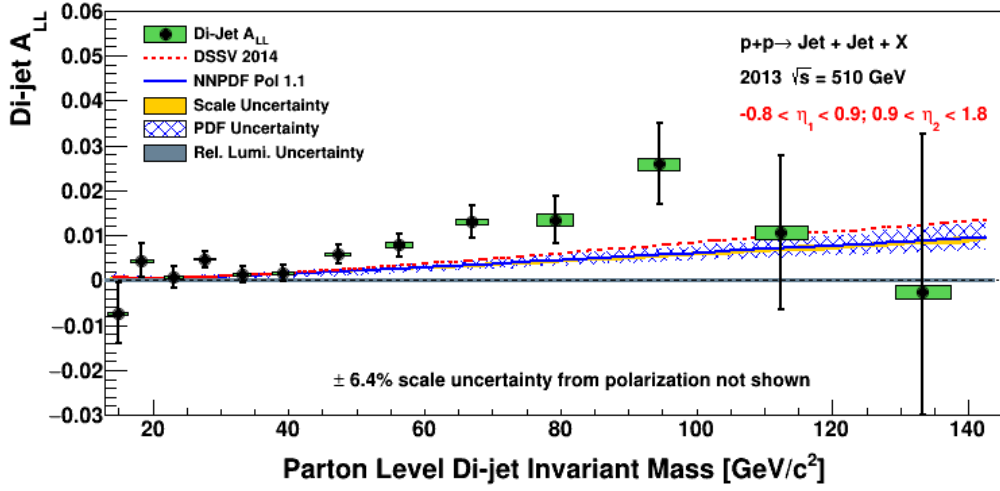


Figure 7.27: Dijet A_{LL} versus parton-level dijet invariant mass for the Barrel-Endcap full topology in 2013.

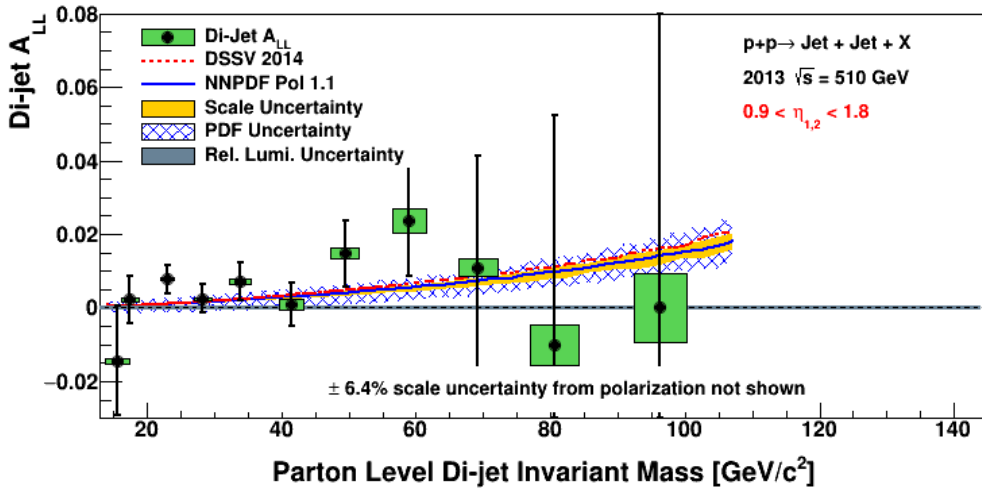


Figure 7.28: Dijet A_{LL} versus parton-level dijet invariant mass for the Endcap-Endcap topology in 2013.

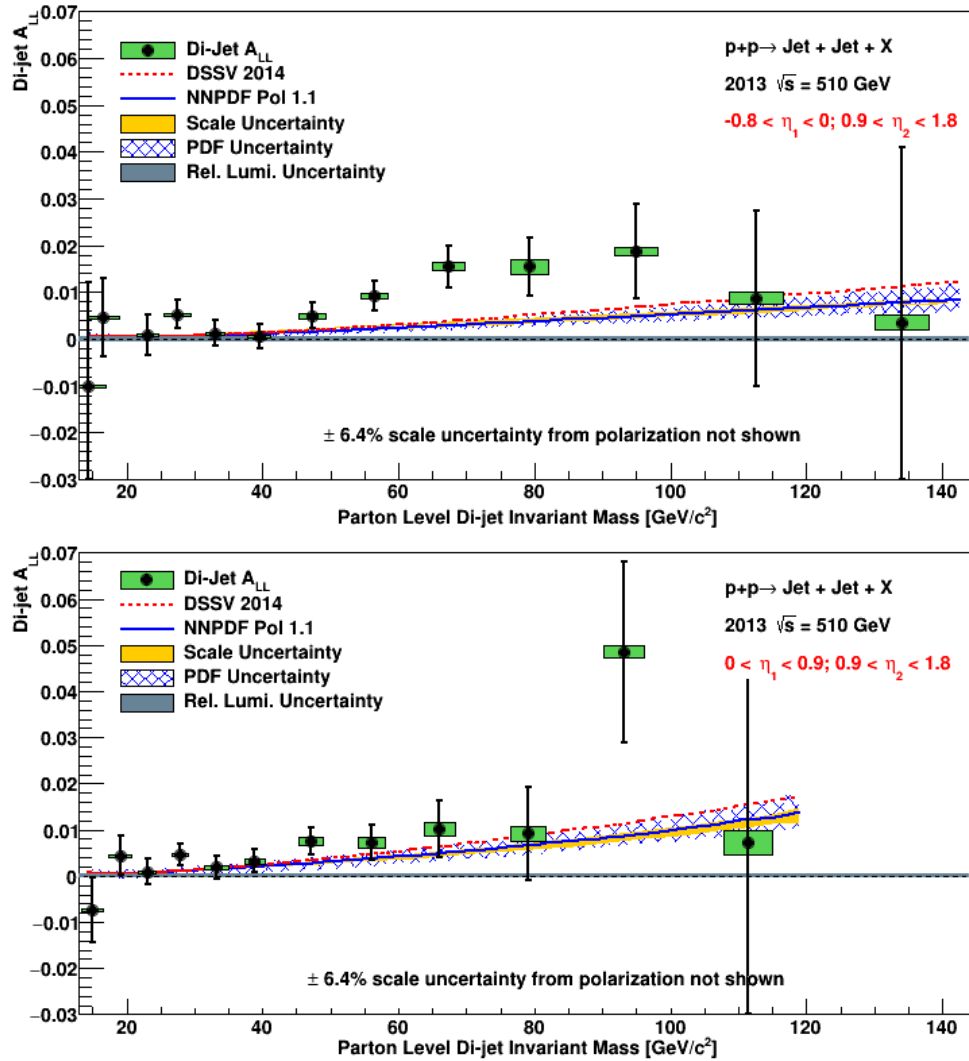


Figure 7.29: Dijet A_{LL} versus parton-level dijet invariant mass for the East Barrel-Endcap (upper plot) and West Barrel-Endcap (lower plot) topologies in 2013.

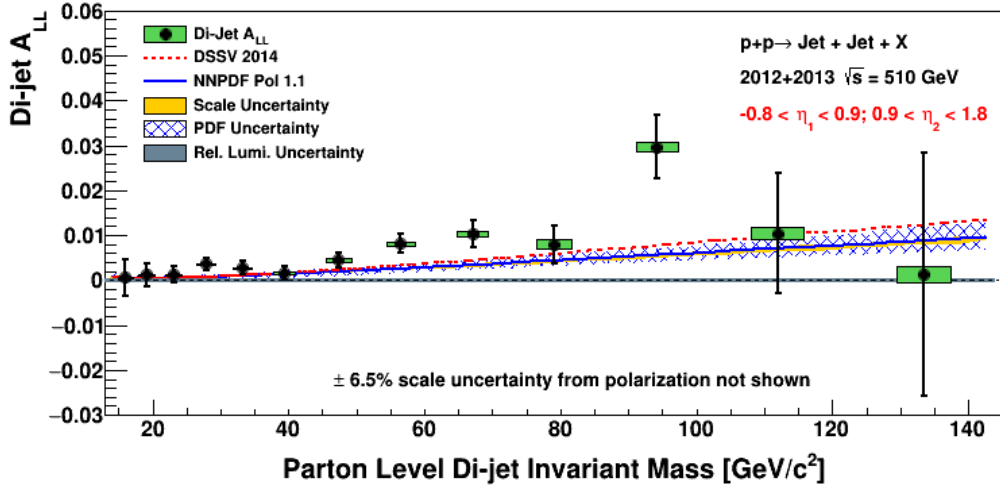


Figure 7.30: Dijet A_{LL} versus parton-level dijet invariant mass for the Barrel-Endcap full topology for the combined 2012+2013 sample.

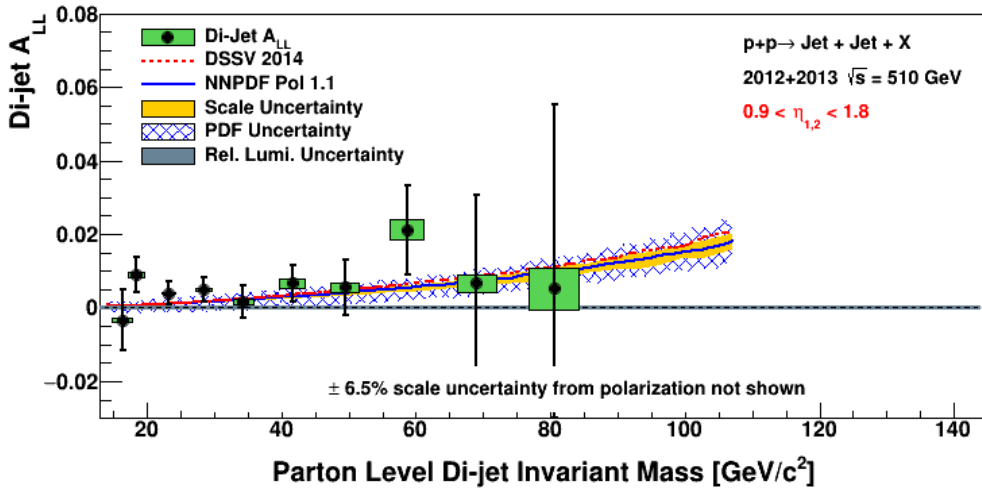


Figure 7.31: Dijet A_{LL} versus parton-level dijet invariant mass for the Endcap-Endcap topology for the combined 2012+2013 sample.

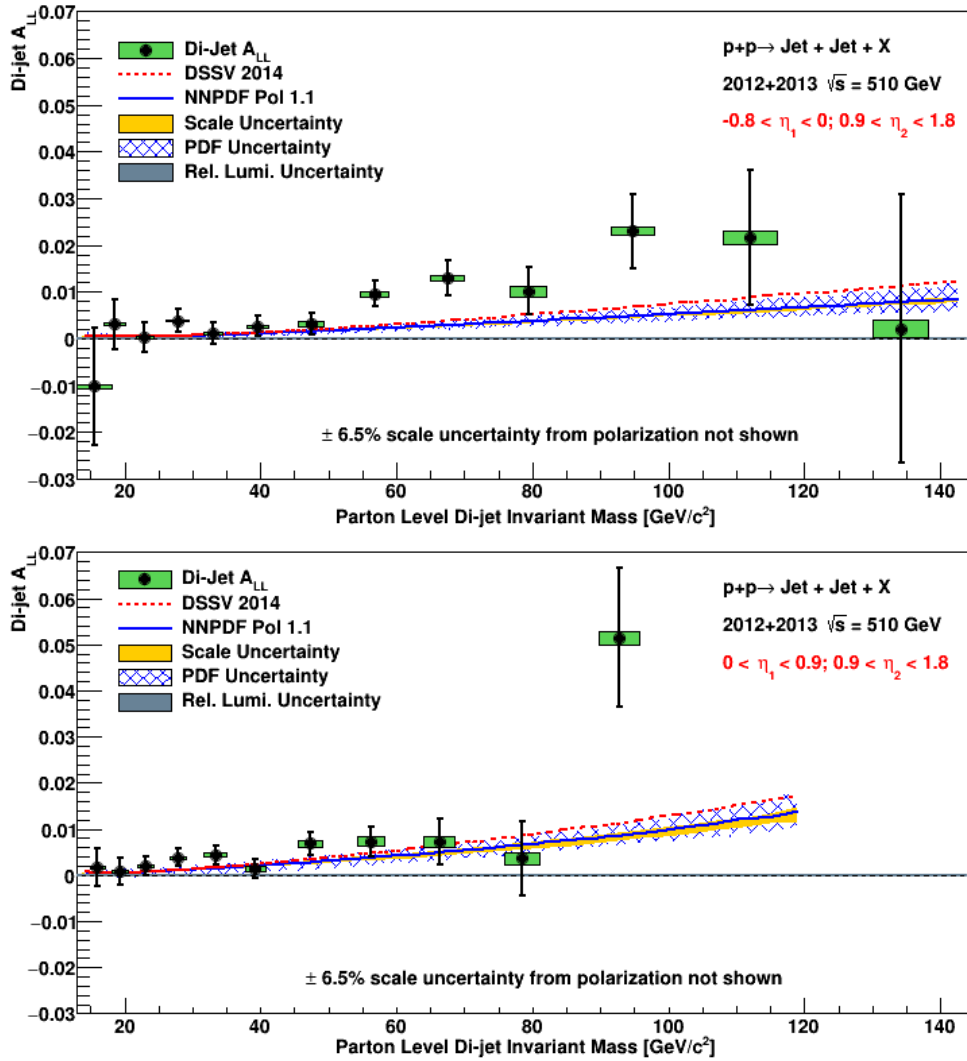


Figure 7.32: Dijet A_{LL} versus parton-level dijet invariant mass for the East Barrel-Endcap (upper plot) and West Barrel-Endcap (lower plot) topologies for the combined 2012+2013 sample.

Barrel-Endcap Full Topology					
Bin	Dijet Mass (GeV)		A_{LL}		
	Mass	Sys. Error	A_{LL}	Stat. Error	Sys. Error
1	16.516	0.877	0.004784	0.004936	0.00016
2	19.616	0.846	-0.00138	0.003356	0.00015
3	23.024	1.008	0.002	0.002606	0.00014
4	28.073	1.121	0.001649	0.00245	0.00014
5	33.34	1.339	0.00599	0.002814	0.00017
6	39.774	1.427	0.001939	0.002836	0.0004
7	47.802	1.73	0.001249	0.00325	0.00026
8	57.085	1.99	0.008789	0.003763	0.00031
9	67.374	2.26	0.005133	0.005109	0.0004
10	79.014	2.492	-0.002007	0.007178	0.00055
11	93.859	2.937	0.036059	0.011612	0.00078
12	111.181	3.762	0.010262	0.020998	0.00128
13	133.64	3.957	0.007281	0.042519	0.00221

Endcap-Endcap					
Bin	Dijet Mass (GeV)		A_{LL}		
	Mass	Sys. Error	A_{LL}	Stat. Error	Sys. Error
1	16.613	1.311	0.001759	0.010071	0.0004
2	19.494	1.005	0.017387	0.007223	0.00064
3	23.564	1.169	-0.005683	0.006152	0.00024
4	28.868	1.335	0.011768	0.006748	0.00038
5	35.66	1.508	-0.014525	0.008589	0.00068
6	41.961	1.856	0.021021	0.009351	0.00088
7	49.612	2.079	-0.012981	0.012796	0.0014
8	58.023	2.429	0.016684	0.020439	0.00194
9	68.55	2.834	-0.001061	0.040014	0.00262
10	80.419	3.853	0.032179	0.082854	0.00653
11	93.213	7.539	0.225632	0.218932	0.00927
12	117.584	7.644	0.117254	0.811721	0.00211
13	123.77	5.389	-3.12721	2.16606	0

Table 7.12: Final dijet A_{LL} for the Barrel-Endcap and Endcap-Endcap topologies, 2012.

East Barrel-Endcap					
Bin	Dijet Mass (GeV)		A_{LL}		
	Mass	Sys. Error	A_{LL}	Stat. Error	Sys. Error
1	16.164	2.589	-0.010354	0.015048	0.00033
2	19.828	1.063	0.002064	0.006817	0.00028
3	22.776	1.026	-0.000141	0.004364	0.00016
4	28.053	1.283	0.001796	0.003701	0.0002
5	33.043	1.336	0.001165	0.004056	0.00019
6	39.446	1.413	0.007852	0.004047	0.00031
7	47.98	1.77	-0.001536	0.004561	0.00029
8	57.497	2.042	0.010553	0.005009	0.00038
9	67.733	2.34	0.007851	0.006405	0.00047
10	79.697	2.555	0.000161	0.008585	0.00063
11	94.495	3.01	0.030194	0.013322	0.00088
12	111.208	3.875	0.040936	0.022981	0.00141
13	134.388	4.005	-0.000105	0.044739	0.00204

West Barrel-Endcap					
Bin	Dijet Mass (GeV)		A_{LL}		
	Mass	Sys. Error	A_{LL}	Stat. Error	Sys. Error
1	16.568	0.798	0.006633	0.005225	0.00017
2	19.566	0.805	-0.002338	0.003856	0.00017
3	23.181	1.084	0.003418	0.003248	0.00019
4	28.096	1.117	0.001948	0.003269	0.00018
5	33.622	1.406	0.010949	0.003906	0.00027
6	40.097	1.514	-0.003064	0.003975	0.0007
7	47.635	1.724	0.005075	0.004631	0.00044
8	56.538	1.946	0.007634	0.0057	0.00052
9	66.76	2.158	0.001629	0.00847	0.00074
10	77.494	2.493	-0.005764	0.013082	0.00107
11	91.956	2.849	0.055758	0.023691	0.00165
12	111.054	3.591	-0.14651	0.051676	0.00279
13	127.604	6.891	0.061632	0.136679	0.01034

Table 7.13: Final dijet A_{LL} for the two Barrel-Endcap topologies, 2012.

Barrel-Endcap Full Topology					
Bin	Dijet Mass (GeV)		A_{LL}		
	Mass	Sys. Error	A_{LL}	Stat. Error	Sys. Error
1	14.859	1.515	-0.007396	0.006763	0.00034
2	18.39	1.733	0.004353	0.003735	0.00025
3	23.017	1.379	0.000694	0.002353	0.00018
4	27.718	1.591	0.004659	0.001833	0.00018
5	33.099	1.379	0.001276	0.001846	0.00022
6	39.178	1.565	0.001594	0.001756	0.00029
7	47.209	1.838	0.005817	0.002048	0.00043
8	56.258	1.993	0.00785	0.002522	0.00054
9	66.896	2.327	0.013082	0.003637	0.00067
10	79.197	2.639	0.01344	0.005327	0.00132
11	94.436	3.116	0.025846	0.008996	0.00129
12	112.479	3.91	0.01057	0.017205	0.00143
13	133.306	4.009	-0.002641	0.035162	0.00159

Endcap-Endcap					
Bin	Dijet Mass (GeV)		A_{LL}		
	Mass	Sys. Error	A_{LL}	Stat. Error	Sys. Error
1	15.567	1.81	-0.014473	0.014907	0.00069
2	17.405	1.298	0.002231	0.006505	0.0006
3	22.973	0.972	0.007849	0.003876	0.00034
4	28.277	1.256	0.002545	0.003889	0.00037
5	33.821	1.586	0.007164	0.004975	0.00078
6	41.412	1.855	0.000948	0.005922	0.00137
7	49.375	2.105	0.014793	0.009056	0.00136
8	58.963	2.552	0.023733	0.015024	0.0033
9	69.197	2.942	0.010962	0.030173	0.00239
10	80.504	3.593	-0.010118	0.062529	0.00534
11	96.31	3.887	-1e-05	0.172146	0.00927
12	112.644	5.568	0.331603	0.499346	0.10707
13	124.269	5.645	-1.60889	1.49604	0.03318

Table 7.14: Final dijet A_{LL} for the Barrel-Endcap and Endcap-Endcap topologies, 2013.

East Barrel-Endcap					
Bin	Dijet Mass (GeV)		A_{LL}		
	Mass	Sys. Error	A_{LL}	Stat. Error	Sys. Error
1	14.311	2.614	-0.009999	0.022199	0.00028
2	16.532	2.37	0.004525	0.008355	0.00032
3	23.071	1.51	0.000814	0.004424	0.0003
4	27.529	1.979	0.005227	0.003044	0.0002
5	32.952	1.368	0.00121	0.002808	0.00027
6	39.512	1.679	0.000591	0.002532	0.00034
7	47.249	1.946	0.004987	0.002813	0.00054
8	56.411	2.05	0.00924	0.00329	0.00066
9	67.314	2.444	0.015518	0.004503	0.0008
10	79.259	2.723	0.01544	0.006271	0.00147
11	94.905	3.225	0.018772	0.010119	0.00084
12	112.636	3.993	0.008693	0.018782	0.00131
13	134.028	4.044	0.00359	0.037495	0.00167

West Barrel-Endcap					
Bin	Dijet Mass (GeV)		A_{LL}		
	Mass	Sys. Error	A_{LL}	Stat. Error	Sys. Error
1	14.91	1.613	-0.007382	0.007101	0.00036
2	19.063	1.652	0.004422	0.004175	0.0003
3	22.998	1.321	0.000875	0.002779	0.0002
4	27.84	1.23	0.004727	0.002296	0.0003
5	33.234	1.782	0.001859	0.002449	0.00039
6	38.84	1.476	0.003226	0.002439	0.00052
7	47.117	1.798	0.007556	0.002988	0.00078
8	56.053	2.017	0.007263	0.003927	0.00121
9	66.028	2.298	0.010198	0.006168	0.00144
10	79.054	2.607	0.009195	0.010098	0.00154
11	93.218	2.986	0.048558	0.019646	0.00132
12	111.439	3.575	0.007179	0.042899	0.0026
13	127.031	4.121	-0.099469	0.101248	0.00532

Table 7.15: Final dijet A_{LL} for the two Barrel-Endcap topologies, 2013.

Barrel-Endcap Full Topology					
Bin	Dijet Mass (GeV)		A_{LL}		
	Mass	Sys. Error	A_{LL}	Stat. Error	Sys. Error
1	15.9401	1.09874	0.000551	0.003987	0.000223
2	19.0683	1.24223	0.001181	0.002496	0.000195
3	23.0201	1.21238	0.001281	0.001746	0.000162
4	27.8454	1.42233	0.003579	0.001468	0.000166
5	33.1715	1.36697	0.002694	0.001544	0.000205
6	39.3432	1.52675	0.00169	0.001493	0.00032
7	47.3775	1.8073	0.004519	0.001733	0.000382
8	56.5143	1.99207	0.008141	0.002095	0.000469
9	67.0568	2.30447	0.010409	0.002963	0.000579
10	79.132	2.58679	0.007954	0.004278	0.001047
11	94.2196	3.04886	0.029677	0.007112	0.001099
12	111.958	3.85055	0.010446	0.013308	0.00137
13	133.442	3.98788	0.001389	0.027097	0.001842

Endcap-Endcap					
Bin	Dijet Mass (GeV)		A_{LL}		
	Mass	Sys. Error	A_{LL}	Stat. Error	Sys. Error
1	16.2852	1.46738	-0.003328	0.008345	0.000491
2	18.3405	1.16678	0.009018	0.004834	0.000618
3	23.1409	1.02798	0.004004	0.003279	0.000312
4	28.4244	1.2757	0.004845	0.003369	0.000372
5	34.283	1.56641	0.001715	0.004305	0.000755
6	41.5692	1.85529	0.006694	0.005003	0.00123
7	49.4541	2.09632	0.005524	0.007392	0.001373
8	58.6333	2.50885	0.02126	0.012105	0.002823
9	68.9625	2.90285	0.006604	0.024091	0.002473
10	80.4732	3.68735	0.005231	0.049911	0.005772
11	95.1268	5.28226	0.086198	0.135323	0.00927
12	114	6.13794	0.272756	0.425313	0.078254
13	124.108	5.56232	-2.09925	1.23097	0.022464

Table 7.16: Final dijet A_{LL} for the Barrel-Endcap and Endcap-Endcap topologies, 2012+2013.

East Barrel-Endcap					
Bin	Dijet Mass (GeV)		A_{LL}		
	Mass	Sys. Error	A_{LL}	Stat. Error	Sys. Error
1	15.5806	2.59687	-0.010242	0.012456	0.000314
2	18.5107	1.58536	0.003048	0.005282	0.000296
3	22.9215	1.2647	0.00033	0.003107	0.000229
4	27.7404	1.69816	0.003843	0.002351	0.0002
5	32.9815	1.35763	0.001195	0.002309	0.000244
6	39.4934	1.60417	0.002634	0.002147	0.000332
7	47.4504	1.8975	0.00319	0.002394	0.000471
8	56.7383	2.04759	0.009636	0.00275	0.000576
9	67.4526	2.4096	0.012982	0.003684	0.000691
10	79.4114	2.66455	0.010124	0.005064	0.001178
11	94.755	3.14634	0.022951	0.008058	0.000855
12	112.064	3.94574	0.021605	0.014543	0.00135
13	134.177	4.02791	0.002065	0.028737	0.001823

West Barrel-Endcap					
Bin	Dijet Mass (GeV)		A_{LL}		
	Mass	Sys. Error	A_{LL}	Stat. Error	Sys. Error
1	15.9856	1.08427	0.00171	0.004208	0.000237
2	19.3344	1.19491	0.000774	0.002833	0.00023
3	23.0753	1.22083	0.00195	0.002112	0.000196
4	27.9246	1.19267	0.003809	0.001879	0.00026
5	33.3435	1.6759	0.004424	0.002075	0.000356
6	39.1838	1.48639	0.001506	0.002079	0.000569
7	47.2693	1.77625	0.006827	0.002511	0.00068
8	56.2091	1.99415	0.007382	0.003234	0.000988
9	66.2817	2.24949	0.007229	0.004986	0.001197
10	78.4715	2.56444	0.00361	0.007994	0.001365
11	92.7038	2.93018	0.051492	0.015123	0.001454
12	111.282	3.58153	-0.055524	0.033007	0.002678
13	127.234	5.10245	-0.042388	0.081357	0.007099

Table 7.17: Final dijet A_{LL} for the two Barrel-Endcap topologies, 2012+2013.

CHAPTER 8

Conclusion

The proton's spin is made up of contributions from the intrinsic spins and orbital angular momenta of its constituent quarks and gluons. Polarized deep inelastic scattering measurements have found that the intrinsic quark spins contribute only about one-third of the proton's total spin; how the intrinsic gluon spins and partonic orbital motion provide the rest remains an open question. One way to probe the gluon contribution is through polarized proton-proton collisions carried out at the Relativistic Heavy Ion Collider, which is the first and only accelerator in the world capable of colliding polarized protons.

This dissertation presented a measurement of the longitudinal double-spin asymmetry A_{LL} for dijet production, an observable which is particularly sensitive to the gluon polarized parton distribution function $\Delta g(x)$, in polarized proton-proton collisions at $\sqrt{s} = 510$ GeV during the 2012 and 2013 RHIC runs. There have been several prior analyses of both inclusive jets and dijets using data from the Solenoidal Tracker at RHIC. The 2009 STAR inclusive jet A_{LL} results, when included in the DSSV and NNPDF global analyses, showed a nonzero gluon polarization for the first time. However, the shape of $\Delta g(x)$ at low values of Bjorken- x in particular remains poorly constrained. The two ways to probe low- x gluons at STAR are jet measurements for pp collisions at higher center-of-mass energies and at more forward pseudorapidities, with dijet measurements providing greater constraints on the initial partonic kinematics than inclusive measurements. Jet reconstruction at larger η requires the Endcap Electromagnetic Calorimeter, and the first jet analysis which used

the EEMC was a measurement of A_{LL} for dijet production using 2009 data at $\sqrt{s} = 200$ GeV. The analysis described in this dissertation is the first measurement of A_{LL} for dijets both in the EEMC region and at $\sqrt{s} = 510$ GeV, a combination which provides the greatest sensitivity to the polarization of low momentum gluons currently possible at STAR.

The partonic momentum fractions of gluons accessible in this measurement are shown in Fig. 8.1, weighted by the partonic \hat{a}_{LL} and separated by topology for dijets with invariant masses between 17 and 20 GeV/ c^2 . Comparison with Figs. 1.10 and 1.12 shows the advantages of a dijet measurement at both forward pseudorapidities and 510 GeV, relative to just one of those conditions. A way to see this effect in the data is to scale the dijet invariant mass by the collision center-of-mass energy. In inclusive jet analyses, results from measurements of A_{LL} at different center-of-mass energies are plotted versus $x_T = 2p_T/\sqrt{s}$, which is correlated with the initial partonic longitudinal momentum fraction x . Analogously, we plot the dijet A_{LL} points versus M/\sqrt{s} in Fig. 8.2. That figure plots the results of both this analysis and the 2009 forward dijet results, where the parton level dijet invariant masses of both measurements have been scaled by their respective energies so that the A_{LL} can be compared directly. The lower kinematic reach of the 510 GeV measurement is readily apparent, as are the greatly improved statistics. The improved statistics are a result of not only the increased integrated luminosities in 2012 and 2013 compared to 2009 (when 21 pb⁻¹ were recorded), but also the inclusion of the dijet triggers in 2013, which were specifically designed to enhance the yield of low invariant mass dijet events.

Plotting A_{LL} versus M/\sqrt{s} also helps demonstrate how the low invariant mass bins provide sensitivity to low- x gluons. From Eq. 1.10c, at leading order, the dijet invariant mass divided by \sqrt{s} is equal to the square root of the product of the partonic momentum fractions, so these bins contain dijet events arising from hard scatterings of partons with low momentum fractions. In particular, Endcap-Endcap events must come from highly asymmetric collisions since one parton is being scattered backwards, so $x_1 \gg x_2$. Then x_2 is indeed very small, exactly as shown in the bottom panel of Fig. 8.1. The mass range in that

figure, $17 < M < 20 \text{ GeV}/c^2$, corresponds to the second-lowest data point in each panel of Fig. 8.2. Partons with such low momentum fractions are overwhelmingly gluons, as can be seen in the unpolarized parton distribution functions shown in Fig. 8.3. Thus, a measurement of A_{LL} for dijets at larger pseudorapidities in 510 GeV pp collisions is very sensitive to low momentum gluons. These results will therefore help to more tightly constrain the size and shape of $\Delta g(x)$ at low Bjorken- x when added to the global analyses of current theoretical groups.

The general agreement of the data with the theory curves for the West Barrel-Endcap topology suggests that their inclusion in global analyses will mostly reduce the uncertainties on $\Delta g(x)$ without significantly changing the values. On the other hand, the East Barrel-Endcap results are significantly more positive than the theoretical predictions in the higher invariant mass bins. Finally, given that there are no other jet data which reach as low in x as the lowest few Endcap-Endcap invariant mass bins, even small deviations from theory in that region could have significant effects. It is unclear how these results will affect the global analyses in a quantitative way, but qualitatively the East-Barrel Endcap data will tend to pull the fits toward larger values of $\Delta g(x)$ in the higher x range, and the Endcap-Endcap data will possibly have a similar effect in the lowest x range.

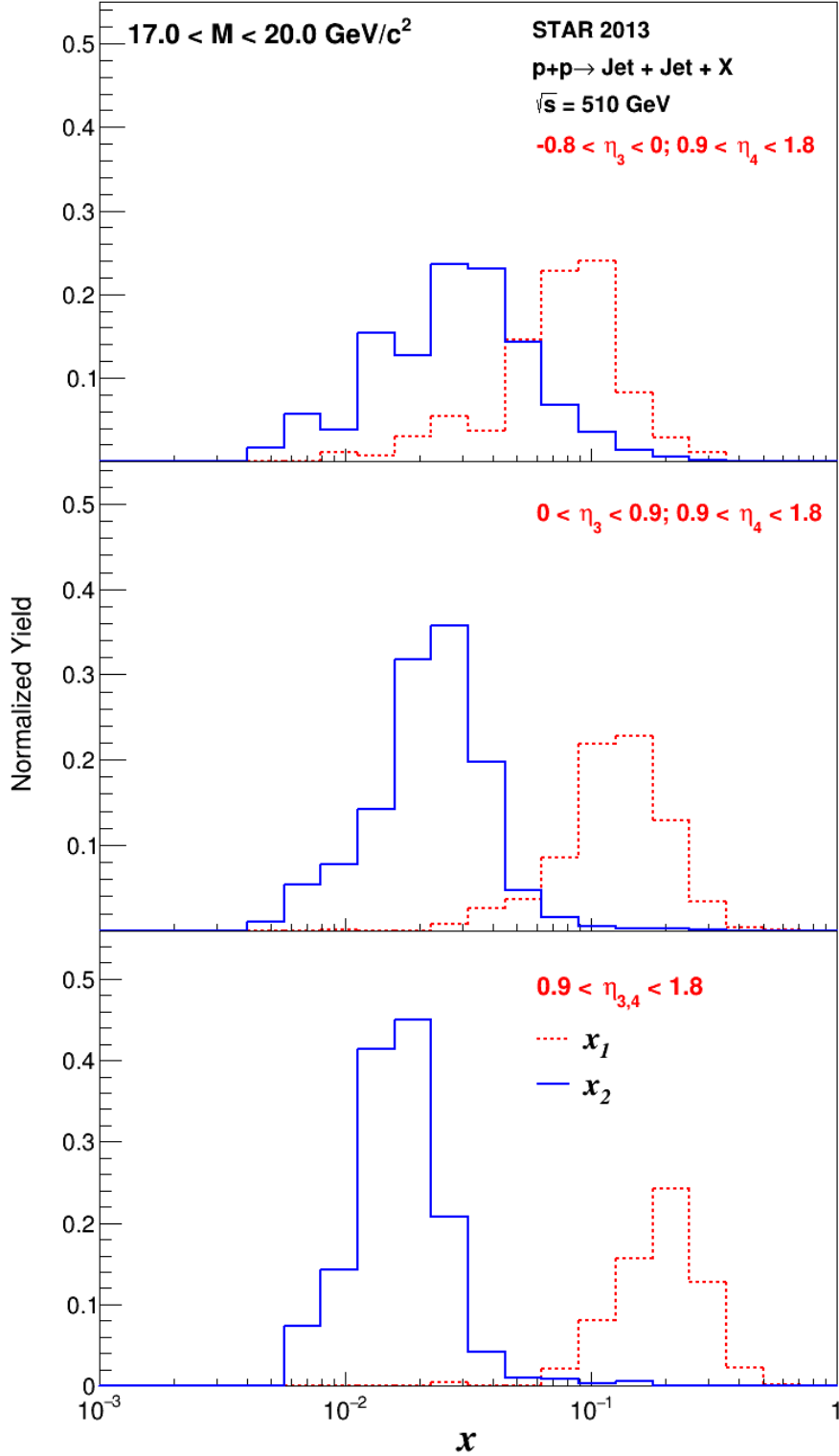


Figure 8.1: Distributions of parton x_1 and x_2 from leading order simulation at $\sqrt{s} = 510$ GeV for East Barrel-Endcap (upper plot), West Barrel-Endcap (middle plot), and Endcap-Endcap (lower plot) topologies. x_1 is always associated with the parton initially moving toward the Endcap.

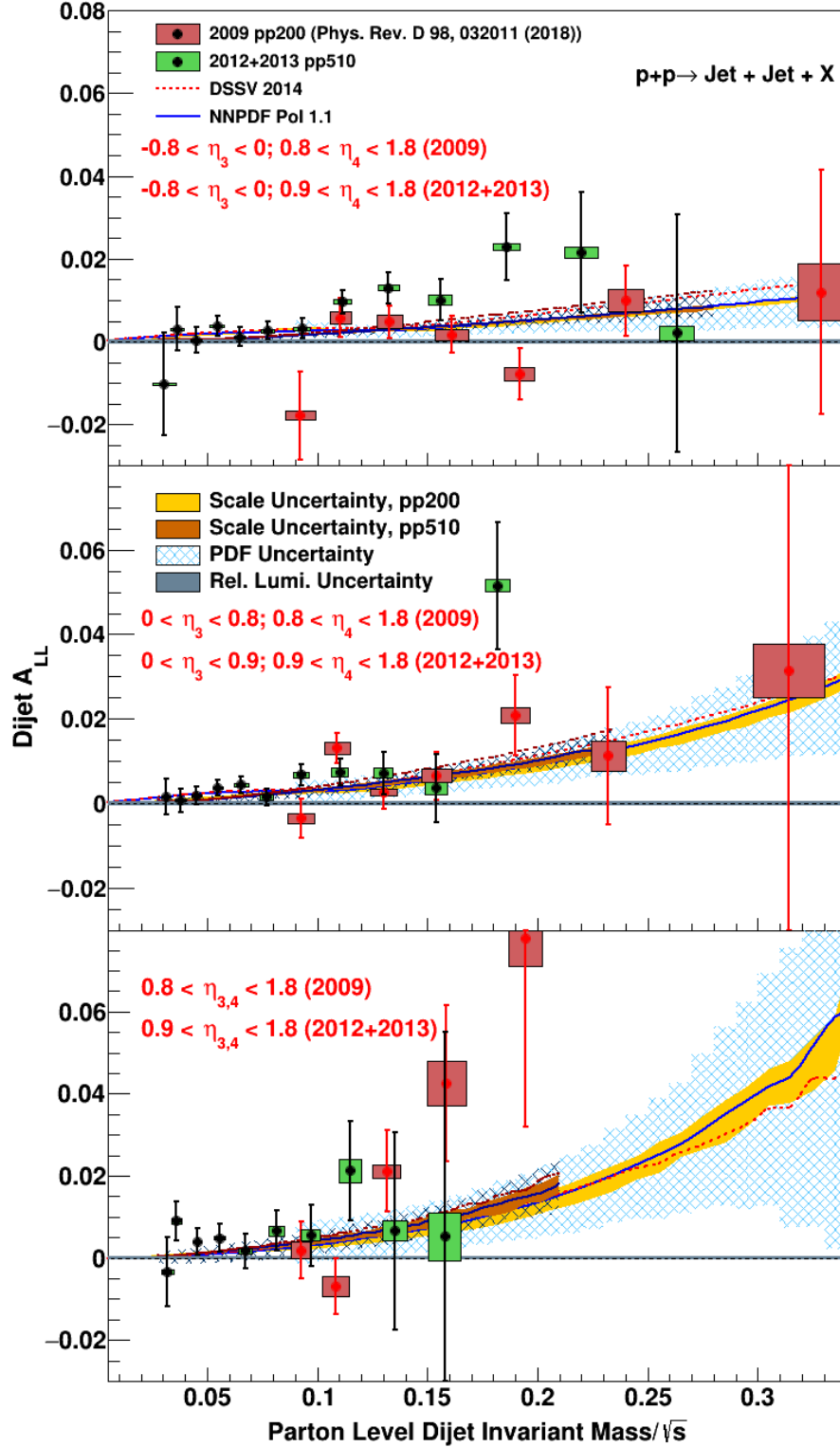


Figure 8.2: Dijet A_{LL} versus parton-level dijet invariant mass divided by \sqrt{s} , for the 2009 [34] and 2012+2013 datasets. Results are shown for the East Barrel-Endcap (top plot), West Barrel-Endcap (middle plot), and Endcap-Endcap (bottom plot) topologies. Note the 2009 analysis used $\eta = 0.8$ as the cutoff between Barrel and Endcap jets.

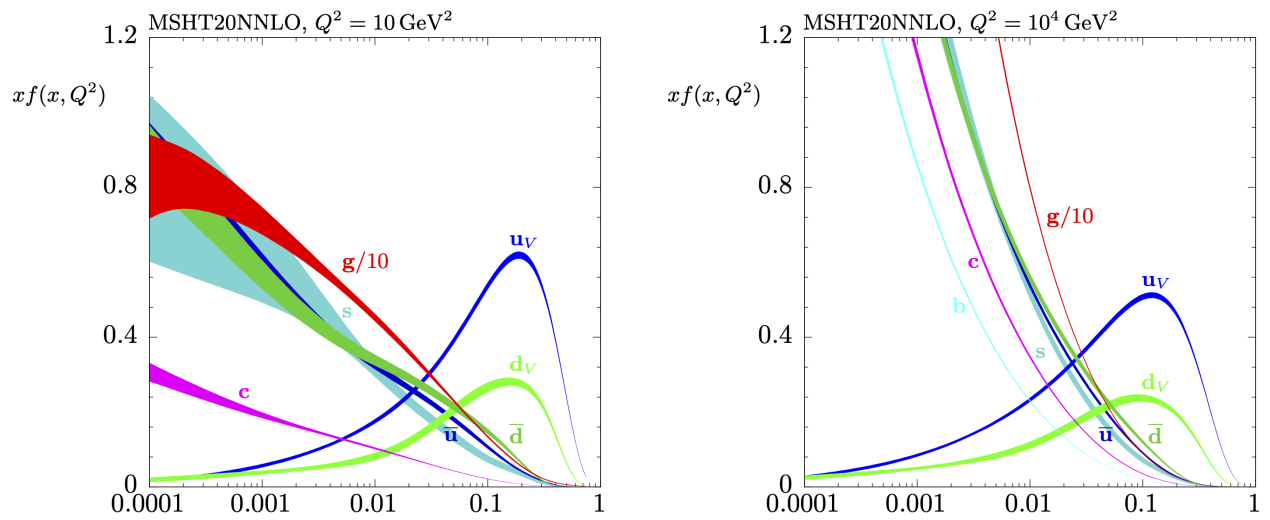


Figure 8.3: NNLO parton distribution functions from the MSHT20 global analysis [71], at two different values of Q^2 . The width of each line is the uncertainty in the PDF for that parton.

Appendix A

Lists of Runs and Fills

A.1 2012 Analysis

List of Runs:

13077066 13077067 13077068 13077069 13077070 13077073 13077075 13077076 13077078
13077081 13078001 13078002 13078003 13078004 13078006 13078007 13078009 13078011
13078012 13078014 13078028 13078035 13078036 13078037 13078039 13078040 13078042
13078043 13078045 13078050 13078051 13078052 13078054 13078055 13078057 13078058
13078063 13078070 13079032 13079033 13079034 13079035 13079036 13079037 13079038
13079073 13079074 13079075 13079076 13079077 13079079 13080001 13080002 13080003
13080004 13080005 13080010 13080011 13080013 13080014 13080015 13080090 13080091
13080092 13080093 13080094 13080095 13080096 13080097 13080098 13080099 13081001
13081004 13081005 13081007 13081020 13082001 13082002 13082003 13082004 13082005
13082006 13082007 13082008 13082009 13082010 13082011 13083067 13083068 13083069
13083070 13083073 13083074 13083076 13083081 13083082 13083084 13084001 13084007
13084008 13084023 13084024 13084027 13084028 13084032 13084034 13084035 13084036
13084037 13084038 13084039 13084040 13084041 13085004 13085005 13085006 13085008
13085009 13085010 13085011 13085028 13085029 13085030 13085031 13085032 13085033
13085034 13085036 13085040 13085041 13085047 13085061 13086002 13086003 13086065
13086067 13086070 13086071 13086072 13086073 13086078 13086079 13086080 13086081

13086082 13086083 13086085 13086087 13086088 13087009 13087010 13087011 13087012
13087013 13087015 13087016 13087025 13090005 13090006 13090007 13090008 13090011
13090012 13090015 13090016 13090017 13090018 13090019 13090021 13090022 13090023
13090035 13090037 13090038 13090039 13090040 13090043 13090048 13090049 13091001
13091005 13091009 13091011 13091012 13091019 13091020 13091023 13091024 13091025
13091027 13091032 13091033 13091034 13091035 13091036 13091037 13091038 13091041
13091043 13091044 13091045 13092005 13092006 13092007 13092008 13092044 13092045
13092046 13093015 13093017 13093018 13093020 13093023 13093024 13093025 13093029
13093030 13093034 13093035 13093036 13093037 13093038 13093044 13093045 13093046
13094001 13094003 13094004 13094005 13094007 13094008 13094009 13094010 13094011
13094013 13094014 13094015 13094016 13094017 13094018 13094020 13094021 13094045
13094050 13094052 13094053 13094054 13094081 13094082 13094083 13094089 13094091
13095001 13095002 13095003 13095004 13095006 13095008 13095009 13095012 13095013
13095014 13095015 13095016 13095017 13095043 13095049 13096001 13096002 13096003
13096004 13096005 13096006 13096060 13096061 13096062 13096063 13096064 13096065
13096066 13096069 13096070 13097001 13097002 13097003 13097004 13097005 13097006
13097007 13097021 13097022 13097023 13097024 13097026 13097027 13097028 13097029
13097032 13097033 13097034 13097035 13097036 13097037 13097038 13097039 13100003
13100004 13100005 13100006 13100008 13100010 13100011 13100012 13100013 13100014
13100015 13100025 13100026 13100027 13100029 13100030 13100031 13100032 13100033
13100034 13100035 13100037 13100038 13100040 13100041 13100042 13100051 13100053
13100054 13100055 13100056 13100057 13100059 13100060 13101001 13101002 13101003
13101004 13101005 13101006 13101007 13101013 13101015 13101021 13101024 13101026
13101027 13101040 13101041 13101042 13101043 13101044 13101045 13101046 13101047
13101048 13101049 13101050 13103003 13103004 13103011 13103013 13103014 13103015
13103016 13103017 13104003 13104004 13104008 13104011 13104012 13104013 13104014
13104019 13104044 13104054 13104056 13104057 13104058 13104059 13104060 13104061

13104062 13104063 13105006 13105007 13105008 13105009 13105010 13105011 13105012
13105014 13105015 13105016 13105017 13105018 13105022 13105038 13105039 13105040
13105041 13106064 13106069 13106071 13106072 13106073 13106074 13106075 13106076
13107001 13107002 13107003 13107015 13107016 13107017 13107019 13107021 13107024
13107025 13107026 13107027 13107028 13107029 13107030 13107032 13107033 13107034
13107059 13107060 13107062 13108001 13108008 13108009 13108010 13108011 13108012
13108013 13108016 13108025 13108026 13108028 13108029 13108031 13108033 13108034
13108040 13108050 13108071 13108072 13108073 13108074 13108079 13109015 13109016
13109017 13109018 13109025 13109026 13109027

List of Fills:

16582 16586 16587 16592 16593 16594 16597 16602 16619 16620 16622 16625 16626 16627
16632 16650 16655 16656 16659 16662 16667 16668 16669 16671 16678 16685 16686 16697
16698 16699 16701 16704 16710 16716 16717 16720 16722 16723 16726 16727 16730 16731
16732 16735

A.2 2013 Analysis

List of Runs:

14081006 14081007 14081009 14081010 14081013 14082029 14082030 14082031 14082033
14082034 14082036 14082037 14083005 14083006 14083007 14083008 14083009 14083019
14083020 14083021 14083022 14083034 14083036 14083038 14083039 14083041 14083043
14083044 14083045 14083047 14083051 14083055 14083056 14083057 14084005 14084008
14084009 14084010 14084013 14084014 14084018 14084019 14084020 14084021 14084057
14084058 14084059 14084061 14085063 14085069 14086001 14086013 14086016 14086018
14086019 14086020 14086022 14087033 14087035 14087036 14087037 14088002 14088003
14088007 14088009 14088010 14088027 14088105 14088108 14088136 14088138 14088140
14088141 14088142 14089001 14089002 14089003 14089004 14089008 14089010 14089011

14089012 14089014 14089015 14089022 14089023 14089034 14089035 14089036 14089037
14089044 14090004 14090005 14090006 14090007 14090008 14090013 14090040 14090041
14090042 14090045 14090046 14090047 14090049 14090050 14090051 14090052 14090053
14091002 14091003 14091004 14091005 14091006 14091008 14091013 14091016 14091017
14091018 14091019 14091020 14091021 14091022 14091023 14091026 14091027 14091028
14091029 14091030 14091033 14091034 14091064 14091065 14092001 14092002 14092004
14092005 14092010 14092011 14092015 14092024 14092030 14092057 14092058 14092061
14092062 14092063 14092065 14092067 14092068 14092071 14092087 14092090 14092091
14092092 14092093 14092097 14092098 14092099 14092100 14092101 14092104 14092105
14092106 14092107 14092108 14092109 14092110 14093001 14093005 14093006 14093007
14093008 14093009 14093010 14093014 14093015 14093016 14093017 14093018 14093019
14093020 14093021 14094005 14094006 14094007 14094008 14094020 14094022 14094024
14095019 14095020 14095022 14095023 14095024 14095025 14095027 14095029 14095034
14095035 14095044 14096010 14096011 14096013 14096014 14096077 14096078 14096082
14096083 14096085 14096098 14096099 14096100 14096101 14096102 14096104 14096105
14096106 14096108 14097005 14097006 14097014 14097018 14097019 14097020 14097021
14097022 14097023 14097026 14097028 14097030 14097033 14097036 14097037 14097038
14097039 14097061 14097062 14097063 14097064 14097065 14097066 14097067 14097068
14097070 14098004 14098015 14098016 14098017 14098026 14098027 14098028 14098029
14098031 14098032 14098033 14098039 14098046 14098047 14099013 14099014 14099015
14099016 14099017 14099018 14099020 14099024 14099025 14099027 14099029 14099030
14099031 14099032 14099033 14099090 14100004 14100009 14100014 14100018 14100021
14100022 14101044 14101048 14101050 14101051 14101052 14101053 14101054 14101060
14101061 14101062 14101063 14101064 14101065 14101066 14101067 14101068 14102029
14102030 14102031 14102032 14102034 14102035 14102036 14102037 14102041 14102042
14102043 14102047 14102049 14104015 14104017 14104018 14104021 14104025 14104026
14104039 14104040 14104041 14104042 14104044 14104046 14104047 14104049 14104050

14104051 14104052 14104053 14104059 14104060 14104061 14104062 14104063 14105001
14105002 14105006 14105007 14105008 14105009 14105011 14105013 14105014 14105015
14105016 14105019 14105020 14105021 14105022 14105024 14105025 14105029 14105031
14105032 14105033 14105034 14105036 14105037 14105038 14105039 14105043 14106002
14106003 14106004 14106005 14106007 14106035 14106036 14106037 14106041 14106042
14106043 14107017 14107018 14107133 14107134 14107139 14107141 14107144 14108001
14108002 14108003 14108005 14108006 14108007 14108013 14108014 14108015 14108017
14108019 14108059 14108077 14108078 14108080 14108081 14108083 14108084 14108085
14108091 14108092 14108093 14108095 14108096 14108097 14109046 14109047 14109052
14109082 14110024 14110044 14110045 14110046 14110048 14110050 14110051 14110052
14110053 14110054 14110055 14110056 14110058 14110059 14110060 14110061 14110062
14110064 14110065 14111036 14111038 14111051 14111052 14111053 14111055 14111056
14111057 14111058 14111060 14111062 14111063 14111064 14111066 14111067 14111070
14111071 14112001 14112023 14112024 14112027 14112031 14112032 14112034 14112035
14112038 14112040 14112041 14112042 14112044 14112094 14112096 14112098 14113001
14113003 14113004 14113006 14113007 14113008 14113009 14113010 14113011 14113012
14113015 14113016 14113017 14113018 14113019 14113036 14113037 14113038 14113039
14113062 14113065 14113066 14113067 14113076 14113078 14113093 14113096 14114002
14114004 14114005 14114006 14114007 14114008 14114011 14114012 14114013 14114014
14114015 14114016 14114018 14114019 14115007 14115008 14115010 14115011 14115012
14115013 14115015 14115017 14115018 14115019 14115020 14115022 14115023 14115024
14116011 14116014 14116015 14116016 14116019 14116020 14117012 14117013 14117014
14117015 14117024 14117025 14117026 14117027 14117028 14117047 14117055 14117056
14117058 14117059 14117061 14117063 14117064 14117069 14118014 14118015 14118016
14118017 14118018 14118020 14118021 14118022 14118023 14118028 14118030 14118032
14118033 14118034 14118035 14118048 14118049 14118051 14118052 14118056 14118059
14118060 14118061 14118063 14118064 14119007 14119008 14119009 14119010 14119014

14119017 14119018 14119019 14119022 14119024 14119026 14119027 14119052 14119053
14119059 14119060 14119061 14120011 14120017 14120018 14120019 14120025 14120026
14122058 14122060 14122061 14122062 14123001 14123002 14123004 14123005 14123008
14123009 14123010 14123015 14123016 14123024 14123025 14123026 14123028 14123029
14123030 14123032 14123033 14123034 14123035 14123037 14123038 14123039 14123040
14123053 14123054 14123056 14123057 14123059 14123060 14123061 14123076 14123077
14123078 14124001 14124003 14124004 14124005 14124006 14124007 14124009 14124013
14124014 14124016 14124017 14124018 14124019 14124025 14124026 14124027 14124028
14124029 14124030 14124033 14124034 14124035 14124036 14124037 14124038 14125002
14125003 14125004 14125056 14125060 14126003 14126004 14126005 14126006 14126008
14126009 14126011 14126012 14126013 14126014 14126015

List of Fills:

17256 17263 17268 17269 17273 17276 17284 17293 17297 17301 17302 17304 17306 17308
17311 17312 17315 17317 17318 17322 17329 17331 17333 17335 17338 17340 17341 17345
17347 17352 17359 17367 17368 17379 17380 17382 17384 17389 17391 17394 17396 17399
17403 17405 17406 17407 17409 17410 17414 17415 17416 17417 17423 17426 17427 17429
17430 17431 17433 17434 17436 17438 17439 17440 17447 17451 17452 17453 17454 17455
17461 17466

Appendix B

Dijet Invariant Mass Derivation

In this Appendix we derive the dijet invariant mass formula 1.11, which is simply the invariant mass of a relativistic system of two 4-vectors. We start by defining the transverse mass $m_T \equiv \sqrt{m^2 + p_x^2 + p_y^2}$ and rapidity $y \equiv \frac{1}{2} \ln \left(\frac{E+p_z}{E-p_z} \right)$. The energy-momentum relation can be rewritten as:

$$E^2 = p^2 + m^2 = p_x^2 + p_y^2 + p_z^2 + m^2 = m_T^2 + p_z^2. \quad (\text{B.1})$$

Rearranging then gives:

$$\left(\frac{E}{m_T} \right)^2 - \left(\frac{p_z}{m_T} \right)^2 = 1. \quad (\text{B.2})$$

This looks like the identity $\cosh^2 y - \sinh^2 y = 1$, so we posit that $E = m_T \cosh y$ and $p_z = m_T \sinh y$. To confirm, we divide the equations to get $p_z/E = \tanh y$, which implies:

$$y = \tanh^{-1} \left(\frac{p_z}{E} \right) = \frac{1}{2} \ln \left(\frac{1 + p_z/E}{1 - p_z/E} \right) = \frac{1}{2} \ln \left(\frac{E + p_z}{E - p_z} \right), \quad (\text{B.3})$$

the definition of rapidity. So now we can write the 4-momentum vector as:

$$P = \begin{bmatrix} E \\ p_x \\ p_y \\ p_z \end{bmatrix} = \begin{bmatrix} m_T \cosh y \\ p_T \cos \phi \\ p_T \sin \phi \\ m_T \sinh y \end{bmatrix}, \quad (\text{B.4})$$

where $p_T = \sqrt{p_x^2 + p_y^2}$ and ϕ is the relative angle. The invariant mass of a dijet system is $M = \sqrt{(P_3 + P_4)^2} = \sqrt{P_3^2 + P_4^2 + 2P_3 \cdot P_4}$, where P_3 and P_4 are the 4-momenta of the two outgoing partons. $P_i^2 = m_i^2$, and the cross term is:

$$\begin{aligned}
2P_3 \cdot P_4 &= 2[m_{T,3}m_{T,4}(\cosh y_3 \cosh y_4 - \sinh y_3 \sinh y_4) - p_{T,3}p_{T,4}(\cos \phi_3 \cos \phi_4 + \sin \phi_3 \sin \phi_4)] \\
&= 2[m_{T,3}m_{T,4} \cosh (y_3 - y_4) - p_{T,3}p_{T,4} \cos (\phi_3 - \phi_4)] \\
&= 2[\sqrt{m_3^2 + p_{T,3}^2} \sqrt{m_4^2 + p_{T,4}^2} \cosh (y_3 - y_4) - p_{T,3}p_{T,4} \cos (\phi_3 - \phi_4)].
\end{aligned} \tag{B.5}$$

Combining all the terms, the dijet invariant mass is:

$$M = \sqrt{m_3^2 + m_4^2 + 2\sqrt{m_3^2 + p_{T,3}^2} \sqrt{m_4^2 + p_{T,4}^2} \cosh (y_3 - y_4) - 2p_{T,3}p_{T,4} \cos (\phi_3 - \phi_4)}. \tag{B.6}$$

Appendix C

Lists of Removed Bunch Crossings

Fill	Bunch Crossing	Fill	Bunch Crossing
16582	0 40 61 62 80 -1	16678	0 40 70 71 -1
16586	0 40 -1	16685	0 23 24 40 -1
16587	0 29 40 -1	16686	0 17 18 40 -1
16592	0 40 -1	16697	0 40 108 109 -1
16593	0 9 10 40 -1	16698	0 40 -1
16594	0 40 -1	16699	0 40 57 -1
16597	0 27 28 40 -1	16701	0 21 22 28 29 40 99 -1
16602	0 40 56 57 108 -1	16704	0 40 90 91 92 101 102 -1
16619-16622	0 40 -1	16710	0 40 98 -1
16625	0 23 24 40 -1	16716	0 40 80 -1
16626	0 12 13 19 20 40 -1	16717	0 9 40 56 65 78 94 101 -1
16627-16632	0 40 -1	16720	0 7 8 40 110 -1
16650	0 40 58 59 -1	16722-16726	0 40 -1
16655	0 40 75 76 -1	16727	0 40 80 -1
16656	0 15 16 40 -1	16730	0 40 88 -1
16659	0 40 81 98 105 107 -1	16731	0 26 40 60 61 -1
16662-16667	0 40 -1	16732	0 40 71 80 -1
16668-16669	0 26 27 40 -1	16735	0 40 -1
16671	0 40 96 97 -1		

Table C.1: Bunch crossings removed for the 2012 analysis.

Fill	Bunch Crossing
17256-17407	69 70
17281	1 2
17318	84
17322	61
17384	29 30
17416	79
17423	13

Table C.2: Bunch crossings removed for the 2013 analysis.

Bibliography

- [1] M. Breidenbach, J. I. Friedman, H. W. Kendall, E. D. Bloom, D. H. Coward, H. DeStaebler, J. Drees, L. W. Mo, and R. E. Taylor. Observed behavior of highly inelastic electron-proton scattering. *Phys. Rev. Lett.*, 23:935—939, 1969.
- [2] E. D. Bloom, D. H. Coward, H. DeStaebler, J. Drees, G. Miller, L. W. Mo, R. E. Taylor, M. Breidenbach, J. I. Friedman, G. C. Hartmann, and H. W. Kendall. High-energy inelastic $e - p$ scattering at 6° and 10° . *Phys. Rev. Lett.*, 23:930—934, 1969.
- [3] R.E. Taylor, Deep inelastic scattering: The early years, *Rev. Mod. Phys.*, 63:573—595, 1991.
- [4] H.W. Kendall, Deep inelastic scattering: Experiments on the proton and the observation of scaling, *Rev. Mod. Phys.*, 63:597—614, 1991.
- [5] J.I. Friedman, Deep inelastic scattering: Comparisons with the quark model, *Rev. Mod. Phys.*, 63:615—627, 1991.
- [6] J. Bjorken, Asymptotic sum rules at infinite momentum, *Phys. Rev.*, 179:1547—1553, 1969.
- [7] W.K.H. Panofsky in *Proceedings of the 14th International Conference on High Energy Physics*, 1968.
- [8] R.P. Feynman, Very high-energy collisions of hadrons, *Phys. Rev. Lett.*, 23:1415—1417, 1969.

- [9] M. Gell-Mann, A schematic model of baryons and mesons, *Physics Letters*, 8:214—215, 1964.
- [10] G. Zweig, An $su(3)$ model for strong interaction symmetry and its breaking. CERN-8182/Th.401, 1964.
- [11] J. Kuti, V.F. Weisskopf, Inelastic lepton-nucleon scattering and lepton pair production in the relativistic quark-parton model, *Phys. Rev. D*, 4:3418, 1971.
- [12] C. Patrignani et al. Review of Particle Physics. *Chin. Phys.*, C40(10):100001, 2016.
- [13] S.D. Bass, The proton spin puzzle: Where are we today?, *Modern Physics Letters A*, 24:1087—1101, 2009.
- [14] S.D. Bass, The spin structure of the proton, *Rev. Mod. Phys.*, 77:1257—1302, 2005.
- [15] M. Anselmino, A. Efremov, E. Leader, The theory and phenomenology of polarized deep inelastic scattering, *Physics Reports*, 261:1—124, 1995.
- [16] S.E. Kuhn, J.P. Chen, E. Leader, Spin structure of the nucleon - status and recent results, *Prog. Part. and Nucl. Phys.*, 63:1—50, 2009.
- [17] E. Leader, *Spin in Particle Physics*. Cambridge University Press, 2005.
- [18] J. Ashman et al. (European Muon Collaboration), A measurement of the spin asymmetry and determination of the structure function g_1 in deep inelastic muon-proton scattering, *Phys. Lett. B*, 206:364—370, 1988.
- [19] J. Ashman et al. (European Muon Collaboration), An investigation of the spin structure of the proton in deep inelastic scattering of polarised muons on polarised protons, *Nucl. Phys. B*, 328:1—35, 1988.
- [20] J.R. Ellis and R.L. Jaffe, A sum rule for deep inelastic electroproduction from polarized protons, *Phys. Rev. D*, 9:1444—1446, 1974.

- [21] R.L Jaffe and A. Manohar, The g1 problem: Deep inelastic electron scattering and the spin of the proton, *Nucl. Phys. B*, 337:509—546, 1990.
- [22] E. Leader, A.V. Sidorov, D.B. Stamenov, Impact of CLAS and COMPASS data on polarized parton densities and higher twist, *Phys. Rev. D*, 75:074027, 2007.
- [23] Christine A. Aidala, Steven D. Bass, Delia Hasch, and Gerhard K. Mallot. The Spin Structure of the Nucleon. *Rev. Mod. Phys.*, 85:655—691, 2013.
- [24] E.C. Aschenauer et al., The RHIC SPIN Program. www.bnl.gov/npp/docs/RHIC-Spin-WriteUp-121105.pdf, 2012.
- [25] J. Beringer et al. (Particle Data Group), Review of particle physics, *Phys. Rev. D*, 86:010001, 2012.
- [26] J. Pumplin, D. R. Stump, J. Huston, H. L. Lai, P. M. Nadolsky, and W. K. Tung, JHEP 07, 012 (2002).
- [27] A. Mukherjee and W. Vogelsang, *Phys. Rev. D* 86, 094009 (2012).
- [28] Daniel de Florian, Rodolfo Sassot, Marco Stratmann, and Werner Vogelsang. Evidence for polarization of gluons in the proton. *Phys. Rev. Lett.*, 113:012001, 2014.
- [29] Emanuele R. Nocera, Richard D. Ball, Stefano Forte, Giovanni Ridolfi, and Juan Rojo. A first unbiased global determination of polarized pdfs and their uncertainties. *Nuclear Physics B*, 887:276—308, 2014.
- [30] L. Adamczyk et al. Precision measurement of the longitudinal double-spin asymmetry for inclusive jet production in polarized proton collisions at $\sqrt{s} = 200$ GeV. *Phys. Rev. Lett.*, 115:092002, 2015.
- [31] A. Adare et al. Inclusive double-helicity asymmetries in neutral-pion and eta-meson production in $\vec{p} + \vec{p}$ collisions at $\sqrt{s} = 200$ GeV. *Phys. Rev.*, D90(1):012007, 2014.

- [32] L. Adamczyk et al. Measurement of the cross section and longitudinal double-spin asymmetry for dijet production in polarized pp collisions at $\sqrt{s} = 200$ GeV. *Phys. Rev. D*, 95:071103, 2017.
- [33] S. Mrenna, T. Sjostrand, and P. Z. Skands. Pythia 6.4 physics and manual. *Journal of High Energy Physics*, 2006(05):026, 2006.
- [34] J. Adam et al. Longitudinal Double-Spin Asymmetries for Dijet Production at Intermediate Pseudorapidity in Polarized pp Collisions at $\sqrt{s} = 200$ GeV. *Phys. Rev. D.*, 98:032011, 2018.
- [35] N.S. Craigie, K. Hidaka, M. Jacob, and F. M. Renard, Phys. Rept. 99, 69 (1983).
- [36] J. Adam et al. Longitudinal double-spin asymmetry for inclusive jet and dijet production in pp collisions at $\sqrt{s} = 510$ GeV. *Phys. Rev. D.*, 100:052005, 2019.
- [37] M. Harrison, T. Ludlam, and S. Ozaki. RHIC project overview. *Nucl. Instrum. Meth. A*, 499(2):235—244, 2003.
- [38] H. Hahn et al. The RHIC design overview. *Nucl. Instrum. Meth. A*, 499:245—263, 2003.
- [39] I. Alekseev, C. Allgower, M. Bai, et al. Polarized proton collider at RHIC. *Nucl. Instrum. Meth. A*, 499:392—414, 2003.
- [40] A. Zelenski, J. Alessi, B. Briscoe, et al. Optically pumped polarized H- ion source for RHIC spin physics. *Rev. Sci. Instrum.*, 73:888—891, 2002.
- [41] Ya.S. Derbenev, et al. *Part. Accel.* 8, 115, 1978.
- [42] A. Zelenski, A. Bravar, D. Graham, W. Haeberli, et al. Absolute polarized H-jet polarimeter development for RHIC. *nucl. Instrum. Meth. A*, 536:248—254, 2005

- [43] H. Okada, I.G. Alekseev, A. Bravar, et al. Measurement of the analyzing power a_N in pp elastic scattering in the CNI region with a polarized atomic hydrogen gas jet target. *Phys. Lett. B*, 638(5):450—454, 2006.
- [44] J. Kiryluk. Local polarimetry for proton beams with the STAR beam beam counters. In *Spin Physics. Polarized electron sources and polarimeters. Proceedings, 16th International Symposium, SPIN 2004*, 718—721, 2005.
- [45] C.A. Whitten. The Beam-Beam Counter: A Local Polarimeter at STAR. In *Polarized Ion Sources, Targets and Polarimetry* (A. Kponou, Y. Makdisi, A. Zelenski, ed.), vol. 980 of *American Institute of Physics Conference Series*, 390—396, 2008.
- [46] W. Llope, J. Zhou, T. Nussbaum, G. Hoffmann, K. Asselta, J. Brandenburg, J. Butterworth, T. Camarda, W. Christie, H. Crawford, et al., arXiv:1403.6855 [physics.ins-det].
- [47] K.H. Ackermann, N. Adams, C. Adler, et al. STAR detector overview. *Nucl. Instrum. Meth. A*, 499:624—632, 2003.
- [48] M. Anderson, J. Berkovitz, W. Betts, et al. The STAR time projection chamber: a unique tool for studying high multiplicity events at RHIC. *Nucl. Instrum. Meth. A*, 499:659—678, 2003.
- [49] F. Bergsma, C.O. Blyth, R.L. Brown, et al. The STAR detector magnet subsystem. *Nucl. Instrum. Meth. A*, 499:633—639, 2003.
- [50] M. Beddo, E. Bielick, T. Fornek, et al. The STAR barrel electromagnetic calorimeter. *Nucl. Instrum. Meth. A*, 499:725—739, 2003.
- [51] C.E. Allgower, B.D. Anderson, A.R. Baldwin, et al. The STAR endcap electromagnetic calorimeter. *Nucl. Instrum. Meth. A*, 499:740—750, 2003.
- [52] F. S. Bieser et al. The STAR trigger. *Nucl. Instrum. Meth. A*, 499:766—777, 2003.

- [53] A. Ali, G. Kramer. Jets and QCD: A Historical Review of the Discovery of the Quark and Gluon Jets and its Impact on QCD. *Eur. Phys. J. H*, 36:245—326, 2011.
- [54] G.P. Salam. Towards Jetography. *Eur. Phys. J. C*, 67:637—686, 2010.
- [55] M. Cacciari, G.P. Salam, and G. Soyez. The Anti-k(t) jet clustering algorithm. *J. High Energy Phys.*, 04:063, 2008.
- [56] M. Cacciari, G.P. Salam, and G. Soyez. FastJet User Manual. *Eur. Phys. J. C*, 72:1896, 2012.
- [57] S. Frixione and G. Ridolfi. *Nucl. Phys. B*, 507:315, 1997.
- [58] T. Sjostrand, S. Mrenna, and P. Skands. PYTHIA 6.4 Physics and Manual. *J. High Energy Phys.*, 0605:026, 2006.
- [59] P. Skands. Tuning Monte Carlo generators: The Perugia tunes. *Phys. Rev. D*, 82:074018, 2010.
- [60] S. Agostinelli *et al.* (Geant4 Collaboration). GEANT4—a simulation toolkit. *Nucl. Instrum. Meth. A*, 506:250—303, 2003.
- [61] B. Abelev *et al.* (ALICE Collaboration). Charged jet cross sections and properties in proton-proton collisions at $\sqrt{s} = 7$ TeV. *Phys. Rev. D*, 91:112012, 2015.
- [62] M. Cacciari and G. P. Salam. Pileup subtraction using jet areas. *Phys. Lett. B*, 659:119—126, 2008.
- [63] A. Hoecker *et al.* TMVA - Toolkit for Multivariate Data Analysis. *PoS*, ACAT:040, 2007.
- [64] L. Adamczyk *et al.* Neutral pion cross section and spin asymmetries at intermediate pseudorapidity in polarized proton collisions at $\sqrt{s} = 200$ GeV. *Phys. Rev. D.*, 89:012001, 2014.

- [65] D. Cronin-Hennessy, A. Beretvas, and P. F. Derwent. *Nucl. Instrum. Meth. A*, 443:37, 2000.
- [66] W. B. Schmidke et al. RHIC Polarization for Runs 9-17, Brookhaven National Laboratory Report **BNL-209057-2018-TECH**, <https://technotes.bnl.gov/PDF?publicationId=209057> (2018).
- [67] Z. Chang, *Inclusive Jet Longitudinal Double-spin Asymmetry A_{LL} Measurements in 510 GeV Polarized pp Collisions at STAR*, Ph.D. thesis, Texas A&M University (2016), arXiv:1907.10368 [hep-ex].
- [68] J. Adams et. al. Measurements of transverse energy distributions in Au+Au collisions at $\sqrt{s_{NN}} = 200$ GeV. *Phys. Rev. C*, 70:054907, 2004.
- [69] L. Huo. In-Jet Tracking Efficiency Analysis for the STAR Time Projection Chamber in Polarized Proton-Proton Collisions at $\sqrt{s} = 200$ GeV. Masters thesis, Texas A&M University, (2012).
- [70] Z. Chang. Inclusive jet cross section status summary: hadron energy deposition in the BEMC. https://drupal.star.bnl.gov/STAR/system/files/jetcrs_summary_2.pdf.
- [71] S. Bailey et. al., arXiv:2012.04684 [hep-ph].